UTS UNIVERSITY OF TECHNOLOGY SYDNEY

Phase field fracture in elastoplastic solids: strain energy decomposition and shell formulations

by Yang Jiang

Thesis submitted in fulfilment of the requirements for the degree of

Doctor of Philosophy

under the supervision of

Principal Supervisor: Dr Jianguang Fang
Co-Supervisor: Prof Chenqing Wu

University of Technology Sydney
Faculty of Engineering and Information Technology

October 2025

CERTIFICATE OF ORIGINAL AUTHORSHIP

I, *Yang Jiang*, declare that this thesis is submitted in fulfilment of the requirements for the award of *Doctor of Philosophy*, in the *School of Civil and Environmental Engineering* (*Faculty of Engineering and Information Technology, FEIT*) at the University of Technology Sydney.

This thesis is wholly my own work unless otherwise referenced or acknowledged. In addition, I certify that all information sources and literature used are indicated in the thesis. This document has not been submitted for qualifications at any other academic institution. This research was supported by an Australian Government Research Training Program (RTP) Scholarship doi.org/10.82133/C42F-K220

Signature:

Production Note:
Signature removed prior to publication.

Date: 13/10/2025

ACKNOWLEDGEMENTS

As I near the end of my PhD journey—a moment I have envisioned countless times—I am filled with both gratitude and joy.

Firstly, I would like to express my deepest gratitude to my family—my parents and sister. They have always prioritized my needs, dedicating everything to support me. Since moving abroad for my studies, I have rarely had the opportunity to visit home, relying instead on video calls to stay connected. Their unwavering encouragement and joy in my achievements have always been my greatest motivation.

I am profoundly grateful to my supervisor, Dr. Jianguang Fang, an exceptional, intelligent, and considerate researcher. I feel incredibly fortunate to have had his guidance throughout my PhD. At the beginning of this journey, he helped me transition quickly into computational mechanics, a new research field for me. His patient mentorship has shaped my research direction, taught me how to write academic papers, and provided invaluable insights. Every discussion with him has been both technically enriching and personally inspiring. Beyond regular meetings, he has always been approachable and responsive. His dedication and mentorship have left a lasting impact, and he remains a true role model to me.

I would also like to extend my heartfelt gratitude to my co-supervisor, Prof. Chengqing Wu, for his invaluable guidance and encouragement. He has continuously inspired me to conduct practical research, bridging the fracture simulations with real-world engineering challenges. Additionally, I am sincerely grateful to Assoc. Prof. Sanjay, Assoc. Prof. Jun Li, and Dr. Xuzhen He for their valuable comments and suggestions, which have significantly contributed to enhancing the quality of this thesis.

I am also thankful to my teammates—Sapan, Cunyi, Sepideh, Meiyu, Di, Saber, Weilong, and Chuwei. Our discussions have broadened my knowledge and enriched my academic journey.

Furthermore, I would like to express my appreciation to my housemates, Feng Shan and Ye Hu. We have always supported each other and created a harmonious living

environment. I am also grateful to all the friends I have met in Sydney for their companionship and encouragement throughout these years.

I extend my sincere thanks to the CSC-UTS Joint Scholarship for providing financial support, enabling me to pursue my studies and live in Sydney.

Lastly, I wish to express my heartfelt appreciation to my girlfriend, Ting. Your unwavering support and understanding have given me the strength to face challenges and keep moving forward in life.

LIST OF PUBLICATIONS RELATED TO THIS RESEARCH

Journal Articles (Published)

[1] **Jiang, Y**., Li, C. Wu, C., Rabczuk, T., & Fang, J. (2023). A double-phase field method for mixed mode crack modelling in 3D elasto-plastic solids with crack-direction-based strain energy decomposition. ***Computer Methods in Applied Mechanics and Engineering***, 405, 115886. (**Chapter 3**)

Journal Articles (To be submitted)

[2] **Jiang, Y**., Li, C. Wu, C., & Fang, J. (2025). A unified strain energy decomposition strategy under the local coordinate system for phase field fracture modelling. (**Chapter 4**)

[3] **Jiang, Y**., Li, C. Wu, C., & Fang, J. (2025). Phase field fracture modelling for elasto-plastic shell incorporated with stress-based fracture initiation criterion. (**Chapter 5**)

[4] **Jiang, Y**., Li, C. Wu, C., & Fang, J. (2025). Phase field fracture in elasto-plastic solids: Application to shell fracture of battery casing. (**Chapter 6**)

[5] **Jiang, Y**., Li, C. Wu, C., & Fang, J. (2025). Dynamic fracture modelling with explicit shell phase field model. (**Chapter 7**)

TABLE OF CONTENTS

LIST OF FIGURES

LIST OF TABLES

LIST OF NOTATIONS

Ω	Arbitrary solid
$\partial\Omega$	External boundary of solid
$\partial\Omega^s$, $\partial\Omega^h$	Neumann boundary and Dirichlet boundary
$\boldsymbol{b}$	Body force within Ω
$\overline{\boldsymbol{u}}$	Boundary displacement on $\partial\Omega^s$
$\boldsymbol{t}$	Traction force on $\partial\Omega^h$
Γ	Sharp crack
Γ_t, Γ_c	Tensile/compression sharp crack
G_f	Crack energy release rate
G_t, G_c	Tensile/compression crack energy release rate
γ_l	Crack density function
γ_t, γ_c	Tensile/compression crack density function
$\boldsymbol{\sigma}$	Nominal stress tensor
$\overline{\boldsymbol{\sigma}}$	Effective (undamaged) stress tensor
$\boldsymbol{n}_1$, $\boldsymbol{n}_2$ and $\boldsymbol{n}_3$	Three principal directions of $\overline{\boldsymbol{\sigma}}$
σ_1, σ_2 and σ_3	Three principal stresses
p	Hydrostatic stress
$\boldsymbol{r}$, $\boldsymbol{s}$ and $\boldsymbol{t}$	Three vectors base of the local coordinate
$\boldsymbol{M}^{rr}$, $\boldsymbol{M}^{ss}$, $\boldsymbol{M}^{tt}$, $\boldsymbol{M}^{rs}$, $\boldsymbol{M}^{sr}$, $\boldsymbol{M}^{rt}$, $\boldsymbol{M}^{tr}$, $\boldsymbol{M}^{st}$, $\boldsymbol{M}^{ts}$	Projection tensor defined by the three base unit vectors
$\bar{\sigma}_{rr}$, $\bar{\sigma}_{ss}$, $\bar{\sigma}_{tt}$, $\bar{\sigma}_{rs}$, $\bar{\sigma}_{rt}$, $\bar{\sigma}_{st}$	Stress components of $\overline{\boldsymbol{\sigma}}$ on the local coordinate system
σ_r^+, σ_r^-, σ_s^+, σ_s^-, σ_t^+, σ_t^-,	Decomposed positive/negative normal stress on three directions
$\overline{\boldsymbol{\sigma}}_{\mathrm{I}}^+$, $\overline{\boldsymbol{\sigma}}_{\mathrm{II}}^+$ and $\boldsymbol{\sigma}^-$	Decomposed tensile, shear and compression components of effective stress.
d	Phase field damage
d_t, d_c	Tensile and shear phase field damage
$\dot{\boldsymbol{\varepsilon}}^p$	Rate of plastic strain tensor
$\dot{\boldsymbol{\varepsilon}}_{\mathrm{I}+}^p$, $\dot{\boldsymbol{\varepsilon}}_{\mathrm{II}+}^p$	Rate of tensile and compression plastic strain tensor
$\bar{\varepsilon}^p$	Accumulated equivalent plastic strain
ξ_t, ξ_c	Tensile/compression accumulated equivalent plastic strain
ψ^e	Elastic stored energy density
ψ^p	Plastic work
ψ^k	Kinematic energy density

ψ^{vis}	Damage viscosity energy density
φ^{d}	Fracture energy density
Φ	Total potential energy
Φ^{int}	Internal potential energy
Φ^{ext}	External force work
Φ^{kin}	Kinetic energy
α, β and γ	Three angle variables used to control the local coordinate system in principal stress space
H_{I}^{ini}, H_{II}^{ini}	Energy thresholds for tensile and shear fracture initiation
H_t, H_c	Tensile and compression fracture driving forces
σ_y	Plastic yield stress
h	Plastic hardening modulus
$\bar{\boldsymbol{s}}$	Effective deviatoric stress tensor
G_{I}, G_{II}	Mode I/II energy release rate
G_{cr}	Critical energy release rate
$F(\alpha,\beta,\gamma)$ and $F(\alpha,\beta)$	F-function energy
F_1 , F_2 , F_3 and F_4	The simplified F-function under four different decomposition types in the unified strain energy decomposition method
$\square^{h}$	History variable of F-function
$\boldsymbol{\varepsilon}^{\mathrm{e}}$	Elastic strain tensor
ν	Poisson's ratio
E	Elastic modulus
λ	Lame constant
G (μ)	Shear modulus
K	Bulk modulus
$\mathbb{C}$	flexural tensor
$state^{t}(X,t)$	State energy for tensile fracture
$state^{c}(X,t)$	State energy for shear fracture
ξ_t^{eff} / ξ_c^{eff}	Effective tensile and shear accumulated strain
ξ_t^{ini} / ξ_c^{ini}	Thresholds of tensile/shear accumulated plastic strain
r_{dt}^{i}, r_{dc}^{i}	Residual vectors for tensile and shear phase fields
K_{ij}^{dt}, K_{ij}^{dc}	Tangent tensors for tensile and shear phase fields
ω	Phase field viscosity parameter
$\boldsymbol{M}$	The mass matrix
$\boldsymbol{P}^{ext}$	External force vector

$\boldsymbol{P}^{int}$	Internal force vector
$\boldsymbol{C}$	viscosity matrix for phase field
$\boldsymbol{Y}$	Phase field residual force
$\boldsymbol{N}_u{}^e$ and $\boldsymbol{N}_d{}^e$	Shape function for the displacement and phase field
$\boldsymbol{B}_u{}^e$ and $\boldsymbol{B}_d{}^e$	Spatial derivatives of the shape functions
F, G, H, N, M, N, L	Hill 48 yield stress parameter
η	Stress triaxiality
$\tilde{\theta}$	Lode angle parameter
A, n, c_1, c_2, c_3	Five Modified Mohr-Column fracture strain parameters
B_1, B_2, B_3, B_4, B_5, B_6 and B_7	Seven independent Bao-Wierzbicki fracture strain parameters
ε^f	Fracture strain
D	Historical damage indicator
P_{ela}	Elastic power
P_{pla}	Plastic power
P_{fra}	Fracture power
P_{vis}	Viscosity power
P_{ext}	The power of external work
$\boldsymbol{D}^e$	Rate of elastic deformation
$\boldsymbol{D}^P$	Rate of plastic deformation
χ	Fraction of dissipated plastic work
T	Temperature
C_p	Heat capacity
$\dot{\varepsilon_{lt}}$, $\dot{\varepsilon_a}$ and χ_0	Three thermal evolution parameters
C_0, C_1 and $\dot{\bar{\varepsilon}_0^p}$	Dynamic-related Johnson-Cook model parameters
T_{room}, T_{melt}	Thermal-related Johnson-Cook model parameters
$b(\dot{\bar{\varepsilon}^p})$	Rate-dependent factor for the dynamic fracture strain
$\bar{\varepsilon}^{p,ani}$	Anisotropic equivalent plastic strain
$\boldsymbol{\beta}$	Anisotropic mapping matrix
ρ	Material density

ABSTRACT

This thesis develops advanced phase-field models for fracture simulation in both solid and thin-walled structures. The research is divided into two main parts: phase-field fracture modelling in solids and shell-based phase-field modelling for thin-walled structures.

In the first part, a double-phase-field model is proposed to separately represent tensile and shear fracture evolution in elastoplastic solids. The model employs a crack-orientation-based decomposition framework, where effective stress and plastic strain are split in a local coordinate system. The tensile and shear damage evolution is governed by the corresponding decomposed stress components, while plastic contributions are incorporated through their respective energy release rates. The model is validated against experimental data and complex three-dimensional benchmark problems, demonstrating its capability to capture different crack modes and mechanical responses. Building upon this, a unified strain energy decomposition strategy is developed to handle arbitrary stress states. By ensuring non-negative tensile, shear, and compressive stress components, this approach generalizes existing decomposition methods and provides consistent results across diverse loading conditions.

In the second part, a shell phase-field model is introduced to simulate fracture propagation in thin-walled structures. The model incorporates five phase-field layers corresponding to Simpson stress integration points, accurately capturing through-thickness fracture evolution. A stress-state-dependent fracture strain formulation is integrated using the Modified Mohr-Coulomb (MMC) criterion for 316L steel and the Bao-Wierzbicki criterion for Ti-6Al-4V. The model is validated against numerical benchmarks and experimental data, successfully reproducing fracture mechanisms in cylindrical and square tube structures. The framework is further applied to battery casing simulations, incorporating anisotropic plasticity and stress-state-dependent fracture criteria, with numerical results closely matching experimental observations.

To extend the model's applicability to dynamic fracture, an explicit shell phase-field

model is developed, integrating temperature evolution from dissipated plastic work. A thermally and rate-dependent Johnson-Cook flow stress model, coupled with the MMC fracture criterion, characterizes strain rate effects and fracture initiation under dynamic loading. The model accurately captures anisotropic plastic deformation and fracture behaviour across various impact scenarios.

This thesis advances phase-field fracture modelling by addressing key challenges in stress-state-dependent fracture evolution, anisotropy, and dynamic loading effects. The findings improve predictive accuracy in fracture simulations for solids and thin-walled structures, with potential applications in structural engineering, battery safety analysis, and impact-resistant materials. Future research directions include uncertainty analysis, integrating non-local plasticity, extending Multiphysics couplings, and further experimental validation of shell phase-field models.

1. INTRODUCTION

1.1 Research background

Crack propagation, which plays great roles on the mechanical behaviour of structure under loading, has been a key technique issue in many different areas of practical engineering, some of them depicted in Figure 1.1. Hence having a deep understanding on the initiation and propagation of fracture in solid has been a significant task for researchers and engineer.

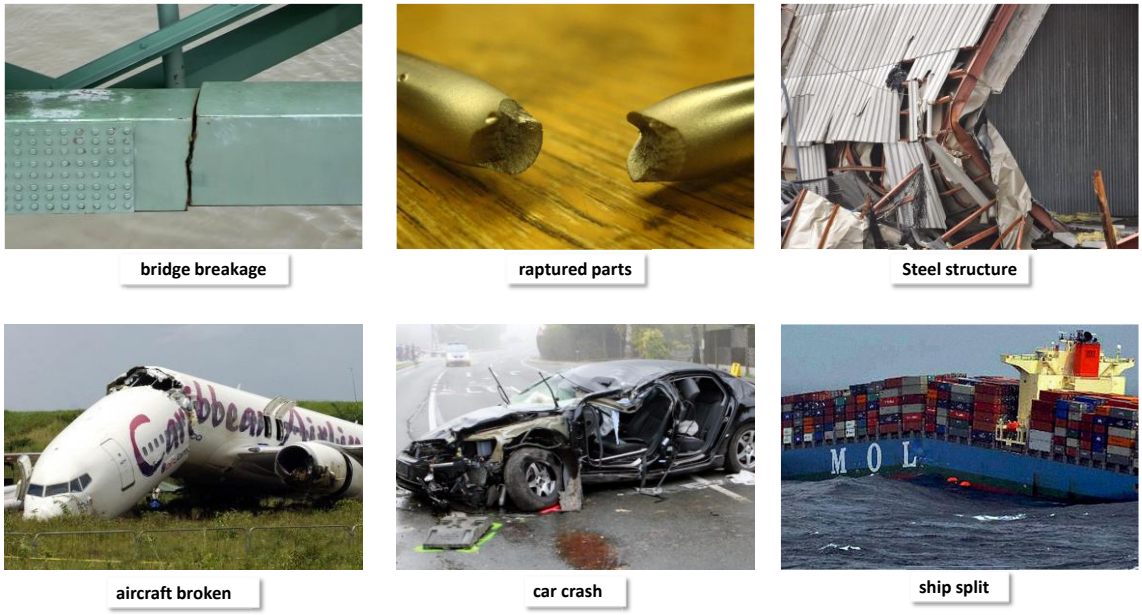

Figure 1.1 fracture behaviours in engineering

Researchers have proposed different numerical methods to model the crack propagation and predict the mechanical response of solid under stress. Basically, those crack modelling methods could be divided into two types: discrete models and diffusive models. The discrete models trace crack path during the loading process and adjust their geometric information simultaneously according to the fracture topology at each increment. All kinds of finite element modelling techniques such as remeshing (Belytschko and Black 1999), Enriched Finite Element Method (Oliver 1996) and Extend Finite Element Method (Geelen, Plews et al. 2020) have been developed to

decouple fracture evolution from the underlying discretization. However, the drawback of such discrete method would become obvious when it comes to complicated crack path evolution such as crack intersection problems especially in 3D condition. Since tracking crack path would consuming extremely huge calculating resource, it's not realistic to apply those techniques to industry for practical engineering design. The diffusive models, instead of tracing the crack topology, use continuous damage variable field to denote the degree of broken at each position within solid.

Within the frame of diffusive models, phase field modelling method has been proposed and developed fast in the past twenty years. Phase field models limit the value of damage variable d from 0-1. It represents intact and totally broken state when phase field variable d is equal to 0 and 1 respectively. Starting from Griffith's theory (Griffiths 1986), this method regularizes the sharp crack Γ as a diffusive area controlled by length scale parameter l_c. Due to the gradient terms of damage variable in the crack surface density function, phase field models could avoid mesh-depended damage localization in numerical modelling.

1.2 Research scope

Phase field model has been proven an effective method for crack modelling in elasto-plastic materials and attracted much attention from researchers and engineers. This current research mainly focuses on two aspects for the solid and shell structures, respectively.

For the 3D solids, one key challenge in the phase field community was to account for the tension-compression asymmetry, which is widely common for most real materials. Though many different strain energy decomposition methods have been proposed to capture this characteristic, i.e. the spectral (Miehe, Schänzel et al. 2015) and volume-deviatoric (Behera, Sudeep et al. 2023) decomposition among many others, those approaches could only take effect under some specific region of stress states. For example, spectral decomposition may predicted accurate fracture path for material under tensile dominate stress state, while may not induce crack initiation for structures under

compression loading. However, real-world structures are frequently exposed to highly diverse stress loadings, which may vary spatially and temporally. Hence, it is necessary to propose a unified decomposition strategy, effective for arbitrary stress states. In addition, the different crack modes mode I and mode II crack have different mechanical properties, i.e. the different crack energy release rate, and therefore must be distinguished.

The fracture behaviours of shell structures are common in practical engineering. Yet there is not much research for applying the phase field model for quasi-static/dynamic shell fracture modelling. Even in the limited literature, such shell phase field model was only verified by several benchmark numerical examples, while the experimental validation was unemployed yet. To accurately predict the mechanical response and fracture behaviour, the stress-state dependent fracture initiation criterion has to be considered. In addition, the difference damage evolution along the thickness should also be distinguished.

Based on the above-discussed research scope, the aims of this research are listed below:

(1) Develop a double-phase-field framework for ductile fracture modelling with distinguished mode I and mode II fracture.

(2) Further propose a unified strain energy decomposition strategy for prediction of reliable fracture path and mechanic response under arbitrary stress states. In addition, compare the numerical results with the two commonly used spectral and volume-deviatoric decomposition method.

(3) Develop a shell phase field formulation where the distinguished damage evolution along shell thickness and stress-state dependent fracture criterion are incorporated. Further, the proposed shell phase field model is validated by both the benchmark example and experimental test results.

(4) Further apply the shell phase field model for the fracture modelling of cylinder battery casing and battery cell, analysing the deformation mode and damage evolution under different abuse tests. Conduct a comprehensive study of the effect

of stress state on the mechanical behaviour of battery structures.

(5) Develop a dynamic shell phase field model, with consideration of the effect of strain rate, stress states, material orientation on the fracture criterion. Besides, the dynamic effect should be incorporated via the strain-rate-dependent flow stress.

1.3 Organisation of the rest of the thesis

The flow chat of this thesis is presented in Figure 1.2. Overall, the rest of the thesis consists of two main parts. Chapter 3 and Chapter 4 focus on the phase field fracture modelling within solids, while Chapter 5 to Chapter 7 focus on the shell phase field fracture modelling. Specifically, they are organised as follows:

Chapter 3 proposes a double-phase-field model to represent the tensile and shear fracture evolution within the elasto-plastic solid. In this model framework, both effective (undamaged) stress and plastic strain are split in the crack-orientation-based coordinate system. The decomposed tensile/shear stress contribute to the tensile/shear damage evolution, respectively; The plastic contribution is coupled by relating the decomposed tensile/shear plastic stain to the corresponding tensile/shear crack energy release rates. Crack surface normal direction, represented by two orientation variables in 3D spatial domains, is determined by the *F*-criterion. The simulation of a single-edge notch specimen under shear loading demonstrates that the ratio between shear and tensile crack energy release rates plays a significant role in the crack mode and mechanical response. Numerical results of a group of uniaxial tension, simple shear and tension shear specimens show good agreement with the experimental data in terms of the force-displacement curve and crack path, exhibiting the validity of the proposed model for capturing different crack modes. This model has also proven effective for complex 3D problems via the third Sandia Challenge example.

Based on the crack-directional decomposition method, **Chapter 4** further developed a unified strain energy decomposition strategy suitable for arbitrary stress states. In this method, the effective stress is decomposed into three non-negative components, namely tensile, shear and compressive stress based on the local coordinate

system (***r*-*s*-*t***), and all of these decomposed strain energies are ensured nonnegative with the consideration of Poisson effect. It is also noted that the proposed unified decomposition approach could recast to volume-deviatoric (V-D), spectral, and crack-directional decomposition methods under specific loading conditions. To further validate this unified decomposition method, it is compared with V-D, and spectral phase field model through a series of numerical examples, covering various stress states loading, including tensile, compression, tensile-shear, compression-shear. The results show that that the unified decomposition strategy is capable of accurately capturing fracture propagation and mechanical response of solids under different stress states.

In **Chapter 5**, we introduce a shell phase-field model with five layers of phase-field variables to accurately predict fracture propagation through the thickness, corresponding directly to the five Simpson stress integration points. Additionally, to accurately capture fracture initiation in real structures, a stress-state-dependent fracture strain formulation was employed in each layer, utilizing the MMC criterion for 316L steel and the Bao-Wierzbicki criterion for Ti-6Al-4V. The proposed model was validated both quantitatively through benchmark numerical examples and qualitatively using experimental data. The simulation of a notched cylinder under axial tension demonstrated that fracture strain significantly affects the load-carrying capacity. The typical "flapping" phenomenon in a cracked cylinder under internal pressure was successfully reproduced. In the three-point bending test of a square tube, the model captured five distinct stages of deformation—elastic deformation, local indentation, side-surface buckling, bulge strap growth, and global bending—all of which closely matched experimental observations. Despite a slight delay in the densification of the Gyroid TPMS structure under axial compression, the two characteristic deformation modes were accurately captured, and the global force-displacement curve aligned well with experimental results.

In **Chapter 6**, the proposed shell phase-field model in Chapter 5 is further applied to simulate and analyse the ductile fracture of a battery casing, supported by experimental validation. The Hill 48 stress model was used to describe the anisotropy in yield stress.

The Bao-Wierzbicki fracture criterion was utilized to account for stress-state-dependent fracture strain. Simulations with the calibrated parameters successfully replicated the experimental deformation modes, fracture progression, and force-displacement responses across three structural tests on the battery casing and cell. In the three-point bending of the battery damage was concentrated at the front and back equatorial points, where the element bending direction transitioned from inward to outward as the indenter advanced. This transition led to damage initiation in the material near the outer and inner surfaces. Moreover, the simulation accurately reproduced the diamond-mode deformation, and the fluctuating force-displacement curve observed in the axial compression test on the battery casing. In the bending of the battery cell, analysis of representative elements showed significant variation in stress states and damage initiation along shell thickness under bending-dominant conditions, with consistent behaviour observed under membrane tensile-dominant conditions.

Chapter 7 further develops an explicit shell phase-field model for simulating dynamic fracture behaviour in thin-walled structures. The model incorporates temperature as a state variable governed by dissipated plastic work and accounts for material anisotropy using the Hill48 yield stress formulation. A thermally and rate-dependent Johnson-Cook flow stress model, coupled with the modified Mohr-Coulomb (MMC) fracture criterion, was employed to characterize fracture initiation under dynamic loading. An anisotropic plastic strain measure was introduced to capture material orientation-dependent fracture behaviour, while phase-field damage evolution was governed by elastic energy and retained plastic work. Model calibration through uniaxial tension, notched tension, hollow centre, and simple shear tests demonstrated its accuracy in capturing strain rate effects and stress-state-dependent fracture initiation. Further validation using the three holes sample under varying loading rate confirmed the model's capability in predicting force-displacement behaviour, fracture evolution, and crack propagation paths. The numerical results closely matched experimental observations, accurately capturing strain localization, triaxial stress effects, and fracture transitions.

Chapter 8 summarizes the key findings of this thesis, discusses its limitations, and outlines directions for future research.

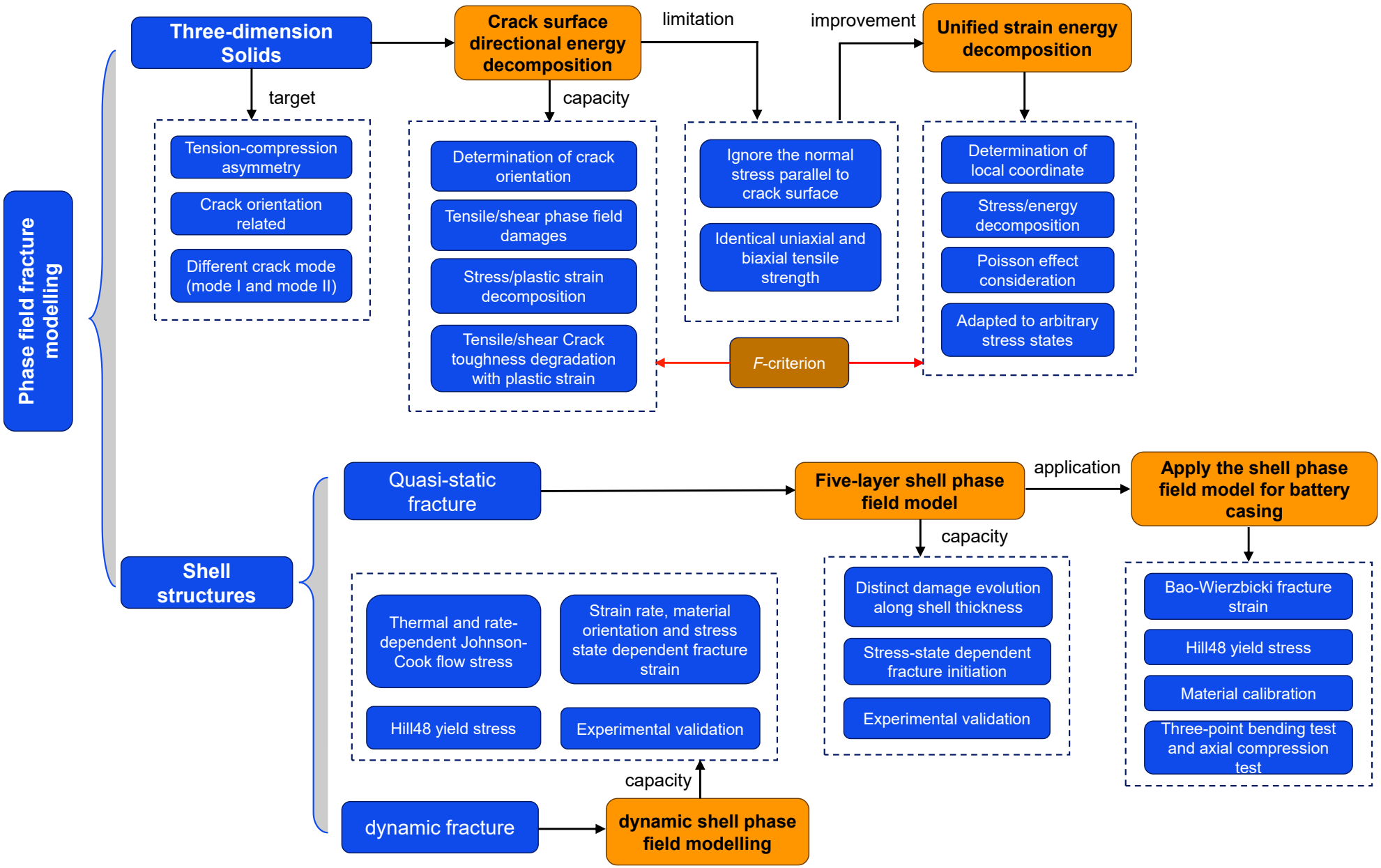

Figure 1.2 Structure organisation of this thesis

2. LITERATURE REVIEW

2.1 Phase field modelling for brittle fracture

Originated from the Griffith's theory, phase field model regularises the sharp crack topology into diffusive region, and the governing equations are deduced by minimising the total potential energy within the solid, including the fracture energy dissipation, elastic energy and external force work. Moreover, to distinguish different mechanical response under tensile and compressive stress state, the phase field model decompose the strain energy into positive and negative part with the assumption that only the positive energy contributes to the fracture evolution.

2.1.1 Crack Regularisation

Based on the Griffith's theory (Griffiths 1986), phase field methods firstly regularise the sharp crack Γ by introducing a diffusive crack surface density function $\gamma_l(d, \nabla d)$, demonstrated in Figure 2.1. The formulation of crack density function can be written as below (Bourdin, Francfort et al. 2008, Miehe, Hofacker et al. 2010, Miehe, Welschinger et al. 2010, Ulmer, Hofacker et al. 2013, Molnár and Gravouil 2017),

$$\gamma_l(d, \nabla d) = \frac{d^2}{2l} + \frac{l}{2}|\nabla d|^2 \tag{2.1}$$

where d represents the phase field variable, and its value lies between 0 and 1. A larger value of d corresponds a higher degree of broken state in solid. When d is equal to 0 and 1, it denotes intact and totally broken situation, respectively. The introduced length scale parameter l controls the crack diffusive area, depicted in Figure 2.1. When l approaches zero, the regularized crack zone converges to a sharp crack.The density function could be deduced from the one-dimension case following the literature (Molnár and Gravouil 2017). Specifically, we consider a 1D bar with cross section Γ, of which there exists a fully open crack in the middle. To approximate the non-smooth crack topology, an exponential function was proposed as below (Miehe, Schänzel et al. 2015, Molnár and Gravouil 2017),

$$d = e^{-|x|/l} \tag{2.2}$$

where l is the length scale parameter, when $l \to 0$, the sharp crack can be recovered. It is noticed that the explicit expression of phase field d in Eq.(2.2) is the solution for the below differential equation,

$$d(x)^2 - l^2 \cdot d''(x)^2 = 0 \tag{2.3}$$

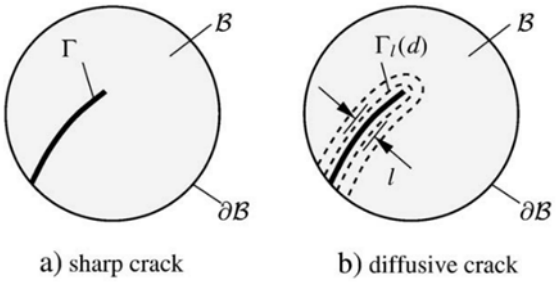

Figure 2.1 Fracture topology. a) Sharp crack surface. b) diffusive crack zone

According to Euler's variational principle, the explicit expression of phase field d in Eq.(2.2) also minimises the integration value in terms of such integrand formulation, expressed as follows,

$$I(d) = \frac{1}{2l}\int_{\Omega} (d^2 + l^2 d'^2) d\Omega \tag{2.4}$$

Then the crack surface density function for one-dimension case could be defined as the integrand in Eq.(2.4) as,

$$\gamma_l(d, d') = \frac{1}{2l}(d^2 + l^2 d'^2) \tag{2.5}$$

Consequently, we can finally obtain the diffusive crack surface density function of Eq.(2.1) after extending Eq.(2.5) into multi-dimension cases.

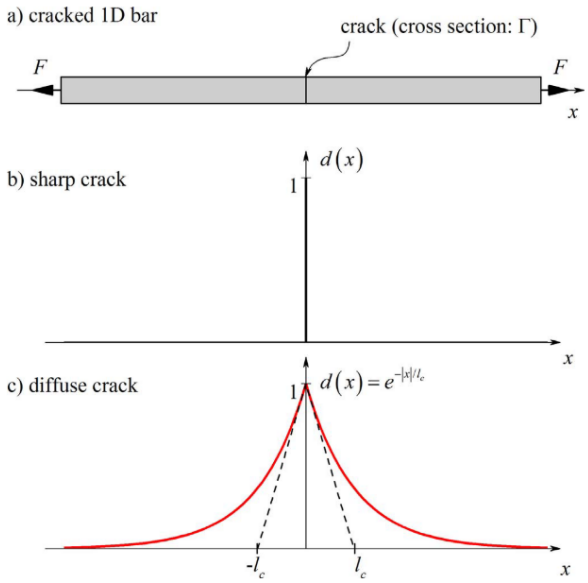

Figure 2.2 (a) 1D bar with a crack at the middle with the cross section Γ. (b) Phase-field for sharp crack at x=0. (c) Diffuse crack at x=0 modelled with function (1) and length scale parameter l (Molnár and Gravouil 2017).

2.1.2 Energy framework for phase field model

2.1.2.1 Degradation on elastic strain energy

Essentially, phase field method replace the sharp crack discontinuity with a finite gradient damage zone (de Borst and Verhoosel 2016). In the sharp crack topology, the component of strain and stress on crack surface should be zero when the crack is open, which results in the strain energy release on the crack surface. In the phase field context, the displacement is assumed continuous on the regularized fracture zone as well as the elastic strain, and the effective (undamaged) stress is calculated with the undamaged elastic modulus. Hence, a degraded function is introduced to describe the nominal stress and degraded released strain energy when damage initiates and propagates. Based on above explain, the degradation function g(d) should be a monotone decreasing function in terms of the phase field variable d. It should also meet such several requirements as below (Miehe, Hofacker et al. 2010, da Silva, Duda et al. 2013, Miehe, Schänzel et al. 2015)

$$\begin{cases} g(d) = 1 & d = 0 \\ g(d) = 0 & d = 1 \\ g'(d) & d = 1 \end{cases} \tag{2.6}$$

A widely adopted quadratic formulation (Bourdin, Francfort et al. 2008, Lorentz,

Cuvilliez et al. 2011, Lorentz and Godard 2011, Wu and Xu 2013, Freddi and Iurlano 2017, Wu 2018) can be written as follows,

$$g(d) = (1-d)^2 \tag{2.7}$$

Except for the quadratic degradation function represented by Eq.(2.7), Borden et al. (Borden, Hughes et al. 2016) proposed an alternative cubic degradation function,

$$g(d) := (1-d)^2[(2-k)d + 1] \tag{2.8}$$

When the parameter k in Eq.(2.8) is equal to two, this cubic function degrades to the normal quadratic formulation. The stress response for phase field models with the normal quadratic and cubic degradation formulation are compared in Figure 2.3. It shows that linear stress response before peak stress can be captured by the cubic degradation function (Borden, Hughes et al. 2016).

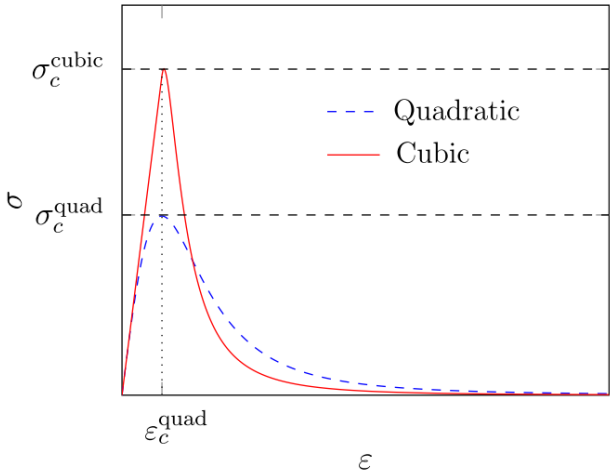

Figure 2.3 Stress-strain relationship for quadratic and cubic degradation function [51].

Moreover, Wu et al. (Wu 2017, Wu, Huang et al. 2021) proposed a unified phase field model, where the degraded function are given as a series of formulations as follows,

$$g(d) = \frac{(1-d)^p}{(1-d)^p + Q(d)} \tag{2.9}$$

where the $Q(d)$ are calculated as below,

$$Q(d) = a_1 d + a_2 d^2 + a_3 d^3 + \cdots + a_m d^m \tag{2.10}$$

Within this unified framework, many related alternative degradation functions then can be recovered by choosing appropriate parameters. This unified phase field framework has been adopted in the following research (Mandal, Nguyen et al. 2019, Wang, Feng et al. 2020, Zhang, Peng et al. 2021) among many other studies. There are still many other

alternative formulations, and part of them are summarized in Table 2.1.

Table 2.1 Alternative degradation functions

Authors	Year	Degradation functions
Lorentz et al.(Lorentz and Godard 2011)	2011	$g(d) := \frac{(1-d)^p}{(1+\rho_0 d)^q}$
Alessi et al. (Alessi, Marigo et al. 2014)	2014	$g(d) := \frac{(1-d)^2}{k-(k-1)(1-d)^2}, k>0$
Kuhn et al. (Kuhn, Schlüter et al. 2015)	2015	$g(d) := 4(1-d)^3 - 3(1-d)^4$
Alessi (Alessi, Ambati et al. 2018)	2015	$g(d) := \frac{(1-d)^2}{1+(k-1)(1-(1-d)^2)}$

2.1.2.2 Thermodynamically consistent variational energy functional

We Consider an arbitrary body $\mathcal{B}$ under loading with displacement boundary $\partial\mathcal{B}^t$ and stress boundary $\partial\mathcal{B}^f$. $\overline{\boldsymbol{\gamma}}$ and $\bar{\boldsymbol{t}}$ are the body force and boundary force respectively. The internal energy in this solid can be divided into two parts: (a) the elastic strain energy; (b) the dissipated fracture energy. With the degradation function in hand, the degraded elastic strain energy can be easily obtained by multiplying the degradation function on the intact stain energy in terms of elastic strain. As for the dissipated fracture energy, we can introduce the energy release rate G_f, which denotes the dissipated energy needed to create per area crack surface. The total dissipated fracture energy could be calculated by multiply this energy release rate on the total crack surface area that can be obtained by integrating the crack density function Eq.(2.1 over the entire solid. Under this framework, the strain energy drives the crack propagation while the crack evolution resistance originates from the released fracture energy (Aldakheel, Mauthe et al. 2014, Miehe, Schänzel et al. 2015). The total potential energy Ψ^{pot} in this system is equal to the internal energy Π^{int} minus the extent energy Π^{ext}, represented as follows,

$$\Phi^{pot} = \Pi^{int} - \Pi^{ext} = \int_{\mathcal{B}} [\phi(\boldsymbol{u}, d) + \varphi(d, \nabla d) - \overline{\boldsymbol{\gamma}} \cdot \boldsymbol{u}] \mathrm{d}V - \int_{\partial\mathcal{B}^f} \bar{\boldsymbol{t}} \cdot \boldsymbol{u} \, \mathrm{d}S \tag{2.11}$$

where $\phi(\boldsymbol{u}, d)$ and $\varphi(d, \nabla d)$ denotes the strain energy density and fracture energy density, and can be calculated by

$$\phi(\boldsymbol{u}, d) = \frac{1}{2}(1-d)^2 \boldsymbol{\varepsilon}(\boldsymbol{u}) : \boldsymbol{E} : \boldsymbol{\varepsilon}(\boldsymbol{u}) \tag{2.12}$$

$$\varphi(d, \nabla d) = G_f \cdot \left(\frac{l}{2} d^2 + \frac{1}{2l_c} \cdot |\nabla d|^2\right) \tag{2.13}$$

To keep stable of the energy framework, the evolution of displacement field $\boldsymbol{u}$ and phase field variable d always leads to a minimum potential energy in the whole system (Marigo, Maurini et al. 2016). Hence, take variation on the total potential energy Φ^{pot}, the following governing equations for the displacement and phase field can be calculated (Miehe, Hofacker et al. 2010, Molnár and Gravouil 2017).

- for the displacement variable $\boldsymbol{u}$:

$$\begin{cases} \nabla \cdot \boldsymbol{\sigma} + t = 0 & \text{in } \mathcal{B} \\ \boldsymbol{\sigma} \cdot \boldsymbol{n} - b = 0 & \text{on } \partial\mathcal{B}^f \\ \boldsymbol{u} = \overline{\boldsymbol{u}} & \text{on } \partial\mathcal{B}^t \end{cases} \tag{2.14}$$

- for the phase field variable d:

$$\begin{cases} \frac{G_f}{l_c} \cdot \left(d - {l_c}^2 \Delta d\right) = 2(1-d) \cdot \left\{\frac{1}{2}\boldsymbol{\varepsilon}(\boldsymbol{u}) : \boldsymbol{E} : \boldsymbol{\varepsilon}(\boldsymbol{u})\right\} & \text{in } \mathcal{B} \\ \nabla d \cdot \boldsymbol{n} = 0 & on\ \partial\mathcal{B} \end{cases} \tag{2.15}$$

2.1.2.3 Crack Irreversibility and history variable

According to Eq.(2.15), the evolution of phase field variable d dependents on the intact strain energy. However, it's noticed that the crack evolution is irreversible, which requires that time derivative of phase field variable d at each point should be non-negative. To implement this, Miehe (Miehe, Hofacker et al. 2010, Miehe, Welschinger et al. 2010) introduced the history variable $\mathcal{H}$, which represents the maximum elastic energy in history at each point within the solid. Obviously, replacing the intact strain energy in Eq.(2.15) with $\mathcal{H}$ will lead to a monotone increasing evolution of phase field variable d. Thus, we can finally obtain the final crack evolution governing equation as follows,

$$\begin{cases} \frac{G_f}{l_c} \cdot \left(d - {l_c}^2 \Delta d\right) = 2(1-d) \cdot \mathcal{H} & \text{in } \mathcal{B} \\ \nabla d \cdot \boldsymbol{n} = 0 & on\ \partial\mathcal{B} \end{cases} \tag{2.16}$$

$$\mathcal{H} = \max_{\tau \in [0, t_n]} \left\{\frac{1}{2}\boldsymbol{\varepsilon}(\boldsymbol{u}, \tau) : \boldsymbol{E} : \boldsymbol{\varepsilon}(\boldsymbol{u}, \tau)\right\} \tag{2.17}$$

2.1.3 Energy Decomposition

The above review has introduced an isotropic phase field model, which does not distinguish tension and compress stress. Nevertheless, it does not agree with the experimental observation that most materials exhibit different behaviours of fracture in tension and compression (You, Waisman et al. 2021). Normally, cracks are easier to initiate and develop under tension than compression. To address this issue, researchers have proposed different approaches to decompose the strain energy into positive and negative part and assume that only the positive part plays roles on the crack evolution. There are plenty of energy decomposition methods, and they can mainly be divided into three classes: (a) volumetric-deviatoric decomposition; (b) spectral decomposition; (c) decomposition based on crack direction.

2.1.3.1 Volumetric-Deviatoric (V-D) decomposition

The V-D decomposition method, firstly proposed by Amor et al. (Amor, Marigo et al. 2009) and Lancioni and Royer-Carfagni (Lancioni and Royer-Carfagni 2009), decomposes the strain tensor into volumetric strain and deviatoric strain tensor. Then deviatoric strain energy is assumed always active for fracture driving force, while the volumetric strain energy contributes to crack propagation only when volumetric strain is positive, written as

$$\varphi_0^+ = \frac{1}{2}\cdot K\cdot\langle tr\left(\varphi_0^+ = \frac{1}{2}\cdot K\cdot\langle tr(\boldsymbol{\varepsilon})\rangle_+{}^2\right)\rangle_+{}^2 + G\cdot\boldsymbol{\varepsilon}^s{:}\,\boldsymbol{\varepsilon}^s \tag{2.18}$$

$$\varphi_0^- = \frac{1}{2}\cdot K\cdot\langle tr(\boldsymbol{\varepsilon})\rangle_-{}^2 \tag{2.19}$$

where K and G are elastic volume and shear modulus respectively, $\boldsymbol{\varepsilon}$ and $\boldsymbol{\varepsilon}^s$ are strain tensor and deviatoric strain tensor respectively. Since the V-D decomposition strategy distinguishes the volume strain and deviatoric strain, stress update would be relatively easier, especially for the calculation of plastic strain increment. Hence, this V-D decomposition has been widely adopted, particularly in some ductile phase field models (Gavagnin, Sanavia et al. 2020, Kristensen and Martínez-Pañeda 2020, Wheeler, Wick et al. 2020, Yin and Kaliske 2020, Ulloa, Wambacq et al. 2021).

2.1.3.2 Spectral decomposition

In contrast to V-D decomposition, spectral decomposition, proposed by Miehe et al. (Miehe, Hofacker et al. 2010, Miehe, Welschinger et al. 2010, Hofacker and Miehe 2012) and also widely adopted (Jeong, Signetti et al. 2018, Wu, Fang et al. 2020, Wambacq, Ulloa et al. 2021), transform the strain tensor into the principle strain space, and distinguish the positive and negative principle strain as well as the correspond strain energy, denoted by

$$\boldsymbol{\varepsilon}^{\pm} = \sum_{i=1}^{3} \langle \varepsilon_i \rangle_{\pm} \boldsymbol{m}_i \otimes \boldsymbol{m}_i \tag{2.20}$$

$$\varphi_0^{\pm} = \frac{1}{2}\lambda \langle \varepsilon_1 + \varepsilon_2 + \varepsilon_3 \rangle_{\pm}^{\ 2} + \mu \left[\langle \varepsilon_1 \rangle_{\pm}^{\ 2} + \langle \varepsilon_2 \rangle_{\pm}^{\ 2} + \langle \varepsilon_3 \rangle_{\pm}^{\ 2} \right] \tag{2.21}$$

Though the spectral decomposition gives understandable concept on the tensile and compress component of strain energy, there are also some limitations on it. For example, when the solid is under compress stress from all three directions, the positive strain energy would be equal to zero, which leads to no driving force for crack initiation and propagation. Hence, this method can not present a shear fracture under compression condition, while it is very common phenomenon in reality.

2.1.3.3 Decomposition based on crack direction

Stenike and Kaliske (Steinke and Kaliske 2018) introduced a novel strain split based on crack direction. This method decomposes the effective (undamaged) stress tensor in a local crack-orientation-based coordinate system, with three base vectors of ***r***, ***s*** and ***t***, as demonstrated in Figure 2.4. The vector ***r*** denotes the unit normal direction on the crack surface, ***s*** represents the slip direction along the crack surface, and ***t*** is the unit vector on the third direction perpendicular to ***r*** and ***s***. After this decomposition, it is assumed that the active part of strain tensor includes the positive normal stress on the crack surface and shear stress along the crack surface, as follows

$$\boldsymbol{\sigma}^{+} = \langle \bar{\sigma}_{rr} \rangle_{+} \cdot \boldsymbol{M}^{rr} + \frac{\lambda}{\lambda+2G} \cdot \langle \bar{\sigma}_{rr} \rangle_{+} \cdot (\boldsymbol{M}^{ss} + \boldsymbol{M}^{tt}) + \bar{\boldsymbol{\sigma}}^{rs} + \bar{\boldsymbol{\sigma}}^{sr} + \bar{\boldsymbol{\sigma}}^{rt} + \bar{\boldsymbol{\sigma}}^{tr}$$

$$\boldsymbol{\sigma}^{-} = \langle \bar{\sigma}_{rr} \rangle_{-} \cdot \boldsymbol{M}^{rr} - \frac{\lambda}{\lambda+2G} \cdot \langle \bar{\sigma}_{rr} \rangle_{+} \cdot (\boldsymbol{M}^{ss} + \boldsymbol{M}^{tt}) + \bar{\boldsymbol{\sigma}}^{st} + \bar{\boldsymbol{\sigma}}^{ts} + \bar{\boldsymbol{\sigma}}^{ss} + \bar{\boldsymbol{\sigma}}^{tt} \tag{2.22}$$

(2.23)

The second term in above two equations explains the strain release on the ***s*** and ***t*** direction when the stress on crack normal direction is degraded. Based on this crack direction energy split strategy, many further studies have been conducted (Storm, Supriatna et al. 2019, Wang, Feng et al. 2020, Fei and Choo 2021, Wang, Shao et al. 2021).

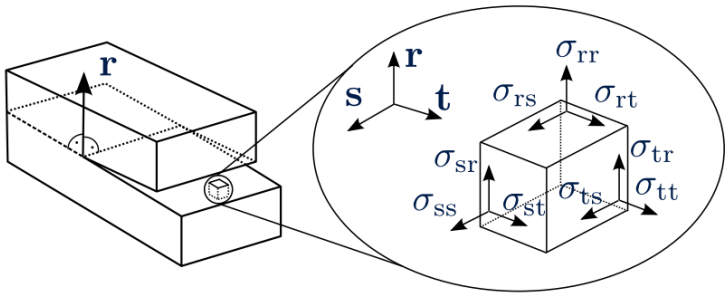

Figure 2.4 Local crack-orientation-based coordinate system (Steinke and Kaliske 2018)

2.1.4 Anisotropic/Hybrid phase field framework

With a specified strain energy split method in hand, one can easily construct the anisotropic phase field model by replace crack driving force with the positive part of the decomposed strain energy in the phase field governing equations (Miehe, Welschinger et al. 2010, Chen, Li et al. 2020). The advantage of aforementioned anisotropic phase field models is that these models can represent the significant anisotropic characteristics of materials and are all thermodynamic consistent models that can be derived from the potential energy variation framework. On the other hand, due to the nonlinear momentum balance equation caused by asymmetric stress response, anisotropic phase field models can cost huge calculation resource especially for 3D problems with complex boundary conditions.

To increase the calculation effectiveness and capture the anisotropy of materials simultaneously, Ambati et al. (Ambati, Gerasimov et al. 2014) introduced a hybrid formulation. This proposed model distinguishes tensile and compress when deducing history variable $\mathcal{H}$ and phase field variable d, while it views solid as isotropic materials when calculating the stress response. Based on Ambati's work, Jeong et al. (Jeong, Signetti et al. 2018) hold the view that hybrid formulation is more realistic for combined loading problems for the residual stiffness in anisotropic model. It has been further proved

that this hybrid framework is capable of producing qualitative and quantitative results similar to those obtained from an anisotropic phase field model, while also reduced the calculation cost rapidly (Ambati, Gerasimov et al. 2014, Zhu 2016, Zhou, Zhuang et al. 2019, Cao, Wang et al. 2022).

2.1.5 Mixed-model phase field model

The energy release rate G_f introduced before denotes the energy needed to dissipate for unit area of crack surface. In the normal phase field model, it does not distinguish tensile fracture and shear fracture. However, it has been proved that energy release rate for shear fracture is much greater than that of tensile fracture in solids (Wong and Einstein 2009, Yu, Shao et al. 2021). It also explains that the shear strength of rock materials is much higher than its tensile strength. To model crack propagation more properly, researchers has proposed the mixed-model phase field method. Zhang (Zhang, Sloan et al. 2017) splits the elastic strain energy into the tensile and shear parts, and introduced two energy release rates corresponding to the tensile and shear fracture, respectively. The driving force for crack propagation is equal to the sum of tensile and shear strain energy divided by their energy release rates. The direction of fracture is given by a so called Φ-criterion, which determine the crack direction on the maximum driving force. Similar research result can also be found in literature (Bryant and Sun 2018, Wang, Feng et al. 2020). Wang et al. (Wang, Yu et al. 2021) proposed a new framework of the phase-field method in which the crack-driving strain energy is identified by the spectral decomposition concerning the principal direction. Fei and Choo (Fei and Choo 2021) proposed a mixed-mode phase field model that adopts the crack direction dependent method. In this framework, normal strain component on the crack normal direction contributes the driving force for I mode fracture, while shear strain component related the crack normal direction contributes to driving force for II mode fracture.

2.2 Phase field modelling for ductile fracture

Phase field method has been extended from brittle fracture to ductile fracture, which commonly occurs in reality. Compared to brittle fracture, where fracture energy serves as

the primary source of dissipation, ductile fracture is accompanied by substantial plastic dissipation resulting from nucleation and micro-void coalescence.(Alessi, Ambati et al. 2018). In the context of ductile phase field model, one needs to consider the interaction among displacement field $\boldsymbol{u}$, plastic strain field $\boldsymbol{\varepsilon^p}$, and phase field variable d simultaneously.

2.2.1 Incorporation of plasticity into phase field formulation

Significant efforts have been made to extend phase-field modelling from brittle fracture to ductile fracture in elasto-plastic solids (Miehe, Welschinger et al. 2014, Miehe, Hofacker et al. 2015, McAuliffe and Waisman 2016, Aldakheel, Wriggers et al. 2017, Dittmann, Aldakheel et al. 2018, Huang and Gao 2019, Dittmann, Aldakheel et al. 2020). There are mainly, to the best of author's knowledge, two directions proposed to handle this problem. The first approach is to continue the variation framework in brittle fracture and couple plastic free energy into the crack evolution, while another direction is to derive governing equation for those three fields from a microforce balance system. Related research on both directions will be summarized as below. Besides, the transformation from brittle to ductile fracture has also attracted the attention of the researchers.

When considering the crack evolution on the elastoplastic materials, one has to couple the damage/phase field variable d into yield surface. The yield stress needs to be degraded during the crack evolution process. That is because when crack initiate, the stress response would be degraded immediately. If yield surface keeps the original shape, the degraded stress would always stay below yield surface. It will lead to pure elastic dominant stress response, which is unrealistic in the ductile fracture phenomenon. To avoid this, Borden et al. (Borden, Hughes et al. 2016) proposed a degraded yield function as follows,

$$f(\boldsymbol{\tau}, \alpha) = \|\boldsymbol{s}\| - g_p(d)\sqrt{\frac{2}{3}}\left(\sigma_y + H_p \cdot \alpha\right) \tag{2.24}$$

where the yield stress is multiplied by the plastic degraded function $g_p(d)$. The plastic degradation function would take the same formulation as the stiffness degradation function to ensure the standard elastoplastic model still work in the damage coupled

system. This strategy of degradation on yield stress works well for J_2 plasticity model. However, when it comes to mean stress coupled yield function or multi-surface yield function, this plastic degradation will lose the efficiency. To address this issue, Choo and Sun (Choo and Sun 2018) postulated that only the undamaged portion of the material can sustain plastic deformation. With this idea, we do not need to degrade the yield stress, while we just replace the real stress with the effective (undamaged) stress in the original yield function.

To couple plasticity on crack evolution, Ambati (Ambati, Gerasimov et al. 2014, Ambati, Gerasimov et al. 2015) introduced a modified stiffness degradation approach, incorporating plastic strain into the governing equation, which is expressed as follows，

$$g(d,\varpi) = (1-d)^{2\varpi^j} \tag{2.25}$$

In this formulation, ϖ is the ratio of equivalent plastic strain $\bar{\varepsilon}^p$ of the critical plastic strain $\bar{\varepsilon}^p_{cr}$. Though the driving force $\mathcal{H}$ is unrelated with plasticity within this framework, the plastic strain $\bar{\varepsilon}^p_{cr}$ would accelerate or slow the evolution of phase field variable d via degraded function $g(d,\varpi)$.

Except for the above idea, other researchers tend to incorporate plastic strain into the driving force directly (Rodriguez, Ulloa et al. 2018, Fang, Wu et al. 2019, Fang, Wu et al. 2019, Kienle, Aldakheel et al. 2019). Miehe et al. (Miehe, Hofacker et al. 2015) extended the driving force for brittle fracture by adding a plasticity term as follows,

$$\mathcal{H}(\boldsymbol{x},t) \max_{\tau\in[0,t]} \langle \frac{w_e+w_p}{w_c} - 1 \rangle_+ \tag{2.26}$$

Similarly, Borden et al. (Borden, Hughes et al. 2016) coupled the plastic work in the driving force, written as

$$l_c \Delta d - \frac{d}{l_c} = \frac{g'(d)\cdot\mathcal{H}_e^+ + g_p'(d)\cdot\langle w_p - w_0\rangle_+}{G_f} \tag{2.27}$$

where w_p is the plastic work and w_0 is a defined threshold, plastic contribution to driving force only works when its value greater than this threshold.

The alternative method for ductile phase field modelling is to associate crack energy release rate with the plastic strain (Yin and Kaliske 2020). It is assumed that fracture

toughness would be reduced as plastic deformation develops. With this assumption, one can build the relationship between plasticity and crack energy release rate G_f and easily couple the plastic contribution to the phase field governing equation. Different formulation of degradation functions is summarised in Table 2.2.

Table 2.2 Formulations of crack energy release rate degradation function with plastic strain

Authors	Year	Degradation functions
Yin and Kaliske (Yin and Kaliske 2020)	2018	$G_c = f(\varepsilon^p)\cdot G_{c0}$ with $f(\varepsilon^p)=\begin{cases}1 & \varepsilon^p < \varepsilon_{cr}^p \\ \frac{1-b}{a^2}\left(\varepsilon^p-a\right)^2 & \varepsilon_{cr}^p \le \varepsilon^p < a+\varepsilon_{cr}^p \\ b & \varepsilon^p \ge a+\varepsilon_{cr}^p\end{cases}$
Huang and Gao (Huang and Gao 2019)	2019	$G_c = G_{c0}\cdot e^{-\frac{\alpha\cdot\varepsilon^p}{\varepsilon_{cr}^p}}$
Zhao et al. (Zhao, Huang et al. 2020)	2020	$G_c=\begin{cases}G_{c0} & \varepsilon^p < \varepsilon_{cr}^p \\ G_{c0}\cdot\left(c+\frac{1-c}{\exp(\varepsilon^p-\varepsilon_{cr}^p)}\right) & \varepsilon^p < \varepsilon_{cr}^p\end{cases}$
Han et al. (Han, Matsubara et al. 2021)	2021	$G_c(\varepsilon^p)=(G_{c,0}-G_{c,\infty})\left(\frac{1+\cos[-\beta_g\cdot\varepsilon^p]}{2}\right)+G_{c,\infty}$
Hu et al. (Hu, Talamini et al. 2021)	2021	$G_c = G_{c0}\cdot\left(b+(1-b)\cdot e^{-a\cdot\langle\xi-\xi^{cr}\rangle_+}\right)$

2.2.2 Mechanical characteristics of AM metallic material

Additive manufacturing (AM) techniques are on the basis of the design data and constitute a novel manufacturing method to produce solid structures by overlaying the raw materials automatically, which is attributed to its complex construction capability with high accuracy and good surface quality. At the same time, it cuts down greatly the time needed design and developing for the new products. Therefore, additive manufacturing techniques are promising to break through the limitations of traditional casting methods and provide the opportunity to realize the transformation and upgrading of the manufacturing industries.

The phase field model has been extended to model the fracture propagation for the AM materials. Ruan et al. (Ruan, Rezaei et al.) proposed a thermodynamic phase field model which incorporates the temperature variables with the crack energy release rate

and apply the proposed model for the crack modelling of AM specimens. It has been concluded that the solidification shrinkage strain has great effects on the formation of the circumferential crack, while the temperature gradient is mostly responsible for the central crack (Ruan, Rezaei et al.). Wilson-Heid et al. (Wilson-Heid and Beese 2019) has investigated the fracture behaviour SLM additively manufactured alloys in two orientations, and revealed that the stress-state-based fracture criterion could capture the failure behaviour more accurately. The GTN (Gurson-Tvergaard-Needleman) model has also been reported for capture the evolution of the microporosity for the AM materials. Yang et al. utilised the modified GTN model to predicted the ductile fracture of SLM-fabricated Ti-6Al4V alloy properly (Yang, Li et al. 2021). Azinpour (Azinpour, Ferreira et al. 2018, Azinpour, Darabi et al. 2020, Azinpour, Sa et al. 2020) further consider the evolution of micro-void defects with Rousselier damage criterion in the phase field framework for AM materials.

2.2.3 Brittle-ductile fracture transformation

The brittle and ductile phase field methods have been introduced for modelling fracture propagation in solids, and it has been pointed out that brittle fracture in rock is often observed under relatively low confining pressure, while higher confining pressure leads to propensity for ductile fracture (Choo and Sun 2018). Hence, there must be some transformation criterion for fracture model transformation. It is important for us to figure out that criterion to understand the stress response when apply phase field numerical method into engineering design.

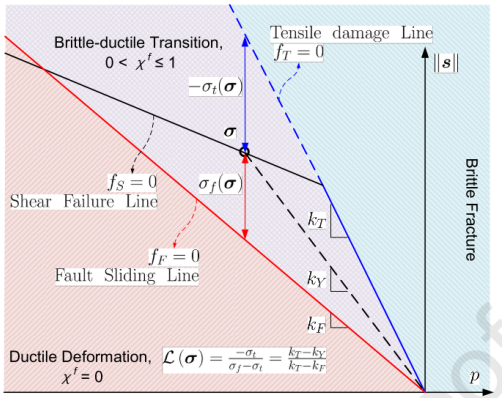

Figure 2.5 three different stress zone in mean-deviatoric stress space and the value of parameter χ^f.

Recently, some work has pay attention on this topic. You et al. (You, Zhu et al. 2020) has proposed a phase field model that incorporates the brittle and ductile fracture. In this work, there are two phase field variable that denote brittle and ductile fracture respectively, and the maximal principal stress was set the brittle-ductile fracture criterion. Ductile fracture stops and only brittle fracture develops when maximal principal stress is positive, while brittle fracture stops, and only ductile fracture develops when maximal principal stress is negative. Differently, Choo's research choose the volumetric strain as a criterion (Choo and Sun 2018). When volumetric strain is positive, the plastic contribution on the crack driving force reduces to zero.

To suggest the shear band phenomenon, based on the maximal principle stress criterion, You et al. (You, Waisman et al. 2021) further introduced a parameter χ^f to denote the fraction of the plastic free energy that goes into fracture generation. The stress space was divided into three zone: brittle fracture zone, ductile fracture zone, plastic shear band zone. The value of χ^f depends on the position where the stress state locates in the stress space. Samaniego (Samaniego, Ulloa et al. 2021) recently proposes a modified degradation on elastic stiffness, which delay the degradation on elastic stress during the phase field variable evolution, while keep plastic deformation at the beginning. In this way, a shear band phenomenon that plasticity deformation continue evolution while elastic stiffness stay original before the ductile initiation would be suggested.

2.3 Shell phase field fracture modelling

The phase-field model has also been applied to fracture analysis using shell element formulations, where the kinematic description follows either the Kirchhoff-Love or Reissner-Mindlin theory. Most researchers focused on the latter, and applied the solid-shell formulation to represent the fracture diffusion with a similar idea to phase field model in three dimension (Ambati and De Lorenzis 2016, Reinoso, Paggi et al. 2017, Reinoso, Durand et al. 2019), while the existing studies for the Kirchhoff-Love thin shell is limited, which is focused in this study.

A significant challenge in implementing the phase-field model for thin shells lies in capturing crack evolution through the shell thickness. Ulmer et al (Ulmer, Hofacker et al. 2012) firstly extend the phase field model for shell fracture modelling, where a single phase field variable was introduced to describe the thickness-through damage, which was jointly driven by the bending reference energy and tensile membrane strain energy on the mid-surface. This concept was adopted by subsequent research, such as Li et al. (Li, Millán et al. 2018), who applied this shell kinematics to simulate tearing in brittle thin sheets using a higher-order phase-field model. Pillai (Pillai, Triantafyllou et al. 2020) implemented the MITC4+ shell element for shell fracture modelling to avoid shear locking, and Ma et al. (Ma, Sun et al. 2024) incorporated the stress-resultants method to account for elasto-plastic materials in ductile shell fractures. Alternatively, Kiendl et al. (Kiendl, Ambati et al. 2016) split the strain energy spectrally through the shell thickness, integrating the tensile component as crack-driving energy, which was implemented via isogeometric analysis (IGA) or mesh-free method (Amiri, Millán et al. 2014, Ambati and De Lorenzis 2016, Proserpio, Ambati et al. 2020, Proserpio, Ambati et al. 2021).

The above-mentioned through-thickness fracture approximation might not accurately capture the distinct damage distribution along the shell thickness, especially under bending load. To address this limitation, Areias et al. (Areias, Rabczuk et al. 2016) introduced two phase-field variables for shell element implementation, representing different fracture propagation behaviours on the top and bottom surfaces of the shell,

while the displacement and angular variables remain based on the mid-reference surface. In a more recent study, Wang et al. (Wang, Han et al. 2022) assumed a linear interpolation of the phase-field distribution along the shell thickness and proposed an explicit implementation for elastoplastic materials.

2.4 Research gaps

The phase field model has been widely employed for fracture modelling and has proven effective in capturing crack propagation and the mechanical response of brittle and ductile materials. However, several challenges remain within this modelling framework.

For the fracture modelling of three-dimension solids, one key challenge is the accurate representation of tension-compression asymmetry. Although various strain energy decomposition strategies have been proposed to address this issue, most existing methods are designed to characterise fracture behaviour under specific stress states. Consequently, these approaches may lead to unphysical simulations when applied to stress states beyond their intended scope. For instance, volume-deviatoric (V-D) decomposition can lead to incorrect fracture driving force under transverse compressive loading conditions (Prakash, Behera et al. 2022), while spectral decomposition is unsuitable for simple shear loading, where the stress may not fully degrade even when the material has completely fractured (Behera, Sudeep et al. 2023, Hesammokri, Yu et al. 2023). Given that the real-world structures are often subjected to complex, spatially and temporally varying stress conditions, there is an urgent need for a unified stress state decomposition approach that remains effective under arbitrary stress states. Moreover, crack orientation significantly influences the mechanical response of materials and should be incorporated into the phase field model framework. However, existing crack orientation-related decomposition methods are predominantly limited to two-dimensional plane strain problems, leaving the behaviour of three-dimensional solids under complex stress states largely unexplored.

For thin-walled structures commonly found in engineering applications, there is a

significant disparity between the thickness scale and the in-plane dimensions. Consequently, employing solid elements for numerical modelling necessitates a large number of elements, leading to excessive computational costs. To address this issue, shell-based phase-field models have been developed. Both single-layer and multi-layer shell phase-field models have been proposed in the literature to simulate fracture propagation in thin-walled structures. However, most of these models have been validated only through benchmark numerical examples, with experimental validation largely absent. Furthermore, fracture initiation has been shown to depend on the stress state of materials, yet this effect has not been incorporated into existing shell phase-field frameworks, limiting their applicability to practical engineering scenarios. Lastly, strain rate plays a critical role in flow stress and fracture initiation in dynamic fracture mechanisms. However, this aspect remains largely unexplored within the shell phase-field framework. Therefore, the integration of strain rate- and stress state-dependent fracture criteria requires further investigation.

This dissertation will focus on advancing phase-field modelling for fracture in both solid and shell structures. For 3D solids, it addresses the challenge of tension–compression asymmetry by developing a unified strain energy decomposition method capable of accurately predicting fracture behaviour under arbitrary stress states, overcoming the limitations of existing spectral and volume–deviatoric approaches. For shell structures, the study extends phase-field modelling to capture stress-state-dependent fracture initiation and thickness-dependent damage evolution, supported by both benchmark and experimental validations. The proposed models are further applied to simulate the fracture and deformation of cylindrical battery casings and cells under different loading conditions, providing insights into stress-state effects. Additionally, a dynamic shell phase-field framework is developed to incorporate strain-rate, stress-state, and material-orientation dependencies, enabling more realistic simulation of fracture processes in engineering structures.

3. CRACK-ORIENTATION BASED STRAIN ENERGY DECOMPOSITION

3.1 Introduction

The recently emerging phase field model has proven to be an effective method for crack propagation modelling. It originated from the variational formulation for brittle fracture by Francfort and Marigo (Francfort and Marigo 1998) and was for the first time numerically implemented by Bourdin et al. (Bourdin, Francfort et al. 2000). The key idea of phase field modelling is to smear the discrete crack topology as a continuous phase field with a length scale parameter. The phase field and displacement field are then coupled, and they can be solved by minimising the total potential energy (Aldakheel, Mauthe et al. 2014, Miehe, Schänzel et al. 2015). Standard isotropic phase field models do not distinguish tensile and compressive stress, which leads to the same fracture driving force and crack propagation under tensile and compressive loads (Miehe, Hofacker et al. 2010, Miehe, Schänzel et al. 2015). Nevertheless, it does not agree with the experimental observation that most materials exhibit different behaviours of fracture in tension and compression (You, Zhu et al. 2020).

To solve this problem, various strategies have been proposed to split the strain energy into positive and negative parts, where only the positive part contributes to crack propagation (Miehe, Hofacker et al. 2010, Miehe, Welschinger et al. 2010, Miehe, Hofacker et al. 2015). Among them, the two most commonly adopted methods are volumetric-deviatoric (V-D) (Amor, Marigo et al. 2009, Lancioni and Royer-Carfagni 2009) and spectral decomposition (Miehe, Hofacker et al. 2010, Miehe, Welschinger et al. 2014). In addition, Zhang et al. (Zhang, Huang et al. 2018) utilised three regularisation functions to smooth the decomposed positive and negative spectral strains, which makes the convergence of Newtown's iteration more robust. Wu et al. (Wu and Xu 2013, Wu and Nguyen 2018) applied the spectral decomposition on the effective (undamaged) stress tensor and formulated the crack driving force only from the positive major principal stress.

Tang et al. (Tang, Zhang et al. 2019) split the strain energy into principal stretch related and volumetric parts for modelling general non-linear elastic mechanical response. Nguyen et al. (Nguyen, Yvonnet et al. 2020) introduced a new projector for strain decomposition that ensures the orthogonality between traction and compression parts.

In the above positive/negative projection based on spectral decomposition, it is assumed that the crack orientation is always aligned with the principal axes of the effective (undamaged) stress (or strain) tensor. This assumption does not always hold, e.g., in case of pre-existing cracks not coaxial to the local strain/stress fields (Wu, Nguyen et al. 2020). To address this issue, a crack-direction-based stress decomposition strategy has been proposed by Strobl and Seelig (Strobl and Seelig 2015, Strobl and Seelig 2016) and further developed by Stenike and Kaliske (Steinke and Kaliske 2018). This strategy decomposes the effective (undamaged) stress in the local crack-direction-based coordinate system, and its positive components contribute to fracture, including normal tensile stress on and shear stress parallel to the crack surface. The crack orientation was assumed as the first principal stress direction, and only tensile damage was considered (Steinke and Kaliske 2018). Luo et al. (Luo, Chen et al. 2021) applied this crack-direction-based split strategy to the decomposition of strain tensor and introduced a stress-driven crack opening indicator. A later study by Stenike et al. (Steinke, Storm et al. 2022) further distinguished the tensile and shear strain energies, and the *F*-criterion (B.Shen and O.Stephansson 1994) was then adopted to determine the crack orientation. Fei and Choo (Fei and Choo 2021) incorporated the friction shear energy on the crack surface and proposed a double-phase field model that distinguishes tensile and shear damage. Nevertheless, most existing crack-direction-based energy decomposition strategies only considered crack propagation in a 2D setting, while complex fracture modelling problems in 3D space remain for further investigation.

Compared to brittle fracture, where fracture energy serves as the primary source of dissipation, ductile fracture is accompanied by substantial plastic dissipation resulting from nucleation and micro-void coalescence (Alessi, Ambati et al. 2018). Significant

efforts have been made to extend phase-field modelling from brittle fracture to ductile fracture in elasto-plastic solids (McAuliffe and Waisman 2016, Aldakheel, Wriggers et al. 2017, Dittmann, Aldakheel et al. 2018, Huang and Gao 2019, Dittmann, Aldakheel et al. 2020). Ambati et al. (Ambati, Gerasimov et al. 2015, Ambati, Kruse et al. 2015) replaced conventional quadratic stiffness degradation with a new one coupled with plastic strain in the governing equation. Borden et al. (Borden, Hughes et al. 2016) proposed the effective plastic work driving energy incorporating the triaxiality to consider its effect on fracture behaviours. You et al. (You, Zhu et al. 2020) utilised two phase field variables to indicate the brittle tensile fracture and compressive shear fracture, respectively, and the plastic work only contributes to compressive shear fracture. Yin et al. (Yin, Steinke et al. 2019, Yin and Kaliske 2020, Han, Matsubara et al. 2021) assumed that the fracture toughness decreases as the plastic deformation develops, and they used a plastic strain dependent fracture energy release rate for damage evolution. More recently, Hu et al. (Hu, Talamini et al. 2021) deduced an alternative effective fracture toughness degradation formulation by introducing the coalescence dissipation. However, these models cannot capture the effect of the crack orientation on the fracture evolution where only a single plastic strain quantity, i.e., accumulated plastic strain, is considered for dealing with the plastic energy driving force or the fracture toughness degradation. When the mixed-mode crack initiates and propagates in a solid, distinguishing the plastic contribution to the tensile and shear fractures remains an open issue. To the authors' best knowledge, there is no study on ductile fracture modelling using the crack-orientation-based phase field framework.

In this study, we propose a ductile double-phase field model to distinguish the tensile and shear fracture damages. Both the effective (undamaged) stress and the plastic strain are split in the crack-orientation-based coordinate system. The decomposed tensile and shear stresses contribute to the crack driving forces for the tensile and shear damages, respectively. The plastic deformation for crack evolution is then coupled by relating the decomposed tensile and shear plastic strain to the corresponding crack energy release

rates. The *F*-criterion is utilised for the determination of 3D crack orientation in solids. The remainder of this paper is organised as follows. Section 2 introduces the formulation of the proposed double-phase field model with crack-orientation-based energy decomposition. Section 3 presents the finite element implementation of this model. Section 4 provides numerical examples, including a numerical example of one element under tension/compression, single-edge notch specimens under tension and shear loading, a group of uniaxial tension, simple shear and tension shear specimens, and the third Sandia Challenge modelling, followed by some conclusions in Section 5.

3.2 Crack direction based double phase field model

3.2.1 Double phase-field definition

Consider an arbitrary body Ω with a shear crack Γ_t and a tensile crack Γ_c as shown in Figure 3.1 (a). the external boundary $\partial\Omega$ consists of the Dirichlet boundary $\partial\Omega^h$ with boundary displacement $\bar{\boldsymbol{u}}$, and the Neumann boundary $\partial\Omega^s$ with boundary traction $\boldsymbol{t}$, which satisfy $\partial\Omega^{\mathrm{h}} \cap \partial\Omega^{\mathrm{s}} = \emptyset$ and $\partial\Omega = \overline{\partial\Omega^{\mathrm{h}} \cup \partial\Omega^{\mathrm{s}}}$. The body force within Ω is represented by $\boldsymbol{b}$. Inspired by literature (You, Zhu et al. 2020, Fei and Choo 2021), here we introduce the concept of tensile and shear damage phase fields d_{t} and d_{c}, which regularises the sharp tensile and shear cracks Γ_t and Γ_c , respectively, demonstrated in Figure 3.1 (b). Their corresponding crack density functions are assumed to have the same form as the standard phase field model, expressed in Eq. (3.1) and Eq.(3.2) respectively. In addition, the energy release rates for tensile and shear cracks (denoted by G_t and G_c respectively) are also distinguished, following the previous studies (Zhang, Sloan et al. 2017, Bryant and Sun 2018, Wang, Feng et al. 2020, Yu, Hao et al. 2022).

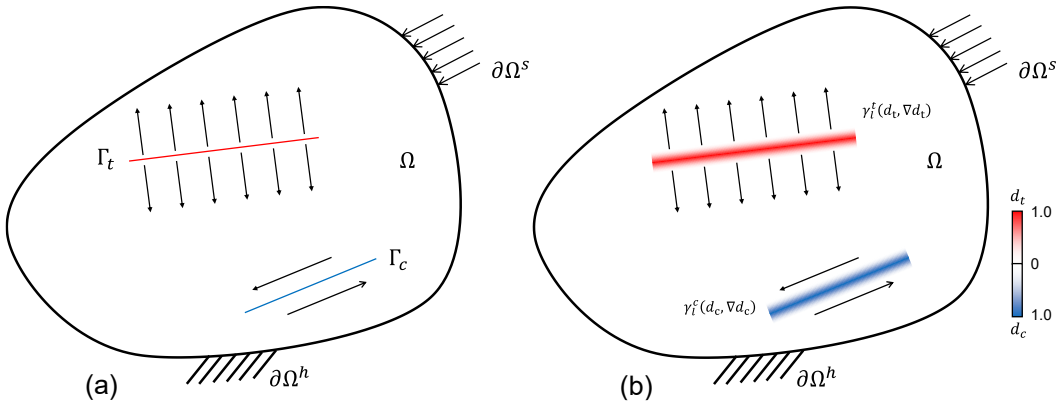

Figure 3.1 Geometric topology of a solid body for (a) sharp tensile and shear crack boundary; (b) regularized tensile and shear damage phase field distribution.

$$\gamma_{\mathrm{t}}(d_{\mathrm{t}},\nabla d_{\mathrm{t}}) = \frac{{d_{\mathrm{t}}}^2}{2l} + \frac{l}{2}|\nabla d_{\mathrm{t}}|^2 \tag{3.1}$$

$$\gamma_{\mathrm{c}}(d_{\mathrm{c}},\nabla d_{\mathrm{c}}) = \frac{{d_{\mathrm{c}}}^2}{2l} + \frac{l}{2}|\nabla d_{\mathrm{c}}|^2 \tag{3.2}$$

3.2.2 Crack-orientation-based stress decomposition

To capture the anisotropic stress response of fractured solids and distinguish the tensile and shear damage, the stress tensor is decomposed in the local crack reference coordinate system (CCS) (see Figure 3.2), where $\boldsymbol{r}$ is the normal direction of the crack surface, while $\boldsymbol{s}$ and $\boldsymbol{t}$ are other two orthonormal vectors. The undamaged stress tensor under this local coordinate system could be written in matrix formulation as,

$$\bar{\boldsymbol{\sigma}} = \begin{bmatrix} \bar{\sigma}_{rr} & \bar{\sigma}_{rs} & \bar{\sigma}_{rt} \\ \bar{\sigma}_{sr} & \bar{\sigma}_{ss} & \bar{\sigma}_{st} \\ \bar{\sigma}_{tr} & \bar{\sigma}_{ts} & \bar{\sigma}_{tt} \end{bmatrix} \tag{3.3}$$

here each scalar component $\bar{\sigma}_{pq}$ (p, q = r, s, or t) represents the normal stress on p surface or shear stress along p surface in q direction and could be calculated via $\bar{\sigma}_{pq} = \bar{\boldsymbol{\sigma}}\colon \boldsymbol{M}^{pq}$. The projection tensor $\boldsymbol{M}^{pq}$ is defined based on the three base unit vectors $\boldsymbol{r}$, $\boldsymbol{s}$ and $\boldsymbol{t}$ in CCS, written by:

$$\begin{cases} \boldsymbol{M}^{rr} = \boldsymbol{r}\otimes\boldsymbol{r}, & \boldsymbol{M}^{rs} = \boldsymbol{r}\otimes\boldsymbol{s}, & \boldsymbol{M}^{rt} = \boldsymbol{r}\otimes\boldsymbol{t}, \\ \boldsymbol{M}^{sr} = \boldsymbol{s}\otimes\boldsymbol{r}, & \boldsymbol{M}^{ss} = \boldsymbol{s}\otimes\boldsymbol{s}, & \boldsymbol{M}^{st} = \boldsymbol{s}\otimes\boldsymbol{t}, \\ \boldsymbol{M}^{tr} = \boldsymbol{r}\otimes\boldsymbol{r}, & \boldsymbol{M}^{ts} = \boldsymbol{r}\otimes\boldsymbol{s}, & \boldsymbol{M}^{tt} = \boldsymbol{r}\otimes\boldsymbol{t} \end{cases} \tag{3.4}$$

Accordingly, the stress tensor corresponding to each component can be expressed by:

$$\begin{cases} \bar{\boldsymbol{\sigma}}^{rr} = \bar{\sigma}_{rr}\cdot\boldsymbol{M}^{rr}, & \bar{\boldsymbol{\sigma}}^{rs} = \bar{\sigma}_{rs}\cdot\boldsymbol{M}^{rs}, & \bar{\boldsymbol{\sigma}}^{rt} = \bar{\sigma}_{rt}\cdot\boldsymbol{M}^{rt}, \\ \bar{\boldsymbol{\sigma}}^{sr} = \bar{\sigma}_{sr}\cdot\boldsymbol{M}^{sr}, & \bar{\boldsymbol{\sigma}}^{ss} = \bar{\sigma}_{ss}\cdot\boldsymbol{M}^{ss}, & \bar{\boldsymbol{\sigma}}^{st} = \bar{\sigma}_{st}\cdot\boldsymbol{M}^{st}, \\ \bar{\boldsymbol{\sigma}}^{tr} = \bar{\sigma}_{tr}\cdot\boldsymbol{M}^{tr}, & \bar{\boldsymbol{\sigma}}^{ts} = \bar{\sigma}_{ts}\cdot\boldsymbol{M}^{ts}, & \bar{\boldsymbol{\sigma}}^{tt} = \bar{\sigma}_{tt}\cdot\boldsymbol{M}^{tt} \end{cases} \tag{3.5}$$

With this stress decomposition strategy, we split the undamaged stress tensor into three parts, namely the tensile stress tensor $\overline{\boldsymbol{\sigma}}_{\mathrm{I}}^{+}$, shear stress tensor $\overline{\boldsymbol{\sigma}}_{\mathrm{II}}^{+}$ and the intact stress tensor $\boldsymbol{\sigma}^{-}$ as defined in Eqs. (3.6)-(3.8), respectively.

$$\overline{\boldsymbol{\sigma}}_{\mathrm{I}}^{+} = \langle \bar{\sigma}_{rr} \rangle_{+} \cdot \boldsymbol{M}^{rr} + \frac{\lambda}{\lambda+2G} \cdot \langle \bar{\sigma}_{rr} \rangle_{+} \cdot (\boldsymbol{M}^{ss} + \boldsymbol{M}^{tt}) \tag{3.6}$$

$$\overline{\boldsymbol{\sigma}}_{\mathrm{II}}^{+} = \overline{\boldsymbol{\sigma}}^{rs} + \overline{\boldsymbol{\sigma}}^{sr} + \overline{\boldsymbol{\sigma}}^{rt} + \overline{\boldsymbol{\sigma}}^{tr} \tag{3.7}$$

$$\boldsymbol{\sigma}^{-} = \langle \bar{\sigma}_{rr} \rangle_{-} \cdot \boldsymbol{M}^{rr} - \frac{\lambda}{\lambda+2G} \cdot \langle \bar{\sigma}_{rr} \rangle_{+} \cdot (\boldsymbol{M}^{ss} + \boldsymbol{M}^{tt}) + \overline{\boldsymbol{\sigma}}^{st} + \overline{\boldsymbol{\sigma}}^{ts} + \overline{\boldsymbol{\sigma}}^{ss} + \overline{\boldsymbol{\sigma}}^{tt} \tag{3.8}$$

with the bracket operator $\langle * \rangle_{\pm} = \frac{1}{2}(* \pm |*|)$. Depending on the sign of $\bar{\sigma}_{rr}$ in Eq.(3.6) and Eq.(3.8), the normal stress on the crack surface contributes to tensile stress or intact stress. It is also noted that the tensile stress tensor includes not only the normal stress on the crack surface but also the second term in Eq.(3.6), which is introduced for describing the lateral elastic deformation release and ensuring all three decomposed parts of the strain energy positive. The reader is referred to the literature (Steinke and Kaliske 2018) for a more detailed explanation.

The nominal stress is obtained by summing up intact stress tensor $\boldsymbol{\sigma}^{-}$ and the degraded tensile stress and shear stress as

$$\boldsymbol{\sigma} = \mathrm{g}(d_t)\overline{\boldsymbol{\sigma}}_{\mathrm{I}}^{+} + \mathrm{g}(d_c)\overline{\boldsymbol{\sigma}}_{\mathrm{II}}^{+} + \boldsymbol{\sigma}^{-} \tag{3.9}$$

where $\mathrm{g}(d_t)$ and $\mathrm{g}(d_c)$ are the degradation functions in terms of tensile damage d_t and shear damage d_c respectively. The standard quadratic formulations are adopted here as $\mathrm{g}(d_t) = (1-d_t)^2$ and $\mathrm{g}(d_c) = (1-d_c)^2$.

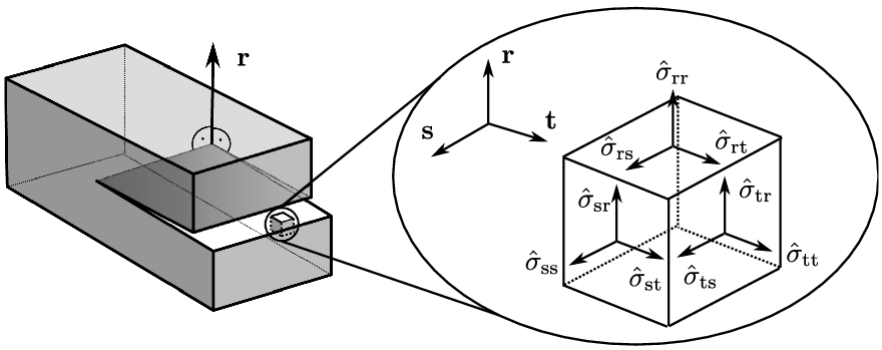

Figure 3.2 crack orientation topology and stress decomposition (Steinke and Kaliske 2018).

3.2.3 Tensile/shear energy release rates degradation

3.2.3.1 Plastic strain decomposition

To distinguish the plastic contribution to the tensile and shear fractures, the plastic strain is split in the local crack orientation-based coordinate system. The decomposition for plastic strain rate is similar to the stress decomposition strategy introduced above, formulated as follows:

$$\dot{\boldsymbol{\varepsilon}}^{p}_{\mathrm{I}+} = \langle \dot{\boldsymbol{\varepsilon}}^{p} : \boldsymbol{M}^{rr} \rangle_{+} \cdot \boldsymbol{M}^{rr} \tag{3.10}$$

$$\dot{\boldsymbol{\varepsilon}}^{p}_{\mathrm{II}+} = \dot{\boldsymbol{\varepsilon}}^{p} : (\boldsymbol{M}^{rs} \otimes \boldsymbol{M}^{rs} + \boldsymbol{M}^{sr} \otimes \boldsymbol{M}^{sr} + \boldsymbol{M}^{rt} \otimes \boldsymbol{M}^{rt} + \boldsymbol{M}^{tr} \otimes \boldsymbol{M}^{tr}) \tag{3.11}$$

It is noticed that the second term in Eq.(3.6) vanishes here in Eq.(3.10) because there is no need to consider Poisson's effect and lateral deformation release when it comes to the plastic strain decomposition. Only the positive normal plastic strain in $\boldsymbol{r}$ direction contributes to the tensile damage.

With that plastic strain rate decomposition in hand, the concept of tensile and shear accumulated plastic strains represented by ξ_t and ξ_c are defined as the integrals of the norm of the tensile and shear plastic strain rate respectively, written as follows,

$$\xi_t = \int_0^t \sqrt{\dot{\boldsymbol{\varepsilon}}^{p}_{\mathrm{I}+} : \dot{\boldsymbol{\varepsilon}}^{p}_{\mathrm{I}+}}\, \mathrm{dt} \tag{3.12}$$

$$\xi_c = \int_0^t \sqrt{\dot{\boldsymbol{\varepsilon}}^{p}_{\mathrm{II}+} : \dot{\boldsymbol{\varepsilon}}^{p}_{\mathrm{II}+}}\, \mathrm{dt} \tag{3.13}$$

3.2.3.2 Energy release rate degradation

To couple the plastic deformation with fracture propagation, the degradation strategy of energy release rate has been widely used (Dittmann, Aldakheel et al. 2018, Huang and Gao 2019, Yin and Kaliske 2020, Zhao, Huang et al. 2020, Hu, Talamini et al. 2021). The energy release rates are not assumed to be constant but monotonically decrease as the accumulated plastic strain increases. Following this idea, the decomposed tensile plastic strain ξ_t and shear plastic strain ξ_c are related to G_t and G_c, respectively.

$$\begin{cases} G_t = f(\xi_t) \cdot G_{t0} \\ G_c = f(\xi_c) \cdot G_{c0} \end{cases} \tag{3.14}$$

where G_{t0} and G_{c0} are initial crack energy release rates. $f(\xi_t)$ and $f(\xi_c)$ are the degradation functions and in this study they are defined as (Hu, Talamini et al. 2021):

$$f(\xi) = b + (1-b)\cdot e^{-a\cdot\langle \xi-\xi^{cr}\rangle_+} \tag{3.15}$$

where the b characterises the residual energy release rate in the final plastic strain state; ξ^{cr} represents the threshold value for the accumulated plastic strain to take effect on the energy release rate; and $a > 0$ is a parameter that controls the decreasing rate of the energy release rate as the plastic strain increases. This function has been plotted in Figure 3.3. The three parameters in a , b and ξ^{cr} in Eq.(3.15) for tensile and shear damages are distinguished by the subscripts as: a_t , b_t , ξ_t^{cr} and a_c , b_c , ξ_c^{cr}.

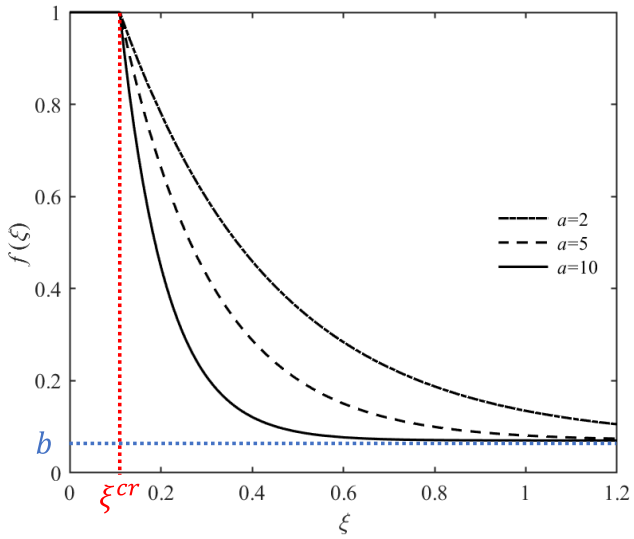

Figure 3.3 Energy Release Rate degradation function $f(\xi)$

3.2.4 Governing equations of double-phase field evolution

3.2.4.1 Energy functional

Under the crack-orientation-based stress decomposition framework, the stress is decomposed into tensile stress, shear stress and intact stress (see Eq.(3.9)). Consequently, the elastic stored energy density ψ^e could also be obtained as the sum of the three corresponding parts of elastic strain energy as follows,

$$\psi^e(\boldsymbol{\varepsilon}^e, d_t, d_c) = \frac{1}{2}(1-d_t)^2\overline{\boldsymbol{\sigma}}_{\mathrm{I}}^{+}:\boldsymbol{\varepsilon}^e + \frac{1}{2}(1-d_c)^2\overline{\boldsymbol{\sigma}}_{\mathrm{II}}^{+}:\boldsymbol{\varepsilon}^e + \frac{1}{2}\boldsymbol{\sigma}^{-}:\boldsymbol{\varepsilon}^e \tag{3.16}$$

To consider the plastic work, the accumulated plastic strain $\bar{\varepsilon}^p$ is introduced as follows,

$$\bar{\varepsilon}^p = \int_0^t \sqrt{\frac{2}{3}\dot{e}_{ij}(t)\cdot\dot{e}_{ij}(t)}\mathrm{d}t \tag{3.17}$$

where the e_{ij} (i, j = 1, 2 and 3) denotes the component of the accumulated plastic strain

tensor. Then, the plastic work density could be written as follows (Li, Fang et al. 2022),

$$\psi^p(\bar{\varepsilon}^p) = \int_0^{\bar{\varepsilon}^p} \bar{\sigma}_y(\bar{\varepsilon}^p)\,\mathrm{d}\bar{\varepsilon}^p \tag{3.18}$$

where $\bar{\sigma}_y$ denotes the undamaged yield stress. Since in this proposed model, the plastic contribution to crack propagation is incorporated via energy release rate degradation rather than via crack driving force, the plastic energy density in Eq.(3.18) is not degraded by phase field damage. Moreover, the linear isotropic hardening (Fang, Wu et al. 2019, Fang, Wu et al. 2019) is considered here for simplification, and thus Eq.(3.18) could be recast as follows,

$$\psi^p(\bar{\varepsilon}^p) = \frac{1}{2}h \cdot \bar{\varepsilon}^{p\,2} + \bar{\sigma}_{y0} \cdot \bar{\varepsilon}^p \tag{3.19}$$

where h and $\bar{\sigma}_{y0}$ denote the hardening modulus and initial yield stress, respectively.

The tensile and shear fracture surface density functions have been introduced in Eq. (3.1) and Eq.(3.2), respectively, as well as their corresponding energy release rates in Eq.(3.14). Therefore, the fracture energy density could be written as

$$\varphi^d = G_t(\xi_t) \cdot \left(\frac{{d_\mathrm{t}}^2}{2l} + \frac{l}{2}|\nabla d_\mathrm{t}|^2\right) + G_c(\xi_c) \cdot \left(\frac{{d_\mathrm{c}}^2}{2l} + \frac{l}{2}|\nabla d_\mathrm{c}|^2\right) \tag{3.20}$$

The total energy functional then could be defined as (Fang, Wu et al. 2019),

$$\Phi = \int_\Omega (\psi^e + \psi^p + \psi^d)\mathrm{d}\Omega - \int_\Omega (\boldsymbol{t}\cdot\boldsymbol{u})\mathrm{d}\Omega - \int_{\partial\Omega^s}(\boldsymbol{b}\cdot\boldsymbol{u})\mathrm{dS} \tag{3.21}$$

where $\boldsymbol{u}$ is the displacement field within the solid. Substitution of Eq.(3.16), (3.19) and (3.20) into Eq.(3.21) leads to

$$\Phi = \int_\Omega \begin{pmatrix} \frac{1}{2}(1-d_t)^2\overline{\boldsymbol{\sigma}}_\mathrm{I}^+ : \boldsymbol{\varepsilon}^e + \frac{1}{2}(1-d_c)^2\overline{\boldsymbol{\sigma}}_\mathrm{II}^+ : \boldsymbol{\varepsilon}^e + \frac{1}{2}\boldsymbol{\sigma}^- : \boldsymbol{\varepsilon}^e \\ +\frac{1}{2}h\cdot\bar{\varepsilon}^{p\,2} + \bar{\sigma}_{y0}\cdot\bar{\varepsilon}^p + G_t(\xi_t)\cdot\left(\frac{{d_\mathrm{t}}^2}{2l} + \frac{l}{2}|\nabla d_\mathrm{t}|^2\right) \\ +G_c(\xi_c)\cdot\left(\frac{{d_\mathrm{c}}^2}{2l} + \frac{l}{2}|\nabla d_\mathrm{c}|^2\right) - \boldsymbol{t}\cdot\boldsymbol{u} \end{pmatrix}\mathrm{d}\Omega - \int_{\partial\Omega^s}(\boldsymbol{b}\cdot\boldsymbol{u})\mathrm{dS} \tag{3.22}$$

3.2.4.2 Phase field variable governing equations

From Eq.(3.22), the total potential energy Φ is a function of the displacement field $\boldsymbol{u}$ and two damages phase fields d_t and d_c. The evolution of damage can be deduced by

minimising Φ with respect to d_t and d_c,

$$\frac{\delta\Phi}{\delta d_t}\dot{d}_t = \int_\Omega \left((1-d_t)\overline{\boldsymbol{\sigma}}_{\mathrm{I}}^{+}:\boldsymbol{\varepsilon}^e\cdot\dot{d}_t + G_t(\xi_t)\frac{d_t}{l}\dot{d}_t + G_t(\xi_t)l\cdot\nabla d_{\mathrm{t}}\cdot\nabla\dot{d}_{\mathrm{t}}\right)\mathrm{d}\Omega = 0 \tag{3.23}$$

$$\frac{\delta\Phi}{\delta d_c}\dot{d}_c = \int_\Omega \left((1-d_c)\overline{\boldsymbol{\sigma}}_{\mathrm{II}}^{+}:\boldsymbol{\varepsilon}^e\cdot\dot{d}_c + G_c(\xi_c)\frac{d_c}{l}\dot{d}_c + G_c(\xi_c)l\cdot\nabla d_{\mathrm{c}}\cdot\nabla\dot{d}_{\mathrm{c}}\right)\mathrm{d}\Omega = 0 \tag{3.24}$$

According to the integration by parts,

$$\int_\Omega \left(G_t(\xi_t)l\cdot\nabla d_{\mathrm{t}}\cdot\nabla\dot{d}_{\mathrm{t}}\right)\mathrm{d}\Omega = \int_{\partial\Omega}(G_t(\xi_t)\cdot l\cdot\nabla d_{\mathrm{t}}\cdot\boldsymbol{n})\mathrm{dS} - \int_\Omega\left[(G_t(\xi_t)\cdot l\Delta d_{\mathrm{t}} + l\cdot\nabla G_t(\xi_t)\cdot\nabla d_{\mathrm{t}})\cdot\dot{d}_t\right]\mathrm{d}\Omega \tag{3.25}$$

$$\int_\Omega \left(G_c(\xi_c)l\cdot\nabla d_{\mathrm{c}}\cdot\nabla\dot{d}_{\mathrm{c}}\right)\mathrm{d}\Omega = \int_{\partial\Omega}(G_c(\xi_c)\cdot l\cdot\nabla d_{\mathrm{c}}\cdot\boldsymbol{n})\mathrm{dS} - \int_\Omega\left[(G_c(\xi_c)\cdot l\Delta d_{\mathrm{c}} + l\cdot\nabla G_c(\xi_c)\cdot\nabla d_{\mathrm{c}})\cdot\dot{d}_c\right]\mathrm{d}\Omega \tag{3.26}$$

where $\boldsymbol{n}$ denotes the outward unit vector normal to the boundary surface on $\partial\Omega$. Substitution of Eq.(3.25) and Eq.(3.26) into Eq.(3.23) and Eq.(3.24) leads to

$$\int_\Omega\left[\left((1-d_t)\overline{\boldsymbol{\sigma}}_I^{+}:\boldsymbol{\varepsilon}^e + G_t(\xi_t)\frac{d_t}{l} - G_t(\xi_t)\cdot l\Delta d_t - l\cdot\nabla G_t(\xi_t)\cdot\nabla d_t\right)\cdot\dot{d}_t\right]\mathrm{d}\Omega = 0 \tag{3.27}$$

$$\int_\Omega\left[\left((1-d_c)\overline{\boldsymbol{\sigma}}_{\mathrm{II}}^{+}:\boldsymbol{\varepsilon}^e + G_c(\xi_c)\frac{d_c}{l} - G_c(\xi_c)\cdot l\Delta d_{\mathrm{c}} - l\cdot\nabla G_c(\xi_c)\cdot\nabla d_{\mathrm{c}}\right)\cdot\dot{d}_c\right]\mathrm{d}\Omega = 0 \tag{3.28}$$

Since both tensile and shear damages are irreversible, $\dot{d}_t$ and $\dot{d}_C$ are nonnegative, and when the crack propagates, $\dot{d}_t > 0$ and $\dot{d}_c > 0$. The governing equations of phase field variables for tensile and shear damage evolutions are then obtained as follows,

$$(1-d_t)\overline{\boldsymbol{\sigma}}_I^{+}:\boldsymbol{\varepsilon}^e + G_t(\xi_t)\frac{d_t}{l} - G_t(\xi_t)\cdot l\Delta d_t - l\cdot\nabla G_t(\xi_t)\cdot\nabla d_t = 0 \tag{3.29}$$

$$(1-d_c)\overline{\boldsymbol{\sigma}}_{\mathrm{II}}^{+}:\boldsymbol{\varepsilon}^e + G_c(\xi_c)\frac{d_c}{l} - G_c(\xi_c)\cdot l\Delta d_{\mathrm{c}} - l\cdot\nabla G_c(\xi_c)\cdot\nabla d_{\mathrm{c}} = 0 \tag{3.30}$$

The equilibrium equation could be formulated by taking the variation of Φ with respect to $\boldsymbol{u}$,

$$\int_\Omega[-(\nabla\cdot\boldsymbol{\sigma}+\boldsymbol{t})\cdot\delta\boldsymbol{u}]\mathrm{d}\Omega + \int_{\partial\Omega^s}[(\boldsymbol{\sigma}\cdot\boldsymbol{n}-\boldsymbol{b})\cdot\delta\boldsymbol{u}]\mathrm{dS} = 0 \tag{3.31}$$

It is worth mentioning that the stress tensor $\boldsymbol{\sigma}$ in Eq.(3.31) represents the degraded

nominal stress which is consistent with Eq.(3.9). The strong form for displacement field $\boldsymbol{u}$ then could be obtained as follows,

$$\nabla \cdot \boldsymbol{\sigma} + \boldsymbol{t} = 0 \qquad \text{in } \Omega \tag{3.32a}$$

$$\boldsymbol{\sigma} \cdot \boldsymbol{n} - \boldsymbol{b} = 0 \qquad \text{on } \partial\Omega^s \tag{3.32b}$$

$$\boldsymbol{u} = \overline{\boldsymbol{u}} \qquad \text{on } \partial\Omega^h \tag{3.32c}$$

3.2.4.3 Plastic formulation

In terms of plasticity, we introduce the undamaged effective stress and assume strain equivalence (Choo and Sun 2018). The commonly used von Mises yield function is adopted here as follows:

$$f_s(\overline{\boldsymbol{\sigma}}) = \sqrt{\frac{3}{2}}\|\overline{\boldsymbol{s}}\| - \sigma_y \tag{3.33}$$

where $\overline{\boldsymbol{s}} = \overline{\boldsymbol{\sigma}} - \frac{1}{3}\bar{\sigma}_{kk}\boldsymbol{\delta}$ (δ_{ij} is the Kronecker delta, satisfying $\delta_{ij} = 1$ when $i = j$ and $\delta_{ij} = 0$ when $i \neq j$) is the deviatoric undamaged stress. The associated plastic flow rule is used, and the plastic strain rate could be calculated by

$$\dot{\boldsymbol{\varepsilon}}^p = \sqrt{\frac{3}{2}}\dot{\bar{\varepsilon}}^p \frac{\bar{\boldsymbol{s}}}{\|\bar{\boldsymbol{s}}\|} \tag{3.34}$$

3.2.5 Determination of the crack direction

3.2.5.1 Crack orientation in principal stress space

This crack orientation is shown in Figure 3.4, where $\boldsymbol{n}_1$, $\boldsymbol{n}_2$ and $\boldsymbol{n}_3$ are the three principal stress directions; $\boldsymbol{r}$ represents the crack surface normal direction and its projection on the $\boldsymbol{n}_1$-$\boldsymbol{n}_2$ surface is denoted by $\boldsymbol{r}'$. In the principal stress space, $\boldsymbol{r}$ can be expressed as:

$$\boldsymbol{r} = (cos\alpha \cdot cos\beta,\ cos\alpha \cdot sin\beta,\ sin\alpha) \tag{3.35}$$

where $\alpha \in \left(-\frac{\pi}{2}, \frac{\pi}{2}\right]$ denotes the angle between $\boldsymbol{r}$ and $\boldsymbol{r}'$, and $\beta \in \left(-\frac{\pi}{2}, \frac{\pi}{2}\right]$ denotes the angle between $\boldsymbol{r}'$ and $\boldsymbol{n}_1$. We specify the other two orthogonal directions $\boldsymbol{s}$ and $\boldsymbol{t}$ as follows:

$$\boldsymbol{s} = (sin\beta, -cos\beta,\ 0) \tag{3.36}$$

$$\boldsymbol{t} = (sin\alpha \cdot cos\beta,\ sin\alpha \cdot sin\beta,\ -cos\alpha) \tag{3.37}$$

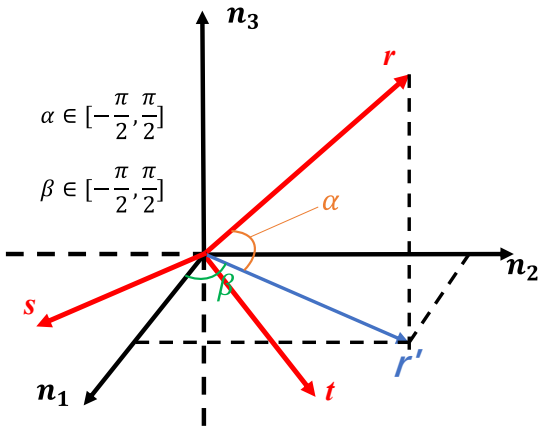

Figure 3.4 crack direction orientation in principal stress space

3.2.5.2 F-criterion

The *F*-criterion was inspired by the maximum energy release rate criterion, namely *G*-criterion (Cotterell and J.R.Rice 1980), where the crack initiates when the strain energy release rate G exceeds the critical energy release rate G_{cr}. It has been pointed out that the total strain energy release rate for mixed-mode crack is the sum of mode I energy release rate G_{I} and mode II energy release rate G_{II} (Fan, Jin et al. 2021). Then, the *G*-criterion could be rewritten as $\frac{G_{\mathrm{I}}}{G_{cr}} + \frac{G_{\mathrm{II}}}{G_{cr}} \geq 1$. The drawback of the *G*-criterion is that it does not consider the difference between mode I fracture toughness G_{Icr} and mode II fracture toughness G_{IIcr} (Shen, Liu et al. 2019). To address this issue, Shen and Stephansson (B.Shen and O.Stephansson 1994) proposed the *F*-criterion, written as

$$F(\theta) = \frac{G_{\mathrm{I}}(\theta)}{G_{crI}} + \frac{G_{\mathrm{II}}(\theta)}{G_{crII}} \tag{3.38}$$

where the critical energy release rate G_{cr} in the *G*-criterion is replaced by G_{Icr} or G_{IIcr}, and θ denotes the angle between the current crack surface direction and the crack propagation direction. The crack initiates when the maximum value of $F(\theta)$ is greater than unity, and it will propagate along the direction that maximises the *F* function (B.Shen and O.Stephansson 1994). The concept of maximum strain energy density for crack evolution in the *F*-criterion is consistent with the experimental result (Chen, Han et al. 2021) and reveals the competition between tensile and shear fracture (Shen, Liu et al. 2019).

In the phase field framework, , Zhang et al. (Zhang, Sloan et al. 2017) and Bryant and Sun (Bryant and Sun 2018) first proposed a similar formulation of damage driving force for mixed-mode crack simulation based on the *F*-criterion, which was then followed by many other studies (Bryant and Sun 2018, Wang, Feng et al. 2020, Fan, Jin et al. 2021, Fei and Choo 2021, Yu, Hao et al. 2022) to identify the crack orientation. The crack evolution driving force H is decomposed into two components: mode I fracture driving force H_I and mode II fracture driving force H_{II}. The *F*-criterion function is defined as the sum of mode I and II crack driving force energies normalised by their corresponding fracture energy release rates G_t and G_c, denoted by

$$F(\alpha,\beta) = \frac{H_{\mathrm{I}}(\alpha,\beta)}{G_t} + \frac{H_{\mathrm{II}}(\alpha,\beta)}{G_c} \tag{3.39}$$

where the $H_{\mathrm{I}}(\alpha,\beta)$ and $H_{\mathrm{II}}(\alpha,\beta)$ are the crack driving forces for tensile and shear fracture, expressed as follows:

$$H_{\mathrm{I}} = \frac{1}{2}\overline{\boldsymbol{\sigma}}_{\mathrm{I}}^{+} : \boldsymbol{\varepsilon}^{e} \tag{3.40}$$

$$H_{\mathrm{II}} = \frac{1}{2}\overline{\boldsymbol{\sigma}}_{\mathrm{II}}^{+} : \boldsymbol{\varepsilon}^{e} \tag{3.41}$$

According to Eqs.(3.6) and (3.7), both $\overline{\boldsymbol{\sigma}}_{\mathrm{I}}^{+}$ and $\overline{\boldsymbol{\sigma}}_{\mathrm{II}}^{+}$ only depend on the crack orientation for a specific undamaged stress state, which means the *F* value in Eq.(3.39) is a function of the crack direction $\boldsymbol{r}$ only. The potential crack direction then could be determined by the solutions of α and β that maximize the *F* value.

In the principal stress space, the undegraded stress tensor $\overline{\boldsymbol{\sigma}}$ and elastic strain tensor $\boldsymbol{\varepsilon}^{\mathrm{e}}$ could be denoted by Eq.(3.42) and Eq.(3.43), respectively.

$$\overline{\boldsymbol{\sigma}} = \begin{bmatrix} \sigma_1 & 0 & 0 \\ 0 & \sigma_2 & 0 \\ 0 & 0 & \sigma_3 \end{bmatrix} \tag{3.42}$$

$$\boldsymbol{\varepsilon}^{\mathrm{e}} = \frac{1}{E} \cdot \begin{bmatrix} \sigma_1 - \nu(\sigma_2+\sigma_3) & 0 & 0 \\ 0 & \sigma_2 - \nu(\sigma_1+\sigma_3) & 0 \\ 0 & 0 & \sigma_3 - \nu(\sigma_1+\sigma_2) \end{bmatrix} \tag{3.43}$$

where the σ_1, σ_2 and σ_3 represent three principal stresses, E and ν are elastic modulus and Poisson's ratio. Substitution Eqs.(3.6), (3.7), (3.35)-(3.37), and (3.40)-(3.43) into Eq.(3.39) leads to the formula of *F* value in Eq.(3.44).

$$F(\alpha,\beta)=\widehat{H}(\sigma_{\mathrm{rr}})\cdot\frac{(1-2\nu)(1+\nu)}{32E(1-\nu)G_t}\cdot[\sigma_1+\sigma_2+2\sigma_3+(\sigma_1+\sigma_2-2\sigma_3)\cdot cos2\alpha+2(\sigma_1-\sigma_2)\,cos^2\alpha\cdot cos2\beta]^2+\frac{(1+\upsilon)cos^2\alpha}{4EG_c}\cdot([\sigma_1+\sigma_2-2\sigma_3+(\sigma_1-\sigma_2)cos2\beta]^2sin^2\alpha+(\sigma_1-\sigma_2)^2sin^22\beta) \quad (3.44)$$

where the $\widehat{H}(x)$ denotes Heaviside function and can be calculated by Eq.(3.45).

$$\widehat{H}(x)=\begin{cases}0; & x<0\\ 1; & others\end{cases} \quad (3.45)$$

According to the sign of σ_{rr}, there exists two cases to maximise the value of F function. Next, we will discuss them below:

1. when $\sigma_{rr}=\ \sigma_1cos^2\alpha\ cos^2\beta+\sigma_2cos^2\alpha\ sin^2\beta+\sigma_3sin^2\alpha<0$

Eq. (44) then would be recast to

$$F(\alpha,\beta)=\frac{(1+\upsilon)cos^2\alpha}{4EG_c}([\sigma_1+\sigma_2-2\sigma_3+(\sigma_1-\sigma_2)cos2\beta]^2sin^2\alpha+(\sigma_1-\sigma_2)^2sin^22\beta) \quad (3.46)$$

Take partial derivatives of $F(\alpha,\beta)$ with respect to α and β, respectively, then we can obtain all the extreme points, which are listed in Table 3.1. It is clearly observed that when crack direction r $=(\frac{\sqrt{2}}{2},0,\frac{\sqrt{2}}{2})$, the F would have its maximum value $\frac{(\sigma_1-\sigma_3)^2(1+\upsilon)}{4EG_c}$ in this case.

Table 3.1 Extreme points for F function when $\sigma_{rr}<0$.

No	α	β	crack direction	F value	$\sigma_{rr}<0$
1	$\frac{\pi}{2}$	$\forall$	$\boldsymbol{r}=(0,0,1)$	0	σ_3
2	0	0	$\boldsymbol{r}=(1,0,0)$	0	σ_2
3	0	$\frac{\pi}{2}$	$\boldsymbol{r}=(0,1,0)$	0	σ_1
4	0	$\pm\frac{\pi}{4}$	$\boldsymbol{r}=(\frac{\sqrt{2}}{2},\frac{\sqrt{2}}{2},0)$	$\frac{(\sigma_1-\sigma_2)^2(1+\upsilon)}{4EG_c}$	$\frac{\sigma_1+\sigma_2}{2}$
5	$\pm\frac{\pi}{4}$	0	$\boldsymbol{r}=(\frac{\sqrt{2}}{2},0,\frac{\sqrt{2}}{2})$	$\frac{(\sigma_1-\sigma_3)^2(1+\upsilon)}{4EG_c}$	$\frac{\sigma_1+\sigma_3}{2}$
6	$\pm\frac{\pi}{4}$	$\frac{\pi}{2}$	$\boldsymbol{r}=(0,\frac{\sqrt{2}}{2},\frac{\sqrt{2}}{2})$	$\frac{(\sigma_2-\sigma_3)^2(1+\upsilon)}{4EG_c}$	$\frac{\sigma_2+\sigma_3}{2}$

2. when $\sigma_{rr}=\ \sigma_1cos^2\alpha\ cos^2\beta+\sigma_2cos^2\alpha\ sin^2\beta+\sigma_3sin^2\alpha\geq0$

In this case, $\widehat{H}(\sigma_{\mathrm{rr}})$ is equal to 1, and then Eq.(3.44) would be recast to,

$$F(\alpha,\beta)=\frac{(1-2\nu)(1+\nu)}{32E(1-\nu)G_t}[\sigma_1+\sigma_2+2\sigma_3+(\sigma_1+\sigma_2-2\sigma_3)\cdot cos2\alpha+2(\sigma_1-\sigma_2)\,cos^2\alpha\cdot cos2\beta]^2+\frac{(1+\upsilon)cos^2\alpha}{4EG_c}\{[\sigma_1+\sigma_2-2\sigma_3+(\sigma_1-\sigma_2)cos2\beta]^2sin^2\alpha+(\sigma_1-\sigma_2)^2sin^22\beta\} \tag{3.47}$$

Take partial derivatives of $F(\alpha,\beta)$ with respect to α and β, respectively, all the extreme points could be obtained as listed in in Table 3.2. The first three solutions have the crack direction along a principal stress axis. The *F* value is proportional to the square of the corresponding principal stress, which must be positive to meet the requirement of positive σ_{rr}. Obviously, only the first principal stress direction could be the potential crack orientation direction in this group of solutions. The last three solutions account for the potential crack surface in σ_1-σ_2, σ_1-σ_3 and σ_2-σ_3 planes. It is noticed that the last three solutions of crack orientation direction ***r*** are consistent with the result for 2D crack propagation (Fei and Choo 2021), while they are just possible solutions in case of $\sigma_{rr}\geq 0$ for 3D problems.

3.2.5.3 Final crack orientation determination method

We now summarise the potential solutions as follows,

a) along the first principal stress direction

$r=(1,0,0)\quad\rightarrow\quad F=\frac{{\sigma_1}^2(1+\upsilon)(1-2\upsilon)}{2EG_t(1-\upsilon)}$, where $\sigma_{rr}=\sigma_1\geq 0$.

b) along the maximum shear stress surface

$r=(\frac{\sqrt{2}}{2},0,\frac{\sqrt{2}}{2})\quad\rightarrow\quad F=\frac{(\sigma_1-\sigma_3)^2(1+\upsilon)(1-2\upsilon)}{2EG_c(1-\upsilon)}$, where $\sigma_{rr}=\frac{\sigma_1+\sigma_3}{2}<0$.

c) potential crack direction in σ_1-σ_2 plane

$r=(cos\beta,sin\beta,0)\quad\rightarrow\quad F=\frac{(1+\upsilon)[(\sigma_1-\sigma_2)^2G_t(1-\upsilon)+2\sigma_1\sigma_2G_c(1-2\nu)]}{2EG_c[2G_t(1-\nu)-G_c(1-2\nu)]}$,

where $\cos^2\beta=\frac{G_t\cdot(\sigma_1-\sigma_2)\cdot(1-\nu)+G_c\cdot\sigma_2(1-2\nu)}{(\sigma_1-\sigma_2)\cdot[2G_t\cdot(1-\nu)-G_c\cdot(1-2\nu)]}\in[0,1]$, $and\ \sigma_{rr}=\frac{G_t(1-\upsilon)(\sigma_1+\sigma_2)}{2G_t(1-\nu)-G_c(1-2\nu)}\geq 0$.

d) potential crack direction in σ_1-σ_3 plane

$r=(cos\alpha,0,sin\alpha)\quad\rightarrow\quad F=\frac{(1+\upsilon)[(\sigma_1-\sigma_3)^2G_t(1-\upsilon)+2\sigma_1\sigma_3G_c(1-2\nu)]}{2EG_c[2G_t(1-\nu)-G_c(1-2\nu)]}$,

where $\cos^2\alpha = \frac{G_t\cdot(\sigma_1-\sigma_3)\cdot(1-\nu)+G_c\cdot\sigma_3(1-2\nu)}{(\sigma_1-\sigma_3)\cdot[2G_t\cdot(1-\nu)-G_c\cdot(1-2\nu)]} \in [0,1]$, $and\ \sigma_{rr} = \frac{G_t(1-\upsilon)(\sigma_1+\sigma_3)}{2G_t(1-\nu)-G_c(1-2\nu)} \geq 0$.

e) potential crack direction in σ_2-σ_3 plane

$r = (0, cos\alpha, sin\alpha) \quad \rightarrow \quad F = \frac{(1+\upsilon)\left[(\sigma_2-\sigma_3)^2G_t(1-\upsilon)+2\sigma_2\sigma_3G_c(1-2\nu)\right]}{2EG_c[2G_t(1-\nu)-G_c(1-2\nu)]}$,

where $\cos^2\alpha = \frac{G_t\cdot(\sigma_2-\sigma_3)\cdot(1-\nu)+G_c\cdot\sigma_3(1-2\nu)}{(\sigma_2-\sigma_3)\cdot[2G_t\cdot(1-\nu)-G_c\cdot(1-2\nu)]} \in [0,1]$, $and\ \sigma_{rr} = \frac{G_t(1-\upsilon)(\sigma_2+\sigma_3)}{2G_t(1-\nu)-G_c(1-2\nu)} \geq 0$.

After comparing the F values at all the five extreme points, we could obtain the maximum value $F^t(\overline{\boldsymbol{\sigma}}, t_n)$ in the current step time t_n, and the corresponding direction is set as the crack orientation $\boldsymbol{r}$ at t_n.

Table 3.2 extreme point for F function when $\sigma_{rr} \geq 0$

No.	α	β	$\boldsymbol{r}$	F	$\sigma_{rr} \geq 0$
1	$\frac{\pi}{2}$	$\forall$	$(0,0,1)$	$\frac{{\sigma_3}^2(1+\upsilon)(1-2\upsilon)}{2EG_t(1-\upsilon)}$	σ_3
2	0	0	$(1,0,0)$	$\frac{{\sigma_1}^2(1+\upsilon)(1-2\upsilon)}{2EG_t(1-\upsilon)}$	σ_1
3	0	$\frac{\pi}{2}$	$(0,1,0)$	$\frac{{\sigma_2}^2(1+\upsilon)(1-2\upsilon)}{2EG_t(1-\upsilon)}$	σ_2
4	0	$\pm acrcos\sqrt{s_1}$	$(cos\beta, sin\beta, 0)$	$\frac{(1+\upsilon)[(\sigma_1-\sigma_2)^2G_t(1-\upsilon)+2\sigma_1\sigma_2G_c(1-2\nu)]}{2EG_c[2G_t(1-\nu)-G_c(1-2\nu)]}$	$\frac{G_t(1-\upsilon)(\sigma_1+\sigma_2)}{2G_t(1-\nu)-G_c(1-2\nu)}$
5	$\pm acrcos\sqrt{s_2}$	0	$(cos\alpha, 0, sin\alpha)$	$\frac{(1+\upsilon)[(\sigma_1-\sigma_3)^2G_t(1-\upsilon)+2\sigma_1\sigma_3G_c(1-2\nu)]}{2EG_c[2G_t(1-\nu)-G_c(1-2\nu)]}$	$\frac{G_t(1-\upsilon)(\sigma_1+\sigma_3)}{2G_t(1-\nu)-G_c(1-2\nu)}$
6	$\pm acrcos\sqrt{s_3}$	$\frac{\pi}{2}$	$(0, cos\alpha, sin\alpha)$	$\frac{(1+\upsilon)[(\sigma_2-\sigma_3)^2G_t(1-\upsilon)+2\sigma_2\sigma_3G_c(1-2\nu)]}{2EG_c[2G_t(1-\nu)-G_c(1-2\nu)]}$	$\frac{G_t(1-\upsilon)(\sigma_2+\sigma_3)}{2G_t(1-\nu)-G_c(1-2\nu)}$

Note: the values $s_1 = \frac{G_t\cdot(\sigma_1-\sigma_2)\cdot(1-\nu)+G_c\cdot\sigma_2(1-2\nu)}{(\sigma_1-\sigma_2)\cdot[2G_t\cdot(1-\nu)-G_c\cdot(1-2\nu)]}$, $s_2 = \frac{G_t\cdot(\sigma_1-\sigma_3)\cdot(1-\nu)+G_c\cdot\sigma_3(1-2\nu)}{(\sigma_1-\sigma_3)\cdot[2G_t\cdot(1-\nu)-G_c\cdot(1-2\nu)]}$ and $s_3 = \frac{G_t\cdot(\sigma_2-\sigma_3)\cdot(1-\nu)+G_c\cdot\sigma_3(1-2\nu)}{(\sigma_2-\sigma_3)\cdot[2G_t\cdot(1-\nu)-G_c\cdot(1-2\nu)]}$ all should lie between 0 and 1;

3.2.6 Crack irreversibility and crack initiation threshold

To avoid crack initiation immediately after a very small loading, a critical value of the accumulated plastic strain $\bar{\varepsilon}_{cr}^{p}$ to initiate a damage is introduced here (Li, Fang et al. 2022). Both tensile and shear fractures would not happen until the accumulated plastic strain $\bar{\varepsilon}^{p}$ reaches that critical threshold $\bar{\varepsilon}_{cr}^{p}$. H_{I}^{ini} and H_{II}^{ini} are then introduced to indicate the energy thresholds for tensile and shear crack initiation. Their values are equal to the tensile and shear strain energy, respectively, when $\bar{\varepsilon}^{p}$ reaches its threshold $\bar{\varepsilon}_{cr}^{p}$. With H_{I}^{ini} and H_{II}^{ini} at hand, the formulation of state energy at time t and position X within the solid that controls the evolution of tensile and shear fracture respectively can be expressed as follows:

$$state^{t}(X,t) = < \frac{1}{2}\bar{\boldsymbol{\sigma}}_{\mathrm{I}}^{+} : \boldsymbol{\varepsilon}^{e} - H_{\mathrm{I}}^{ini} >_{+} \tag{3.48}$$

$$state^{c}(X,t) = < \frac{1}{2}\bar{\boldsymbol{\sigma}}_{\mathrm{II}}^{+} : \boldsymbol{\varepsilon}^{e} - H_{\mathrm{II}}^{ini} >_{+} \tag{3.49}$$

Then the history variables of driving forces for the tensile and shear crack propagations are introduced as follows to avoid crack healing during the unloading process,

$$H_t = \max_{\tau\in[0,t_n]} state^{t}(X,\tau) \tag{3.50}$$

$$H_c = \max_{\tau\in[0,t_n]} state^{c}(X,\tau) \tag{3.51}$$

similarly, the thresholds of tensile/shear accumulated plastic strain for energy release rate degradation are defined as ξ_t^{ini} and ξ_c^{ini}, which are equal to ξ_t and ξ_c, respectively when $\bar{\varepsilon}^{p}$ reaches its threshold $\bar{\varepsilon}_{cr}^{p}$. The effective tensile and shear accumulated strain ξ_t^{eff} and ξ_c^{eff} then could be obtained by Eq.(3.52) and Eq.(3.53).

$$\xi_t^{eff} = \xi_t - \xi_t^{ini} \tag{3.52}$$

$$\xi_c^{eff} = \xi_c - \xi_c^{ini} \tag{3.53}$$

With the driving forces for tensile and shear fracture in hand, the damage evolutions of Eq.(3.29) and Eq.(3.30) can be reformulated as follows:

$$2(1-d_t)H_t - G_{t0}\left[l\nabla f_t\left(\xi_t^{eff}\right)\cdot\nabla d_{\mathrm{t}} + f_t\left(\xi_t^{eff}\right)\cdot l\Delta d_{\mathrm{t}} - f_t\left(\xi_t^{eff}\right)\frac{d_t}{l}\right] = 0 \tag{3.54}$$

$$2(1-d_c)H_c - G_{c0}\left[l\nabla f_c\left(\xi_c^{eff}\right)\cdot\nabla d_{\mathrm{c}} + f_c\left(\xi_c^{eff}\right)\cdot l\Delta d_{\mathrm{c}} - f_c\left(\xi_c^{eff}\right)\frac{d_c}{l}\right] = 0 \tag{3.55}$$

3.3 Finite element implementation

In this section, the proposed double-phase field model for elasto-plastic solids is numerically implemented in commercial finite element code ABAQUS/Standard via user

subroutines UEL and UMAT. The solid is discretised with three layers of elements, which share the same nodes, while representing different DOFs, namely displacements and tensile and shear phase field variables respectively. A widely used staggered strategy (Miehe, Hofacker et al. 2010, Ambati, Gerasimov et al. 2015, Molnár and Gravouil 2017, Fang, Wu et al. 2019) has been adopted here for decoupling and solving problems of stress response and crack evolution. Within this framework, crack driving forces as well as the tensile/shear energy release rates are frozen at the last increment for solving tensile and shear phase fields in UEL, while the tensile and shear damages are fixed at the last increment when calculating stress response in UMAT. Only at the end of each increment would their values be updated for the next increment. More details can be referred to our previous open-source implementation (Fang, Wu et al. 2019). Meanwhile, a similar staggered scheme is applied to the crack direction $\boldsymbol{r}$ to increase the convergence.

3.3.1 Stress update

The stress update is accomplished via UMAT, which is called at each integral point of the displacement elements. According to Eq.(3.9), the calculation of the nominal stress starts from obtaining the undamaged (effective) stress, which is then decomposed in the crack-orientation-based coordinate system and degraded with the tensile and shear phase field damages. It is noted that the update of undamaged stress is consistent with the standard elasto-plastic algorithm. The von Mises yield function as well as associated flow rule is adopted here for simplicity, while the proposed model works for any elasto-plastic constitutive models.

In UMAT subroutine, the total strain increment $\Delta\boldsymbol{\varepsilon}$ is given at the start of each increment, which could be decomposed into the elastic strain and plastic strain according to additive decomposition of strain tensor as follows,

$$\Delta\boldsymbol{\varepsilon} = \Delta\boldsymbol{\varepsilon}^{\boldsymbol{e}} + \Delta\boldsymbol{\varepsilon}^{p} \tag{3.56}$$

Then our task is to solve the stress increment $\Delta\boldsymbol{\sigma}$ as well as the plastic strain increment $\Delta\boldsymbol{\varepsilon}^{p}$. In this section, to be concise, the subscript of variables denotes the increment number. The return-mapping algorithm (Dunne and Petrinic 2005, Neto, Peric et al. 2011) then could be applied for solving the elasto-plastic undamaged stress. Firstly, the strain increment $\Delta\boldsymbol{\varepsilon}$ is assumed to be all contributed by elastic strain. Then the trial elastic strain $\boldsymbol{\varepsilon}_{n+1}^{e\,trial}$ and trial accumulated plastic strain $\bar{\varepsilon}_{n+1}^{p\,trial}$ are given as

$$\boldsymbol{\varepsilon}_{n+1}^{e\,trial} = \boldsymbol{\varepsilon}_{n}^{e} + \Delta\boldsymbol{\varepsilon} \tag{3.57a}$$

$$\bar{\varepsilon}_{n+1}^{p\,trial} = \bar{\varepsilon}_{n}^{p} \tag{3.57b}$$

The corresponding trial deviatoric stress $\bar{\boldsymbol{s}}_{n+1}^{trial}$ and trial hydrostatic stress p_{n+1}^{trial} are obtained as

$$\bar{\boldsymbol{s}}_{n+1}^{trial} = 2G\ \boldsymbol{\varepsilon}_{d\,n+1}^{e\,trial} \tag{3.58a}$$

$$p_{n+1}^{trial} = K\ \varepsilon_{v\,n+1}^{e\,trial} \tag{3.58b}$$

where G and K are the shear modulus and bulk modulus. $\boldsymbol{\varepsilon}_{d\,n+1}^{e\,trial}$ and $\varepsilon_{v\,n+1}^{e\,trial}$ represent the trial elastic deviatoric strain and volume strain, respectively.

The trial stress state is then checked with the following yield criterion as follows,

$$\Phi\left(\bar{\boldsymbol{s}}_{n+1}^{trial}, \sigma_{y\,n+1}^{trial}\right) = \sqrt{\frac{3}{2}}\left\|\bar{\boldsymbol{s}}_{n+1}^{trial}\right\| - \bar{\sigma}_{y\,n+1}^{trial}(\bar{\varepsilon}_{n+1}^{p\,trial}) \tag{3.59}$$

where $\bar{\sigma}_y$ denotes the yield stress, and the superscript trial represents its value of the trial state. If $\Phi \leq 0$, then the stress state lies within the elastic domain and the trial stress state is the right solution. Otherwise, the yield surface evolves into a new state in this current increment and the return-mapping scheme needs to be applied to update the stress state. By referring to (Dunne and Petrinic 2005) one obtains

$$\boldsymbol{\varepsilon}_{n+1}^{e} = \boldsymbol{\varepsilon}_{n+1}^{e\,trial} - \Delta\gamma \cdot \sqrt{\frac{3}{2}}\frac{\bar{\boldsymbol{s}}_{n+1}^{trial}}{\|\bar{\boldsymbol{s}}_{n+1}^{trial}\|} \tag{3.60a}$$

$$\bar{\varepsilon}_{n+1}^{p} = \bar{\varepsilon}_{n}^{p} + \Delta\gamma \tag{3.60b}$$

$$\Phi\left(\bar{\boldsymbol{s}}_{n+1}, \bar{\sigma}_{y\,n+1}\right) = \sqrt{\frac{3}{2}}\|\bar{\boldsymbol{s}}_{n+1}\| - \bar{\sigma}_{y\,n+1}\left(\bar{\varepsilon}_{n+1}^{p}\right) = 0 \tag{3.60c}$$

where $\Delta\gamma$ is the plastic multiplier. Combining Eq.(3.58a) and Eq.(3.60a), one obtains

$$\bar{\boldsymbol{s}}_{n+1} = \left(1 - \frac{\Delta\gamma \cdot 3G}{q_{n+1}^{trial}}\right)\bar{\boldsymbol{s}}_{n+1}^{trial} \tag{3.61}$$

where $q_{n+1}^{trial} = \sqrt{\frac{3}{2}}\left\|\bar{\boldsymbol{s}}_{n+1}^{trial}\right\|$ is the von Mises equivalent stress for the trial stress tensor.

Next, the following equation in terms of $\Delta\gamma$ could be derived by substituting Eqs.(3.61) and (3.60b) into Eq. (3.60c).

$$\Phi(\Delta\gamma) = q_{n+1}^{trial} - \Delta\gamma \cdot 3G - \bar{\sigma}_y\left(\bar{\varepsilon}_{n}^{p} + \Delta\gamma\right) = 0 \tag{3.62}$$

Then, Eq.(3.62) can be solved by utilising the Newtown-Raphson iteration method. With $\Delta\gamma$ in hand, the elastic strain tensor, accumulated plastic strain and stress tensor could be obtained easily by substituting $\Delta\gamma$ into Eqs.(3.60a) and (3.61). In addition to the classical return mapping method adopted here, using smoothing functions instead of the Kuhn–Tucker complementarity conditions (Scheunemann, Nigro et al. 2020, Zhou, Lu et al.

2022) could be an alternative for stress update in the future when more complex elastoplastic models are involved.

The degradation of undamaged stress could then be conducted as **Algorithm** 1.

3.3.2 Phase field calculation

The phase field governing equation of Eqs.(3.54) and (3.55) could be rewritten in the weak form as follows,

$$\int_\Omega \left\{-2(1-d_t)\frac{H_t}{G_{t0}\cdot f(\xi_t)}\delta d_t + \frac{d_t\cdot\delta d_t}{l} + l\nabla d_t\cdot\nabla\delta d_t\right\}d\Omega = 0 \tag{3.63}$$

$$\int_\Omega \left\{-2(1-d_t)\frac{H_c}{G_{c0}\cdot f(\xi_c)}\delta d_t + \frac{d_c\cdot\delta d_t}{l} + l\nabla d_c\cdot\nabla\delta d_c\right\}d\Omega = 0 \tag{3.64}$$

The tensile and shear phase fields are discretised as follows,

$$d_t = \sum_{i=1}^{N_{node}} N^i\cdot d_t^i, \quad d_c = \sum_{i=1}^{N_{node}} N^i\cdot d_c^i \tag{3.65}$$

where $N^i(\boldsymbol{x})$ stands for the shape function for the *i*th node in terms of the local element coordinate $\boldsymbol{x}$, and d_t^i and d_c^i is the tensile and shear phase field value at the *i*th node.

Then, the variation of them could be written as,

$$\delta d_t = \sum_{i=1}^{N_{node}} N^i\cdot\delta d_t^i, \quad \delta d_c = \sum_{i=1}^{N_{node}} N^i\cdot\delta d_c^i \tag{3.66}$$

Their corresponding derivatives of phase field variation can be written as,

$$\delta\nabla d_t = \sum_{i=1}^{N_{node}} \boldsymbol{B}^i\cdot\delta d_t^i, \quad \delta\nabla d_c = \sum_{i=1}^{N_{node}} \boldsymbol{B}^i\cdot\delta d_c^i \tag{3.67}$$

where $\boldsymbol{B}^i = \nabla N^i(\boldsymbol{x})$ is the derivation of shape function $N^i(\boldsymbol{x})$.

The residual vectors for tensile and shear phase fields as well as their corresponding tangents then read as,

$$r_{dt}^i = \int_\Omega \left\{\left[-2(1-d_t)H_t + f(\xi_t)\frac{G_{t0}\cdot d_t}{l}\right]N^i + f(\xi_t)G_{t0}l(\boldsymbol{B}^i)^T\nabla d_t\right\}dV \tag{3.68}$$

$$r_{dc}^i = \int_\Omega \left\{\left[-2(1-d_c)H_c + f(\xi_c)\frac{G_{t0}\cdot d_c}{l_c}\right]N^i + f(\xi_c)G_{t0}l(\boldsymbol{B}^i)^T\nabla d_c\right\}dV \tag{3.69}$$

$$K_{ij}^{dt} = \frac{\partial r_{dt}^i}{\partial d_t^j} = \int_\Omega \left\{\left[2H_t + f(\xi_t)\frac{G_{t0}}{l}\right](N^i)^T N^j + f(\xi_t)G_{t0}l(\boldsymbol{B}^i)^T\boldsymbol{B}^j\right\}dV \tag{3.70}$$

$$K_{ij}^{dc} = \frac{\partial r_{dc}^i}{\partial d_c^j} = \int_\Omega \left\{\left[2H_c + f(\xi_c)\frac{G_{c0}}{l}\right](N^i)^T N^j + f(\xi_c)G_{c0}l(\boldsymbol{B}^i)^T\boldsymbol{B}^j\right\}dV \tag{3.71}$$

Algorithm 1: UMAT stress update at integration point

Input: undamaged stress $\overline{\boldsymbol{\sigma}}_{(n)}$; crack direction $\boldsymbol{r}_{(n)}$; strain increment $\Delta\boldsymbol{\varepsilon}_{(n+1)}$; accumulated plastic strain $\bar{\varepsilon}^{p}{}_{(n)}$; crack initial plastic strain $\bar{\varepsilon}^{p}_{cr}$; tensile and shear phase field d_t and d_c; crack driving forces $H_{t_{(n)}}$ and $H_{c_{(n)}}$.

Output: crack driving forces $H_{t_{(n+1)}}$ and $H_{c_{(n+1)}}$; effective accumulated plastic strains ξ_t^{ef} and ξ_c^{ef}; stress response $\boldsymbol{\sigma}_{(n+1)}$; degraded stiffness matrix $\boldsymbol{C}$; crack direction $\boldsymbol{r}_{(n+1)}$.

1. update $\overline{\boldsymbol{\sigma}}_{(n+1)}$, $\bar{\varepsilon}^{p}{}_{(n+1)}$, $\boldsymbol{\varepsilon}^{e}$ and plastic strain increment $\Delta\boldsymbol{\varepsilon}^{p}_{(n+1)}$ according to Eqs. (3.59) and (3.60a).

2. decompose $\overline{\boldsymbol{\sigma}}_{(n+1)}$ into $\overline{\boldsymbol{\sigma}}^{+}_{\mathrm{I}\ (n+1)}$, $\overline{\boldsymbol{\sigma}}^{+}_{\mathrm{II}(n+1)}$ and $\boldsymbol{\sigma}^{-}{}_{(n+1)}$ according to crack direction $\boldsymbol{r}_{(n)}$ with Eqs. (3.6)-(3.8).

3. update the stress $\boldsymbol{\sigma} = (1-d_t)^2 \cdot \overline{\boldsymbol{\sigma}}^{+}_{\mathrm{I}\ (n+1)} + (1-d_c)^2 \cdot \overline{\boldsymbol{\sigma}}^{+}_{\mathrm{II}(n+1)} + \boldsymbol{\sigma}^{-}{}_{(n+1)}$

4. Calculate the transform matrix

$\widetilde{\boldsymbol{D}}_{trans} = (1-d_t)^2 \cdot \hat{H}(\sigma_{\mathrm{rr}}) \cdot \left[\boldsymbol{M}^{rr} + \frac{\lambda}{\lambda+2G} \cdot (\boldsymbol{M}^{ss} + \boldsymbol{M}^{tt})\right] \otimes \boldsymbol{M}^{rr} + (1-d_c)^2 \cdot (\boldsymbol{M}^{rs} \otimes \boldsymbol{M}^{rs} + \boldsymbol{M}^{sr} \otimes \boldsymbol{M}^{sr} + \boldsymbol{M}^{rt} \otimes \boldsymbol{M}^{rt} + \boldsymbol{M}^{tr} \otimes \boldsymbol{M}^{tr}) + \hat{H}(-\sigma_{\mathrm{rr}}) \cdot \boldsymbol{M}^{rr} \otimes \boldsymbol{M}^{rr} - \hat{H}(\sigma_{\mathrm{rr}}) \cdot \frac{\lambda}{\lambda+2G} \cdot (\boldsymbol{M}^{ss} + \boldsymbol{M}^{tt}) \otimes \boldsymbol{M}^{rr} + (\boldsymbol{M}^{st} \otimes \boldsymbol{M}^{st} + \boldsymbol{M}^{ts} \otimes \boldsymbol{M}^{ts} + \boldsymbol{M}^{tt} \otimes \boldsymbol{M}^{tt} + \boldsymbol{M}^{ss} \otimes \boldsymbol{M}^{ss})$.

5. update $\boldsymbol{C} = \widetilde{\boldsymbol{D}}_{trans} : \overline{\boldsymbol{C}}^{\boldsymbol{ep}}$

6. decompose $\Delta\boldsymbol{\varepsilon}^{p}_{(n+1)}$ into $\Delta\boldsymbol{\varepsilon}^{p}_{I+}$ and $\Delta\boldsymbol{\varepsilon}^{p}_{II+}$ with Eqs. (3.10) and (3.11), and obtain the accumulated tensile and shear plastic strain $\xi_{t_{(n+1)}}$ and $\xi_{c_{(n+1)}}$ with Eqs. (3.12) and (3.13).

7. Calculate the thresholds of tensile/shear energy and plastic strain for the corresponding crack initiation.

if $\bar{\varepsilon}^{p}{}_{(n+1)} \leq \bar{\varepsilon}^{p}_{cr}$, **then**

$H^{ini}_{\mathrm{I}\ (n+1)} = \frac{1}{2}\overline{\boldsymbol{\sigma}}^{+}_{\mathrm{I}} : \boldsymbol{\varepsilon}^{e}$, $H^{ini}_{\mathrm{II}\ (n+1)} = \frac{1}{2}\overline{\boldsymbol{\sigma}}^{+}_{\mathrm{II}} : \boldsymbol{\varepsilon}^{e}$, $\boldsymbol{\xi_t^{ini}}_{\mathbf{(n+1)}} = \boldsymbol{\xi}_{\boldsymbol{t}_{(\boldsymbol{n+1})}}$, $\boldsymbol{\xi_c^{ini}}_{\mathbf{(n+1)}} = \boldsymbol{\xi}_{\boldsymbol{c}_{(\boldsymbol{n+1})}}$

else

$H^{ini}_{\mathrm{I}\ (n+1)} = H^{ini}_{\mathrm{I}\ (n)}$, $H^{ini}_{\mathrm{II}\ (n+1)} = H^{ini}_{\mathrm{II}\ (n)}$, $\xi_t^{ini}{}_{(\mathrm{n}+1)} = \xi_t^{ini}{}_{(\mathrm{n})}$, $\xi_c^{ini}{}_{(\mathrm{n}+1)} = \xi_c^{ini}{}_{(\mathrm{n})}$

end if

8. Update the state energy $state^{t}(X,t)$ and $state^{c}(X,t)$ with Eqs.(3.48) and (3.49).

9. Update the crack driving force for tensile and shear crack propagation,

$$H_{t_{(n+1)}} = max\left\{state^{t}(X,t), H_{t_{(n)}}\right\}$$

$$H_{c_{(n+1)}} = max\left\{state^{c}(X,t), H_{c_{(n)}}\right\}$$

10. obtain effective tensile/shear accumulated plastic strain by

$\xi_t^{ef}{}_{(\mathrm{n}+1)} = \xi_{t_{(n+1)}} - \xi_t^{ini}{}_{(\mathrm{n}+1)}$, $\xi_c^{ef}{}_{(\mathrm{n}+1)} = \xi_{c_{(n+1)}} - \xi_c^{ini}{}_{(\mathrm{n}+1)}$

11. update the crack direction $\boldsymbol{r}_{(n+1)}$ according to undamaged stress state $\overline{\boldsymbol{\sigma}}_{(n+1)}$using steps illustrated in Final crack orientation determination method.

3.4 Numerical examples

This section presents a series of numerical examples to validate the proposed double phase field model. Firstly, the one element under tension and shear loading is modelled and compared with the analytical solution to validate the numerical implementation proposed in Section 3. Next, the specimens of single-edge notch under tension and shear loading are conducted to explore the effect of several key model parameters on the mechanical response and crack evolution path. Then, the capacity of this model for capturing different crack modes is demonstrated by the simulation of a group of specimens under uniaxial tension, simple shear and tension shear loading, which is then compared with the experimental result. Finally, the third Sandia challenge is simulated to validate the 3D crack propagation modelling of this proposed model. It is noted that tensile and shear crack energy release rate G_{t} and G_{c} are crucial parameters. For the first, second and third numerical examples, we set the values of G_{t} and G_{c} for parametric analysis. In terms of the fourth and fifth numerical examples, the tensile energy release rate G_{t} is set as 9.3 kN/m taken from the literature (Ambati, Gerasimov et al. 2015), while the shear crack energy release rate G_{c} is calibrated as 1.5 times G_{t} to best match numerical crack evolution path with the experimental observation.

3.4.1 One element tension and shear

The numerical example of one cubic solid element under tension and shear are conducted respectively to verify the finite element implementation of this proposed double-phase field model for different crack modes. The corresponding parameters are listed in Table 3.3, and the loading boundary is demonstrated in Figure 3.5. The homogeneous solutions are derived by ignoring the derivative term in Eqs.(3.54) and (3.55), then the tensile and shear phase fields could be simplified as,

$$d_t^{hom} = \frac{2H_t l_t}{2H_t l + G_{t0} \cdot f(\xi_t)} \tag{3.72}$$

$$d_c^{hom} = \frac{2H_c l_c}{2H_c l + G_{c0} \cdot f(\xi_c)} \tag{3.73}$$

The analytical and numerical results are compared in Figure 3.5. It has been demonstrated that the stress response and damage solution of numerical data agree well with analytical solutions for both tensile and shear loading. Also, the crack propagation parameter a_t and a_c which control the decreasing speed of tensile and shear energy release rates respectively, greatly impact damage evolution. As a_t or a_c increases, the value of G_t or G_c reduces faster under the same plasticity deformation, which leads to

faster crack evolution as well as stress degradation.

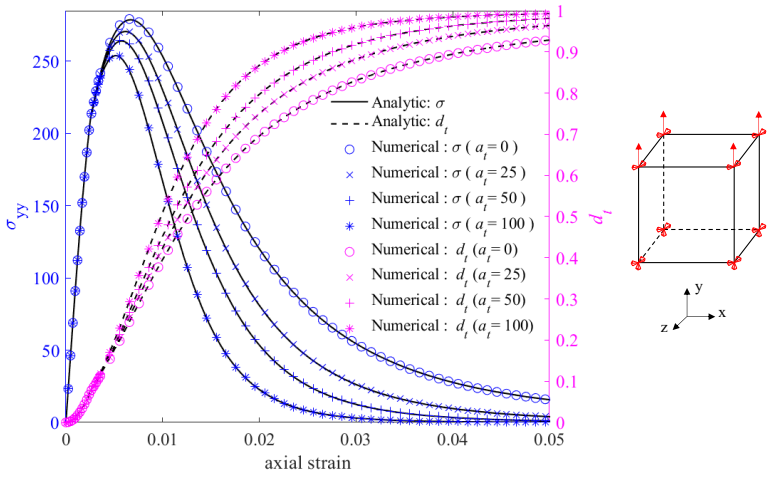

(a) tension

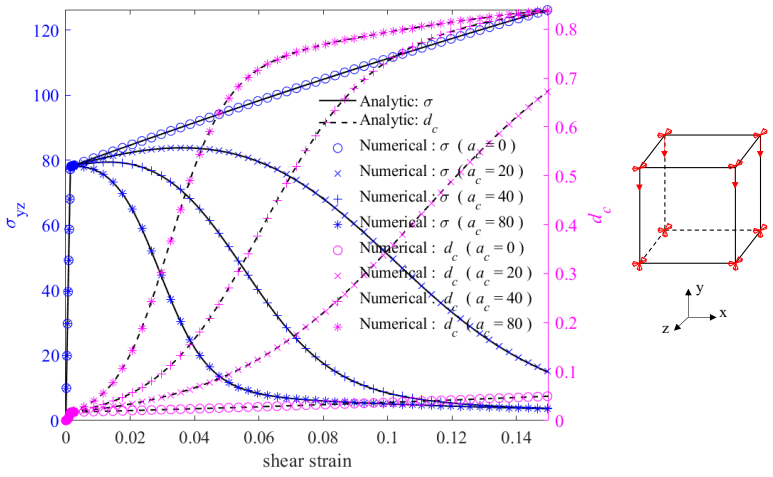

(b) shearing

Figure 3.5 Comparison of numerical result and analytical solution under uniaxial tension and simple shear loading

Table 3.3 parameters for one element numerical modelling

Type	Parameters	Value
elastic	E	72000 MPa
	ν	0.3
plastic	σ_{y0}	140 MPa
	h	600 MPa
Damage evolution	G_{t0}	7.6 kN/m
	G_{c0}	13. 5 kN/m
	a_t	0 / 25 / 50 / 100
	b_t	0.01
	a_c	0 / 20 / 40 / 80
	b_c	0.01

3.4.2 Single-edge tension

Single-edge notch tension loading has been widely studied to validate numerical techniques (Wu, Nguyen et al. 2020, Li, Shen et al. 2021, Yu, Hao et al. 2022). The geometry and boundary condition of the tensile loading condition is depicted in Figure 3.6(a). The bottom surface of the plate is fixed in all three directions, while the top surface is fixed in x and z directions and loaded in y direction. In this example, we apply our proposed phase field model to model the mode I crack propagation. We have set a group of specimens with different values of parameters a_t and b_t to explore their effects on mechanical response in this model, which describe the relationship between energy release rate and accumulated tensile plastic strain via Eq.(3.15). The elastic parameters are set as Young's modulus E= 145 GPa, and Poisson's ratio υ= 0.3. In terms of plasticity characteristics, this proposed phase field model is capable of incorporating any plastic models for different materials. Here we adapt the von Mises plasticity models with linear strain hardening. The initial yield stress σ_{y0} is set as 508.6 MPa, and the strain hardening modulus H is set as 2.38 GPa, which is calibrated from our experiment specimen (Li, Fang et al. 2022). The initial tensile and shear energy release rates G_{t0} and G_{c0} are set as 2.7 and 20.31 kN/m respectively.

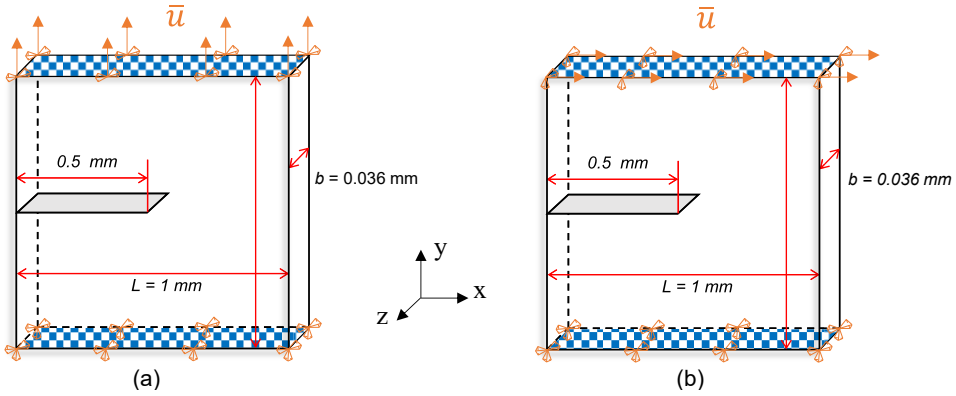

Figure 3.6 Geometry and boundary condition for single-edge notched plate (a) under tensile loading (b) under shear loading

The force-displacement curves for specimens with different fracture energy release rate degradation parameters a_t and b_t are plotted in Figure 3.7. At the beginning of loading, all specimens have experienced a short elastic stage where the loading forces show a sharp linear increase until the applied displacement reaches 0.005 mm. The stress then develops beyond yield stress and the plastic deformation initiates. It is noted that force-displacement curves for specimens with different a_t and b_t start to distinguish at this time, though they have a similar trend. Here we take one specimen (a_t=4, b_t=0.05)

for example to analyse the force-displacement curve. Due to strain hardening, the force continues to rise at a decreasing rate until reaching its peak point at the displacement of 0.06 mm. It is also observed from Figure 3.8 that the phase field damage for this specimen develops and localises at the notch. Subsequently, the force decreases quickly with the displacement, corresponding to the horizontal crack propagation from the notch to the right edge of this plate. When the displacement reaches 0.19 mm, this specimen is totally broken with a crack through the specimen, and the structure fully loses its load-carrying capacity.

The crack propagations for specimens with a fixed $b_t = 0.05$ and different values for a_t (a_t=4, 8, and 12) are demonstrated in Figure 3.8. The last column in Figure 3.8 shows the final crack paths in 3D view. Overall, fractures for all specimens initiate at the central notch point and then propagate along the horizontal surface to the right edge. Meanwhile, it can also be observed that specimens with a larger value of the parameter a_t shows a faster crack initiation and propagation, leading to a lower force under the same displacement, which is depicted in Figure 3.7. Once the plastic strain initiates, the increase of the undamaged stress as well as elastic strain is affected by strain hardening and becomes much slower compared with the elastic stage. Consequently, the effective strain energy that drives tensile damage evolution (see Eq.(3.29)) shows a similar trend, which limits the elastic contribution to crack propagation. On the other hand, dramatically degraded energy release rates due to the increased tensile accumulated plastic strain (see Eq.(3.15)) would then reduce the energy required to create a crack remarkably, which plays a more significant role in crack propagation compared with the elastic strain energy. For this reason, the specimen with a larger a_t which controls the decrease rate of energy release rate in Eq.(3.15) has a steeper decrease of fracture energy release rates and hence shows faster crack initiation and propagation in Figure 3.8 as well as lower loading force in Figure 3.7.

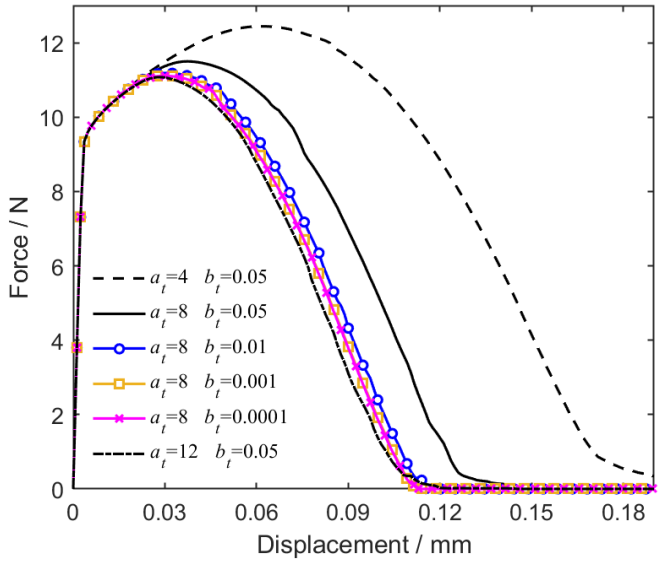

Figure 3.7 loading force versus displacement for Tension loading on Single-edge specimen with different model parameters a_t and b_t.

The parameter b_t in Eq. (15) is often set as a very small number to indicate the residual fracture energy release rate for the ultimate plastic strain (Steinke and Kaliske 2018). To explore the effect of parameter b_t on the mechanical response, a group of specimens with a fixed a_t (a_t=8) and different values of b_t (b_t=0.05, 0.01, 0.001, and 0.0001) are conducted, their load-displacement curves are presented in Figure 3.7. It is found that the specimen shows a lower strength (i.e., maximum force) as the parameter b_t decreases from 0.05 to 0.01. However, the impact of b_t on mechanical response could be neglected when b_t is smaller than 0.01.

The local crack surface normal direction around the crack tip area is demonstrated by white arrows in Figure 3.8, which represent the crack direction $\boldsymbol{r}$ at the position of the arrow tails. Since the specimen is under tensile loading, the direction $\boldsymbol{r}$ is expectedly along the vertical major principal stress direction, perpendicular to the horizontal crack path.

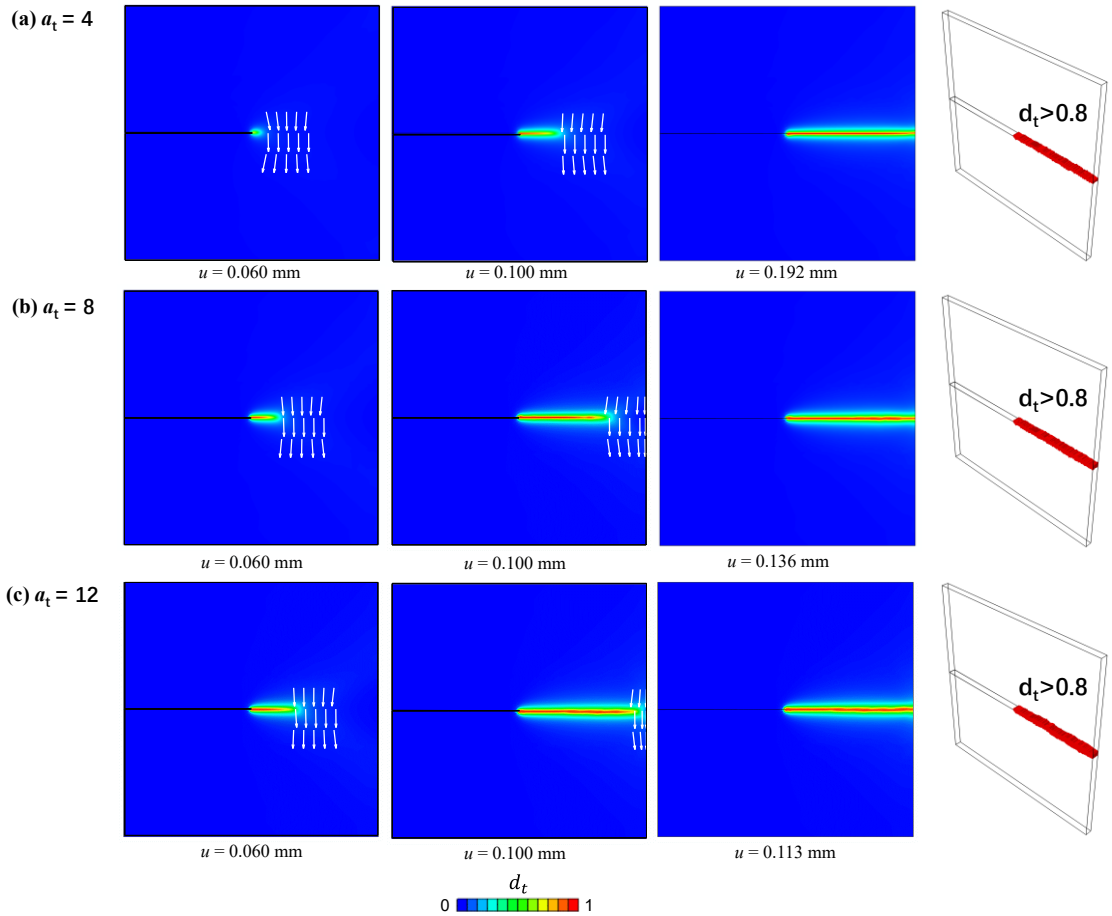

Figure 3.8 Tensile and shear phase field contour during the shear loading on the single-edge specimen.

3.4.3 Single-edge shear

For the single-edge notch shearing specimen, its geometry, and boundary and loading conditions are depicted in Figure 3.6(b). For most existing elastic/elasto-plastic phase field models where the tensile and shear fracture energy release rates are not distinguished (Molnár and Gravouil 2017, Wu and Nguyen 2018, Zhang and Luo 2021, Zhou, Hu et al. 2022), their crack propagation path is either from the centre to the bottom right corner or along the horizontal surface. Nevertheless, (Yu, Hao et al. 2022) the ratio between shear and tensile energy release rates G_c/G_t has been demonstrated to play a great role on the crack mode and crack path. Hence, we conduct a group of numerical tests under different values of G_c/G_t (G_c/G_t=1, 1.4, 2, 2.4, 3, 5 and 10) while fixing G_t at 2.7 kN/m, to explore its effect on the mechanical response.

Figure 3.9 demonstrates the tensile and shear phase field propagations of three specimens (G_c/G_t = 1, 2 and 5), which represent three different crack modes respectively: shear dominant mode, mixed mode and tension dominant mode. The last column in Figure

3.9 also depicts the final crack paths in 3D view. The shear dominant mode occurs in the specimen with $G_c/G_t \leq 1.4$. In this case, shear damage d_c initiates at central notch and then develops along the horizontal direction to the right edge of the plate, while the tensile damage d_t remains zero during loading process in the whole specimen except for minor tensile damage localised at the central notch.

In terms of the mixed mode, the specimen with G_c/G_t=2 shows a complex crack pattern. Both tensile damage d_t and shear damage d_c initiate at the central notch point, and then d_t propagates towards the bottom right corner while d_c evolves horizontally until displacement u reaches 0.14 mm. It is also noticed that the value of d_t has reached 1 along the tensile crack path during this process, which means that a fully broken tensile fracture surface has been formed. In addition, the shear damage d_c is less than 0.5 along the horizontal shear damage path, and the material there remains load bearing. Next, tensile damage d_t continues to develop along its initial inclined direction, while the shear damage zone formed during the beginning stage starts to move along the existing tensile crack path rather than keeps extending on the horizontal surface. This transition of shear damage evolution results from the constantly developing tensile fracture path.

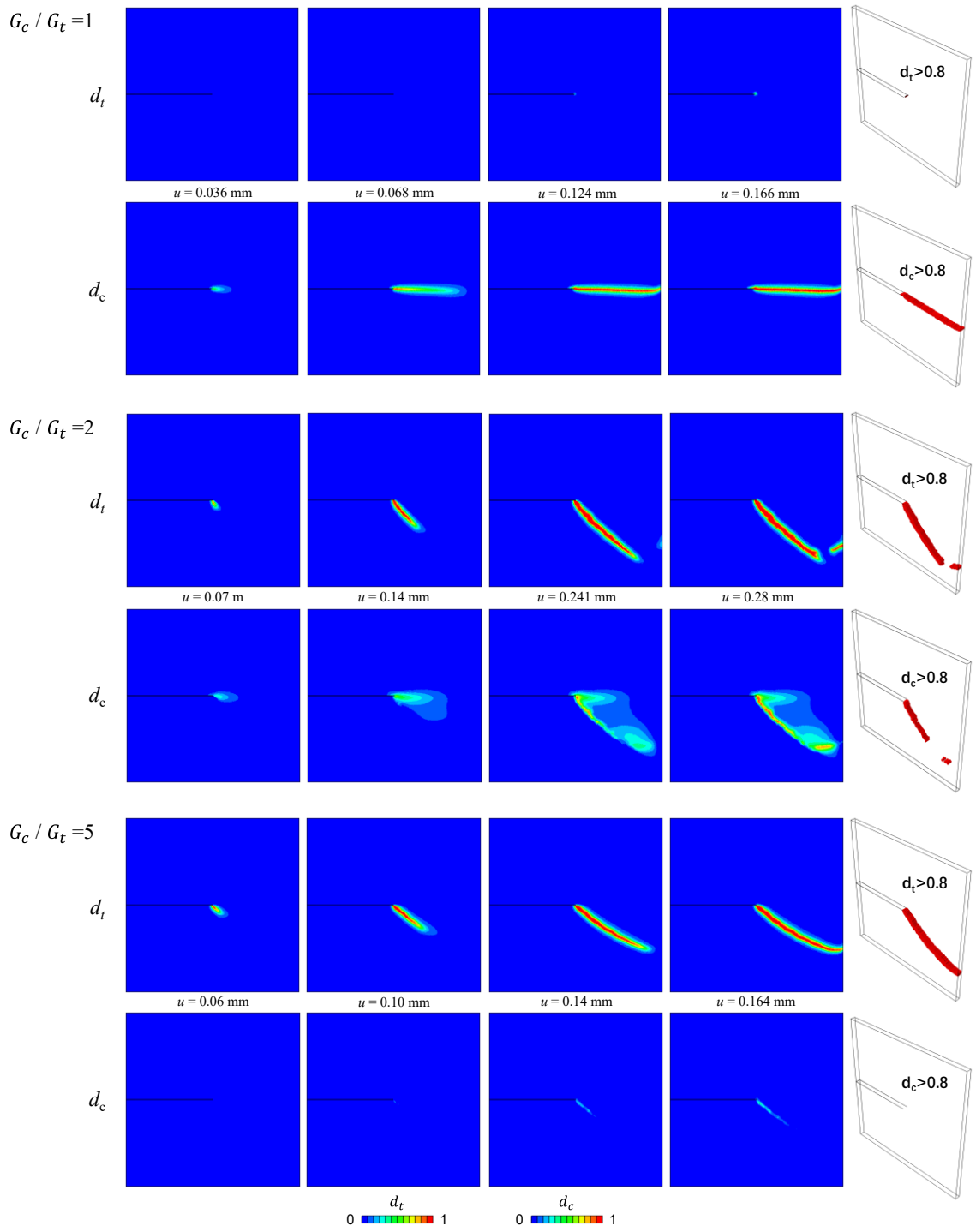

Figure 3.9 Tensile and shear phase field contour during the shear loading process on the single-edge specimen

As the fully broken tensile fracture surface develops, new crack tips form. Materials located at those crack tips provide tangential forces along the tensile crack path to sustain the external horizontal force, which leads to the shear damage zone moving along the tensile crack path. When the applied displacement reaches 0.24 mm, the tensile crack tip is close to the bottom right corner, and the existing tensile fracture path stops the evolution,

and new tensile damage initiates on the right edge of the plate. Meanwhile, the shear damage d_c starts to initiate a horizontal path which then develops and connects the new tensile crack zone.

When G_c/G_t is larger than 2.4, the specimens exhibit the tensile dominant crack mode. The tensile fracture initiates at the central notch and then develops to the bottom right. During the crack propagation towards the bottom right corner of the specimen, its inclination angle relative to the horizontal direction decreases, and the crack path ends in the horizontal direction when developing to the right edge of the plate. Figure 3.10 summarizes the relationship between the initial inclination angle and G_c/G_t. It is observed that the initial inclination angle has shown a significant reduction when G_c/G_t increases from 2 to 3, while the inclination angle remains at a stable value at around 38° once G_c/G_t goes beyond 3.

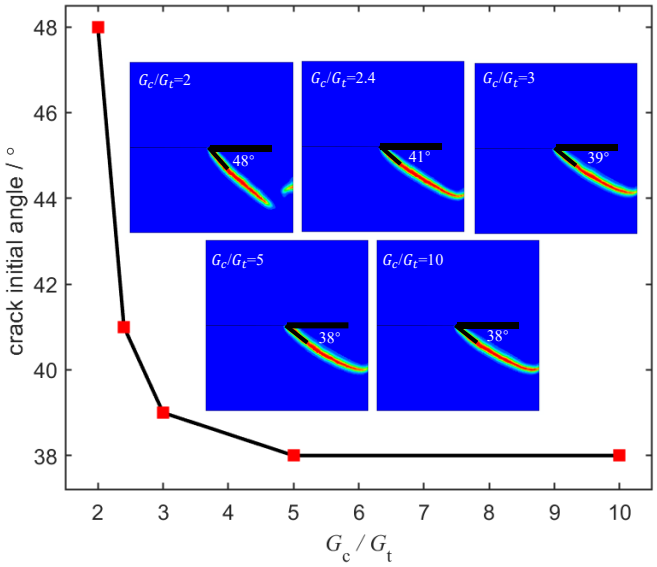

Figure 3.10 Crack initial direction for specimens of different G_c/G_t

Figure 3.11 plots force-displacement curves for all specimens with different G_c/G_t values. It is observed that the specimen shows obvious strengthening as G_c/G_t rises from 1 to 2, which results from a larger G_c leading to higher shear fracture resistance during shear crack propagation, though the mixed crack mode appears when G_c/G_t is equal to 2. Nevertheless, the specimen shows a lower load-carrying capacity when G_c/G_t increases from 2 to 2.4 when the tensile dominant crack appears. The reduction of load-carrying capacity is due to the change of crack mode. It is observed from Figure 3.9 that there develop both tensile and shear cracks in the mixed mode specimen ($G_c/G_t = 2$), which dissipates a larger fracture energy under the same applied displacement compared with

tensile dominant mode specimen ($G_c/G_t \geq 2.4$). Consequently, a larger external force for the mixed mode specimen is generated for the larger fracture energy for the applied displacement. When G_c/G_t goes beyond 2.4, tensile cracks dominate the specimen, which means G_t rather than G_c takes effect on the crack evolution. Noted that G_t is fixed in this study, all tensile dominant specimens exhibit a similar force-displacement response depicted in Figure 3.11.

The local crack directions $\boldsymbol{r}$ in the crack tip zone are plotted as white arrows on tensile and shear damage contour which represents the local crack surface normal direction at the location of arrow tails in Figure 3.12. It is observed that directions $\boldsymbol{r}$ around the crack tip zone are approximately perpendicular to the damage evolution path, which shows the consistence of local crack directions and macroscopic fracture surface. Meanwhile, it is also necessary to emphasise that the crack propagation is not only determined by the local crack direction, it also depends on the distribution of crack driving forces as well as the accumulated plastic strain according to Eq. (54) and Eq. (55).

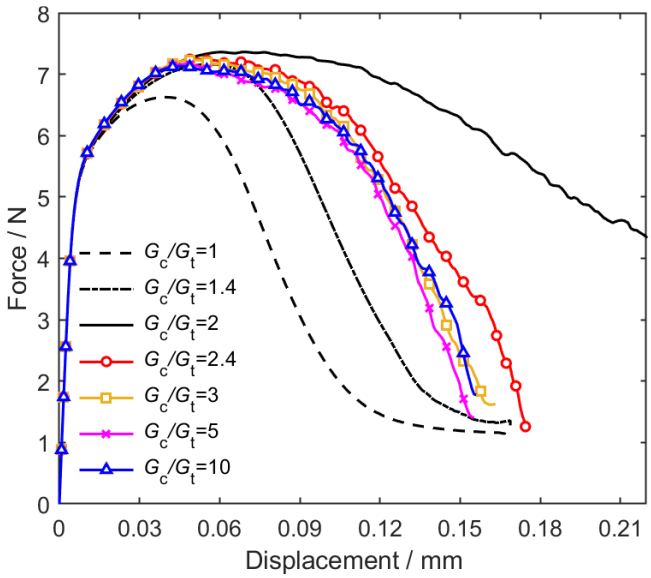

Figure 3.11 Loading displacement curve for the single-edge specimen of different ratios of G_c/G_t under shear loading

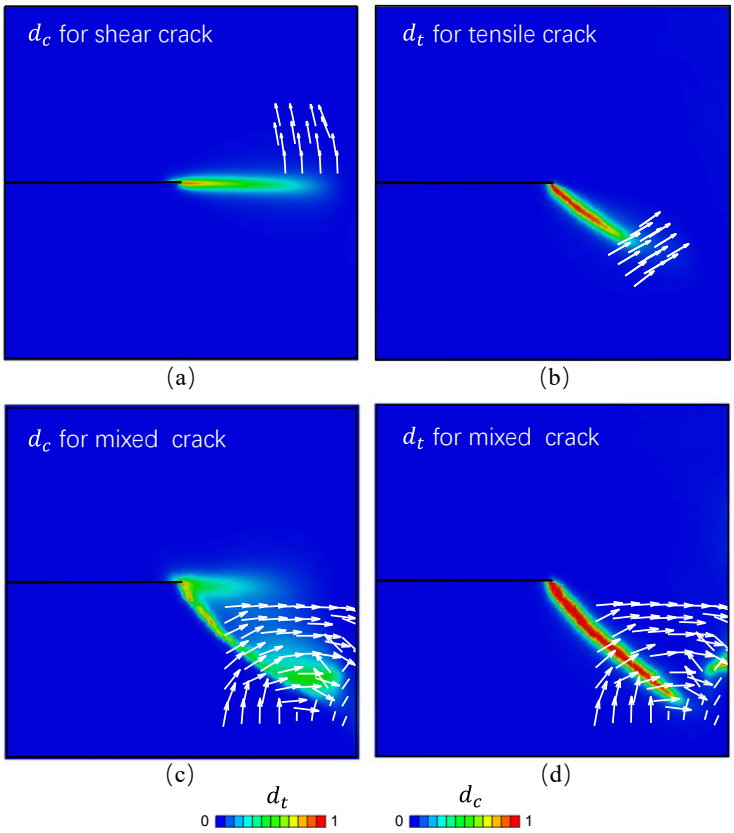

Figure 3.12 crack direction around the crack tip area on the damage contour: (a) d_c for shear crack dominant mode; (b) d_t for tensile crack dominant mode; (c) d_c for mixed crack mode; (d) d_t for mixed crack mode;

3.4.4 Uniaxial tension, simple shear and tension-shear specimens

To illustrate this proposed crack-direction-based ductile phase field model's capability to modelling crack propagation of different crack modes, specimens subject to uniaxial tension (UT), simple shear (SS), and tension-shear (TS) are studied. The geometry as well as elastic/plastic parameters in this study keeps consistent with that in (Bao and Wierzbicki 2004), as shown in Figure 15 (a). The fracture strain or crack initiation strain $\bar{\varepsilon}_{cr}^{p}$ is viewed as a stress state dependent material parameter, and it has distinct values for uniaxial tension, simple shear and tension-shear loading conditions (Li, Fang et al. 2022). Phenomenological ductile fracture criteria, such as the modified Mohr-Coulomb (MMC) model, could be used to calibrate the fracture strain surface in terms of stress triaxiality and Lode angle parameter (Li, Fang et al. 2022). Once the fracture strain surface has been calibrated via experimental data, the fracture strain for any stress state can be calculated. In this study, since we focus on double phase field modelling, fracture strain values are assigned for different specimens to match the global force-displacement response for simplicity. All material parameters for this group of numerical examples are

listed in Table 3.4.

Table 3.4 parameters for uniaxial tension, simple shear, and tension-shear modelling

Type	Parameters	Value
elastic	E	74633 MPa
	υ	0.3
plastic	σ_{y0}	300.4 MPa
	Strain hardening	(Bao and Wierzbicki 2004)
Damage evolution	G_{t0}	9.3 kN/m
	G_{c0}	13.95 kN/m
	a_t	6
	b_t	1e-4
	a_c	20
	b_c	1e-4
Damage initiation	$\bar{\varepsilon}_{cr}^{p}\ (UT)$	0.3
	$\bar{\varepsilon}_{cr}^{p}\ (SS)$	0.15
	$\bar{\varepsilon}_{cr}^{p}\ (TS)$	0.14

The loading force-displacement curves are compared with experimental data in Figure 3.13. It can be observed that the numerical results match experiment data well. For all three specimens, the forces have shown a linear increase with the displacement at the beginning stage, followed by a long strain hardening stage when plastic deformations appear, and the forces continue to increase with a decreasing rate. Next, cracks initiate when the applied displacement reaches 6 mm for UT specimen, 2.2 mm for SS specimen and 2.6 mm for TS specimen respectively. After crack initiation, the forces show rapid decreases until structures totally broken. The final shear and tensile damage contours are presented in Figure 3.14 accompanied with pictures of corresponding experimental crack paths. We can find that the tensile and shear damage dominate the fracture propagation for UT and SS specimen respectively, while both of them develop in TS specimen. Moreover, there exists an inclination angle between the fracture surface and horizontal direction for UT specimen under the combined effect of tensile and shear stress, which is consistent with the experimental crack path. In terms of TS specimen, damage is localised through the cross-section at the upper left notch, while the experimental crack path develops symmetrically at the lower right notch corner. Due to the symmetry of geometry as well as the loading condition, it has equal possibility to develop cracks at either of the two locations and a small material defect or perturbation in numerical simulation would affect the results.

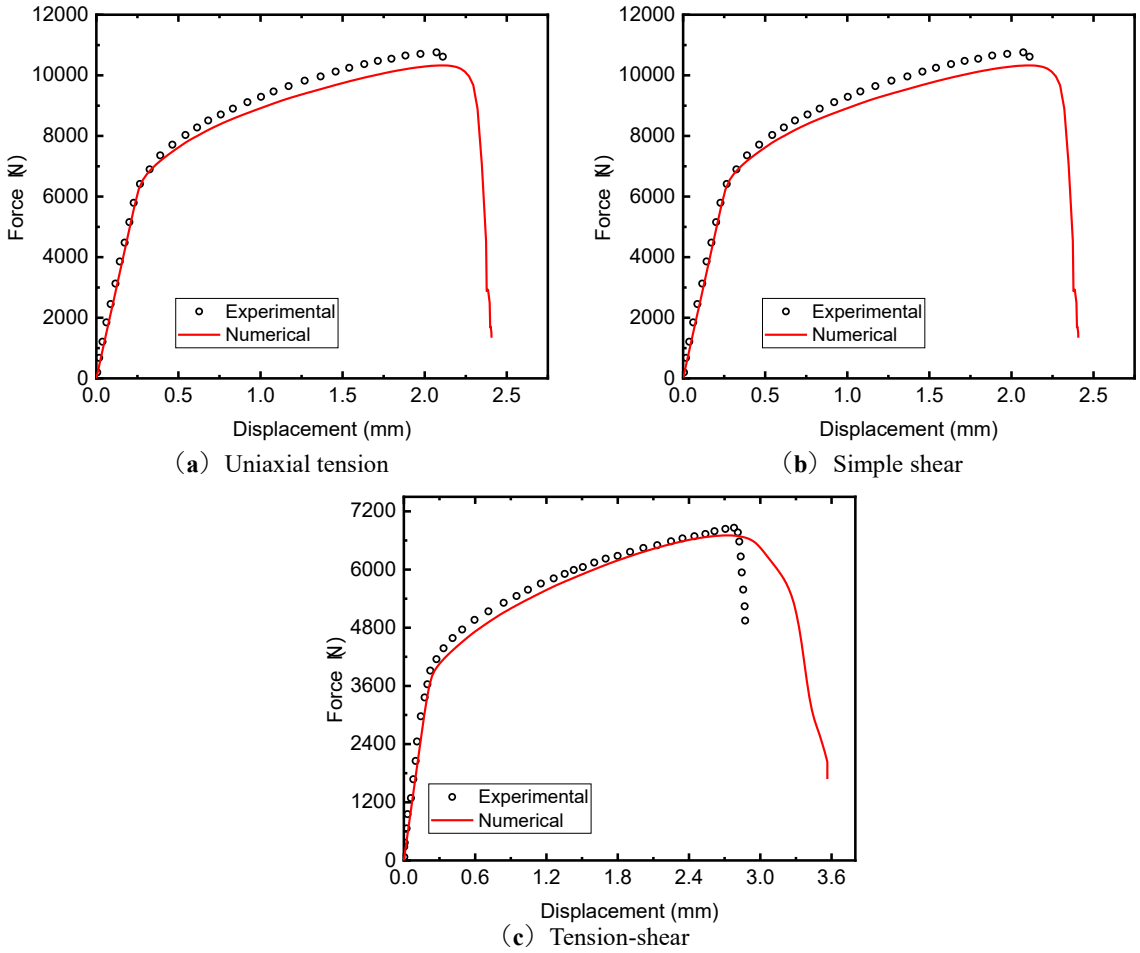

Figure 3.13 loading force versus displacement for UT, SS and TS specimen compared with experimental data

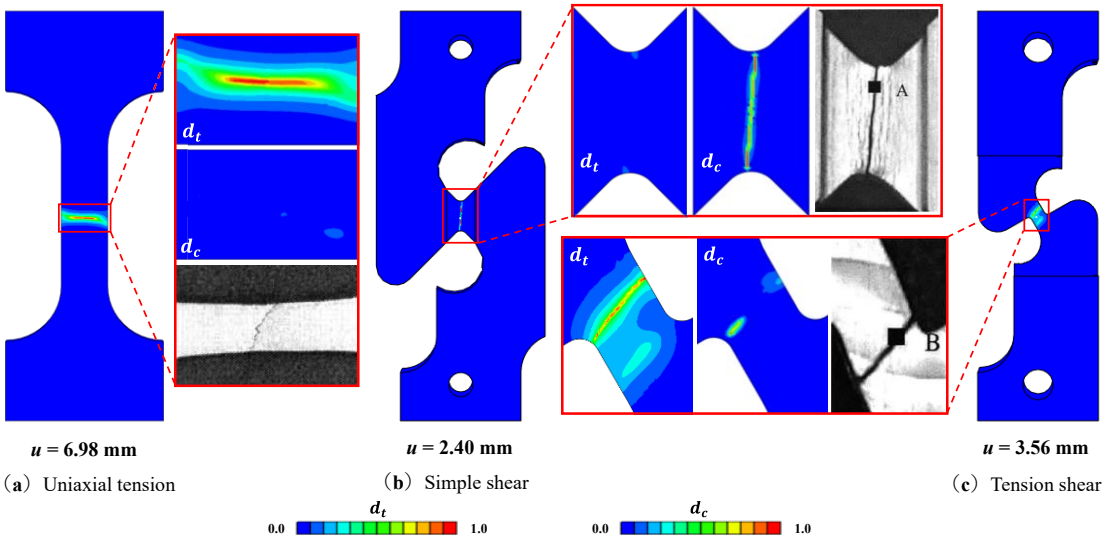

Figure 3.14 Tensile and shear phase field contours compared with experiment result from (Bao 2003)

3.4.5 The third Sandia challenge

Lastly, we conduct the crack modelling for the well-known third Sandia Fracture Challenge (SDF3) experiments on a complex 3D specimen launched by Sandia National Laboratories in 2019 (Behzadinasab and Foster 2019, Karlson, Alleman et al. 2019, Kramer, Ivanoff et al. 2019, Kramer, Jones et al. 2019, Spear, Czabaj et al. 2019, Tancogne-Dejean, Gorji et al. 2019, Behzadinasab and Foster 2020). The purpose is to demonstrate the capability of this proposed phase field model for modelling real 3D stress problems.

In this SDF3 crack modelling, the geometry of specimen as well as material parameters is originated from reference (Kramer, Jones et al. 2019). Figure 3.15 presents a steel bar of SDF3 specimen, inside which several distinctly orientated hollow geometries are intersected including three through cylinders, an elliptical truncated cone and a sphere. Because of the complex 3D geometry, SDF3 specimens were additively manufactured rather than conventionally machined. The elasto-plastic parameters are calibrated from a group of tensile calibration tests with the same material in (Kramer, Jones et al. 2019). Fracture parameters including fracture strain ep_{cr} are calibrated to match the force-displacement best in this paper, and all parameters are listed in Table 3.5. This FE model contains 62,547 nodes and 166,716 elements in total, and its element mesh within one quarter of gauge area has been presented in Figure 3.15.

Table 3.5 parameters for SDF3 numerical modelling

Type	Parameters	Value
elastic	E	175000 MPa
	v	0.3
plastic	σ_{y0}	488.8 MPa
	Strain hardening	(Kramer, Jones et al. 2019)
Damage evolution	G_{t0}	9.3 kN/m
	G_{c0}	13.95 kN/m
	a_t	12
	b_t	1e-3
	a_c	12
	b_c	1e-3
Damage initiation	$\bar{\varepsilon}_{cr}^{p}$	0.45

Figure 3.16 demonstrates the force-displacement curve of numerical result accompanied by experiment data, together with the numerical result without considering damage propagation for comparison. At the beginning of loading process, the specimen

experiences a linear elastic stage, when the force grows fast with the displacement before 0.05 mm. Next, the stress develops beyond the initial yield stress and plastic strain initiates accompanied by strain hardening, and the force continues to increase until the peak of around 8000 N when the displacement reaches 0.6 mm. When the displacement is 0.6-0.7 mm, the slight load decrease is attributed to necking effect. Then fracture initiates when the displacement reaches around 0.7 mm. Meanwhile, the force-displacement curve of damage included modelling starts to diverge from the simulated curve which does not consider damage evolution. Since then, crack continues to develop and the force decreases quickly until the specimen is broken.

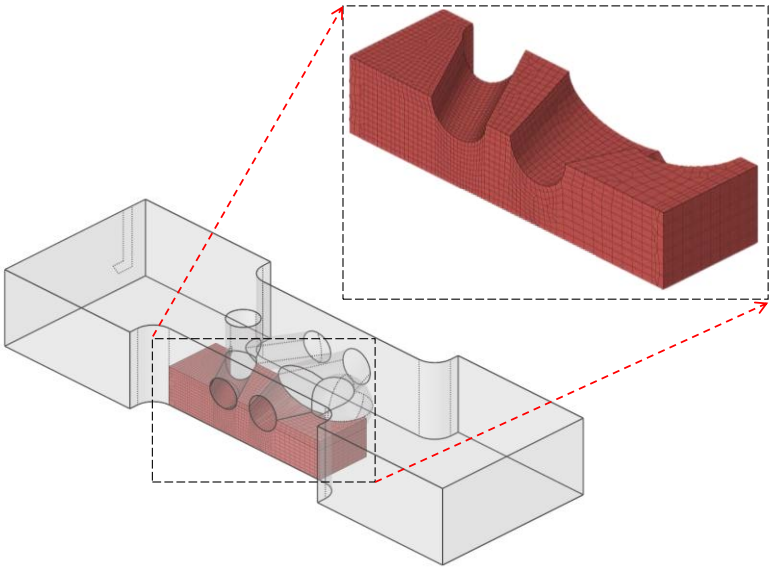

Figure 3.15 Geometry information and mesh elements of third Sandia challenge specimen

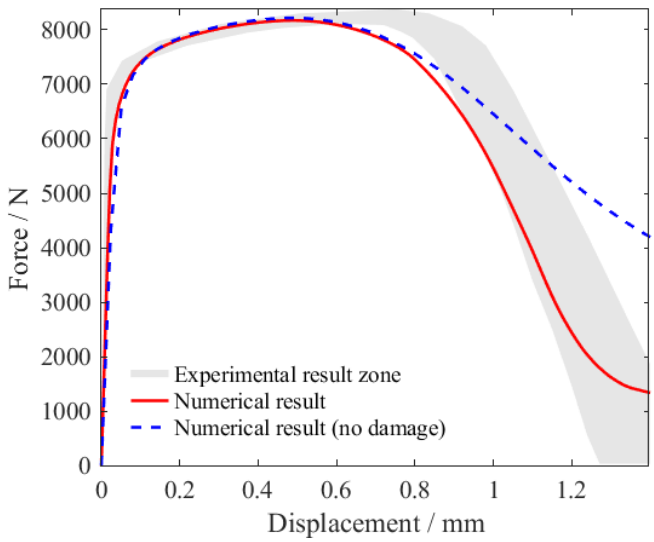

Figure 3.16 load versus displacement for experiment and numerical data of third Sandia

specimen

It is observed that the numerical result generally agrees well with experiment data except for some acceptable difference at peak force stage. The loading force rises to its maximum value when the applied displacement reaches around 0.6 mm and 0.8 mm for numerical and experiment data respectively. Since the phase field damage does not even initiate yet, that slightly earlier decrease of loading force in the numerical simulation is because of the calibrated strain hardening data in (Kramer, Jones et al. 2019) rather than damage parameters.

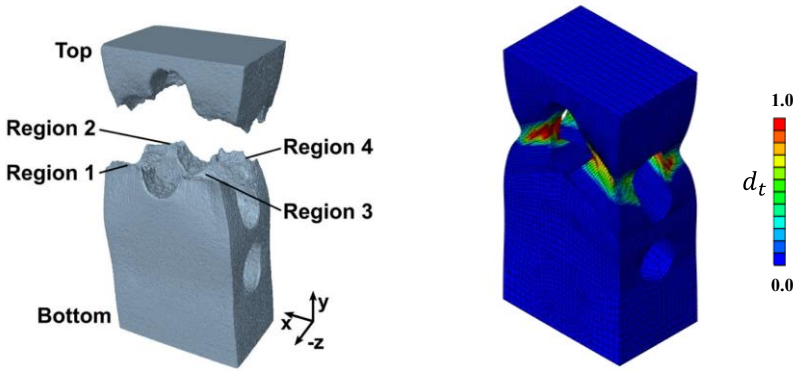

(a) 3D CT reconstruction (b) numerical damage contour on deformable solid

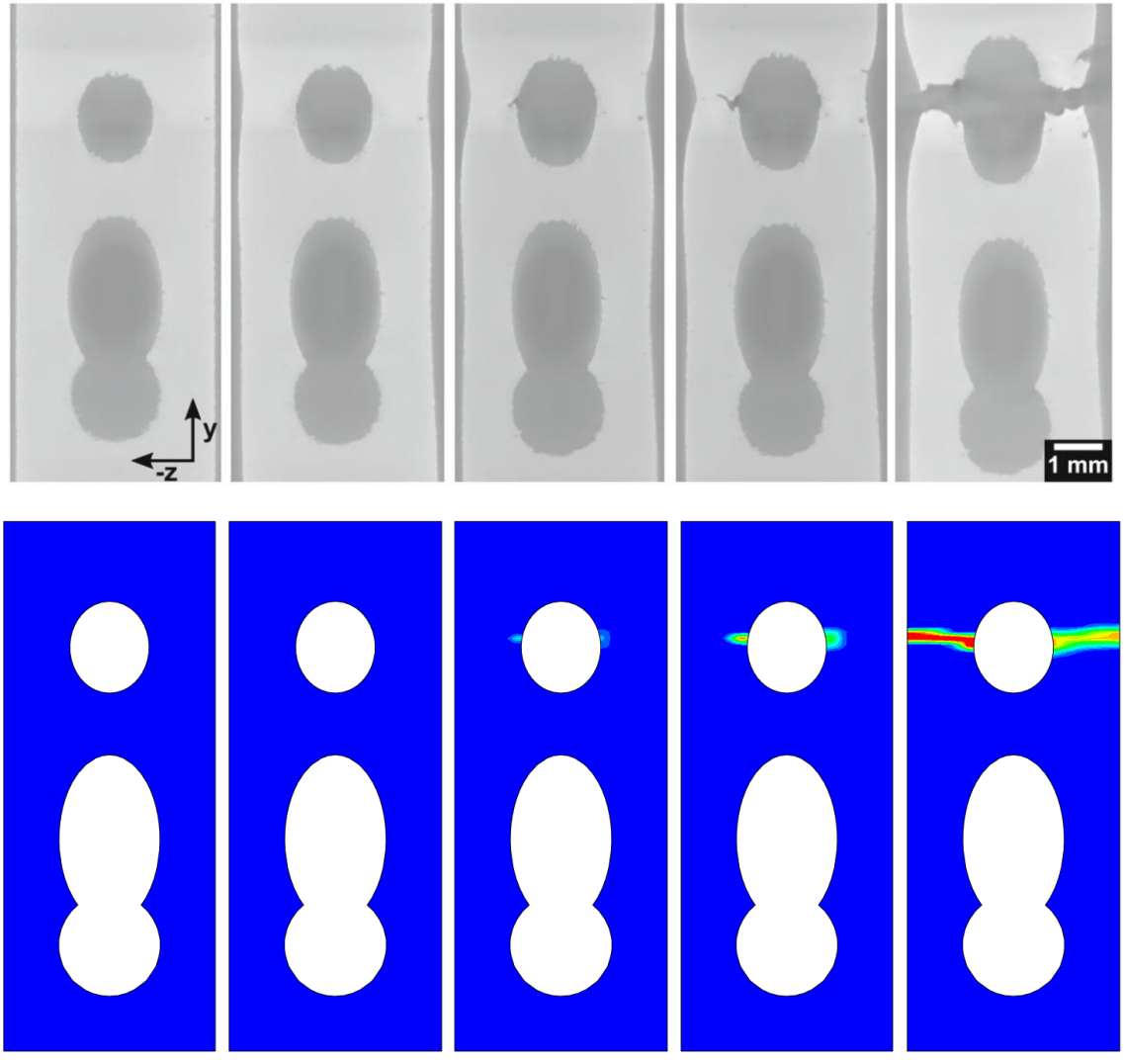

Before loading u=0.3 mm u=0.7 mm u=0.83 mm broken

(c) Slice damage contour compared with micro CT data figure

Figure 3.17 Third Sandia crack path compare between numerical result and experiment CT data

Figure 3.17 (a) and (b) show the 3D reconstruction image according to micro-CT data and numerical damage contour respectively, for the gauge area of specimen after

loading. It can be seen that the failure areas for both numerical and experiment results are located at the four ligaments around the intersected hollow cylinder channel area. It is noted that the last SFC3 example is conducted here only to show this model's capability for complex 3D problems. Since this SDF3 loading condition is applying tensile force on specimen, only the tensile damage is presented here, while the shear damage is very small despite its complicated geometry shape.

SFC3 specimen was scanned by micro-CT in reference (Kramer, Ivanoff et al. 2019) at five stages of loading process, and Figure 3.17(c) depicts the slice images in *yz* plane, which are compared with numerical slice damage contour at the same cross section. It can be observed that the fracture path development of numerical results shows good agreement with experiment CT data. In this specific slice, crack initiates at the middle of side walls of the cylinder channel, and develop along the horizontal direction to outside surface of the specimen, forming a through fracture path. It is also noted that the crack damage contour for both numerical and experiment results in Figure 3.17(c) are not strictly symmetric about the middle *xy* surface. Once a crack initiates at one side of the specimen due to material defects or numerical errors, the loading condition becomes asymmetric and will in turn affect the following asymmetric crack propagation.

3.5 Summary

To model fracture propagation in 3D solids for different crack modes, this study has proposed a double phase field model with strain energy decomposition based on the crack-orientation-based coordinate system. The tensile and shear components of decomposed strain energy contribute to the crack propagation of tensile and shear damage phase field d_{t} and d_{c}, respectively. The plastic contribution for crack evolution is coupled by associating the decomposed tensile and shear plastic strains with the correspond fracture energy release rates G_t and G_c. This proposed model is implemented through ABAQUS subroutines UEL and UMAT with a staggered solution method for tensile/shear damage phase field and displacement field.

Five numerical examples are conducted for parametric analysis and model effectiveness verification. In the first example of one element under tension and compression loading, the agreement between the numerical results and analytical solutions indicates the correctness of the implementation of this proposed model. The second example of single-edge notch specimens with different values of a_t and b_t subject

to uniaxial tension have demonstrated that a larger a_t as well as a smaller b_t lead to lower material strength, while the effect of b_t could be negligible when it is smaller than 0.01. The third simulation on single-edge shear loading specimens have proven that the G_c/G_t plays great roles on the crack mode: when G_c/G_t is less than or equal to 1.4, shear crack dominate the specimen failure, when G_c/G_t is equal to 2, mixed crack mode appears, and when G_c/G_t is larger or equal than 2.4, tensile crack dominates the failure. Meanwhile, the mixed crack mode specimen has showed the highest load bearing capability among all specimens. In the fourth numerical example, a group of uniaxial tension, simple shear and tension-shear specimens is considered, which shows good agreement with experiment data in terms of crack path and load versus displacement curve, which demonstrates the capability of this proposed double phase field model for different crack mode modelling. Lastly, the third Sandia challenge example is modelled and compared with experiment data, demonstrating capability of this proposed phase field model for complex 3D crack propagation modelling.

This study has presented an effective numerical method for mixed-mode ductile fracture within the phase field framework in a 3D setting. There are many interesting topics for future studies based on this proposed double-phase-field framework. For example, uncertainty analysis could be conducted on material parameters (Khodadadian, Noii et al. 2020, Feng, Wang et al. 2021, Noii, Khodadadian et al. 2021). Moreover, the developed model can be extended to dynamic fracture to investigate the mechanical behaviour of materials and structures under impact and blast loads (Dinachandra and Alankar 2020, Liu, Wang et al. 2022).

4. A UNIFIED STRAIN ENERGY DECOMPOSITION STRATEGY

4.1 Introduction

The accurate prediction of fracture behaviour and stress response in materials has garnered significant interest within the computational mechanics community (T.N.Bittencourt 1996, Feng, Wu et al. 2023). Numerical models for fracture modelling are typically classified into two categories based on their representation of fracture topology: discrete fracture models and continuous damage models. Discrete fracture models, such as cohesive zone models (Elices, Guinea et al. 2002, Xie and Waas 2006, Nguyen, Bui et al. 2017), the Embedded Finite Element Method (Annavarapu, Hautefeuille et al. 2012, Roubin, Vallade et al. 2015), and the eXtended Finite Element Method (XFEM) (Chessa, Smolinski et al. 2001, Zi and Belytschko 2003), involve tracking crack topology and require complex remeshing, leading to high computational costs. In contrast, continuous damage models offer a more computationally efficient approach by conceptualizing the cracked solid as a continuous damage zone (Løland 1980, Lemaitre 1985).

Among these models, the phase field model has attracted considerable attention. Originally proposed by Francfort and Marigo (Francfort and Marigo 1998) and further developed by Bourdin et al. (Bourdin, Francfort et al. 2008), the phase field model is derived by minimising the total potential energy, which comprises the strain energy and fracture energy (Miehe, Hofacker et al. 2010, Miehe, Welschinger et al. 2010, Ambati, Gerasimov et al. 2014, Miehe, Schänzel et al. 2015, Wu and De Lorenzis 2016, Molnár and Gravouil 2017). Due to its efficiency, robustness, and simplicity in numerical implementation (Fang, Wu et al. 2020), the phase field approach has been extensively applied to simulate complex fracture phenomena, such as ductile fracture (Ambati, Kruse et al. 2015, Borden, Hughes et al. 2016, Miehe, Aldakheel et al. 2016, Roth and Mohr 2016, Alessi, Marigo et al. 2018, Dittmann, Aldakheel et al. 2018, Fang, Wu et al. 2019, Fang, Wu et al. 2019), dynamic fracture(Karma, Kessler et al. 2001, Borden, Verhoosel et al. 2012, Wang, Ye et al. 2020), hydraulic fracture (Miehe and Mauthe 2016, Wilson and Landis 2016, Ehlers and Luo 2017), and hydrogen embrittlement fractures(Martínez-Pañeda, Golahmar et al. 2018, Wu, Mandal et al. 2020). Nevertheless, the phase field model still encounters challenges in capturing asymmetrical tension-compression

behaviour that is commonly exhibited by various materials in real-world conditions, such as rocks and metals (B.Shen and O.Stephansson 1994, Du, Zhang et al. 2020, You, Zhu et al. 2020). This limitation arises from the identical strain energy density under tensile and compressive loading of the same magnitude, which contributes equally to fracture evolution in the formulation of standard phase field models.

To overcome this issue, researchers have proposed various strain energy decomposition approaches, splitting the total strain energy into positive and negative components, with the presumption that only the positive part drives fracture propagation. Notably, Volumetric-Deviatoric (V-D) (Amor, Marigo et al. 2009, Lancioni and Royer-Carfagni 2009) and spectral decomposition (Miehe, Hofacker et al. 2010, Miehe, Welschinger et al. 2010, Miehe, Schänzel et al. 2015) are prevalent in the phase field context and have proven effective under specific loading conditions, as evidenced by experimental comparisons (Pham, Ravi-Chandar et al. 2017, Santillán, Mosquera et al. 2017, Chukwudozie, Bourdin et al. 2019). Nevertheless, the effectiveness of those two approaches could not be maintained across arbitrary stress states (Cao, Wang et al. 2022, Prakash, Behera et al. 2022, Behera, Sudeep et al. 2023). For example, V-D decomposition can result in incorrect stress fields and fracture driving force under transverse compressive loading conditions (Prakash, Behera et al. 2022); spectral decomposition is inappropriate under simple shear loading where the stress response will never be totally degraded at material points where the damage variable has been even fully developed (Behera, Sudeep et al. 2023, Hesammokri, Yu et al. 2023).

Based on these two decomposition strategies, numerous modifications have been proposed to enhance their flexibility. Within the V-D decomposition framework, Spetz et al. (Spetz, Denzer et al. 2020, Spetz, Denzer et al. 2021) further divided the deviatoric strain energy into positive and negative components based on the principal values of the deviatoric strain tensor. Similarly, Hesammokri et al. (Hesammokri, Yu et al. 2023) employed a strategy where the additional decomposition of the deviatoric strain energy was based on the principal strain. Compared to the original V-D decomposition, these refined models demonstrate improved capability in representing tensile fracture configurations. However, this enhancement may come at the cost of reduced accuracy under other stress states, such as simple shear stress loading, where a portion of the strain energy always remains reserved and does not contribute to fracture propagation. Building on spectral decomposition, a thermodynamically consistent positive-negative projection

for the principal strain was proposed and implemented to maintain the major symmetry of the material stiffness matrix (Wu and Cervera 2018, Nguyen, Yvonnet et al. 2020). Nevertheless, this approach overlooks cracks induced by shear-stress-dominant loading conditions. Alternatively, recent research (Cao, Wang et al. 2022) introduced a hybrid model that combines spectral and V-D decompositions using a weighted parameter to optimize performance across different stress states. However, fine-tuning this weighting parameter presents a significant challenge.

In addition to V-D and spectral decomposition, the so-called direction-based strain energy decomposition method has also obtained significant attention (Steinke and Kaliske 2018, Storm, Supriatna et al. 2019, Steinke, Storm et al. 2022, Jiang, Li et al. 2023). In this approach, the effective stress is decomposed within a crack-orientation-based coordinate system. The crack orientation is typically determined either by maximising the *F*-criterion energy dissipation (Bryant and Sun 2018, Wang, Feng et al. 2020, Fei and Choo 2021, Steinke, Storm et al. 2022, Jiang, Li et al. 2023, Sun, Lu et al. 2023) or by aligning with the gradient direction of the phase field variable (Strobl and Seelig 2015, Luo, Chen et al. 2021). These models have proven effective in capturing both tensile and shear fractures and enhancing the adaptability of the phase field model. However, they still exhibit limitations when simulating solids under high stress triaxiality conditions, such as biaxial and triaxial tension. Under these stress states, once the crack surface is assumed, only the tensile stress normal to crack-surface contributes to fracture propagation, while the tensile stress components in other directions are neglected for damage evolution. Consequently, such crack-direction-based phase field models tend to predict identical equiaxial and uniaxial tensile strengths, which contradicts experimental observations for most materials (Giovan and Sines 2006, Hannon and Tiernan 2008).

To the best knowledge of the authors, most existing phase field decomposition strategies are tailored to characterise fracture behaviour in solids subjected to one or several limited stress state regions. However, real-world structures are frequently exposed to highly diverse stress loadings, which may vary spatially and temporally. In this study, we aim to introduce a unified strain energy decomposition approach capable of effectively capturing fracture propagation under arbitrary stress states. The remainder of this paper is organised as follows. Section 2 reviews the framework of standard phase field model and two classic strain energy decomposition methodologies, the Volumetric-Deviatoric and spectral decomposition. Section 3 demonstrates the formulation of the proposed

unified decomposition phase field model, including the effective stress decomposition, governing equation of phase field evolution, and determination and updating of the local coordinate system. Section 4 explains the explicit implementation of the proposed model. Section 5 presents a series of numerical examples comparing the simulation outcomes of the proposed decomposition approach with those derived from the Volumetric-Deviatoric and spectral decomposition methods.

4.2 Formulation of standard phase field model

4.2.1 Energy functional

As demonstrated in Figure 4.1(a), let us consider an arbitrary body Ω inside which lies a sharp crack Γ. Its external boundary $\partial\Omega$ consists of Dirichlet boundary $\partial\Omega^h$ and Neumann boundary $\partial\Omega^s$, which satisfies $\partial\Omega^h \cap \partial\Omega^s = \emptyset$ and $\partial\Omega = \overline{\partial\Omega^h \cup \partial\Omega^s}$. Under this configuration, $\boldsymbol{b}$, $\boldsymbol{t}$ and $\overline{\boldsymbol{u}}$ represent the body force within Ω, the traction force on $\partial\Omega^h$ and boundary displacement on $\partial\Omega^s$ respectively. Following the phase field theory (Miehe, Welschinger et al. 2010, Miehe, Schänzel et al. 2015, Wu and De Lorenzis 2016, Molnár and Gravouil 2017), the sharp crack Γ then could be regularised as a diffusive damage field d pictured in Figure 4.1(b), where length scale parameter l_c controls the fracture width. The value of d varies from zero to one, which indicates intact state and totally broken state, respectively. With this fracture regularisation methodology in hand, the crack density function γ could be obtained as follows,

$$\gamma(d, \nabla d) = \frac{d^2}{2l_c} + \frac{l_c}{2}|\nabla d|^2 \tag{4.1}$$

Accordingly, the fracture energy density function is obtained as follows,

$$\varphi^f(d, \nabla d) = G_f \cdot \gamma(d, \nabla d) = G_f \cdot \left(\frac{d^2}{2l_c} + \frac{l_c}{2}|\nabla d|^2\right) \tag{4.2}$$

where G_f represents the crack energy release rate, indicating the energy required for generating per unit area of the crack surface. The internal potential energy within body Ω is then obtained by,

$$\Phi^{int}(\boldsymbol{u}, d) = \int_\Omega \left(\varphi^e(\boldsymbol{u}, d) + \varphi^f(d, \nabla d)\right) \mathrm{d}\Omega \tag{4.3}$$

In Eq.(4.2), φ^e represents the elastic strain energy density, which is calculated as follows in standard phase field theory (Miehe, Welschinger et al. 2010, Molnár and Gravouil 2017, Fang, Wu et al. 2019),

$$\varphi^e(\boldsymbol{u}, d) = (1-d)^2 \cdot \varphi_0^e(\boldsymbol{u}) \tag{4.4}$$

where φ_0^e signifies the undamaged elastic strain energy density. Meanwhile, the external

force work is given by,

$$\Phi^{ext}(\boldsymbol{u}) = \int_{\Omega} (\boldsymbol{b} \cdot \boldsymbol{u}) \mathrm{d}\Omega + \int_{\partial\Omega^h} (\boldsymbol{t} \cdot \boldsymbol{u}) \mathrm{d}S \tag{4.5}$$

The kinetic energy of the body Ω is written by,

$$\Phi^{kin}(\boldsymbol{u}) = \int_{\Omega} \frac{1}{2} \rho \dot{\boldsymbol{u}} \cdot \dot{\boldsymbol{u}} \mathrm{d}\Omega \tag{4.6}$$

where ρ represents the density of material. According to (Borden, Verhoosel et al. 2012, Ren, Zhuang et al. 2019, Wang, Ye et al. 2020), the Lagrangian of the solid then can be calculated as,

$$L(\boldsymbol{u}, \ddot{\boldsymbol{u}}, d) = \Phi^{kin}(\boldsymbol{u}) + \Phi^{ext}(\boldsymbol{u}) - \Phi^{int}(\boldsymbol{u}, d) = \int_{\Omega} \left\{ \frac{1}{2} \rho \dot{\boldsymbol{u}} \cdot \dot{\boldsymbol{u}} - \varphi^{e}(\boldsymbol{u}, d) - \varphi^{f}(d, \nabla d) + \rho \boldsymbol{b} \cdot \boldsymbol{u} \right\} \mathrm{d}\Omega + \int_{\partial\Omega^h} (\boldsymbol{t} \cdot \boldsymbol{u}) \mathrm{d}S \tag{4.7}$$

With expression of Lagrangian in hand, the governing equations for the stress response and phase field evolution then could be derived through least action principle (Borden, Verhoosel et al. 2012, Ren, Zhuang et al. 2019, Wang, Ye et al. 2020) as,

$$\begin{cases} \nabla \cdot \boldsymbol{\sigma} + \boldsymbol{b} = \rho\, \ddot{\boldsymbol{u}} & \text{in } \Omega \\ \boldsymbol{\sigma} \cdot \boldsymbol{n} - \boldsymbol{t} = 0 & \text{on } \partial\Omega^h \\ \boldsymbol{u} = \overline{\boldsymbol{u}} & \text{on } \partial\Omega^s \end{cases} \tag{4.8}$$

$$\begin{cases} \frac{G_f}{l_c} \left(d - {l_c}^2 \Delta d \right) - 2(1-d)\varphi_0^e = 0 & \text{in } \Omega \\ \nabla d \cdot \boldsymbol{n} = 0 & \text{on } \partial\Omega \end{cases} \tag{4.9}$$

where $\boldsymbol{\sigma} = \frac{\partial \varphi^e(\boldsymbol{u}, d)}{\partial \boldsymbol{\varepsilon}^e}$ denotes the stress tensor; and $\boldsymbol{n}$ represents the normal direction on the boundary surface $\partial\Omega$. For the purpose of explicit implementation in this study, Eq.(4.9) is rewritten with a time-dependent form (Miehe, Welschinger et al. 2010, Wang, Ye et al. 2020) as,

$$\dot{d} = \begin{cases} \frac{1}{\omega} \langle 2(1-d)\varphi_0^e - \frac{G_f}{l_c} \left(d - {l_c}^2 \Delta d \right) \rangle_+ & d < 1 \\ 0 & \text{otherwise} \end{cases} \tag{4.10}$$

where ω denotes the viscous parameter for phase field evolution; the bracket operator $\langle * \rangle_+ = \frac{1}{2}(* + |*|)$ is incorporated for avoiding the damage healing.

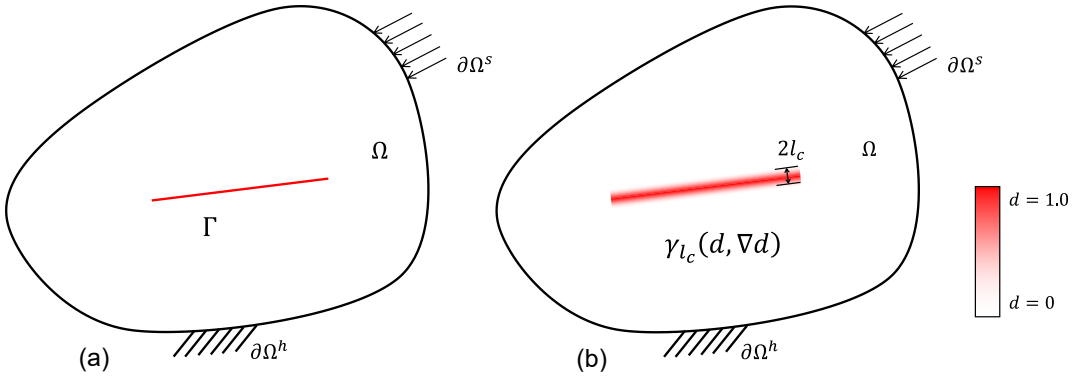

Figure 4.1 Configuration of phase field damage regularisation. (a) sharp crack Γ; (b)diffusive damage zone

4.2.2 Commonly used strain energy decomposition method

To capture the asymmetric fracture propagation and mechanic response of materials under tension and compression loading, various strain energy decomposition approaches have been proposed (Amor, Marigo et al. 2009, Miehe, Hofacker et al. 2010, Miehe, Welschinger et al. 2010). The general idea is to decompose the elastic strain energy φ_0^e in Eq.(4.10) into tensile component φ_0^{e+} and compressive component φ_0^{e-}, of which only the tensile part is degraded and contributes to the crack propagation. Eq.(4.4) then is rewritten by

$$\varphi^e(\boldsymbol{u}, d) = (1-d)^2 \cdot \varphi_0^{e+}(\boldsymbol{u}) + \varphi_0^{e-} \tag{4.11}$$

Accordingly, the expression of stress response $\boldsymbol{\sigma}$ is updated to

$$\boldsymbol{\sigma} = (1-d)^2 \cdot \frac{\partial \varphi_0^{e+}(\boldsymbol{u})}{\partial \boldsymbol{\varepsilon}^e} + \frac{\partial \varphi_0^{e-}(\boldsymbol{u})}{\partial \boldsymbol{\varepsilon}^e} \tag{4.12}$$

Meanwhile, the governing equation of phase field evolution is updated by replacing the undamaged elastic strain energy φ_0^e with its positive component φ_0^{e+} as

$$\dot{d} = \begin{cases} \frac{1}{\omega}\langle 2(1-d)\varphi_0^{e+} - \frac{G_f}{l_c}\left(d - {l_c}^2 \Delta d\right)\rangle_+ & d < 1 \\ 0 & \text{otherwise} \end{cases} \tag{4.13}$$

Among the various decomposition methods, the Volume-Deviatoric (V-D)(Amor, Marigo et al. 2009) and spectral decomposition (Miehe, Hofacker et al. 2010, Miehe, Welschinger et al. 2010) methods are most widely adopted for the phase field modelling. For V-D phase field model, the elastic strain energy is decomposed as follows

$$\begin{cases} \varphi_0^{e+}(\boldsymbol{u}) = \frac{K}{2}\langle tr\boldsymbol{\varepsilon}^e\rangle_+^{\ 2} + \mu(\boldsymbol{\varepsilon}_{dev}^e : \boldsymbol{\varepsilon}_{dev}^e) \\ \varphi_0^{e-}(\boldsymbol{u}) = \frac{K}{2}\langle tr\boldsymbol{\varepsilon}^e\rangle_-^{\ 2} \end{cases} \tag{4.14}$$

where $K = \frac{E}{3(1-2\nu)}$ and $\mu = \frac{E}{2(1+\nu)}$ denote the bulk modulus and shear modulus respectively; $\boldsymbol{\varepsilon}_{dev}^e = \boldsymbol{\varepsilon}^e - tr(\boldsymbol{\varepsilon}^e)\mathbf{I}$, representing the deviatoric strain with the second-

order identity tensor **I**; the bracket operation is defined as $\langle * \rangle_{\pm} = \frac{1}{2}(* \pm |*|)$. In the V-D decomposition approach, the deviatoric strain energy always contributes to the fracture driving force, while volumetric part only takes effect when volume strain is positive.

For spectral decomposition method, the positive and negative components of elastic strain energy decomposition are expressed as follows

$$\begin{cases} \varphi_0^{e+}(\boldsymbol{u}) = \frac{\lambda}{2}\langle tr\boldsymbol{\varepsilon}^e \rangle_+^{\ 2} + G\sum_{i=1}^{3}\langle \boldsymbol{\varepsilon}_i^e \rangle_+^{\ 2} \\ \varphi_0^{e-}(\boldsymbol{u}) = \frac{\lambda}{2}\langle tr\boldsymbol{\varepsilon}^e \rangle_-^{\ 2} + G\sum_{i=1}^{3}\langle \boldsymbol{\varepsilon}_i^e \rangle_-^{\ 2} \end{cases} \tag{4.15}$$

where $\lambda = \frac{E\nu}{(1+\nu)(1-2\nu)}$, denotes the lame constant; $\boldsymbol{\varepsilon}_i^e = \varepsilon_i^e \boldsymbol{n_i} \otimes \boldsymbol{n_i}$, is the component of strain tensor corresponding to the *i*-th principal strain value ε_i^e and *i*-th principal strain direction $\boldsymbol{n_i}$. It can be seen from Eq.(4.15) that the elastic strain is decomposed in the spectral space, and only the strain energy produced by the positive principal stain contributes to the fracture propagation.

Specifically, it was highlighted that the Volumetric-Deviatoric (V-D) decomposition is efficient for predicting cracks induced by deviatoric stress, while the spectral decomposition method demonstrates superior performance in modelling fracture propagation under tensile loading (Cao, Wang et al. 2022). However, the applicability of both methods may be contingent on specific stress states rather than being universally applicable. Given the complex loading conditions in practical engineering, material stress states change over time. Therefore, there is a need to develop a unified and effective strain energy decomposition strategy that remains valid under various complex stress states.

4.3 Strain Energy decomposition under the local coordinate system

In this study, we introduce a novel strain energy decomposition approach where the total elastic strain energy is decomposed on the local coordinate system into three components, namely tensile, shear and compressive stress. Among them, only the first two parts contribute to the fracture propagation after being regularised by corresponding tensile and shear crack energy release rate G_t and G_c. The local coordinate system is determined by maximising the modified *F*-criterion energy dissipation.

4.3.1 Effective stress decomposition

In this proposed unified decomposition method, the undamaged (effective) stress is decomposed on the local coordinate system (LCS), characterised by three orthotropic directions ***r***, ***s*** and ***t***, as shown in Figure 4.2. In this configuration, stress components $\bar{\sigma}_{pq}$

could be calculated by

$$\bar{\sigma}_{pq} = \bar{\boldsymbol{\sigma}}\, \boldsymbol{M}^{pq} \tag{4.16}$$

where the second-order projection tensor $\boldsymbol{M}^{pq}$ (p, q = r, s, or t) are constructed based on three orthotropic directions $\boldsymbol{r}$, $\boldsymbol{s}$ and $\boldsymbol{t}$ by

$$\begin{cases} \boldsymbol{M}^{rr} = \boldsymbol{r} \otimes \boldsymbol{r}, \boldsymbol{M}^{rs} = \boldsymbol{r} \otimes \boldsymbol{s}, \boldsymbol{M}^{rt} = \boldsymbol{r} \otimes \boldsymbol{t}, \\ \boldsymbol{M}^{sr} = \boldsymbol{s} \otimes \boldsymbol{r}, \boldsymbol{M}^{ss} = \boldsymbol{s} \otimes \boldsymbol{s}, \boldsymbol{M}^{st} = \boldsymbol{s} \otimes \boldsymbol{t}, \\ \boldsymbol{M}^{tr} = \boldsymbol{r} \otimes \boldsymbol{r}, \boldsymbol{M}^{ts} = \boldsymbol{r} \otimes \boldsymbol{s}, \boldsymbol{M}^{tt} = \boldsymbol{r} \otimes \boldsymbol{t} \end{cases} \tag{4.17}$$

Subsequently, the effective stress could be decomposed into tension, shear, and compressive components, written as,

$$\bar{\boldsymbol{\sigma}}_{\boldsymbol{I}}^{+} = \sigma_r^{+} \cdot \boldsymbol{M}^{rr} + \sigma_s^{+} \cdot \boldsymbol{M}^{ss} + \sigma_t^{+} \cdot \boldsymbol{M}^{tt} \tag{4.18}$$

$$\bar{\boldsymbol{\sigma}}_{\boldsymbol{II}}^{+} = \bar{\sigma}_{rs} \cdot (\boldsymbol{M}^{rs} + \boldsymbol{M}^{sr}) + \bar{\sigma}_{rt} \cdot (\boldsymbol{M}^{rt} + \boldsymbol{M}^{tr}) + \bar{\sigma}_{st} \cdot (\boldsymbol{M}^{st} + \boldsymbol{M}^{ts}) \tag{4.19}$$

$$\bar{\boldsymbol{\sigma}}^{-} = \sigma_r^{-} \cdot \boldsymbol{M}^{rr} + \sigma_s^{-} \cdot \boldsymbol{M}^{ss} + \sigma_t^{-} \cdot \boldsymbol{M}^{tt} \tag{4.20}$$

From Eqs.(4.18)-(4.20), it can be seen that all six shear stress components contribute to the shear stress tensor $\bar{\boldsymbol{\sigma}}_{\boldsymbol{II}}^{+}$, while the three normal stress components in $\boldsymbol{r}$, $\boldsymbol{s}$ and $\boldsymbol{t}$ direction are further split into tensile and compressive parts: σ_r^{+} and σ_r^{-}; σ_s^{+} and σ_s^{-}; σ_t^{+} and σ_t^{-} respectively. To distinguish the tensile and compressive stress, one straightforward approach involves utilising the signs of normal stress. While this method offers simplicity, it neglects the influence of the Poisson effect, which can lead to the non-orthogonal decomposed tensile and compressive stresses, potentially leading to unrealistic negative decomposed strain energy (Steinke and Kaliske 2018). To overcome such drawback, here we refer to Wu et al. (Wu and Cervera 2018, Wu, Nguyen et al. 2020), and project the tensile and compressive part of normal stresses on direction $\boldsymbol{r}$, $\boldsymbol{s}$ and $\boldsymbol{t}$ by

$$\begin{cases} \sigma_r^{+} = \langle \bar{\sigma}_{rr} \rangle_{+}, & \sigma_r^{-} = \bar{\sigma}_{rr} - \sigma_r^{+}, \\ \sigma_s^{+} = \langle \max\left(\bar{\sigma}_{ss}, \ \frac{\upsilon}{1-\upsilon}\bar{\sigma}_{rr}\right) \rangle_{+}, & \sigma_s^{-} = \bar{\sigma}_{ss} - \sigma_s^{+}, \\ \sigma_t^{+} = \langle \max\left(\bar{\sigma}_{tt}, \ \upsilon(\bar{\sigma}_{rr} + \bar{\sigma}_{ss}), \ \frac{\upsilon}{1-\upsilon}\bar{\sigma}_{rr}\right) \rangle_{+}, & \sigma_t^{-} = \bar{\sigma}_{tt} - \sigma_t^{+}, \end{cases} \tag{4.21}$$

where the sequence of directions $\boldsymbol{r}$, $\boldsymbol{s}$ and $\boldsymbol{t}$ is default as $\bar{\sigma}_{rr} \geq \bar{\sigma}_{ss} \geq \bar{\sigma}_{tt}$ for simplification. The proof of non-negativity for the decomposed strain energy is detailed in the subsequent sections. With decomposed effective stress $\bar{\boldsymbol{\sigma}}_{\boldsymbol{I}}^{+}$, $\bar{\boldsymbol{\sigma}}_{\boldsymbol{II}}^{+}$ and $\bar{\boldsymbol{\sigma}}^{-}$ in hand, the nominal stress response can be obtained by aggregating the intact stress with the degraded tensile and shear stress as

$$\boldsymbol{\sigma} = (1-d)^2 \cdot (\bar{\boldsymbol{\sigma}}_{\boldsymbol{I}}^{+} + \bar{\boldsymbol{\sigma}}_{\boldsymbol{II}}^{+}) + \bar{\boldsymbol{\sigma}}^{-} \tag{4.22}$$

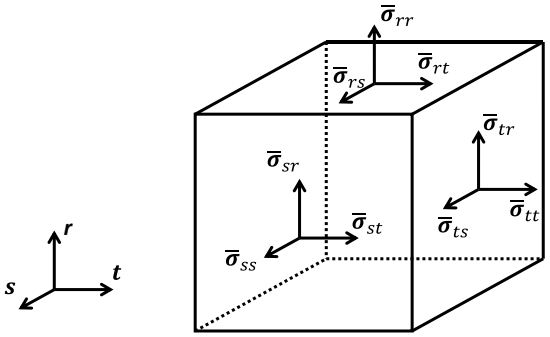

Figure 4.2 Effective stress decomposition configuration

4.3.2 Strain energy decomposition

The total elastic strain energy $\varphi_0^e(\boldsymbol{u})$ in Eq.(4.4) can be calculated by

$$\varphi_0^e = \frac{1}{2}\overline{\boldsymbol{\sigma}}:\boldsymbol{\varepsilon}^{\mathrm{e}} \tag{4.23}$$

In this proposed unified decomposition phase field model, the total strain energy φ_0^e is partitioned into three distinct components, namely tension crack driving force H_{I}, shear crack driving force H_{II} and compression strain energy H_n, which aligns with the principles of effective stress decomposition. Each component can be quantitatively obtained as follows,

$$H_{\mathrm{I}} = \frac{1}{2}\overline{\boldsymbol{\sigma}}_{\mathrm{I}}^{+}:\boldsymbol{\varepsilon}^{\mathrm{e}} \tag{4.24}$$

$$H_{\mathrm{II}} = \frac{1}{2}\overline{\boldsymbol{\sigma}}_{\mathrm{II}}^{+}:\boldsymbol{\varepsilon}^{\mathrm{e}} \tag{4.25}$$

$$H_{\mathrm{n}} = \frac{1}{2}\boldsymbol{\sigma}^{-}:\boldsymbol{\varepsilon}^{\mathrm{e}} \tag{4.26}$$

According to Eqs.(4.18)-(4.20), the three parts of decomposed stress are orthogonal to each other with the following orthogonal condition acquired.

$$\begin{cases} \overline{\boldsymbol{\sigma}}_{\mathrm{I}}^{+}:\mathbb{C}:\overline{\boldsymbol{\sigma}}_{\mathrm{II}}^{+} = 0 \\ \overline{\boldsymbol{\sigma}}_{\mathrm{I}}^{+}:\mathbb{C}:\boldsymbol{\sigma}^{-} = 0 \\ \overline{\boldsymbol{\sigma}}_{\mathrm{II}}^{+}:\mathbb{C}:\boldsymbol{\sigma}^{-} = 0 \end{cases} \tag{4.27}$$

where $\mathbb{C}$ represents the flexural tensor. Substitution of Eq.(4.27) into Eqs.(4.24)-(4.26) could lead to

$$H_{\mathrm{I}} = \frac{1}{2}\overline{\boldsymbol{\sigma}}_{\mathrm{I}}^{+}:\boldsymbol{\varepsilon}^{e} = \frac{1}{2}\overline{\boldsymbol{\sigma}}_{\mathrm{I}}^{+}:\mathbb{C}:(\overline{\boldsymbol{\sigma}}_{\mathrm{I}}^{+} + \overline{\boldsymbol{\sigma}}_{\mathrm{II}}^{+} + \overline{\boldsymbol{\sigma}}^{-}) = \frac{1}{2}\overline{\boldsymbol{\sigma}}_{\mathrm{I}}^{+}:\mathbb{C}:\overline{\boldsymbol{\sigma}}_{\mathrm{I}}^{+} \geq \mathbf{0} \tag{4.28}$$

$$H_{\mathrm{II}} = \frac{1}{2}\overline{\boldsymbol{\sigma}}_{\mathrm{II}}^{+}:\boldsymbol{\varepsilon}^{e} = \frac{1}{2}\overline{\boldsymbol{\sigma}}_{\mathrm{II}}^{+}:\mathbb{C}:(\overline{\boldsymbol{\sigma}}_{\mathrm{I}}^{+} + \overline{\boldsymbol{\sigma}}_{\mathrm{II}}^{+} + \overline{\boldsymbol{\sigma}}^{-}) = \frac{1}{2}\overline{\boldsymbol{\sigma}}_{II}^{+}:\mathbb{C}:\overline{\boldsymbol{\sigma}}_{II}^{+} \geq \mathbf{0} \tag{4.29}$$

$$H_{\mathrm{n}} = \frac{1}{2}\overline{\boldsymbol{\sigma}}^{-}:\boldsymbol{\varepsilon}^{\mathrm{e}} = \frac{1}{2}\overline{\boldsymbol{\sigma}}^{-}:\mathbb{C}:(\overline{\boldsymbol{\sigma}}_{\mathrm{I}}^{+} + \overline{\boldsymbol{\sigma}}_{\mathrm{II}}^{+} + \overline{\boldsymbol{\sigma}}^{-}) = \frac{1}{2}\overline{\boldsymbol{\sigma}}^{-}:\mathbb{C}:\overline{\boldsymbol{\sigma}}^{-} \geq \mathbf{0} \tag{4.30}$$

Apparently, the nonnegativity of those three decomposed components of strain energy could be ensured from the above formulations.

4.3.3 Governing equation of the unified decomposition phase field model

In the governing equations of standard phase field model (see Eq.(4.2)), the crack energy release rate is assumed to be identical for tensile (mode I) fracture and shear (mode II) fracture. Nevertheless, it does not agree with the experimental observation where mode II fracture toughness is normally much larger than mode I fracture (Richard, Schramm et al. 2014, Wang, Wang et al. 2020). To capture the different mechanical properties between these two crack modes, we incorporate the *F*-function into the phase field framework (Zhang, Sloan et al. 2017). The governing equation of the phase field model Eq.(4.10) can then be rewritten as

$$\dot{d} = \begin{cases} \frac{1}{\omega}\langle 2(1-d)\left(\frac{H_{\mathrm{I}}}{G_t}+\frac{H_{\mathrm{II}}}{G_c}\right) - \frac{1}{l_c}\left(d - {l_c}^2\Delta d\right)\rangle_+ & d<1 \\ 0 & \text{otherwise} \end{cases} \tag{4.31}$$

Though the above formulation resembles the mixed-mode phase field model in (Zhang, Sloan et al. 2017), the novelty of this study lies in the strain energy decomposition, which depends on different stress states and shows much larger flexibility for capturing different crack modes. Moreover, to avoid the unrealistic fracture healing behaviour, the history variable Φ^h of *F*-function is introduced as the maximum *F*-function value during the whole loading process

$$\Phi^h = \max_{t\in(0,t_n]}\left(\frac{H_I(t)}{G_t}+\frac{H_{II}(t)}{G_c}\right) \tag{4.32}$$

where t_n represents the current time. Replacing the fracture driving force $\left(\frac{H_I(t)}{G_t}+\frac{H_{II}(t)}{G_c}\right)$ with Φ^h in Eq.(4.31) leads to the final governing equations of phase field evolution,

$$\dot{d} = \begin{cases} \frac{1}{\omega}\langle 2(1-d)\Phi^h - \frac{1}{l_c}\left(d - {l_c}^2\Delta d\right)\rangle_+ & d<1 \\ 0 & \text{otherwise} \end{cases} \tag{4.33}$$

4.3.4 Determination of the local coordinate system

4.3.4.1 Configuration of local coordinate system

In this study, the principal stress space is adopted as the reference coordinate system for simplicity. As depicted in Figure 4.3, the local coordinate system (LCS) is characterised by three mutually orthogonal axes ***r***, ***s*** and ***t***, which could be expressed in the principal stress as below,

$$\boldsymbol{r} = (\sin\alpha,\ \cos\alpha\cdot\cos\beta,\ \cos\alpha\cdot\sin\beta)^T \tag{4.34}$$

$$\boldsymbol{s} = (-\cos\alpha\cdot\sin\gamma,\ \sin\beta\cdot\cos\gamma+\sin\alpha\cdot\cos\beta\cdot\sin\gamma,\ -\cos\beta\cdot\cos\gamma+\sin\alpha\cdot\sin\beta\cdot\sin\gamma)^T \tag{4.35}$$

$$\boldsymbol{t} = (-\cos\alpha\cdot\cos\gamma,\ \sin\alpha\cdot\cos\beta\cdot\cos\gamma-\sin\beta\cdot\sin\gamma,\ \cos\beta\cdot\sin\gamma+\sin\alpha\cdot\sin\beta\cdot$$

$\cos\gamma)^T$ (4.36)

where $\alpha \in \left(-\frac{\pi}{2}, \frac{\pi}{2}\right]$ denotes the angle between $\boldsymbol{r}$ and its projection $\boldsymbol{r}'$ on $\boldsymbol{n}_2 - \boldsymbol{n}_3$ plane, and $\beta \in \left(-\frac{\pi}{2}, \frac{\pi}{2}\right]$ denotes the angle between $\boldsymbol{r}'$ and $\boldsymbol{n}_2$. For given parameters α and β, the direction $\boldsymbol{r}$ is specified, and the angular variable $\gamma \in \left(0, \frac{\pi}{2}\right]$ is then introduced to control the orientation of the remaining axes $\boldsymbol{s}$ and $\boldsymbol{t}$. As demonstrated in Figure 4.3, when γ is set as zero, direction $\boldsymbol{s}$ aligns vertical to $\boldsymbol{r}'$ within $\boldsymbol{n}_2$-$\boldsymbol{n}_3$ plane.

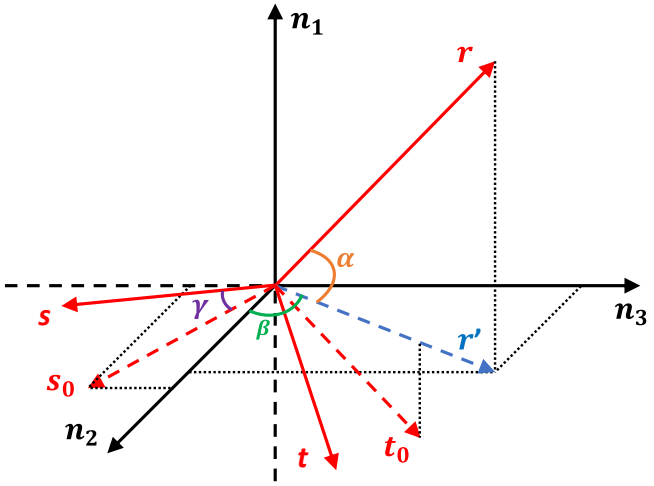

Figure 4.3 Local coordinate system in principle stress space

4.3.4.2 Modified F-criterion for determination of LCS

The *F*-criterion originates from the *G*-criterion (Cotterell and J.R.Rice 1980), where the crack initiates when the sum of the mode I crack energy release G_I and mode II crack energy release rate G_{II} exceeds the critical energy release rates G_{cr}, written as $\frac{G_I}{G_{cr}} + \frac{\mathrm{G}_{II}}{G_{cr}} \geq 1$. However, such criterion could not distinguish between the tensile and shear crack energy release rate.

The crack driving force, as defined by the *F*-function energy in this proposed phase field model, is intrinsically linked to the tensile strain energy H_I and shear strain energy H_{II}, both of which are contingent upon the selection of the LCS for a given stress state. This relationship underscores the sensitivity of *F*-function to the LCS orientation and is formulated as,

$$F(\alpha, \beta, \gamma) = \frac{H_I(\alpha,\beta,\gamma)}{\mathrm{G}_t} + \frac{H_{II}(\alpha,\beta,\gamma)}{\mathrm{G}_c} \tag{4.37}$$

Building upon prior research (Fei and Choo 2021, Steinke, Storm et al. 2022, Jiang, Li et al. 2023), we adopt the postulate that the potential LCS at the integration point is the one maximising its crack driving force, as quantified by the *F*-function energy. In the pursuit

of identifying the optimal LCS, a straightforward strategy initially involved optimising the *F*-function in terms of the three angular variables α, β and γ. This approach, however, unveiled a substantial complexity when directly incorporating them into the *F*-function expression. Alternatively, a novel methodology is proposed in this paper for searching the optimal *F*-function solution which focus on three normal stress on the LCS.

As indicated in Eq.(4.23), the sum of its decomposed strain energy components, tensile strain energy H_{I}, shear strain energy H_{II} and intact strain energy H_{n}, should be equal to the total strain energy φ_0^e. Then H_{II} could be expressed by,

$$H_{\mathrm{II}} = \varphi_0^e - H_{\mathrm{I}} - H_n \tag{4.38}$$

Substitution of Eq.(4.38) into Eq.(4.37) yields

$$F(\alpha,\beta,\gamma) = H_{\mathrm{I}}(\alpha,\beta,\gamma)\cdot\frac{\mathrm{G}_c-\mathrm{G}_t}{\mathrm{G}_t\cdot\mathrm{G}_c} - H_n(\alpha,\beta,\gamma)\cdot\frac{1}{\mathrm{G}_c} + \varphi_0^e\cdot\frac{1}{\mathrm{G}_c} \tag{4.39}$$

In this *F*-function, only H_I and H_n are involved, both of which only depend on the three decomposed normal stresses $\bar{\sigma}_{rr}$, $\bar{\sigma}_{ss}$ and $\bar{\sigma}_{tt}$. For a given stress state, these three normal stresses are related by,

$$\bar{\sigma}_{tt} = 3p - \bar{\sigma}_{rr} - \bar{\sigma}_{ss} \tag{4.40}$$

where $p = \frac{1}{3}(\sigma_1 + \sigma_2 + \sigma_3)$ denotes the hydrostatic pressure. Eq.(4.39) can be rewritten in terms of $\bar{\sigma}_{rr}$ and $\bar{\sigma}_{ss}$ as

$$F(\bar{\sigma}_{rr},\bar{\sigma}_{ss}) = H_I(\bar{\sigma}_{rr},\bar{\sigma}_{ss})\cdot\frac{\mathrm{G}_c-\mathrm{G}_t}{\mathrm{G}_t\cdot\mathrm{G}_c} - H_c(\bar{\sigma}_{rr},\bar{\sigma}_{ss})\cdot\frac{1}{\mathrm{G}_c} + \varphi_0^e\cdot\frac{1}{\mathrm{G}_c} \tag{4.41}$$

Consequently, our objective is then to maximise *F*-function with proper selection $\bar{\sigma}_{rr}$ and $\bar{\sigma}_{ss}$.

According to Eq.(4.21), the projected tensile/compressive components of normal stress are summarised in Table 4.1. There exist as much as four decomposition types for a given stress state, which depends on the value of $\bar{\sigma}_{rr}$, $\bar{\sigma}_{ss}$ and $\bar{\sigma}_{tt}$. The conditions for achieving these four decomposition types are listed in Table 4.1, and the corresponding results of *F*-function are denoted by F_1, F_2, F_3 and F_4 respectively, written by

$$F_1 = -\frac{1+\nu}{E\cdot G_c}\left[\bar{\sigma}_{rr}{}^2 + \bar{\sigma}_{ss}{}^2 + \bar{\sigma}_{rr}\cdot\bar{\sigma}_{ss} - 3p(\bar{\sigma}_{rr}+\bar{\sigma}_{ss})\right] - \frac{9p^2}{2E\cdot G_c} \tag{4.42}$$

$$F_2 = \frac{\bar{\sigma}_{rr}{}^2(1+\nu)(1-2\upsilon)}{2EG_t(1-\upsilon)} - \frac{1+\nu}{EG_c}\left[\bar{\sigma}_{rr}{}^2 + \bar{\sigma}_{ss}{}^2 + \bar{\sigma}_{rr}\cdot\bar{\sigma}_{ss} - 3p(\bar{\sigma}_{rr}+\bar{\sigma}_{ss})\right] - \frac{9p^2}{2EG_c} \tag{4.43}$$

$$F_3 = \frac{(1+\nu)\cdot[G_c(1-\nu)-2G_t]}{2EG_cG_t}\cdot\left(\bar{\sigma}_{rr}{}^2 + \bar{\sigma}_{ss}{}^2\right) - \frac{(1+\nu)\cdot(\nu G_c+G_t)}{EG_cG_t}\bar{\sigma}_{rr}\bar{\sigma}_{ss} + \frac{(1+\nu)3p}{EG_c}\cdot(\bar{\sigma}_{rr} + \bar{\sigma}_{ss})\frac{9p^2}{2E\cdot G_c} \tag{4.44}$$

$$F_4 = \frac{(G_c - G_t)(1+\nu)}{EG_cG_t}\left[\bar{\sigma}_{rr}{}^2 + \bar{\sigma}_{ss}{}^2 + \bar{\sigma}_{rr}\cdot\bar{\sigma}_{ss} - 3p(\bar{\sigma}_{rr}+\bar{\sigma}_{ss})\right] + \frac{9p^2(G_c-G_t)}{2EG_cG_t} \quad (4.45)$$

It is necessary to emphasise that though Eqs.(4.42)-(4.45) have different formulations for each decomposition type, these four functions are continuous within the global domain of $\bar{\sigma}_{rr}$ and $\bar{\sigma}_{ss}$, which results from the continuous definition of the tensile stress $\overline{\boldsymbol{\sigma}}_{\mathrm{I}}^{+}$ and compressive stress $\overline{\boldsymbol{\sigma}}^{-}$ in Eq.(4.21).

Table 4.1 Possible value of decomposed tension stress and compression stress

Type	Conditions	$\boldsymbol{\sigma}_r^+$	$\boldsymbol{\sigma}_r^-$	$\boldsymbol{\sigma}_s^+$	$\boldsymbol{\sigma}_s^-$	$\boldsymbol{\sigma}_t^+$	$\boldsymbol{\sigma}_t^-$
1	$\bar{\sigma}_{rr} \le 0$	0	$\bar{\sigma}_{rr}$	0	$\bar{\sigma}_{ss}$	0	$3p - \bar{\sigma}_{rr} - \bar{\sigma}_{ss}$
2	$\bar{\sigma}_{rr} > 0$ and $\bar{\sigma}_{ss} - \frac{\nu\cdot\bar{\sigma}_{rr}}{1-\nu} \le 0$	$\bar{\sigma}_{rr}$	0	$\frac{\nu\cdot\bar{\sigma}_{rr}}{1-\nu}$	$\bar{\sigma}_{ss} - \frac{\nu\cdot\bar{\sigma}_{rr}}{1-\nu}$	$\frac{\nu\cdot\bar{\sigma}_{rr}}{1-\nu}$	$3p - \frac{\bar{\sigma}_{rr}}{1-\nu} - \bar{\sigma}_{ss}$
3	$\bar{\sigma}_{rr} > 0,\ \bar{\sigma}_{ss} - \frac{\nu\cdot\bar{\sigma}_{rr}}{1-\nu} > 0$, and $\bar{\sigma}_{rr} + \bar{\sigma}_{ss} - \frac{3p}{1+\nu} \ge 0$	$\bar{\sigma}_{rr}$	0	$\bar{\sigma}_{ss}$	0	$\nu\cdot(\bar{\sigma}_{rr}+\bar{\sigma}_{ss})$	$3p - (\nu+1)\cdot(\bar{\sigma}_{rr}+\bar{\sigma}_{ss})$
4	$\bar{\sigma}_{rr} > 0,\ \bar{\sigma}_{ss} - \frac{\nu\cdot\bar{\sigma}_{rr}}{1-\nu} > 0$, and $\bar{\sigma}_{rr} + \bar{\sigma}_{ss} - \frac{3p}{1+\nu} < 0$	$\bar{\sigma}_{rr}$	0	$\bar{\sigma}_{ss}$	0	$3p - \bar{\sigma}_{rr} - \bar{\sigma}_{ss}$	0

4.3.4.3 Definition domain of $\bar{\sigma}_{rr}$ and $\bar{\sigma}_{ss}$

Under the principal stress space, the matrix form of elastic strain and undamaged stress tensor $\overline{\boldsymbol{\sigma}}$ are written as follows:

$$\boldsymbol{\varepsilon}^{\mathrm{e}} = \frac{1}{E}\cdot\begin{bmatrix}\sigma_1 - \nu(\sigma_2+\sigma_3) & 0 & 0\\ 0 & \sigma_2 - \nu(\sigma_1+\sigma_3) & 0\\ 0 & 0 & \sigma_3 - \nu(\sigma_1+\sigma_2)\end{bmatrix} \quad (4.46)$$

$$\overline{\boldsymbol{\sigma}} = \begin{bmatrix}\sigma_1 & 0 & 0\\ 0 & \sigma_2 & 0\\ 0 & 0 & \sigma_3\end{bmatrix} \quad (4.47)$$

where σ_1, σ_2 and σ_3 represent the three principal stresses. The normal effective stress of $\bar{\sigma}_{rr}$ and $\bar{\sigma}_{ss}$ then could be calculated by substituting Eqs.(4.16), (4.34)-(4.36), and (4.47) into Eq.(4.17), as follows,

$$\bar{\sigma}_{rr} = \sigma_1\cdot sin^2\alpha + \sigma_2\cdot cos^2\alpha\cdot cos^2\beta + \sigma_3\cdot cos^2\alpha\cdot sin^2\beta \quad (4.48)$$

$$\bar{\sigma}_{ss} = \sigma_1\cdot cos^2\alpha\cdot sin^2\gamma + \sigma_2\cdot(sin\beta\cdot cos\gamma + sin\alpha\cdot cos\beta\cdot sin\gamma)^2 + \sigma_3\cdot(sin\alpha\cdot sin\beta\cdot sin\gamma - cos\beta\cdot cos\gamma)^2 \quad (4.49)$$

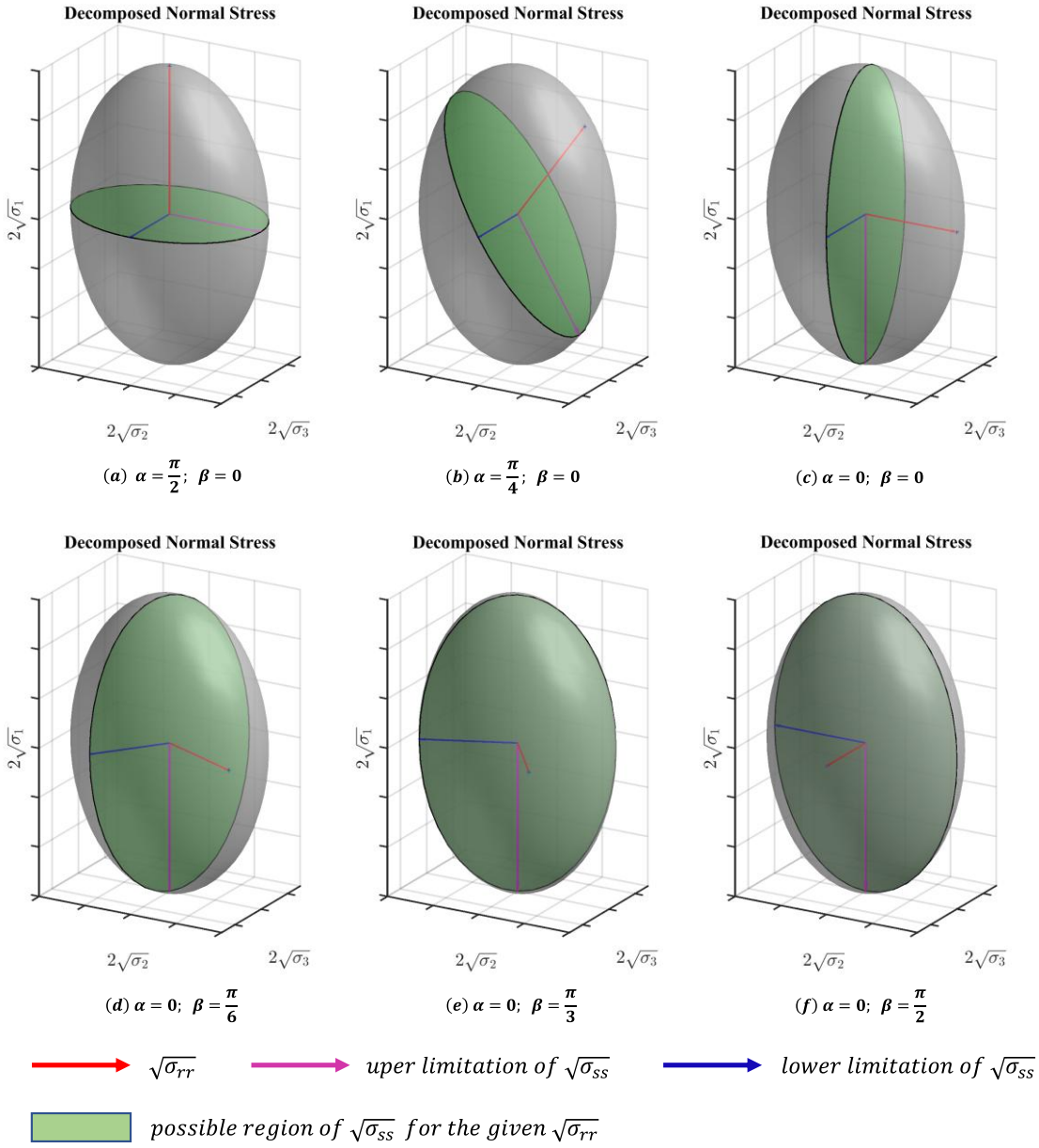

Figure 4.4 The value of $\bar{\sigma}_{rr}$ and $\bar{\sigma}_{ss}$ change with different decomposition directions

Analysis of Eqs.(4.48) and (4.49) reveals that the behaviour of $\bar{\sigma}_{rr}$ and $\bar{\sigma}_{ss}$ can be analogised to an elliptical curve, as demonstrated in Figure 4.4, the three principal axes of which are $2\sqrt{\sigma_1}$, $2\sqrt{\sigma_2}$ and $2\sqrt{\sigma_3}$, respectively. $\bar{\sigma}_{rr}$ and $\bar{\sigma}_{ss}$ can be calculated as the square of the distance from ellipse centre to its surface along the direction $\boldsymbol{r}$ and $\boldsymbol{s}$, which are controlled by angular variable α and β.

As shown in Figure 4.4(a-c), when β is fixed at zero, and α changes from $\frac{\pi}{2}$ to zero, the value of $\bar{\sigma}_{rr}$ changes from σ_1 to σ_2; while the lower limit of $\bar{\sigma}_{ss}$ keeps constant, and the upper limit of $\bar{\sigma}_{ss}$ increases from σ_2 to σ_1; Meanwhile, when α is fixed at zero, and β changes from 0 to $\frac{\pi}{2}$, as shown in Figure 4.4(c-f), the value of $\bar{\sigma}_{rr}$ changes from σ_2 to σ_3,

while the lower limit of $\bar{\sigma}_{ss}$ increases from σ_2 to σ_1, and the upper limit of $\bar{\sigma}_{ss}$ keeps constant at σ_1. Accordingly, the definition domain of $\bar{\sigma}_{rr}$ and $\bar{\sigma}_{ss}$ could be written by

$$\begin{cases} \sigma_2 \le \bar{\sigma}_{ss} \le \sigma_1 + \sigma_2 - \bar{\sigma}_{rr} & when\ \bar{\sigma}_{rr} \ge \sigma_2 \\ \sigma_2 + \sigma_3 - \bar{\sigma}_{rr} \le \bar{\sigma}_{ss} \le \sigma_1 & when\ \bar{\sigma}_{rr} \le \sigma_2 \\ \bar{\sigma}_{rr} \ge \bar{\sigma}_{ss} \ge \bar{\sigma}_{tt} = 3p - \bar{\sigma}_{rr} - \bar{\sigma}_{ss} \end{cases} \tag{4.50}$$

In Eq.(4.50), the last constraint is added for achieving unique sequence of *r*, *s* and *t*. Consequently, the blue shaded area in Figure 4.5 illustrates the final definition region for $\bar{\sigma}_{rr}$ and $\bar{\sigma}_{ss}$. It's noted that the previous statements are described assuming a sort of ellipse, which implies that involved three principal stresses are positive. Nevertheless, those insight remain effective even with negative principal stresses, which can be derived directly from Eqs.(4.48) and (4.49). The above interpretation is provided to assist the reader in better understanding this concept.

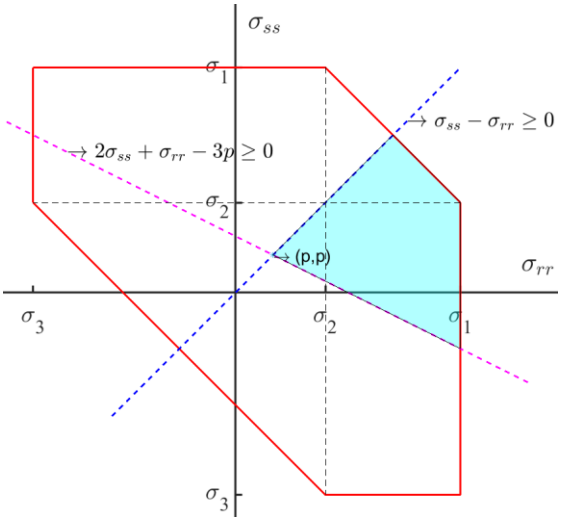

Figure 4.5 Definition domain of decomposed normal stress $\bar{\sigma}_{rr}$ and $\bar{\sigma}_{ss}$

4.3.4.4 Solution for maximum F-criterion value

For a specific stress state (the three principal stresses σ_1, σ_2, and σ_3 have been given), the decomposition type and *F*-function formulation depend only on the value of normal stress $\bar{\sigma}_{rr}$ and $\bar{\sigma}_{ss}$, as discussed in Section 4.3.4.2. In this section, the *F*-function under different stress states is discussed case by case for solving its theoretical maximum value. Figure 4.6 and Figure 4.7 depictured the distribution of decomposition type in terms of normal stress $\bar{\sigma}_{rr}$ and $\bar{\sigma}_{ss}$ under distinct stress states. Apparently, given a specific stress state identified by the three principal stresses, the normal stresses $\bar{\sigma}_{rr}$ and $\bar{\sigma}_{ss}$ could be determined by the selection of local coordinate system (LCS). For example, when the LCS is identical to the principal stress directions, the normal stresses are equal to the

principal stresses. Under each potential selection of LCS, the normal stress is determined, and therefore the decomposition type will be also specified.

Since the formulations of F-function for four different decomposition type in Eqs.(4.42)-(4.45) are all simple second-order polynomial functions in terms of $\bar{\sigma}_{rr}$ and $\bar{\sigma}_{ss}$, it is easy to obtain their maximum value within corresponding subdomain. By comparing them, the overall maximum F-function across the entire definition domain is finally determined.

The final results of potential optimal solutions of $\bar{\sigma}_{rr}$ and $\bar{\sigma}_{ss}$ to achieve the maximum F-function are summarized in Table 4.2. It is interesting to find that this proposed unified decomposition phase field model could recaster to several common-adopted energy split approaches under specific stress states. For example, when hydrostatic pressure $p \leq 0$, one potential solution for type I region is $\bar{\sigma}_{rr} = p$, $\bar{\sigma}_{rr} = p$, which represents the Volume-Deviatoric decomposition (Amor, Marigo et al. 2009); and when $p > 0$ and $\frac{\nu}{1-\nu} \leq \frac{\sigma_3}{\sigma_1+\sigma_2-\sigma_3}$, the optimal solution is given as $\bar{\sigma}_{rr} = \sigma_1$, $\bar{\sigma}_{ss} = \sigma_2$, which denotes the spectral decomposition(Miehe, Hofacker et al. 2010, Miehe, Welschinger et al. 2010). In addition, the solution of $\bar{\sigma}_{rr} = \sigma_1$, $\bar{\sigma}_{ss} = 0$ will be obtained for uniaxial tension loading. This result will lead to the decomposed tensile stress of $\sigma_r^+ = \sigma_1$, $\sigma_s^+ = \sigma_t^+ = \frac{\upsilon\sigma_1}{1-\upsilon}$, which keeps consistent with the directional-based strain energy decomposition approach proposed in (Steinke and Kaliske 2018, Steinke, Storm et al. 2022).

The potential solutions listed in Table 4.2 also reveal the competition between tensile and shear energy dissipation to some extent. For example, when $p \leq 0$, and $\frac{\nu}{1-\nu} \geq \frac{\sigma_2}{\sigma_1}$, the potential solution is $\bar{\sigma}_{rr} = p$, $\bar{\sigma}_{ss} = p$ for type I region, and $\bar{\sigma}_{rr} = \sigma_1$, $\bar{\sigma}_{ss} = \frac{\sigma_2+\sigma_3}{2}$ for type II region. The maximin F-function energy for those two regions F_1^{max} and F_2^{max} essentially reflect the shear and tensile strain energy dissipation respectively, written as

$$F_1^{max} = -\frac{(1-2\nu)(\sigma_1+\sigma_2+\sigma_3)^2}{6EG_c} \tag{4.51}$$

$$F_2^{max} = \frac{2(1-\nu-2\nu^2){\sigma_1}^2}{4EG_t(1-\nu)} - \frac{2{\sigma_1}^2-4\nu\sigma_1(\sigma_2+\sigma_3)+(1-\nu)(\sigma_2+\sigma_3)^2}{4EG_c} \tag{4.52}$$

The final configuration of LCS then is determined for choosing the larger energy dissipation between F_1^{max} and F_2^{max}. Comparing Eq.(4.51) and Eq.(4.52), we could conclude that

$$\begin{cases} F_1^{max} \geq F_2^{max} & when\ \frac{G_c}{G_t} \leq \frac{(2\sigma_1-\sigma_2-\sigma_3)^2}{6{\sigma_1}^2} \cdot \frac{1-\upsilon}{1-2\upsilon} \\ F_1^{max} < F_2^{max} & otherwise \end{cases} \tag{4.53}$$

It can be seen from Eq.(4.53) that this competition between tensile and shear energy dissipation is related not only to the stress state but also depends on the ratio of shear and tensile energy release rate as well as the Poison's ratio simultaneously.

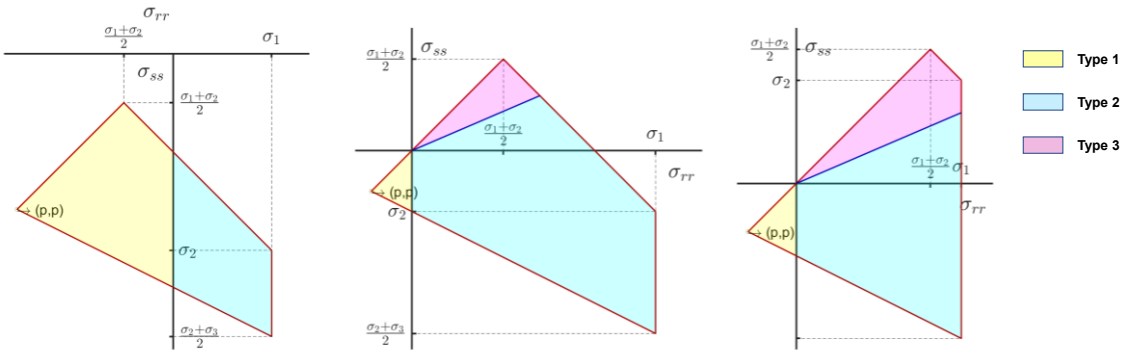

(a) $\frac{\sigma_2}{\sigma_1} \leq -1$ (b) $-1 < \frac{\sigma_2}{\sigma_1} \leq \frac{v}{1-v}$ (c) $\frac{\sigma_2}{\sigma_1} > \frac{v}{1-v}$

Figure 4.6 Decomposition type distribution on the definition domain of normal stresses for different stress states with hydrostatic pressure p≤0

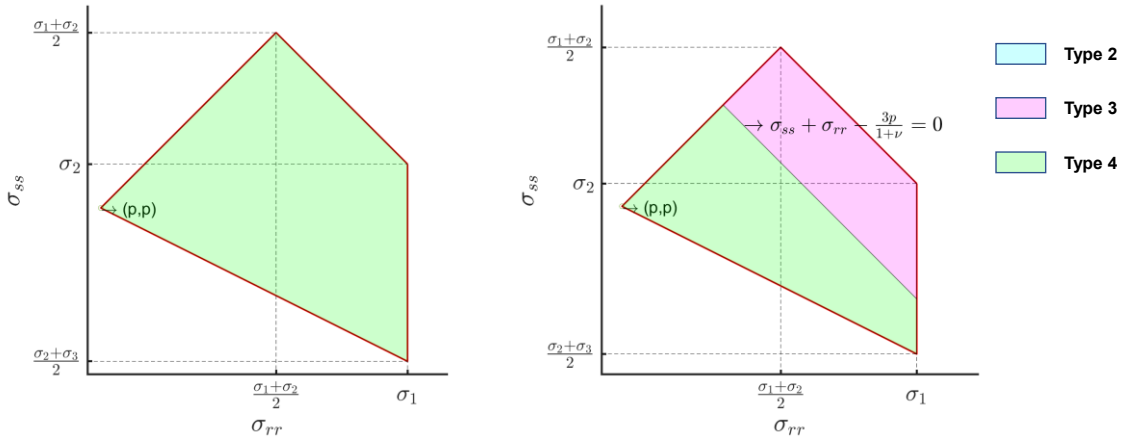

(a) $\frac{v}{1-v} \leq \frac{\sigma_3}{\sigma_1+\sigma_2-\sigma_3}$ (b) $\frac{\sigma_3}{\sigma_1+\sigma_2-\sigma_3} < \frac{v}{1-v} \leq \frac{\sigma_2+\sigma_3}{2\sigma_1}$

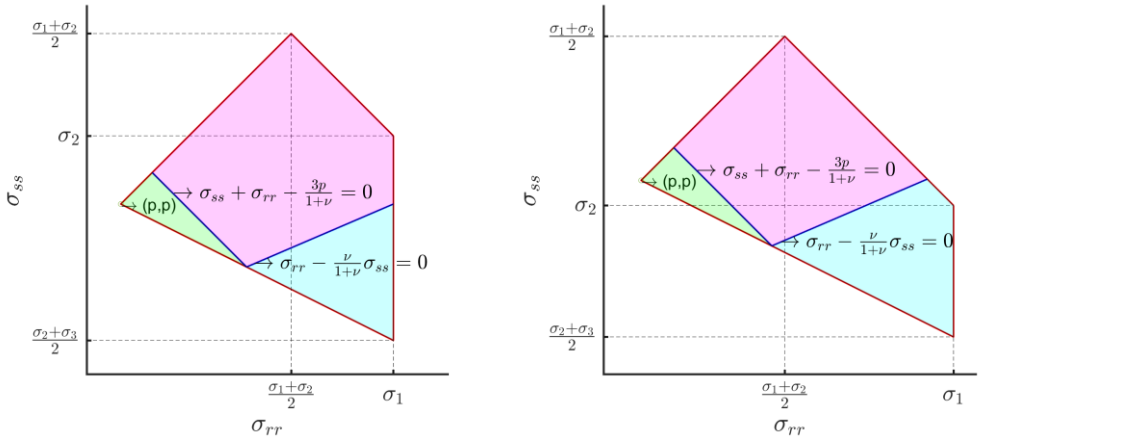

(c) $\frac{\sigma_2+\sigma_3}{2\sigma_1} < \frac{v}{1-v} \leq \frac{\sigma_2}{\sigma_1}$ (d) $\frac{v}{1-v} > \frac{\sigma_2}{\sigma_1}$

Figure 4.7 Decomposition type distribution on the definition domain of normal stresses for different stress states with hydrostatic pressure p>0

4.3.4.5 Update of local coordinate configuration

To update the LCS, two conditions must be satisfied in this study. Firstly, the *F*-function value needs to exceed the history *F*-function variable Φ^h, which prevents altering of the coordinate configuration during unloading.

Secondly, the material on the original weak surface needs to keep stable when new crack surface is generated. This concept of stability can be explained by Figure 4.8, where a solid was loaded by tension force with changed directions. It was firstly loaded vertically, producing a horizontal weak surface $\boldsymbol{r_0}$ with damage variable *d*. Then, the loading direction changed to be along the 45 degree. Under the new stress condition, the potential weak surface $\boldsymbol{r}$ is along the -45 degree. Nevertheless, to ensure the development of this new weak surface, on the one hand, tension stress on the potential weak surface $\boldsymbol{r}$ needs to exceed the undamaged material strength; one the other hand, the remained material strength on surface $\boldsymbol{r_0}$ has to sustain the current stress loading. Otherwise, the damage will continue to develop on the original weak surface $\boldsymbol{r_0}$. It is noted that the above interpretation only considers simple tension stress. To achieve compatibility for complex loading conditions of this model, a unified stress formulation (Zhang and Eckert 2005) is incorporated to indicate the unified stress along arbitrary directions at one material point, written as

$$h_s = \frac{\langle \bar{\sigma}_{rr} \rangle_+}{f_{ht}} + \frac{\sqrt{{\bar{\sigma}_{rs}}^2 + {\bar{\sigma}_{rt}}^2}}{f_{hc}} \tag{4.54}$$

where $\bar{\sigma}_{rr}$ represents the normal stress; $\bar{\sigma}_{rs}$ and $\bar{\sigma}_{rt}$ denote the two shear stress components. To ensure the updating of the crack surface, the following condition should be catered

$$\frac{h_s^{\boldsymbol{r}}}{strength^{\boldsymbol{r}}} > \frac{h_s^{\boldsymbol{r}_0}}{strength^{\boldsymbol{r}_0}} \tag{4.55}$$

where $h_s^{\boldsymbol{r}}$ and $h_s^{\boldsymbol{r}_0}$ represent the unified stress on the current potential crack surface $\boldsymbol{r}$ and the and original weak surface $\boldsymbol{r}_0$; and $strength^{\boldsymbol{r}}$ and $strength^{\boldsymbol{r}_0}$ represent the corresponding material strength on those two surfaces. For simplification, here we assume that the material strength on surface $\boldsymbol{r}_0$ is degraded by the phase field damage as below,

$$strength^{\boldsymbol{r}_0} = (1-d)^2 strength^{\boldsymbol{r}} \tag{4.56}$$

Substitution of Eq.(4.56) into Eq.(4.55) lead to the second constraint for the updating of local coordinate system as,

$$(1-d)^2 h_s^r > h_s^{r_0} \tag{4.57}$$

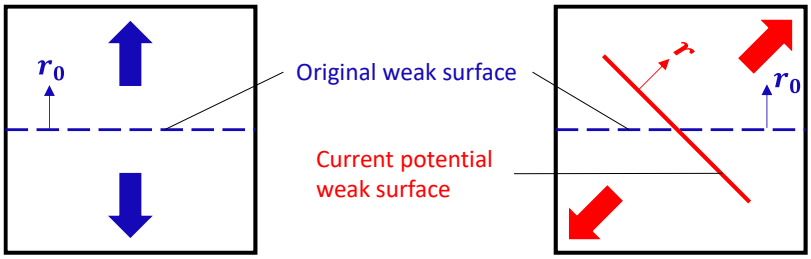

Figure 4.8 Configuration of local coordinate system altering under tension loading

Table 4.2 Possible solutions of σ_{rr} and σ_{ss} for achieving maximum value of the F function under different stress states

No	Conditions	Additional condition	σ_{rr}	σ_{ss}	Type
1	$p \le 0, and\ \frac{\nu}{1-\nu} \ge \frac{\sigma_2}{\sigma_1}$		p	p	I
			σ_1	$\frac{\sigma_2+\sigma_3}{2}$	II
2	$p \le 0, and\ \frac{\nu}{1-\nu} < \frac{\sigma_2}{\sigma_1}$		p	p	I
			σ_1	$\frac{\sigma_2+\sigma_3}{2}$	II
			σ_1	σ_2	III
3	$p > 0, and\ \frac{\nu}{1-\nu} \le \frac{\sigma_3}{\sigma_1+\sigma_2-\sigma_3}$		σ_1	σ_2	IV
4	$p > 0, and$ $\frac{\sigma_3}{\sigma_1+\sigma_2-\sigma_3} < \frac{\nu}{1-\nu} \le \frac{\sigma_2+\sigma_3}{2\sigma_1}$	$\frac{G_c}{G_t} \ge \frac{\sigma_2-\sigma_3}{\sigma_2(1-\upsilon)-\upsilon\sigma_1}$	σ_1	σ_2	III
		$\frac{G_c}{G_t} < \frac{\sigma_2-\sigma_3}{\sigma_2(1-\upsilon)-\upsilon\sigma_1}$	σ_1	$\frac{G_t(\sigma_2+\sigma_3)-G_c\upsilon\sigma_1}{2G_t-G_c(1-\upsilon)}$	III
5	$p > 0, and\ \frac{\sigma_2+\sigma_3}{2\sigma_1} < \frac{\nu}{1-\nu} \le \frac{\sigma_2}{\sigma_1}$	$\frac{G_c}{G_t} \ge \frac{(2\sigma_1-\sigma_2-\sigma_3)(1-\nu)}{2\sigma_1(1-2\nu)}$	σ_1	σ_2	III
			σ_1	$\frac{\sigma_2+\sigma_3}{2}$	II
		$\frac{G_c}{G_t} < \frac{(2\sigma_1-\sigma_2-\sigma_3)(1-\nu)}{2\sigma_1(1-2\nu)}$	σ_1	σ_2	III
			$\frac{3pG_t(1-\nu)}{3G_t(1-\nu)-2G_c(1-2\nu)}$	$\frac{3p[G_t(1-\nu)-G_c(1-2\nu)]}{3G_t(1-\nu)-2G_c(1-2\nu)}$	II
6	$p > 0, and\ \frac{\nu}{1-\nu} > \frac{\sigma_2}{\sigma_1}$	$\frac{G_c}{G_t} \ge \frac{(2\sigma_1-\sigma_2-\sigma_3)(1-\nu)}{2\sigma_1(1-2\nu)}$	σ_1	$\frac{\sigma_2+\sigma_3}{2}$	II
		$\frac{G_c}{G_t} < \frac{(2\sigma_1-\sigma_2-\sigma_3)(1-\nu)}{2\sigma_1(1-2\nu)}$	$\frac{3pG_t(1-\nu)}{3G_t(1-\nu)-2G_c(1-2\nu)}$	$\frac{3p[G_t(1-\nu)-G_c(1-2\nu)]}{3G_t(1-\nu)-2G_c(1-2\nu)}$	II

4.4 Numerical implementation

In this proposed unified phase field model, the strain energy decomposition depends on the local coordinate system, which changes with stress states. Hence, implicit implementation of such complex formulation may be numerically impossible due to the significant challenge of calculating the consistent stiffness matrix for stress updating. To avoid the convergence challenges, here we adopt the explicit algorithm for the model implementation. With the governing equations of Eq.(4.9) and Eq.(4.33) for both displacement and phase field evolution in hand, we utilise the ABAQUS user subroutine VUEL and VUMAT to implemented the proposed unified phase field model explicitly with a staggered strategy. In VUMAT, the local coordinate system is determined according to the current stress state. Subsequently, the effective stress is decomposed on that local coordinate system, based on which the effective stress is decomposed and nominal stress response is calculated with the phase field variable from VUEL. Lastly, fracture driving force Φ^h is calculated and passed to the VUEL at the end of this current increment. In VUEL, the velocity of phase field evolution is simply calculated according to Eq.(4.33).

4.4.1 Spatial discrete for phase field and displacement variable

In this study, the given body Ω is discretised by the hexahedral elements, and then the displacement field and phase field viable are approximated with the shape function as follows,

$$\boldsymbol{u}^e(\boldsymbol{x},t) = \sum_{i=1}^{nnode} N_{u_i}^{\ e}(x) \cdot \boldsymbol{u}_i^e \tag{4.58a}$$

$$d^e(\boldsymbol{x},t) = \sum_{i=1}^{nnode} N_{d_i}^{\ e}(x) \cdot d_i^e \tag{4.58b}$$

where $\boldsymbol{u}^e(\boldsymbol{x},t)$ and $d^e(\boldsymbol{x},t)$ represent the displacement and phase field variable at the $\boldsymbol{x}$ position of the *e*-th element for the current time t; $nnode$ denotes the total number of the element nodes; $\boldsymbol{u}_i^e$ and d_i^e denote displacement and phase field variable at the i-th node; $N_{u_i}^{\ e}(x)$ and $N_{d_i}^{\ e}(x)$ represent shape functions of the *i*-th node for displacement and phase field interpolation respectively. Correspondingly, the displacement acceleration and phase field evolution velocity could be obtained

$$\ddot{\boldsymbol{u}}^e(\boldsymbol{x},t) = \sum_{i=1}^{nnode} N_{u_i}^{\ e}(x) \cdot \ddot{\boldsymbol{u}}_i^e \tag{4.59a}$$

$$\dot{d}^e(\boldsymbol{x},t) = \sum_{i=1}^{nnode} N_{d_i}^{\ r}(x) \cdot \dot{d}_i^e \tag{4.59b}$$

With the discretised displacement and phase field in hand, the weak form of governing

equations of Eq.(4.8) and Eq.(4.10) could be rewritten as

$$\boldsymbol{M}\ddot{\boldsymbol{u}}^N = \boldsymbol{P}^{ext} - \boldsymbol{P}^{int} \tag{4.60}$$

$$\boldsymbol{C}\dot{\boldsymbol{d}}^N = \boldsymbol{Y}\left(\Phi^h, d\right) \tag{4.61}$$

where the $\boldsymbol{u}^N$ and $\boldsymbol{d}^N$ are the basic variables in this coupled displacement-phase field problem, which represent the displacement and phase field value at all nodes within Ω. The mass matrix $\boldsymbol{M}$, external force vector $\boldsymbol{P}^{ext}$, internal force vector $\boldsymbol{P}^{int}$, viscosity matrix $\boldsymbol{C}$, and the phase field residual force $\boldsymbol{Y}$ are written as below,

$$\boldsymbol{M} = \underset{e=1}{\overset{N_e}{\boldsymbol{A}}} \int_{\Omega^e} \rho \boldsymbol{N}_u{}^e(\boldsymbol{x})^T \boldsymbol{N}_u{}^e(\boldsymbol{x}) \mathrm{d}V \tag{4.62}$$

$$\boldsymbol{P}^{ext} = \underset{e=1}{\overset{N_e}{\boldsymbol{A}}} \left\{ \int_{\Omega^e} \boldsymbol{N}_u{}^e(\boldsymbol{x})^T \boldsymbol{b} \mathrm{d}V \right\} + \underset{e=1}{\overset{N_e^t}{\boldsymbol{A}}} \left\{ \int_{\partial\Omega^e} \boldsymbol{N}_u{}^e(\boldsymbol{x})^T \boldsymbol{t} \mathrm{d}S \right\} \tag{4.63}$$

$$\boldsymbol{P}^{int} = \underset{e=1}{\overset{N_e}{\boldsymbol{A}}} \int_{\Omega^e} \boldsymbol{B}_u{}^e(\boldsymbol{x})^T \boldsymbol{\sigma} \mathrm{d}V \tag{4.64}$$

$$\boldsymbol{C} = \underset{e=1}{\overset{N_e}{\boldsymbol{A}}} \int_{\Omega^e} \eta \boldsymbol{N}_d{}^e(\boldsymbol{x})^T \boldsymbol{N}_d{}^e(\boldsymbol{x}) \mathrm{d}V \tag{4.65}$$

$$\boldsymbol{Y} = -\underset{e=1}{\overset{N_e}{\boldsymbol{A}}} \int_{\Omega^e} \left\{ \left[\frac{d}{l_c} - 2(1-d)\Phi^h \right] \boldsymbol{N}_d{}^e(\boldsymbol{x})^T d + l_c \boldsymbol{B}_d{}^e(\boldsymbol{x})^T \nabla d \right\} \mathrm{d}V \tag{4.66}$$

where N_e denotes the total number of elements; N_e^t is the number of elements with boundary surface; operator $\underset{e=1}{\overset{N_e}{\boldsymbol{A}}}$ represents assembling the matrix or vector for global nodes from the integration within each element. $\boldsymbol{B}_u{}^e(\boldsymbol{x})$ and $\boldsymbol{B}_d{}^e(\boldsymbol{x})$ represent space gradient of the shape for the displacement and phase field at position $\boldsymbol{x}$ in the e-th element.

4.4.2 Time-discrete scheme

The aforementioned equations will be resolved through explicit integration strategy applied to both the stress update and the evolution of phase field. Referring to the previous study (Wang, Ye et al. 2020, Hu, Tan et al. 2023), two time-discrete strategies, the central difference method and forward difference method are adopted for solving the displacement and phase field evolution respectively. For the displacement integration, it could be solved as follows

$$\ddot{\boldsymbol{u}}^k(\boldsymbol{t}_\mathrm{n}) = \boldsymbol{M}^{-1} \cdot (\boldsymbol{P}^{ext} - \boldsymbol{P}^{int}) \tag{4.67}$$

$$\dot{\boldsymbol{u}}^k\left(\tfrac{t_\mathrm{n}+t_{\mathrm{n}+1}}{2}\right) = \dot{\boldsymbol{u}}^k\left(\tfrac{t_{\mathrm{n}-1}+t_\mathrm{n}}{2}\right) + \ddot{\boldsymbol{u}}^k(t_\mathrm{n}) \cdot \tfrac{t_{\mathrm{n}+1}-t_{\mathrm{n}-1}}{2} \tag{4.68}$$

$$\boldsymbol{u}^k(t_{\mathrm{n}+1}) = \boldsymbol{u}^k(t_\mathrm{n}) + \dot{\boldsymbol{u}}^k\left(\tfrac{t_\mathrm{n}+t_{\mathrm{n}+1}}{2}\right) \cdot (t_{\mathrm{n}+1} - t_\mathrm{n}) \tag{4.69}$$

where $\ddot{\boldsymbol{u}}^k(t_\mathrm{n})$, $\dot{\boldsymbol{u}}^k(t_\mathrm{n})$ and $\boldsymbol{u}^k(t_\mathrm{n})$ represent the acceleration, velocity and displacement

of kth node at time of n-th increment t_{n}. Meanwhile, special treatments are required for the initial time integration, which are written as

$$\dot{\boldsymbol{u}}^k\left(\frac{t_0+t_1}{2}\right) = \dot{\boldsymbol{u}}^k(t_0) + \ddot{\boldsymbol{u}}^k(t_{\mathrm{n}}) \cdot \frac{t_1}{2} \tag{4.70}$$

$$\boldsymbol{u}^k(t_1) = \boldsymbol{u}^k(t_0) + \dot{\boldsymbol{u}}^k\left(\frac{t_0+t_1}{2}\right) \cdot (t_1 - t_0) \tag{4.71}$$

For the phase field evolution, it could be integrated by

$$\dot{d}^k(t_{\mathrm{n}}) = \boldsymbol{C^{-1}} \cdot \boldsymbol{Y} \tag{4.72}$$

$$d^k(t_{\mathrm{n+1}}) = d^k(t_{\mathrm{n}}) + \dot{d}^k(t_{\mathrm{n}}) \cdot (t_{\mathrm{n+1}} - t_{\mathrm{n}}) \tag{4.73}$$

where $d^k(t_{\mathrm{n}})$ and $\dot{d}^k(t_{\mathrm{n}})$ represent the phase field variable and its velocity at kth node at t_{n}.

4.5 Numerical Examples

In this section, the numerical implantations of phase field models are validated by comparing the numerical outcomes of the single-element example under uniaxial tension and biaxial tension with the corresponding theoretical solution. Afterwards, the effectiveness of the proposed unified phase field model is demonstrated by comparing its simulation results with other three decomposition strategies of a series of numerical examples, including dogbone tension/compression, perforated asymmetric bending, and triaxial compression test on the pre-cracked cylinder, which cover uniaxial tension, uniaxial compression, tension-shear, compression-shear loading conditions. Among them, the experimental observation of the last example is also demonstrated for the comparison with the numerical results.

4.5.1 One element validation

In this one-element test, we firstly derive the analytical solutions for the isotropic and UNIFIED phase field models under uniaxial tension and biaxial tension loading condition. Next, the numerical modelling with a series of viscosity parameter η are conducted, the simulation results of which are compared with the analytical solutions for validating the numerical implementation. Lastly, we perform cyclic loading tests on four different phase field models (isotropic, spectral, V-D, and UNIFIED) and compare their results. The parameters used in the single-element test are detailed in Table 4.3.

Table 4.3 model parameters for one element validation

Type	Parameters	Value
elastic	Elastic modulus E	2100000 MPa
	Poison's ratio υ	0.3
Damage	Tensile crack energy release rate G_t	5 N/mm
	Shear crack energy release rate G_c	30 N/mm
	Length scale l_c	1 mm

4.5.1.1 Uniaxial tension

The homogeneous formulation of phase field evolution can be derived by ignoring the gradient term in the phase field governing equation of Eq.(4.31), which is written as

$$d = \frac{2\mathcal{H}l_c}{2\mathcal{H}l_c+G_t} \tag{4.74}$$

where $\mathcal{H}$ represents the fracture driving force for the uniaxial or biaxial tension loading, and it could represent the tensile strain energy $\mathcal{H}_I$ in Eq.(4.24) for the unified phase field model and the total strain energy φ_0^e in Eq.(4.23) for the isotropic phase field model respectively.

The loading condition of uniaxial loading tension is demonstrated in Figure 4.9(a). The analytical solution of the uniaxial loading with unified phase filed model could be obtained as follows (see Appendix for detailed deduction),

$$\begin{cases} \varepsilon_{xx} = -\frac{(1-d)^2\varepsilon_{zz}\nu(1-\nu)}{2\nu^2(1-d)^2+(1+\nu)(1-2\nu)} \\ \sigma_{zz} = \frac{E\varepsilon_{zz}(1-d)^2(1-\nu)}{2\nu^2(1-d)^2+(1+\nu)(1-2\nu)} \\ \mathrm{H}_{UT}^{LCSD} = \frac{E{\varepsilon_{zz}}^2(1-\nu)(\nu+1)(1-2\nu)}{2[2\nu^2(1-d)^2+(1+\nu)(1-2\nu)]^2} \end{cases} \tag{4.75}$$

Based on Eq.(4.75), the analytical solution of damage evolution and axial stress response are plotted in Figure 4.9(a), accompanied with the numerical results with a series of viscosity parameter η. It is found that both numerical stress-strain and d-strain curves converge to the analytical solutions when η is less than 10^{-5} N·s/mm^2.

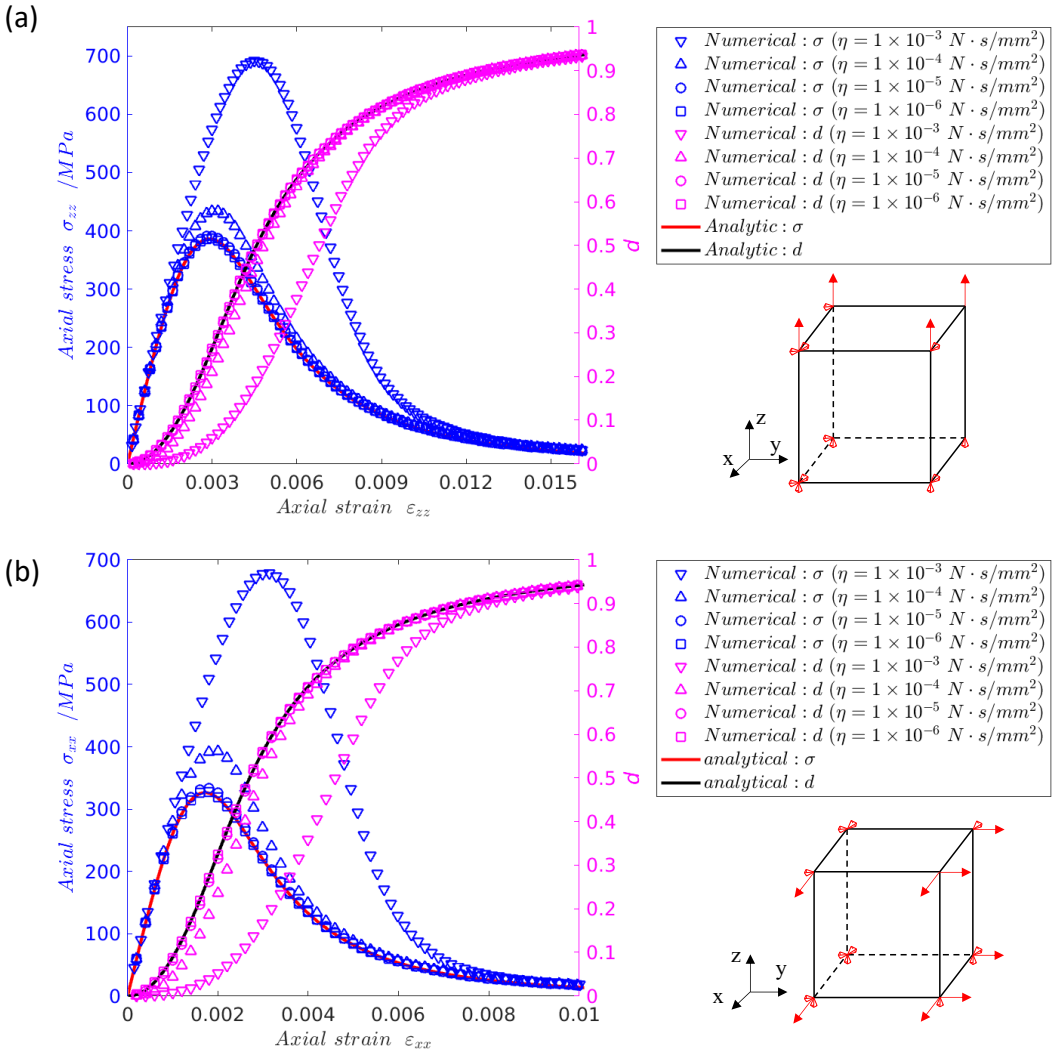

Figure 4.9 Simulation results of stress response and phase field evolution using the unified phase field model with different viscosity parameters η for one element test under (a) uniaxial tension loading (b) biaxial tension loading

4.5.1.2 Biaxial tension

For the biaxial tension loading, as demonstrated in Figure 4.9(b), the tested element was equally extracted in x and y direction, while kept free in z direction. The analytical solution of biaxial loading test with unified and isotropic phase field model is obtained respectively as follows (see detailed deduction in Appendix),

$$\begin{cases} \varepsilon_{zz}^{LCSD} = -\dfrac{2\varepsilon_{xx}\nu(1-d)^2}{2\nu^2(1-d)^2+(1+\nu)(1-2\nu)} \\ \sigma_{xx}^{LCSD} = \dfrac{(1-d)^2 E\varepsilon_{xx}}{2\nu^2(1-d)^2+(1+\nu)(1-2\nu)} \\ \mathrm{H}_{BT}^{LCSD} = \dfrac{E{\varepsilon_{xx}}^2(1+\nu)(1-2\nu)}{[2\nu^2(1-d)^2+(1+\nu)(1-2\nu)]^2} \end{cases} \tag{4.76}$$

$$\begin{cases} \varepsilon_{zz}^{iso} = -\frac{2\varepsilon_{xx}\nu}{1-\nu} \\ \sigma_{xx}^{iso} = \frac{E\varepsilon_{xx}(1-d)^2}{1-\nu} \\ \mathrm{H}_{BT}^{iso} = \frac{E\varepsilon_{xx}^2}{1-\nu} \end{cases} \tag{4.77}$$

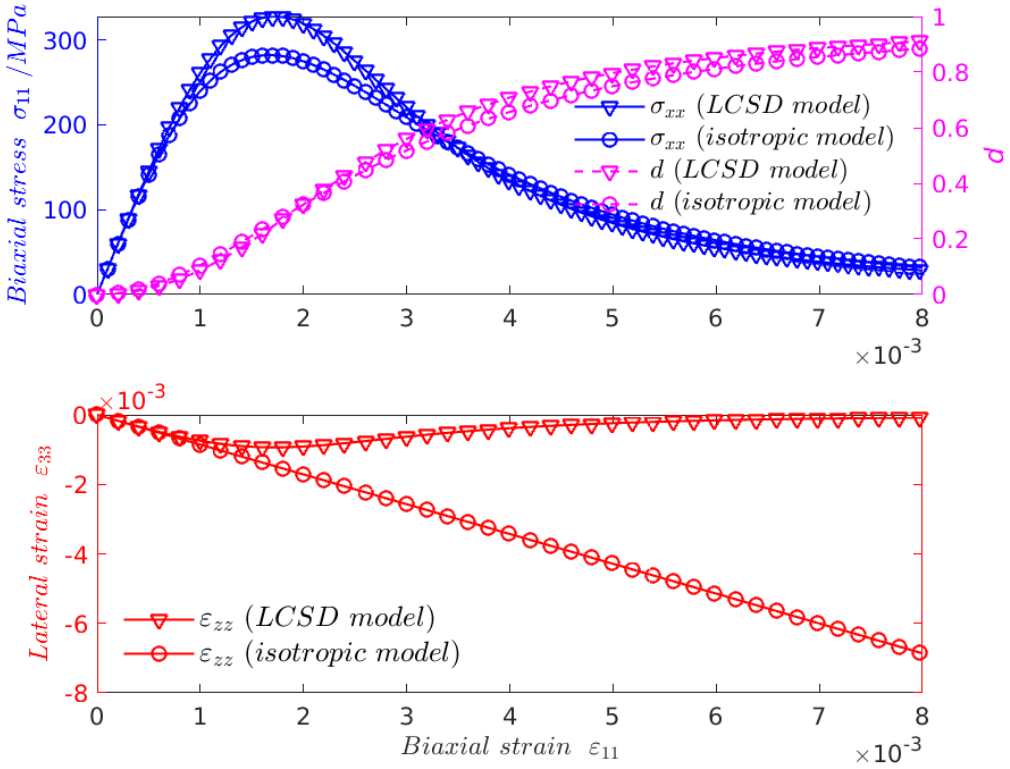

Figure 4.10 Axial stress, phase field evolution and lateral strain versus axial strain for unified phase field model and standard phase field model

The comparison between the analytical solutions and numerical results across varying viscosity parameters η, is depicted in Figure 4.9(b), which reveals that simulation results align closely with the analytical solution when η is lower than 10^{-8} kN·s/mm^2. Moreover, a comparative analysis was conducted between the unified model and an isotropic phase field model, as illustrated in Figure 4.10. In this comparison, viscosity parameter η are both set at 10^{-8} kN·s/mm^2 to isolate and minimise numerical errors. As depictured in Figure 4.10(a), the phase field damage initially evolves slightly faster in isotropic model than in unified model. However, after the axial strain reaches approximately 0.2%, the damage development accelerates more rapidly in the local coordinate system. According to Eq.(4.75), the evolution of phase field depends on the fracture driving force *H*. Therefore, the differing rates of damage evolution in the two models can be mathematically explained by calculating the ratio between the two fracture driving forces as below,

$$\frac{\mathrm{H}_{BT}^{LCSD}}{\mathrm{H}_{BT}^{iso}} = \frac{(1-\nu)(1+\nu)(1-2\nu)}{[2\nu^2(1-d)^2+(1+\nu)(1-2\nu)]^2} \tag{4.78}$$

Eq.(4.78) reveals that the ratio of $\frac{\mathrm{H}_{BT}^{LCSD}}{\mathrm{H}_{BT}^{iso}}$ monotonically increases as the phase field develops. Specifically, when the damage variable d is equal to zero and one, this ratio is found to be a set of reciprocals, namely $\frac{1-\nu-2\nu^2}{1-\nu}$ and $\frac{1-\nu}{1-\nu-2\nu^2}$ respectively. This analysis suggests that damage evolves more rapidly in the isotropic model when d is small, and conversely, in the unified phase field model when d is comparatively large, which is consistent with the numerical results depicted in Figure 10(a). As a result, the stress response is significantly influenced by the evolution of damage. As also shown in Figure 10(a), the stress response, σ_{xx}^{LCSD} is marginally higher than σ_{xx}^{iso} until the axial strain approximates 0.35%. Beyond this point, the stress response in the isotropic model becomes larger, demonstrating an inverse trend to the evolution of the phase field.

Although the differences in phase field evolution and stress response between the unified and isotropic models are relatively minor, there is a significant variation in the lateral strain in the z direction between these two models. As illustrated in Figure 10(b), the lateral strain (ε_{zz}^{iso}) in the isotropic model increases linearly with axial strain, even after the material has completely fractured. In contrast, the LCSD phase field model accounts for the release of lateral strain upon full fracture formation. According to Eq.(4.77), the lateral strain in the unified model is correlated with damage and decreases to zero as the phase field develops to one, offering a more realistic simulation of material behaviour. This concept of lateral strain release is also considered in the directional strain energy decomposition strategy, as referenced in previous studies. However, to the best knowledge of the authors, those models face limitations in addressing biaxial tension problems due to the challenges in determining the proper crack surface under such stress state.

4.5.1.3 Cycling loading

As shown in Figure 4.11(a), the cyclic loading force is applied to the z-axis of a single element, while the boundary surfaces along the other two axes are left unconstrained. Initially, a nominal tensile strain of 0.3% is incrementally applied $(LO \rightarrow LA)$. and then gradually reduced to a zero $(LA \rightarrow LB)$. Following this, the element undergoes compression in the opposite direction until a compressive strain of -1.5%

($LB \rightarrow LC$), after which the strain is relieved ($LC \rightarrow LD$) . Finally, the tensile strain is reapplied, increasing to 3% ($LD \rightarrow LE$).

The stress response and phase field evolution versus axial strain curve for four different strain energy decomposition approaches throughout the entire loading process are depicted in Figure 11(b). During the first phase of tension loading, the phase field evolution rates in the unified, isotropic, and spectral phase field models are similar to one another and noticeably higher than that in the V-D model. The slower damage evolution of the V-D model results in higher stress response compared to the other three decomposition approaches. This discrepancy in V-D model is attributed to decomposing the total strain energy into volumetric and deviatoric components for even uniaxial tension loading, with the latter being treated as shear fracture energy and regulated by higher shear fracture energy release rate. During the unloading phase of the first tension loading, the damage remains constant, and the V-D decomposition method exhibits the highest modulus among all four models.

When compression loading is applied, the isotropic model exhibits an asymmetric mechanical response similar to that during tension loading, reaching its peak stress firstly. In contrast, the V-D model captures the asymmetrical stress response under compression loading, showing higher compressive strength compared to the isotropic model. The unified phase field model displays a unilateral effect, with a sudden increase in Young's modulus when compression strain is applied, until a peak is reached at -0.75%. Beyond this point, it is observed that the local coordinate system changes, and the unified phase field model degraded to V-D decomposition model, with identical damage evolution and stress response, as the final solution of the crack orientation demonstrated in Section 4.3.4.4. The spectral decomposition approach, on the other hand, does not show a decreasing trend in stress response in the z direction during this stage, despite the accumulation of damage due to tension strain in the other two directions. During the unloading phase of compression loading, the spectral model exhibits the largest Young's modulus, followed by the unified, V-D, and isotropic phase field models.

During the second tension loading phase, the isotropic and spectral models exhibit a markedly low stress response due to the significant damage accumulation experienced prior to this loading. Conversely, the stress response and damage evolution in the V-D and unified models remain closely aligned, with stress increasing to a modest peak at an

axial strain of approximately 1.2%. Beyond this point, damage continues to accumulate, and the stress response gradually diminishes to zero. This observed consistency between the V-D and unified models can be attributed to local coordinate system of the unified model remaining unchanged, as it does not meet the stability condition necessary for updating the local coordinate system, a point elaborated upon in Section 3.5.

This cyclic loading example effectively illustrates the advantages of the proposed unified model in its ability to model mechanical behaviour across various stress states. In contrast, other models demonstrate effectiveness only within specific stress domains, rather than exhibiting universal applicability.

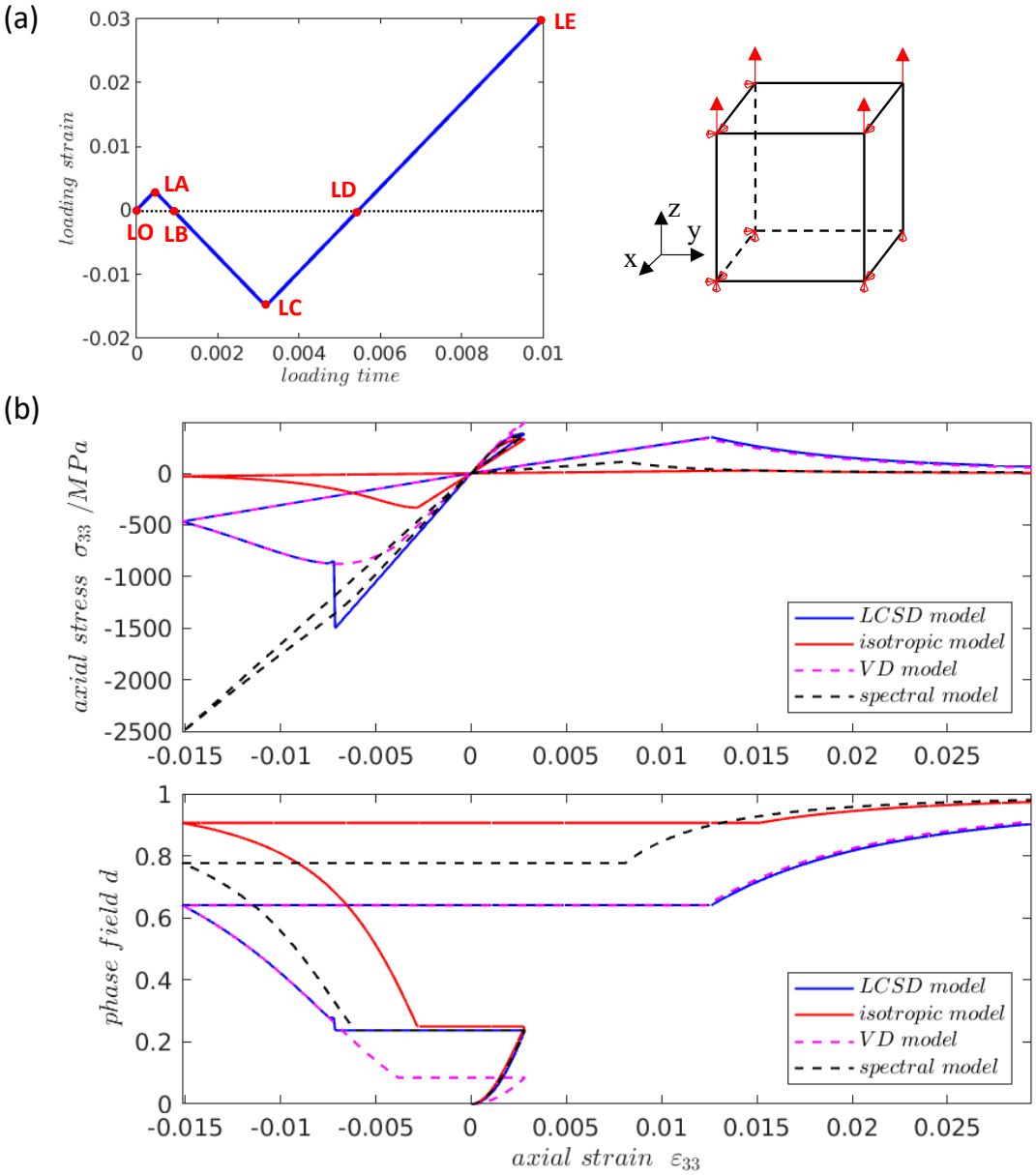

Figure 4.11 (a) Boundary condition and loading path for the one element cycling loading; (b) simulation results of stress response and phase field evolution with four different models (unified, isotropic, V-D and spectral phase field models)

4.5.2 Dogbone Tension

The dogbone tension test was carried out using the proposed unified phase field model to validate its performance under tensile stress conditions, in comparison with isotropic, spectral, and V-D decomposition approaches. The geometry of this specimen with thickness of 5 mm and load condition for the uniaxial tension test are demonstrated in Figure 4.12 (a), and the mesh details are presented in Figure 4.12 (c). The model parameters for this simulation are listed in Table 4.4.

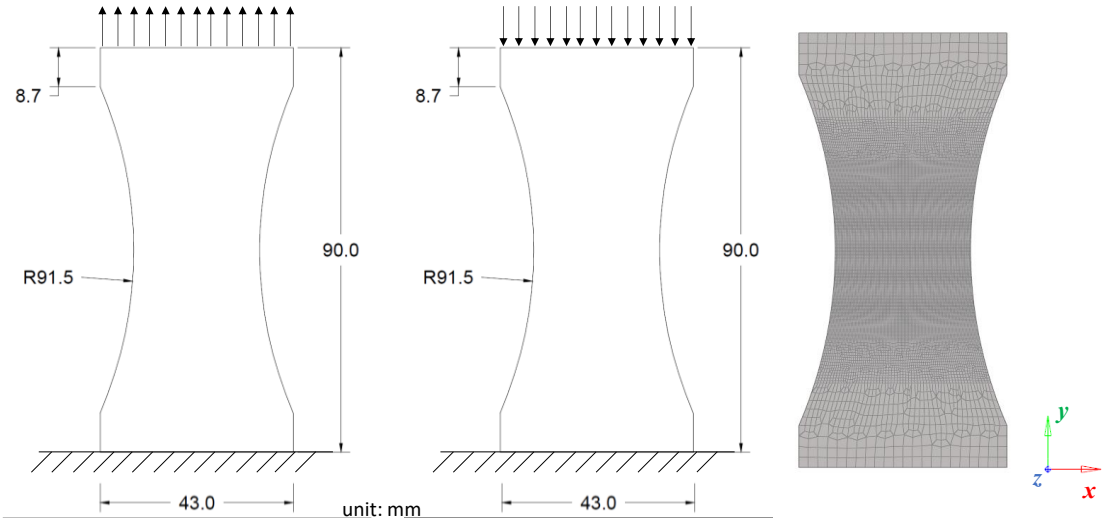

(a) Uniaxial tension (b) Uniaxial compression (c) Mesh information

Figure 4.12 Geometry and boundary condition for dogbone specimen under tensile/compressive uniaxial loading

Table 4.4 parameters for dogbone specimen

Type	Parameters	Value
elastic	Elastic modulus E	25850 MPa
	Poison's ratio υ	0.18
Damage	Tensile crack energy release rate G_t	0.1 N/mm
	Shear crack energy release rate G_c	0.5 N/mm
	Length scale l_c	0.1
	Damage viscosity parameter η	5.0×10^{-8} kN·s/mm^2

The force-displacement curves for the four decomposition strategies are presented in Figure 4.13. It is found that the reaction forces for all of the phase field models demonstrate identical linear rising at the initial stage until the loading displacement reaching at 0.08 mm, when the force-displacement curve for the V-D model diverges from those of the other models, displaying a higher load-carrying capacity. Following this divergence, all curves continue to rise at a diminishing rate until they abruptly drop to zero when the loading displacement reaches approximately 0.37 mm for the V-D model and 0.24 mm for the other three models. The peak reaction forces are around 12 kN for the V-D model, followed by 7.9 kN for both the Spectral and unified models, and the Isotropic model shows the lowest peak force at approximately 7.6 kN.

Throughout the entire loading process, the force-displacement curves of the Spectral and unified models are very similar, both slightly higher than isotropic model. In this dogbone tension specimen, the unified model will automatically align the crack

surface normal direction along the loading direction to achieve maximum F-function energy dissipation as outlined in Table 4.2. Consequently, both the unified and spectral models categorise most of the strain energy into the tensile component, corresponding to the tensile fracture toughness, leading to simulation results that are slightly higher than the isotropic phase field model. Conversely, the V-D model shows the highest load-carrying capacity due to its decomposed deviatoric energy for uniaxial tension loading, which is assumed to generate shear fractures corresponding to a higher fracture toughness. However, this assumption is not suitable for the dogbone specimen under uniaxial tension stress, which predominantly produces mode I fractures.

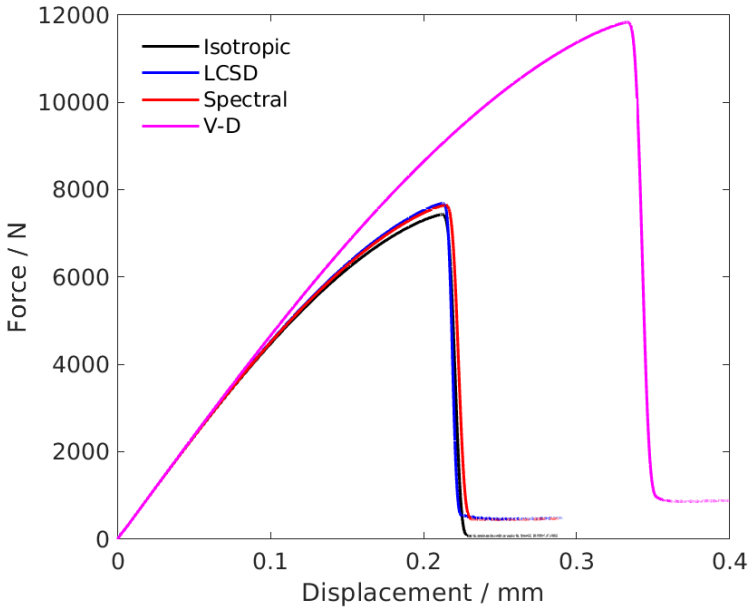

Figure 4.13 Force-displacement curve for dogbone specimen under tension loading for different decomposition models

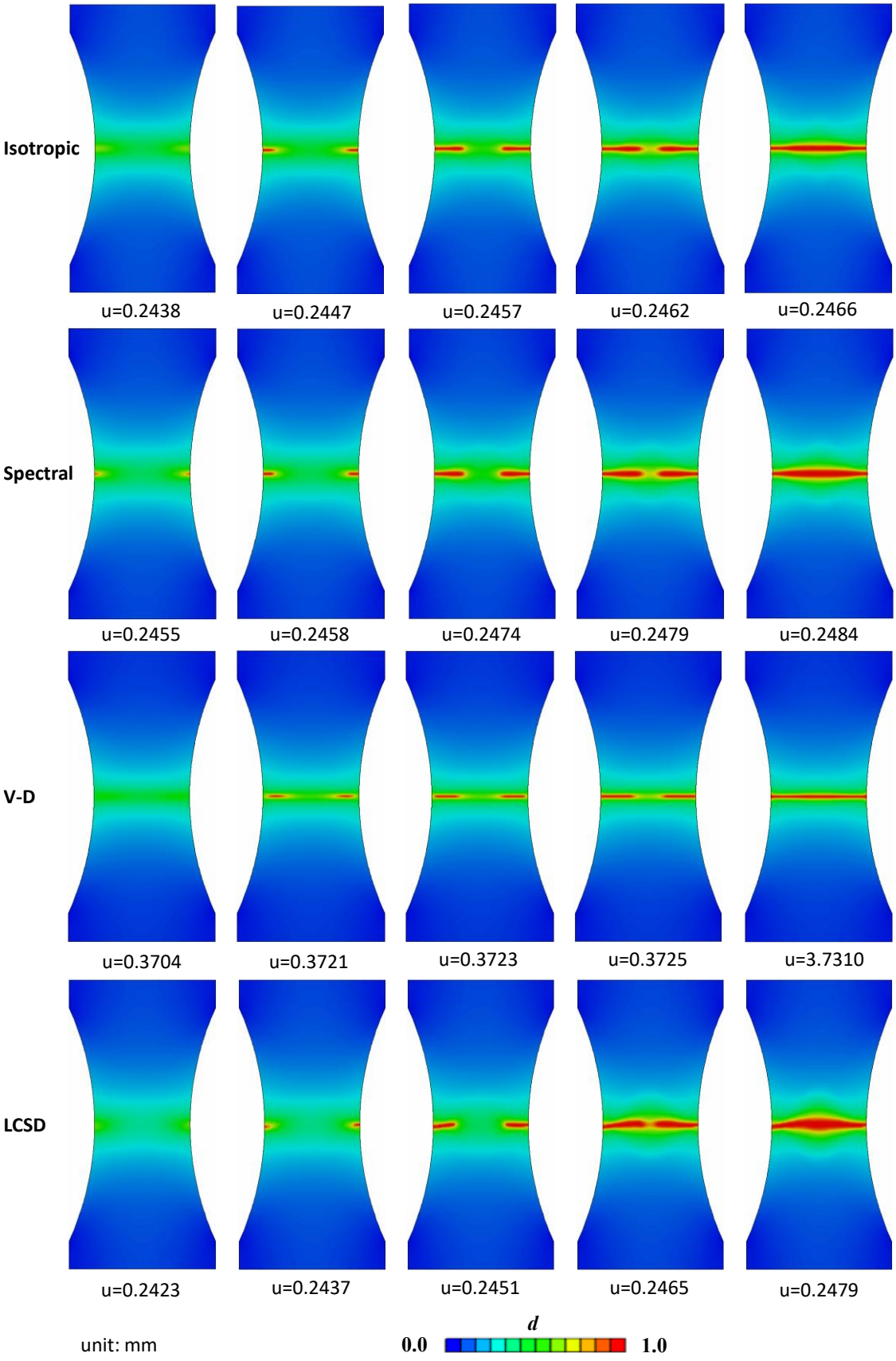

Figure 4.14 Phase field damage evolution of dogbone specimen under tensile loading.

Figure 4.14 illustrates the phase field evolution process of four different decomposition models, each specimen featuring a horizontal fracture region approximately at the middle of its vertical edge. Notably, the crack nucleation initiated from the two side edges when the loading displacement reached at around 0.245 mm for isotropic, spectral and unified model. Meanwhile, for the V-D model, damage initiated with 1 mm offset inside the edges as applied displacement increased to 0.372 mm. After fracture initiation, a through brittle fracture path was formed immediately, which corresponds to the sudden drop of reaction force in Figure 4.13 for each decomposition phase field model.

4.5.3 Dogbone Compression

In the second numerical example, the aforementioned dogbone specimen with identical material parameters is subjected to a uniaxial compressive force exerted upon its upper surface, with its bottom face fixed in three directions, as depicted in Figure 4.12 (b). It is also noted that the front and back surface of dogbone specimen are fixed in the z direction in case of the potential bulking. Hence, this dogbone compression test can be viewed as a plane strain problem. Due to the symmetric mechanical response under tension/compression loading for isotropic model, this test was conducted using only the spectral, V-D, and unified models.

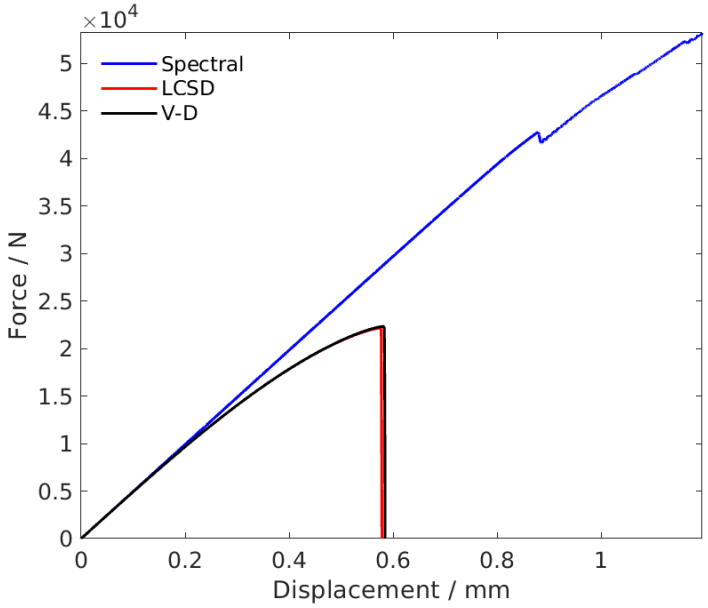

Figure 4.15 Force-displacement curve for dogbone specimen under compression loading for different decomposition models

The load-displacement curves of these three phase field models are depicted in

Figure 4.15. Initially, all models exhibit a linear stress response until the loading displacement reaches approximately 0.2 mm. Subsequently, the reaction forces of V-D and unified models increase with a decreasing modulus until reaching around 0.58 mm, when they abruptly drop to zero. Conversely, the spectral model maintains a linear stress response until a slight drop is observed when the loading displacement reaches around 0.88 mm. After this point, the curve continues to rise until the end of this loading process.

Figure 4.16 illustrates the evolution of phase field damage for the three decomposition approaches. For the spectral model, damage nucleation initiates at the centre of the top surface when the applied displacement reached 0.88 mm and rapidly extends downward towards the centre of the specimen, corresponding to the slight drop in reaction force seen in Figure 4.15. During the compressive loading process, the materials along the vertical midline of the dogbone specimen develops compressive strains in the *y*-direction and extension strains in the *x*-direction, facilitating fracture propagation along a vertical path. Despite the phase field damage along this vertical fracture path reaching one, as shown in Figure 4.16, the stress response in the *y*-direction does not decrease due to the undegraded compressive stress in spectral phase field model.

In the V-D model, fractures initiate symmetrically at the midpoints of the two edges of the dogbone specimen side, which then propagate toward the specimen's interior at an inclined angle, being approximately 45° to the horizontal. When applied displacement increased to 0.577 mm, those two branches intersect at the one-third position along the vertical midline, continuing to propagate upwards and bifurcating to form an X-shaped fracture topology. In the examination of the dogbone specimen under compression, the fracture evolution within the V-D phase field model is exclusively attributed to the deviatoric stress component, as delineated by Eq.(4.14). Concurrently, it is observed that the maximal deviatoric stresses manifest along the two diagonal lines of the dogbone specimen, which are oriented at angles of 45 degrees and -45 degrees relative to the horizontal axis. This stress distribution precipitates localised damage accumulation at these specific orientations, culminating in the emergence of an X-shaped crack propagation path.

The phase field evolution of unified model closely mirrors that of the V-D model up to the point of coalescing at around 0.582 mm. However, the subsequent fracture path significantly diverges, with initiation occurring on the left side only and the primary

fracture path developing along an inclined line at 45 degrees. As loading displacement increases, the crack path extends to the right side of the specimen, forming a connected inclined crack surface. Unlike the V-D model, the unified phase field model considers the local crack orientation or alignment with the material's stress field. Once a primary fracture path is established, the overall deformation and stress distribution will lead to an updated fracture orientation that aligns consistently across the specimen, and other cracks tend to be suppressed.

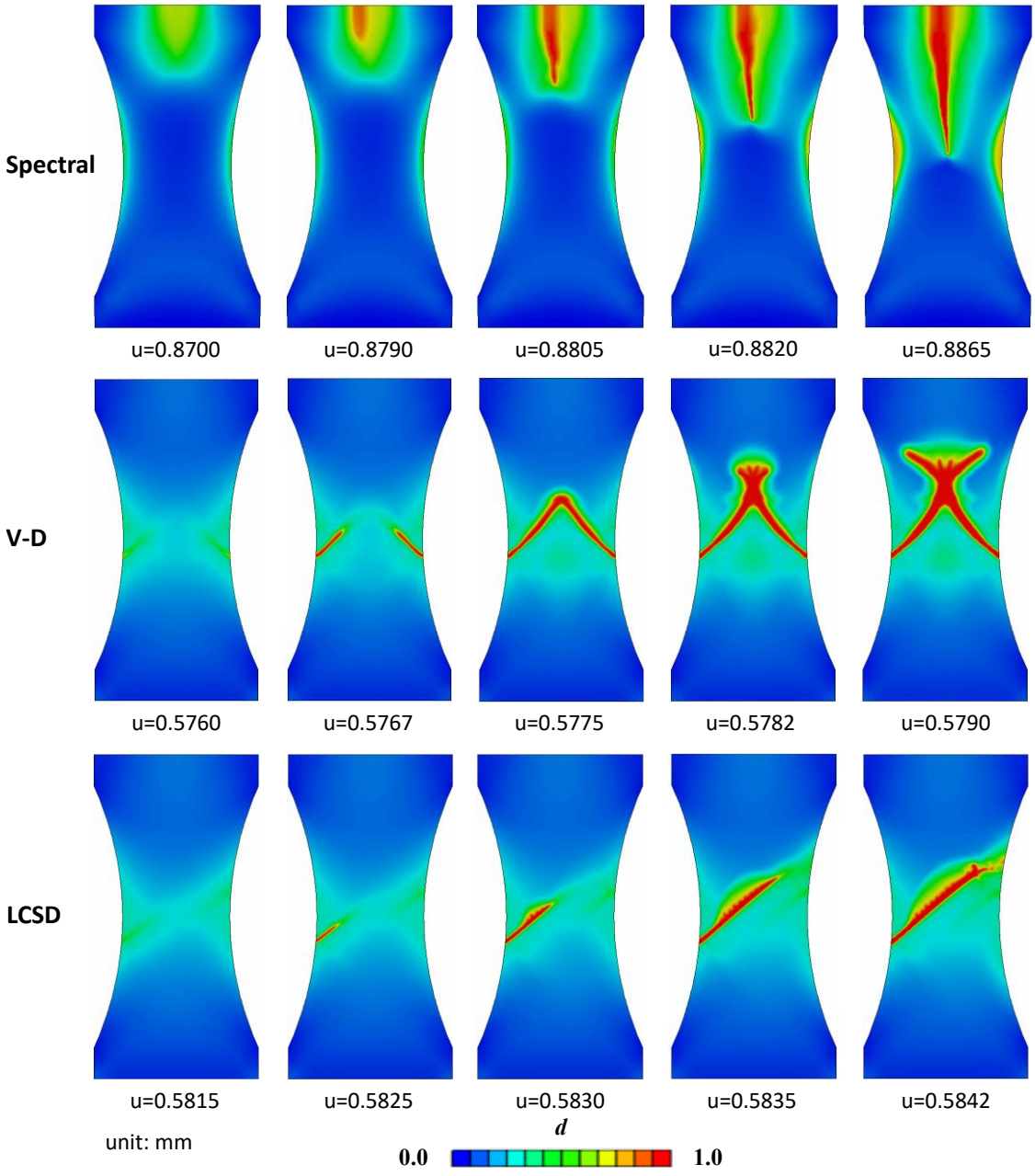

Figure 4.16 Crack path of dogbone specimen under compression loading for three different decomposition methods

4.5.4 Perforated asymmetric bending test

The Perforated Asymmetric Bending Test (PABT) has been thoroughly investigated through both experimental and numerical methods, with its detailed geometry and boundary conditions showcased in Figure 4.17. As demonstrated in Figure 4.17, we marked three points (point A, B and C) on the geometry configuration of this PABT specimen for easier description in the following paragraph. They are located at the pre-crack notch tip, the bottom-left edge of the third hole, the top-right edge of the third hole, respectively. All material parameters in this study are referred to (Molnár and Gravouil 2017) and detailed in Table 4.5, except for the shear fracture toughness G_c set as five times of tensile fracture toughness G_t. Simulation results of this PABT specimen for phase field models incorporating four different strain energy decomposition strategies (unified, V-D, spectral, and isotropic) are demonstrated and analysed.

Table 4.5 model parameters for PABT specimen

Type	Parameters	Value
elastic	Elastic modulus E	20800 MPa
	Poison's ratio υ	0.3
Damage	Tensile crack energy release rate G_t	1 N/mm
	Shear crack energy release rate G_c	5 N/mm
	Length scale l_c	0.025 mm
	Viscosity parameter η	2×10^{-7}kN·s/mm^2

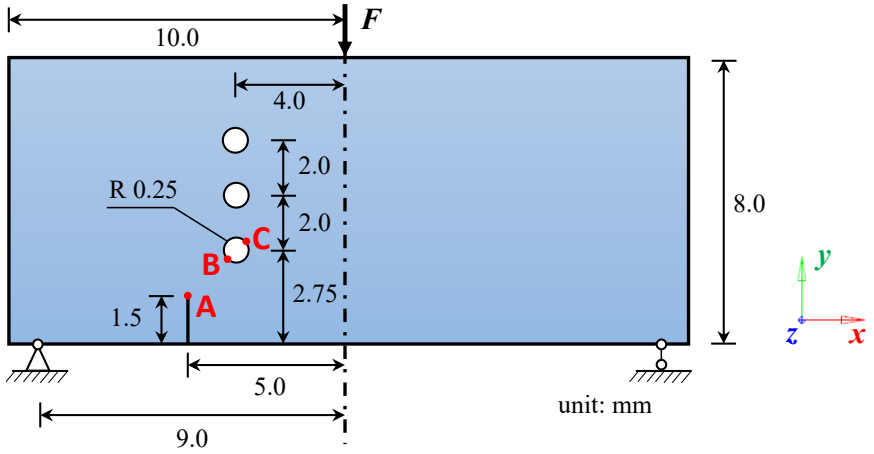

Figure 4.17 Geometry and boundary condition of the perforated asymmetric bending test specimen.

The force-displacement curves for all the four phase field models are compared in Figure 4.18. It can be seen that the reaction forces of all four models showed linear growth with identical modulus as the applied displacement increased initially. Subsequently,

fracture initiated at point A and quickly developed to point B, occurring at a displacement of approximately 0.11 mm for the V-D model and 0.08 mm for the other three models. After the formation of the first fracture path, a rapid decline of reaction force was observed to nearly zero in the isotropic phase field model, while the reaction forces in other three models experienced brief drops followed by rerising and exceeding the first peak forces. The second peak forces occurred when applied displacement reached approximately 0.11 mm, 0.12 mm, and 0.16 mm for the unified, spectral and V-D models, as demonstrated in Figure 4.18. After the second peak points, reaction forces in those three models fell down rapidly, corresponding to the quick propagation of the second crack path initiating at point C, which leads to the final structure collapse.

During this loading process, the isotropic phase field model demonstrated the least load-carrying capacity, which results from quick damage nucleation at point C after the formation of the first fracture path. The principal strain distributions at that moment in isotropic phase field model is depicted in Figure 4.19, which focused on the area around point C where the second fracture path would initiate. It can be seen from Figure 4.19 that the strain profile around point C demonstrated tensile maximum principal strain, negligible medium principal strain, and compressive minimum principal strain. It is also noted that the compressive minimum principal strain direction aligns its final fracture path (see Figure 4.20). In isotropic phase field model, the effective stress is degraded isotropically regardless of its compressive/effective stress state. Hence, the degraded strength along the fracture path direction accelerates its fracture propagation, compared with other decomposition models.

Meanwhile, the unified phase field model and spectral model yielded very close simulation results. In this numerical example, stress state at the crack tip area is dominated by the tensile first principal stress with its direction $\boldsymbol{n}_1$ vertical to the crack path. Hence, under such stress state, the local crack surface direction $\boldsymbol{r}$ in unified model would be aligned along $\boldsymbol{n}_1$ according to the solution of local coordinate system, summarised in Table 4.2, which accounts for the identical decomposed tensile strain energy for the unified and spectral model. Nevertheless, the decomposed shear strain energy in the unified model produced by shear stress within the σ_2-σ_3 provided addition, though very limited, crack driving forces, resulting in the slightly quicker damage evolution and lower load force compared with the spectral phase field model. In addition, the V-D model

demonstrated the highest peak reaction force. The highest loading-carry capacity be attributed to larger dissipation fracture toughness for decomposed deviatoric strain energy in the V-D decomposition model. Nevertheless, as aforementioned, the fracture path evolution in this specimen is mainly caused by the tensile principal stress rather than deviatoric stress in this specimen. In this case, the V-D decomposition method could overestimate the material strength for the mode I dominant fracture path.

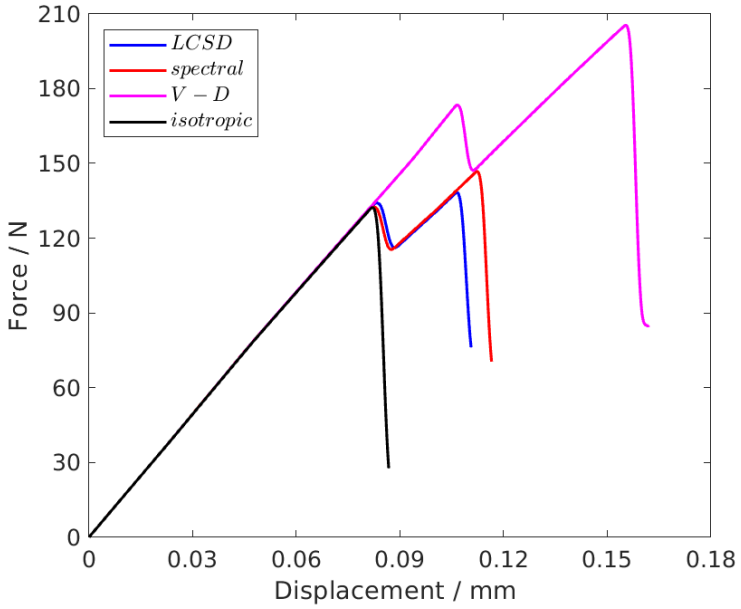

Figure 4.18 Force-displacement curve for dogbone specimen under compression loading for different decomposition models

Figure 4.20 compares the final fracture paths predicted by the four models, accompanied by the experimental observation. In general, all the four numerical models have predicted similar fracture path, which initiated at point A and developed along a straight line to point B, then went through the third hole. It is also noted that the predicted fracture path does not math the experimental observation perfectly, where the fracture path skipped the third hole. As explained by (Molnár and Gravouil 2017), the damage evolution path in numerical modelling would be attracted when it approaching the holes due to the stress concentration. The subsequent predicted fracture path in the V-D and spectral phase field model continued to grow along the incline at around 60 degrees to horizontal axis. Alternatively, in the unified and isotropic models, the second fracture path originated at point C and developed with a rising inclination and approached the second hole, demonstrating a better agreement with the experimental result.

(a) Configuration of the first fracture path

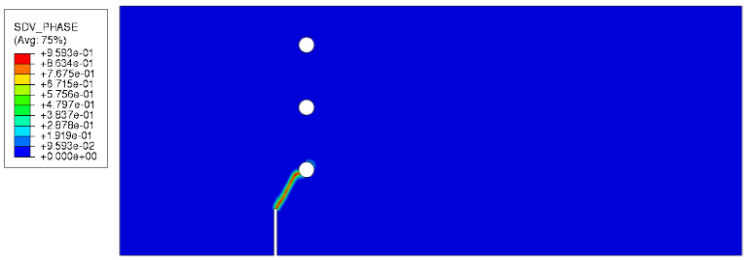

(b) Maximum Principal Strain

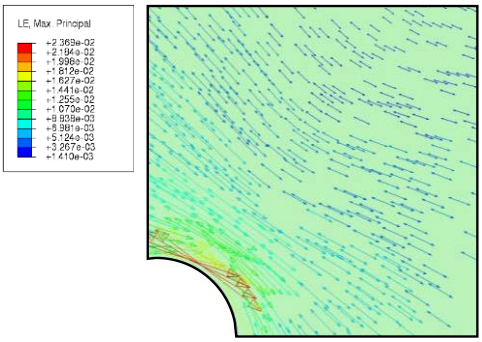

(c) Intermediate Principal Strain

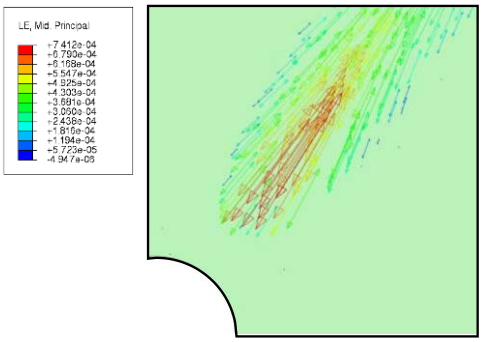

(d) Minimum Principal Strain

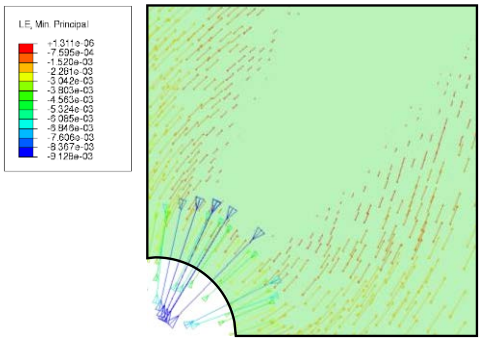

Figure 4.19 Configuration of the first crack path and principal strain distribution around the Point C area after the formation of the first fracture path

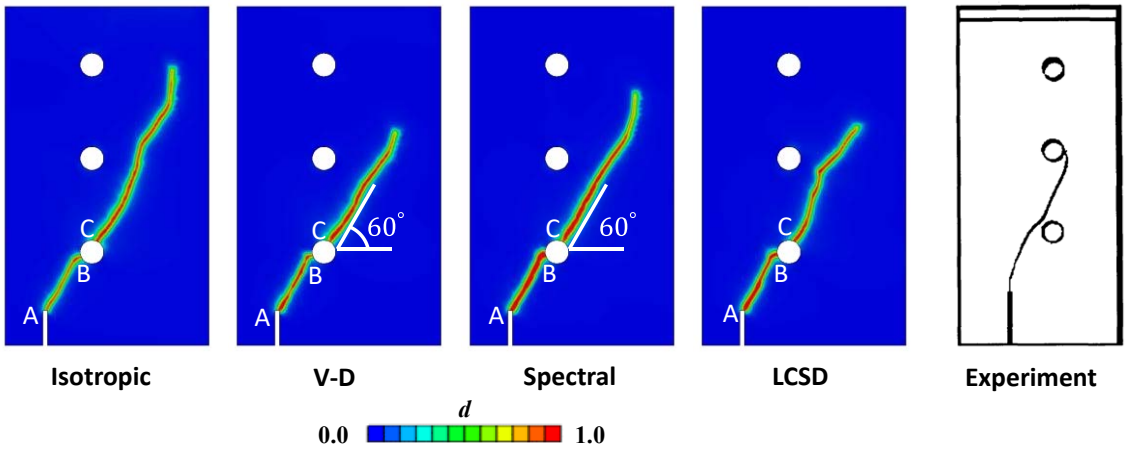

Figure 4.20 Simulation results of crack propagation for phase field models with Isotropic, Spectral, V-D and unified strain energy decomposition approaches.

4.5.5 Triaxial test on pre-cracked cylinder specimen

The triaxial compression test on a pre-cracked cylindrical sandstone specimen is simulated using the proposed unified phase field model to validate its efficacy under complex 3D stress states, in comparison with isotropic, V-D and spectral decomposition models. As depicted in Figure 4.21, the geometry of the sandstone specimen features a diameter of 50 mm and a height of 100 mm as referenced in (Huang, Gu et al. 2015). It includes two parallel inclined flaws, each at a 30° angle, with a length of 25 mm and a width of 0.8 mm. In this numerical example, the pre-cracked cylinder is firstly subjected to confined pressure of 10 MPa, then applied by axial stress on the top surface through displacement control.

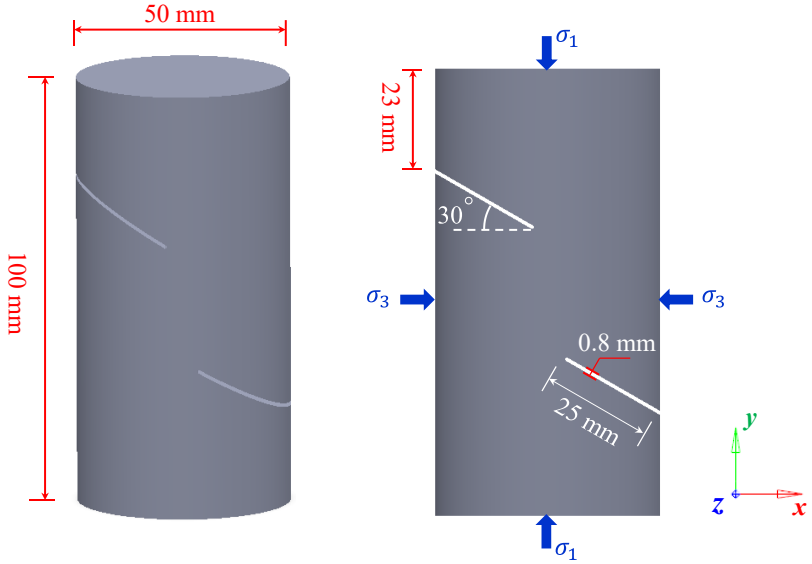

Figure 4.21 Geometry and loading condition of cylinder specimen with two parallel pre-existing flaws (Huang, Gu et al. 2015)

Figure 4.22 presents the stress-strain curve for the confined triaxial compression test. The initial axial stresses of all the four phase field models experienced identical linear increase. With the axial strain increasing to 0.1%, the isotropic phase field model reached its peak stress, followed by its fluctuating descent to zero at the axial strain of 0.42%. On the contrast, the axial stress in the spectral model exhibited a consistently rising trend, resulting from its governing equations where compressive stress in the *y*-direction is not degraded, even though the local damage along the crack path has fully developed, illustrated in Figure 4.23. For the V-D model, its axial stress underwent a nonlinear when the axial strain grew to 0.3% and then rose with decreasing rate until the axial strain reaching 0.7%. After this point, the loading stress experienced a certain degree of strengthening due to the contact between the two pre-cracked notch surfaces. For the unified model, the specimens exhibited a linear stress response until the axial strain reaches approximately 0.3%. Afterward, the axial stress continued to grow to 55 Mpa with a decreasing modulus until a sudden drop occurring when the applied axial strain increases to around 0.8%, which corresponds to the formation of the fracture path connecting the two notches observed in Figure 4.23.

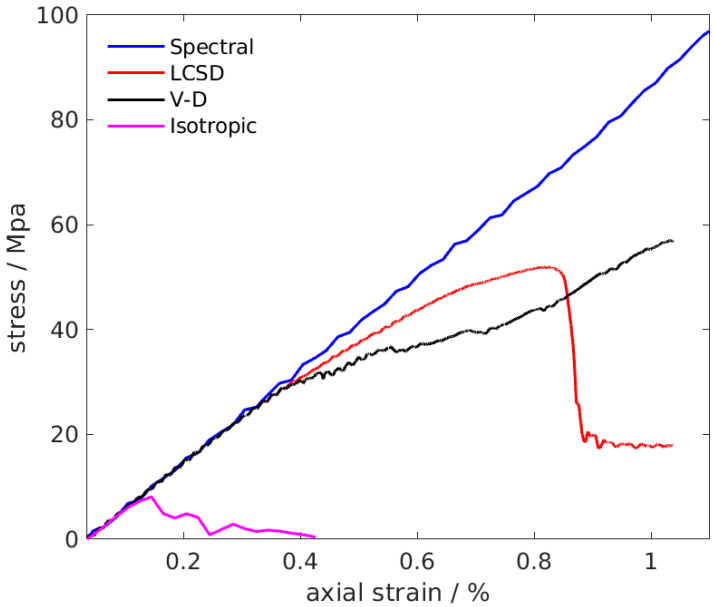

Figure 4.22 Force-displacement curve for triaxial compression

Figure 4.23 compares the final fracture paths across different models with experimental observations. In spectral phase field model, similar to the fracture topology of the dogbone compression loading, tensile fracture along the vertical loading direction was captured while shear damage is ignored, which corresponds to its governing equation without considering the fracture propagation driven by shear strain energy (see Eq.(4.15)).

For the V-D phase field model, the two pre-existing flaws closed when the compressive axial strain increased to 0.7. Under such configuration, large amount of the axial load was passed through the two contacted notch surfaces, decelerating the development of inclined shear band between two notches. On the other hand, high Mises stress around the notch positions due to the stress concentration leads to damage evolution, driving crack propagation and resulting in the final horizontal fracture path shown in Figure 4.23. The unified phase field model demonstrates superior performance in this numerical example, accurately capturing both the shear secondary fracture and the tensile wing fracture initiated from the two notches, closely matching experimental results.

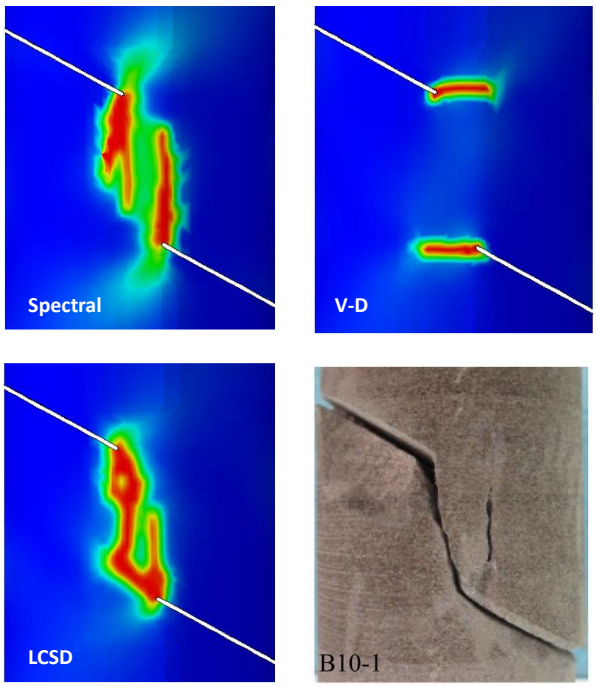

Figure 4.23 Comparison of final fracture topology for V-D, Spectral, and unified phase field model accompanied by the experimental crack path

4.6 Summary

To capture the fracture behaviour under all kinds of complex stress states properly, this study proposed a unified strain energy decomposition approach, where the strain energy is split on the local coordinate system into three components, namely tensile, shear and compression parts. The local coordinate is determined by maximising the *F*-criterion function energy, the sum of the tensile and shear strain energy normalised by corresponding tensile/shear crack energy release rate. An innovative method focusing on three normal stresses is proposed to search for its optimized configuration. This proposed a unified strain energy decomposition approach could recast to the commonly adopted

spectral, V-D and crack-surface-based strain energy decomposition under specific load conditions. Also, the proposed model can reveal the competition between tensile and shear energy dissipation under complex stress states, which depends on the stress states, tensile/shear fracture toughness and the Poison's ratio. The proposed unified phase field model is implemented explicitly via the ABAQUS subroutines VUEL and VUMAT. This implementation is validated via the one element test, where uniaxial tension and uniaxial compression test is conducted, and the numerical results matches the homogenous analytical solution.

In this study, the unified decomposition method for phase field modelling is compared with isotropic, V-D, and spectral approaches through a series of numerical examples, covering various stress states loading, including tensile, compression, tensile-shear, compression-shear. In the dogbone compression test, the spectral model showed unphysical load-displacement curve with infinite growth even though the phase field damage has fully developed; The unified and V-D model demonstrated similar load-force curve, while they have predicted different crack path, with unrealistic X-shape for V-D model, and inclined fracture surface for unified model. For the perforated asymmetric bending test (PABT) where the tensile stress dominates, the simulation result by unified and spectral model showed proper mechanical response, similar to the isotropic damage model, while the V-D model predicted larger loading-carry capacity caused by the unsuitable deviatoric energy dissipation for the tensile dominant fracture in this specimen. In the last triaxial compression test specimen, the proposed unified strain energy showed best performance for reproducing the experimental fracture propagation process, compared with other approaches

5. DEVELOPMENT OF FIVE-LAYER SHELL PHASE FIELD MODEL

5.1 Introduction

Predicting fracture bahaviour and load-carrying capacity of shell structures properly is a crucial issue due to its significant application in many industrial fields, such as aerospace, automotive, pipelines, and civil engineering. To address this, various numerical models have been proposed. Conventional cohesive zone fracture models represent crack topology by inserting interface elements at the boundaries of structural elements (Cirak, Ortiz et al. 2005, Zavattieri 2006, Munjiza, Lei et al. 2013). The extended finite element method (XFEM) has also been adapted to model crack evolution in shell structures, introducing an enriched displacement field to capture the discontinuities in displacement associated with crack formation and propagation (Areias and Belytschko 2004, Zarrinzadeh, Kabir et al. 2020). Nevertheless, these models require tracking the crack topology throughout numerical analysis, which demands considerable computational effort.

In contrast to the aforementioned discrete models, continuous damage models regularise sharp crack topologies into diffusive damage zones, thus eliminating the need for crack path tracking. Among these, the phase-field model has gained significant attention and developed rapidly over the last two decades due to its efficiency, robustness, and simplicity in numerical implementation (Fang, Wu et al. 2020). Initially proposed for modelling brittle fracture by Francfort and Marigo (Francfort and Marigo 1998), adapted for various types of fracture simulations, including ductile fracture (Ambati, Kruse et al. 2015, Borden, Hughes et al. 2016, Miehe, Aldakheel et al. 2016, Roth and Mohr 2016, Alessi, Marigo et al. 2018, Dittmann, Aldakheel et al. 2018, Fang, Wu et al. 2019, Fang, Wu et al. 2019), dynamic fracture (Karma, Kessler et al. 2001, Borden, Verhoosel et al. 2012, Wang, Ye et al. 2020), hydraulic fracture (Miehe and Mauthe 2016, Wilson and Landis 2016, Ehlers and Luo 2017), and hydrogen embrittlement fractures (Martínez-Pañeda, Golahmar et al. 2018, Wu, Mandal et al. 2020). The phase-field model has also been applied to fracture analysis using shell element formulations, where the kinematic description follows either the Kirchhoff-Love or Reissner-Mindlin theory. Most researchers focused on the latter, and applied the solid-shell formulation to represent the

fracture diffusion with a similar idea to phase field model in three dimension (Ambati and De Lorenzis 2016, Reinoso, Paggi et al. 2017, Reinoso, Durand et al. 2019), while the existing studies for the Kirchhoff-Love thin shell is limited, which is focused in this study.

A significant challenge in implementing the phase-field model for thin shells lies in capturing crack evolution through the shell thickness. Ulmer et al (Ulmer, Hofacker et al. 2012) firstly extend the phase field model for shell fracture modelling, where a single phase field variable was introduced to describe the thickness-through damage, which was jointly driven by the bending reference energy and tensile membrane strain energy on the mid-surface. This concept was adopted by subsequent research, such as Li et al. (Li, Millán et al. 2018), who applied this shell kinematics to simulate tearing in brittle thin sheets using a higher-order phase-field model. Pillai (Pillai, Triantafyllou et al. 2020) implemented the MITC4+ shell element for shell fracture modelling to avoid shear locking, and Ma et al. (Ma, Sun et al. 2024) incorporated the stress-resultants method to account for elasto-plastic materials in ductile shell fractures. Alternatively, Kiendl et al. (Kiendl, Ambati et al. 2016) split the strain energy spectrally through the shell thickness, integrating the tensile component as crack-driving energy, which was implemented via isogeometric analysis (IGA) or mesh-free method (Amiri, Millán et al. 2014, Ambati and De Lorenzis 2016, Proserpio, Ambati et al. 2020, Proserpio, Ambati et al. 2021).

However, the above-mentioned through-thickness fracture approximation might not accurately capture the distinct damage distribution along the shell thickness, especially under bending load. To address this limitation, Areias et al. (Areias, Rabczuk et al. 2016) introduced two phase-field variables for shell element implementation, representing different fracture propagation behaviours on the top and bottom surfaces of the shell, while the displacement and angular variables remain based on the mid-reference surface. In a more recent study, Wang et al. (Wang, Han et al. 2022) assumed a linear interpolation of the phase-field distribution along the shell thickness and proposed an explicit implementation for elastoplastic materials. While these shell phase-field models show promise, most have only been validated against a limited number of benchmark numerical examples, with few studies comparing their results to experimental observations. Even in the limited literature that does make such comparisons, the focus has primarily been on quantitatively validating crack path evolution, often neglecting qualitative analysis related to load-carrying capacity, which limits their potential for practical industrial applications.

To address this gap, we propose a shell phase-field model for ductile fracture modelling, introducing five layers of phase-field variables to describe material damage, corresponding to the five Simpson integration points of stress integration. This model is validated both quantitatively and qualitatively with experimental data. Meanwhile, to accurately capture fracture initiation, we incorporate two fracture initiation criteria: the Modified Mohr-Coulomb criterion for 316L steel and the Bao-Wierzbicki fracture strain for Ti-6Al-4V alloy. The remainder of this paper is organized as follows: Section 5.2 introduces the formulation and construction of the shell phase-field model. Section 5.3 presents the explicit implementation, featuring five layers of phase-field variables interacting with the stress field. Section 5.4 provides several numerical examples, beginning with a single-element analysis, followed by two benchmark examples of notched cylinders under uniaxial tension and internal pressure, respectively. The section concludes with two experimental validation cases: three-point bending of a square-cut tube and the Gyroid TPMS under axial compression.

5.2 Formulation of elastoplastic phase field model for shell element

5.2.1 Kinematics of shell element configuration

In general, the shell problems could be categorised into thick and thin shell problems, whose kinematic description follow the Reissner-Mindlin or Kirchhoff-Love theory respectively (Ebenfeld 1999) . In this study, we concentrated on the latter assumption, wherein the effects of transverse shear deformation are considered negligible. As demonstrated in Figure 5.1, the thin-wall structure in three-dimension space with thickness of t is meshed by the four-node shell elements on its reference surface (mid-surface). Except for the global coordinates system ($\boldsymbol{x}$, $\boldsymbol{y}$ and $\boldsymbol{z}$), the local coordinate system ($\boldsymbol{t}_1$, $\boldsymbol{t}_2$ and $\boldsymbol{t}_3$) is also constructed based on the local reference surface to describe the shell element configuration, where $\boldsymbol{t}_3$ represents the local normal direction to the reference surface, while $\boldsymbol{t}_1$ and $\boldsymbol{t}_2$ are two orthogonal directions, following the below condition,

$$\boldsymbol{t}_i \cdot \boldsymbol{t}_j = \delta_{ij} \tag{5.1}$$

where δ_{ij} is the Kronecker delta. With the local coordinate system, the position of a material point within shell element is defined as,

$$\boldsymbol{x}(\boldsymbol{S}_i) = \overline{\boldsymbol{x}}(\boldsymbol{S}_\alpha) + \bar{f}_{33}(\boldsymbol{S}_\alpha)\boldsymbol{t}_3(\boldsymbol{S}_\alpha)S_3 \tag{5.2}$$

where $\boldsymbol{S}_\alpha$ (α ranges from 1 to 2) are local surface coordinates within reference plane, and

$S_3 \in [-\frac{t}{2}, \frac{t}{2}]$ is the coordinate on $\boldsymbol{t}_3$ direction; $\boldsymbol{x}(\boldsymbol{S}_i)$ and $\bar{\boldsymbol{x}}(\boldsymbol{S}_\alpha)$ represent the position of material point $\boldsymbol{S}_i$ and its projecting point $\boldsymbol{S}_\alpha$ on the reference plane; $\bar{f}_{33}$ is the thickness increase factor, which is assumed to be constant along the thickness direction.

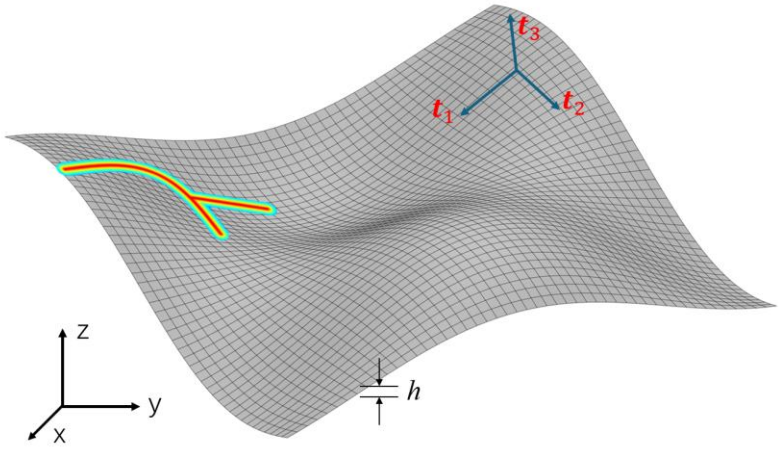

Figure 5.1 Global and local coordinates of the shell element configuration

Based on Eq.(5.2), the gradient of the position can be expressed as,

$$\begin{cases} \dfrac{\partial \boldsymbol{x}}{\partial \boldsymbol{S}_\alpha} = \dfrac{\partial \bar{\boldsymbol{x}}}{\partial \boldsymbol{S}_\alpha} + \bar{f}_{33} \dfrac{\partial \boldsymbol{t}_3}{\partial \boldsymbol{S}_\alpha} S_3 \\ \dfrac{\partial \boldsymbol{x}}{\partial \boldsymbol{S}_3} = \bar{f}_{33} \boldsymbol{t}_3 \end{cases} \tag{5.3}$$

where the derivative of $\bar{f}_{33}$ with respect to $\boldsymbol{S}_\alpha$ has been neglected. Its components within the reference plane can be obtained as below,

$$f_{\alpha\beta} = \boldsymbol{t}_\alpha \cdot \frac{\partial \boldsymbol{x}}{\partial S_\beta} = \bar{f}_{\alpha\beta} + B_{\alpha\beta} \bar{f}_{33} S_3 \tag{5.4}$$

where the reference surface deformation gradient $\bar{f}_{\alpha\beta}$ and reference normal gradient $B_{\alpha\beta}$ are defined as follows,

$$\begin{cases} \bar{f}_{\alpha\beta} \overset{\text{def}}{=} \boldsymbol{t}_\alpha \cdot \dfrac{\partial \boldsymbol{x}}{\partial S_\beta}\Big|_{S_3=0} = \boldsymbol{t}_\alpha \cdot \dfrac{\partial \bar{\boldsymbol{x}}}{\partial S_\beta} \\ B_{\alpha\beta} \overset{\text{def}}{=} \boldsymbol{t}_\alpha \cdot \dfrac{\partial \boldsymbol{t}_3}{\partial S_\beta} \end{cases} \tag{5.5}$$

In the original shell configuration, $\bar{\boldsymbol{X}}$ represents the position of the projecting point on the reference plane. The original normal direction to reference plane $\boldsymbol{T}_3$ is defined by

$$\boldsymbol{T}_3 = \left(\frac{\partial \bar{\boldsymbol{X}}}{\partial S_a} \times \frac{\partial \bar{\boldsymbol{X}}}{\partial S_b}\right) \Big/ \left|\frac{\partial \bar{\boldsymbol{X}}}{\partial S_a} \times \frac{\partial \bar{\boldsymbol{X}}}{\partial S_b}\right| \tag{5.6}$$

where S_a and S_b are coordinates of two arbitrary two unparalleled directions within the reference plane of shell element. The rest two directions $\boldsymbol{T}_1$ and $\boldsymbol{T}_2$ then could be determined by specifying $\boldsymbol{T}_1$ parallel to the projection of one desired direction on the reference plane, for example, the global $\boldsymbol{x}$ direction or printing direction of the additive manufactured shell structure.

5.2.2 Regularised fracture topology

In this study, five Simpson points along the shell thickness are adopted for stress integration. Meanwhile, five layers of phase field variables are introduced to describe the corresponding damage evolution on layers of those integration points. The fracture topology of shell structure is demonstrated in Figure 5.2 (a). The shell solid Ω with thichness of t got a through-thickness sharp crack Γ, and it was under the constraint of Neumann boundary $\partial\Omega^s$ and Dirichlet boundary $\partial\Omega^h$. In each layer of the integration point, the sharp crack Γ is regularised with diffusive phase field variable d, from the totally broken state ($d = 1$) to the intact state ($d = 0$) of material with the length scale parameter l_c, demonstrated as Figure 5.2 (b) and (c). Accordingly, the crack surface density function γ is introduced referring to standard phase field formulation in three-dimension space, written as below,

$$\gamma(d, \nabla d) = \frac{d^2}{2l_c} + \frac{l_c}{2}|\nabla d|^2 \tag{5.7}$$

where ∇d denotes the phase field gradient along each layer of shell surface. It is noted that the gradient of phase field along the thickness direction is ignored here for simple implementation. In this approach, though the damage evolution across integration layers could not be coupled directly, they could still affect each other through the redistribution of stress field. This concept has been widely adopted in the existing literature [32, 35, 36] and proved to be effective for achieving accurate simulation results with economic computational resources.

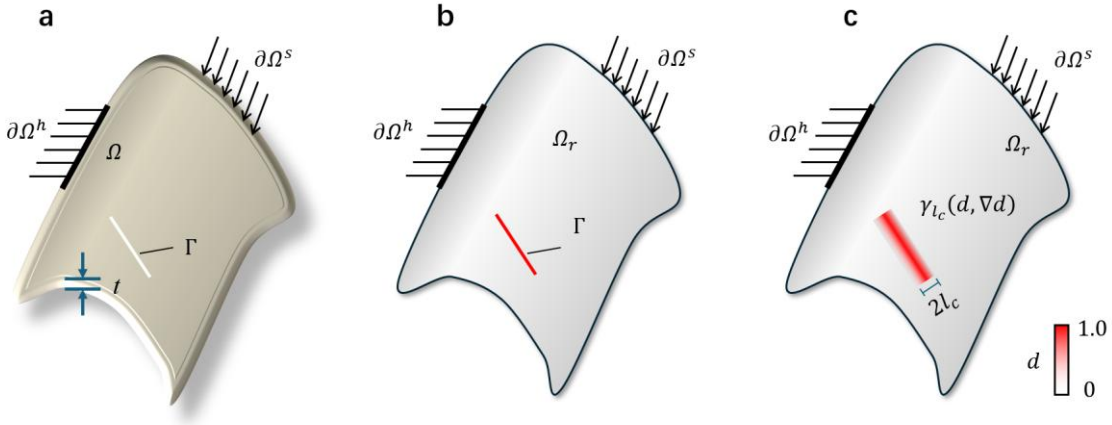

Figure 5.2 Regularisation of sharp crack to damage zone based on l_c. (a) fracture topology of the shell (b) sharp crack on shell reference surface; (c) regularised phase field distribution on shell reference surface

5.2.3 Energy function and governing equations

The total energy function within the shell could be written following our previous work (Fang, Wu et al. 2019, Li, Fang et al. 2022, Jiang, Li et al. 2023, Li, Fang et al. 2024) as below,

$$\Phi = \int_{-\frac{h}{2}}^{\frac{h}{2}} \int_{\Omega^r} \left(\psi^e + \psi^p + \psi^k + \psi^f + \psi^{vis}\right) \mathrm{d}S\mathrm{d}h - \int_{-\frac{h}{2}}^{\frac{h}{2}} \left(\int_{\Omega^r} (\boldsymbol{t} \cdot \boldsymbol{u}) \mathrm{d}S - \int_{\partial\Omega_r^s} (\boldsymbol{b} \cdot \boldsymbol{u}) \mathrm{d}s \right) \mathrm{d}h \tag{5.8}$$

where h is the shell thickness; $\boldsymbol{t}$, $\boldsymbol{b}$, and $\boldsymbol{u}$ denote the body force on Ω, boundary traction on $\partial\Omega_r^s$, and displacement within shell; ψ^e, ψ^p, ψ^k, ψ^f and ψ^{vis} represent the elastic strain energy, plastic work , kinematic energy, fracture energy, and damage viscosity energy density functions per area on Ω^r, respectively. The elastic strain energy density ψ^e can be obtained as follows,

$$\psi^e(\boldsymbol{u}, d) = \mathrm{g}(d) \cdot \psi_0^e = \frac{1}{2} \cdot \mathrm{g}(d) \cdot \overline{\boldsymbol{\sigma}} : \boldsymbol{\varepsilon}^e \tag{5.9}$$

where $\mathrm{g}(d) = (1-d)^2$ is quadratic strain energy degradation function. $\boldsymbol{\varepsilon}^e$ and $\overline{\boldsymbol{\sigma}}$ represent the elastic strain tensor and corresponding (undamaged) effective stress tensor. It is noted that the update of stress state for the shell element is based on the local coordinate $\boldsymbol{t}_1$-$\boldsymbol{t}_2$-$\boldsymbol{t}_3$,as shown in Figure 5.1. In this study, we focused on the thin shell element where the stress components $\bar{\sigma}_{33}$, $\bar{\sigma}_{13}$ and $\bar{\sigma}_{23}$ are all excluded for calculation, resulting in much higher computational efficiency compared with 3D phase field model. The plastic density ψ^p is calculated by,

$$\psi^p(\bar{\varepsilon}^p, d) = \mathrm{g}(d) \cdot \psi_0^p = \mathrm{g}(d) \cdot \int_0^{\bar{\varepsilon}^p} \bar{\sigma}_y(\bar{\varepsilon}^p)\, \mathrm{d}\bar{\varepsilon}^p \tag{5.10}$$

where $\bar{\varepsilon}^p$ and $\bar{\sigma}_y$ represent the accumulated plastic strain and corresponding (undamaged) effective yield stress. In Eq.(5.10) the plastic work is degraded as the phase field develops, leading to degraded yield stress, following our previous work (Fang, Wu et al. 2019, Fang, Wu et al. 2019, Li, Fang et al. 2022). The kinematic energy density ψ^k is written as,

$$\psi^k(\dot{\boldsymbol{u}}) = \frac{1}{2} \rho \dot{\boldsymbol{u}} \cdot \dot{\boldsymbol{u}} \tag{5.11}$$

where ρ is the material density; $\dot{\boldsymbol{u}}$ denotes the displacement rate. The fracture energy ψ^f and damage viscosity energy density ψ^{vis} functions are given by

$$\psi^f(d, \nabla d) = G_f \cdot \left(\frac{d^2}{2l_c} + \frac{l_c}{2} |\nabla d|^2 \right) \tag{5.12}$$

$$\psi^{vis}(\dot{d}) = \int_0^t \left(\frac{\omega}{2} \dot{d} \cdot \dot{d} \right) \mathrm{d}\tau \tag{5.13}$$

where G_f is the crack energy release rate, denoting the required energy for generating a unit area of crack surface; ω is the introduced viscosity parameter (Li, Fang et al. 2024); $\dot{d}$ denotes the damage evolution rate; t represents the current loading time.

Substitution of Eqs.(5.9)-(5.13) into Eq.(5.8) leads to the final total energy function Φ, as below,

$$\Phi(\boldsymbol{u}, \bar{\varepsilon}^p, d) = \int_{-\frac{h}{2}}^{\frac{h}{2}} \int_{\Omega^r} \left\{ \frac{1}{2}(1-d)^2 \overline{\boldsymbol{\sigma}} : \boldsymbol{\varepsilon}^e + (1-d)^2 \cdot \int_0^{\bar{\varepsilon}^p} \bar{\sigma}_y(\bar{\varepsilon}^p) \mathrm{d}\bar{\varepsilon}^p + \frac{1}{2}\rho \dot{\boldsymbol{u}} \cdot \dot{\boldsymbol{u}} + G_f \cdot \left(\frac{d^2}{2l_c} + \frac{l_c}{2} |\nabla d|^2 \right) + \int_0^t \left(\frac{\omega}{2} \dot{d} \cdot \dot{d} \right) \mathrm{d}\tau \right\} \mathrm{d}\Omega^r \mathrm{d}h - \int_{-\frac{h}{2}}^{\frac{h}{2}} \left\{ \int_{\Omega^r} (\boldsymbol{t} \cdot \boldsymbol{u}) \mathrm{d}\Omega^r - \int_{\partial\Omega_r^s} (\boldsymbol{b} \cdot \boldsymbol{u}) \mathrm{ds} \right\} \mathrm{d}h \tag{5.14}$$

By taking variation on total energy function Φ, the governing equations for displacement field and phase field in strong form could be obtained as follows (Li, Fang et al. 2024),

$$\begin{cases} \nabla \cdot \boldsymbol{\sigma} + \boldsymbol{b} = \rho\, \ddot{\boldsymbol{u}} & \text{in } \Omega \\ \boldsymbol{\sigma} \cdot \boldsymbol{n} - \boldsymbol{t} = 0 & \text{on } \partial\Omega_r^s \\ \boldsymbol{u} = \overline{\boldsymbol{u}} & \text{on } \partial\Omega_r^h \end{cases} \tag{5.15}$$

$$\begin{cases} \dot{d} = \frac{1}{\omega} \langle 2(1-d)\left(\varphi_0^e + \varphi_0^p\right) - \frac{G_f}{l_c}\left(d - {l_c}^2 \Delta d\right) \rangle_+ & \text{in } \Omega \\ \nabla d \cdot \boldsymbol{n} = 0 & \text{on } \partial\Omega \end{cases} \tag{5.16}$$

5.2.4 Hill 48 Plastic formulation

To consider the anisotropic mechanic behaviour, especially for the additive manufacturing structures, the Hill 48 plastic model is adopted in this current study. For three-dimension case, the formulation of Hill 48 yield stress is written as,

$$\bar{f}(\overline{\boldsymbol{\sigma}}) = \sqrt{F(\bar{\sigma}_{yy} - \bar{\sigma}_{zz})^2 + G(\bar{\sigma}_{zz} - \bar{\sigma}_{xx})^2 + H(\bar{\sigma}_{xx} - \bar{\sigma}_{yy})^2 + 2N{\bar{\sigma}_{xy}}^2 + 2M{\bar{\sigma}_{xz}}^2 + 2L{\bar{\sigma}_{yz}}^2} \tag{5.17}$$

where F, G, H, L, M, and N are material parameters; $\bar{\sigma}_{xx}$, $\bar{\sigma}_{yy}$, $\bar{\sigma}_{zz}$, $\bar{\sigma}_{xy}$, $\bar{\sigma}_{xz}$ and $\bar{\sigma}_{yz}$ are six stress components of the (undamaged) effective stress tensor. For shell element, the stress update is based on the local coordinates and those stress components related to the thickness direction are set to zero and Eq.(5.17) could be rewritten as,

$$\bar{f}(\overline{\boldsymbol{\sigma}}) = \sqrt{(H+G){\bar{\sigma}_{11}}^2 + (H+F){\bar{\sigma}_{22}}^2 - 2H\bar{\sigma}_{11}\bar{\sigma}_{22} + 2N{\bar{\sigma}_{12}}^2} \tag{5.18}$$

where the local coordinate directions $\boldsymbol{t}_1$-$\boldsymbol{t}_2$ are parallel to local shell surface, and $\boldsymbol{t}_1$ denotes the projection of printing direction on the local surface. Such simplification in shell element could significantly reduced its computation cost for updating the stress and plastic strain compared with its counterpart in the solid element.

5.2.5 Fracture initiation criteria and crack irreversibility

From Eq.(5.16), it is noted that the unrealistic fracture would initiate immediately even under a negligible loading. To capture fracture initiation for ductile material properly, the fracture strain has to be incorporated into this proposed shell phase field model. It has been widely discussed in literature(Bai and Wierzbicki 2009, Li, Fang et al. 2022, Li, Fang et al. 2023, Yang, Guo et al. 2023, Li, Fang et al. 2024) that the ductile fracture strain depends on the stress state rather than a constant value. For instance, the modified Mohr-Coulomb (MMC) criterion (Bai and Wierzbicki 2009, Da Silva Santos, Sarzosa et al. 2022) has been applied to describe the ductile fracture initiation regarding the stress triaxiality and Lode angle parameter, and lately incorporated into the phase field framework (Li, Fang et al. 2022, Li, Fang et al. 2023). Moreover, a so-called Bao-Wierzbicki model was introduced to model the damage initiation for Ti-6Al-4V alloy where the fracture strain depends only on the stress triaxiality (Bao and Wierzbicki 2004).

Due to the proved high accuracy of modelling fracture initiation, the above mentioned MMC and Bao-Wierzbicki model are adopted here to predict the fracture bahaviour for additively manufactured 316L and Ti-6Al-4V materials, respectively. Though only those two specific fracture criterions are studied here, the selection of fraction initiation model is quite flexible in this proposed shell phase field model, which can be easily substituted with alternative models depending on the materials under investigation. The modified M-C (MMC) fracture criterion is expressed as follows,

$$\varepsilon^f(\eta,\tilde{\theta}) = \left\{\frac{A}{c_2}\left[c_3 + \frac{3(1-c_3)}{2\sqrt{3}-3}\left(\sec\left(\frac{\tilde{\theta}\pi}{6}\right)-1\right)\right]\left[\sqrt{\frac{1+{c_1}^2}{3}}\cos\left(\frac{\tilde{\theta}\pi}{6}\right) + c_1\left(\eta + \frac{1}{3}\sin\left(\frac{\tilde{\theta}\pi}{6}\right)\right)\right]\right\}^{-\frac{1}{n}} \tag{5.19}$$

where η and $\tilde{\theta}$ are stress triaxiality and Lode angle parameter respectively; A, n, c_1, c_2, c_3 are five MMC fracture strain parameters, which could be calibrated by conducting loading test on specimen under different stress states. Readers are encouraged to refer to our previously published paper (Li, Fang et al. 2022, Li, Fang et al. 2024) for further details. Regarding the Bao-Wierzbicki fracture locus, the fracture strain is assumed to be dependent of stress triaxiality only as,

$$\varepsilon^f(\eta) = \begin{cases} \frac{B_1}{3\eta+1} + B_2 - B_1 & -\frac{1}{3} < \eta \leq 0 \\ \frac{B_5}{B_3}\eta^2 + \frac{B_4 - B_2 - B_3 \cdot B_5}{B_3}\eta + B_2 & 0 < \eta \leq B_3 \\ (B_4 - B_7)e^{-B_6(\eta - B_3)} + B_7 & \eta > B_3 \end{cases} \tag{5.20}$$

where B_1, B_2, B_3, B_4, B_5, B_6 and B_7 are seven independent Bao-Wierzbicki fracture strain parameters. Moreover, the fracture strain is cut-off when the triaxiality is less than -0.33 to avoid the unrealistic fracture initiation for metal material under compression stress state. According to Eq.(5.19) and Eq.(5.20), both MMC and Bao-Wierzbicki fracture strain are plotted in Figure 5.3. Additionally, For the nonproportional loading, a historical damage indicator D is calculated by,

$$D(\bar{\varepsilon}^p) = \int_0^{\bar{\varepsilon}^p} \frac{d\bar{\varepsilon}^p}{\varepsilon^f(\eta, \tilde{\theta})} \tag{5.21}$$

where $\bar{\varepsilon}^p$ represents the equivalent plastic strian. As the accumulation of $\bar{\varepsilon}^p$ during the loading process, the indicator D increases with a stress state-dependent rate. With the indicator D in hand, the fracture energy threshold H^{ini} is then defined as the strain energy when $D = 1$. Following (Miehe, Hofacker et al. 2015, Li, Fang et al. 2022, Jiang, Li et al. 2023), a state energy formulation $state(X, t)$ is introduced to indicate the crack crack driving force at position X and at time t within the shell Ω as below,

$$state(X, t) =< \varphi_0^e + \varphi_0^p - H^{ini} >_+ \tag{5.22}$$

To avoid the unrealistic fracture healing, the history energy function H is then defined as the maximum state energy during the loading process,

$$H = \max_{\tau \in [0, t_n]} state^t(X, \tau) \tag{5.23}$$

Replacing the term of $\left(\varphi_0^e + \varphi_0^p\right)$ in Eq.(5.16) with H could lead to the final phase field evolution governing equations,

$$\begin{cases} \dot{d} = \frac{1}{\omega}\langle 2(1-d)H - \frac{G_f}{l_c}\left(d - {l_c}^2 \Delta d\right)\rangle_+ & \text{in } \Omega \\ \nabla d \cdot \boldsymbol{n} = 0 & \text{on } \partial\Omega \end{cases} \tag{5.24}$$

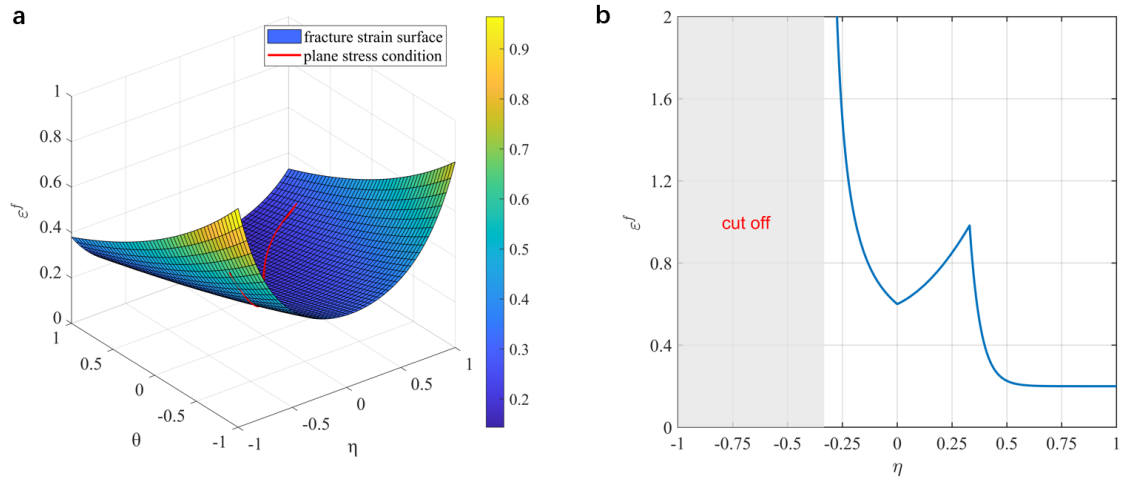

Figure 5.3 Stress-dependent fracture strain. (a) MMC fracture strain along with stress triaxiality and Lode angle parameter; (b) Bao-Wierzbicki fracture strain along with stress triaxiality

5.3 Numerical examples

5.3.1 One element

To validate the implementation of the proposed shell phase field model, a one-element test was conducted numerically with different model parameters and compared with analytical solution. The boundary condition is depictured in Figure 5.4(c) where a four-node shell element, with dimension of 1.0 × 1.0 mm, is constrained as follows: the bottom left node is fully fixed in both $\boldsymbol{x}$ and $\boldsymbol{y}$ directions, while the bottom right node is constrained only in the $\boldsymbol{y}$ direction; Additionally, an extraction force is applied in the $\boldsymbol{y}$ direction at the two nodes along the top edge. In this section, the effect of viscosity parameter ω and fracture strain ε_{cr} on the phase field evolution and mechanical response were studied by conducting two groups of numerical examples respectively, and all the related model parameters are presented in Table 5.1.

5.3.1.1 Different fracture viscosity parameter

To easily deduce the analytical solution, the anisotropic Hill48 yield criterion in Eq.(5.18) is degraded into von Mise yield criterion and the linear hardening is assumed. Moreover, the fracture strain is simplified as a constant value, here just take it as 0.4 for instance. The homogenous solution of shell phase field evolution can be solved easily by ignoring the gradient term and viscosity fracture energy in Eq.(5.24) (Wang, Han et al. 2022), and the deduced expression could be rewritten as,

$$d = \frac{2Hl_c}{2Hl_c + G_f} \tag{5.25}$$

where H represents the phase field history variable and is set zero until the equivalent plastic strain reaching 0.4.

Table 5.1 Model parameters for one-element test

Type	Parameters	Value
Elastic	E	210 GPa
	υ	0.3
Plastic	σ_0	700 MPa
	h	800 MPa
Fracture	G_f	1.0 N/mm
	l_c	1.0 mm
	ε_{cr}	0.1, 0.2, 0.3 and 0.4

The stress-strain and damage-strain curves for the one element tension test with different viscosity parameters are demonstrated in Figure 5.4 along with the analytical solution. All the numerical and analytical stress-strain curves initially demonstrated rapid increase, corresponding to the short elastic stage until the stress σ_{yy} growing to 700 Mpa. Then materials stepped into the elasto-plastic stage where most deformation was due to the plastic dissipation, while the slow increase of stress response resulted from the linear plastic hardening. It is also noted that all of the numerical and analytical stress-strain results exhibited identical curves before fracture imitation when the plastic strain increased to the fracture strain of 0.4, with stress peaking at approximate 1000 MPa. After this point, stress-strain curves dropped immediately due to quick growing of phase field damage. It is also found that as the viscosity parameter ω decreases from 10^{-4} to $10^{-7}\mathrm{kN}\cdot\mathrm{s}/mm^2$, the phase field damage developed faster, and stress dropped in a quicker rate. In addition, when ω reaches $10^{-6}\mathrm{kN}\cdot\mathrm{s}/mm^2$, the numerical result in terms of both phase field evolution and stress-strain curve converged to the analytical solution, indicating the correct implementation of this shell phase field model.

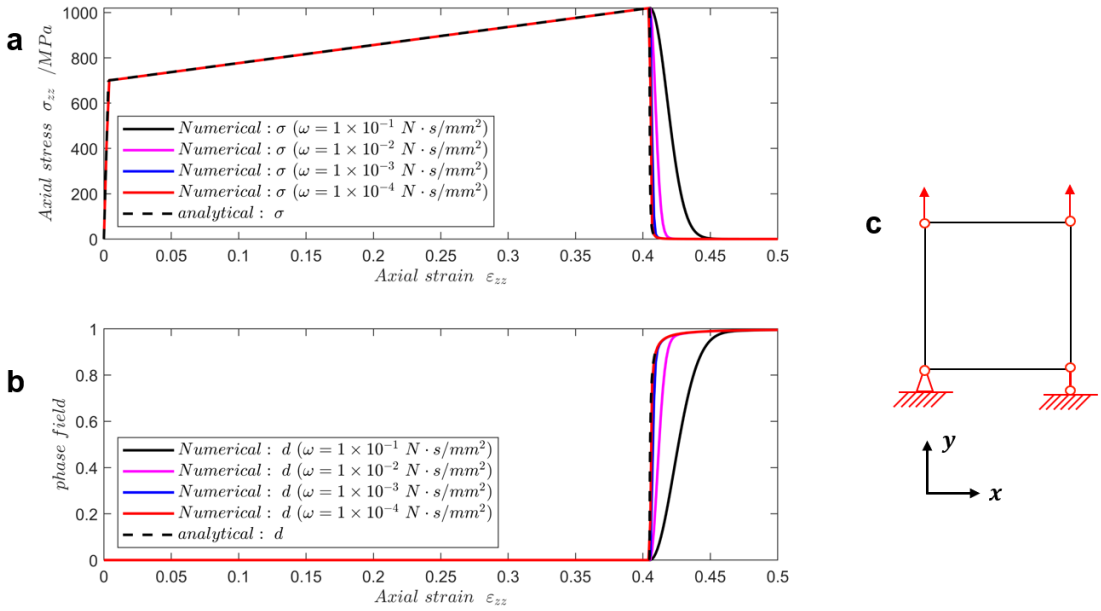

Figure 5.4 Uniaxial tension stress-strain and damage evolution for specimens with different viscosity parameters. (a) stress-strain curve; (b) phase field-strain curve; (c) boundary condition of the one-element tension test

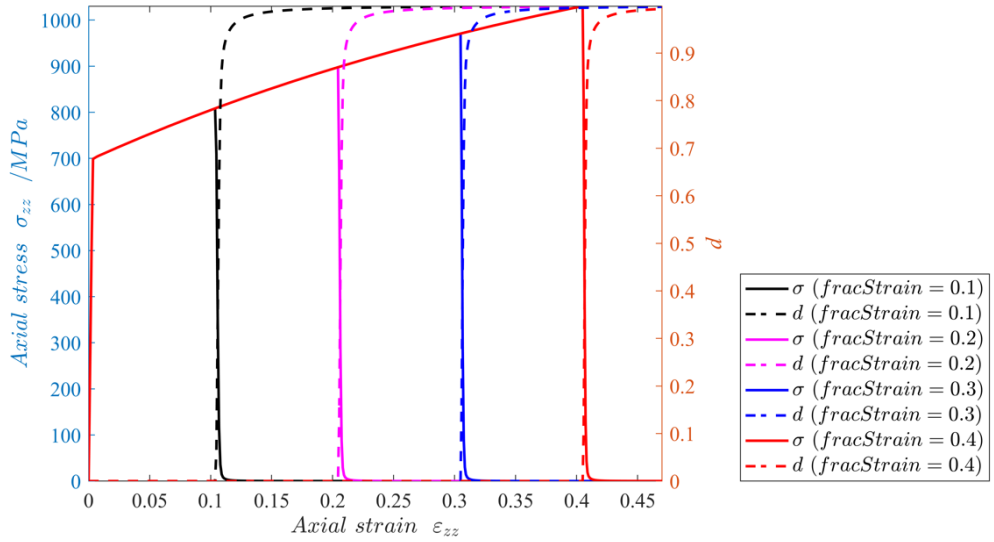

Figure 5.5 Uniaxial tension stress-strain and damage evolution for specimens with different fracture initiation strains

5.3.1.2 Different fracture strain

In the second group of one-element tension test, four numerical examples were conducted where the fracture viscosity parameter was fixed as $10^{-6}\mathrm{kN}\cdot\mathrm{s}/mm^2$, while the fracture strain was set as 0.1, 0.2, 0.3 and 0.4 respectively. The widely used Voce hardening law (Voce 1955) was adopted here to describe the hardening, written as below,

$$\sigma_y(\bar{\varepsilon}^p) = \sigma_{y0} + m_1\left(1 - e^{-m_2\cdot\bar{\varepsilon}^p}\right) \tag{5.26}$$

where σ_y and $\bar{\varepsilon}^p$ represent the yeiled stress and equivalent plastic strain; σ_{y0}, m_1 and m_2 are three nonlinear hardening parameters, and their values are all listed in Table 5.1.

The phase field evolution and stress strain along with the axial strain were plot in Figure 5.5. The stress-strain curves for all specimens exhibit an initial sharp increase during the elastic stage, followed by nonlinear plastic hardening once the stress exceeds 700 MPa. During the elasto-plastic loading stage, plastic deformation dominates the total strain, with a gradual increase in stress due to material hardening. As the plastic strain approaches the fracture strain in these numerical simulations, phase-field damage begins to develop rapidly, causing the stress to reach peak values of approximately 810 MPa, 900 MPa, 970 MPa, and 1030 MPa, respectively, followed by a rapid decline.

5.3.2 Notched cylinder under axial tension

In this example, a notched cylinder shell is examined, which has been tested in the previous studies(Ambati and De Lorenzis 2016, Ma, Sun et al. 2024). The geometry and boundary conditions are depicted in Figure 5.6(a). The shell, with a radius *R*=5 mm, length *L*=15 mm and thickness *h*=0.125 mm, contains a circumferential through-thickness pre-crack with length of $a_0 = \Theta R$, where $\Theta = \pm 10°$. The shell is fixed at its left end, while an axial tensile displacement is applied to its right end until complete failure. As shown in Figure 5.6(b), only half of the shell is simulated with symmetric boundary conditions. The model is meshed with 15,825 shell elements, with a denser mesh around the pre-crack in the middle. The mesh size in this dense area is 0.04 mm.The material parameters are referred from previous studies (Ambati and De Lorenzis 2016, Ma, Sun et al. 2024) and listed in Table 5.2.

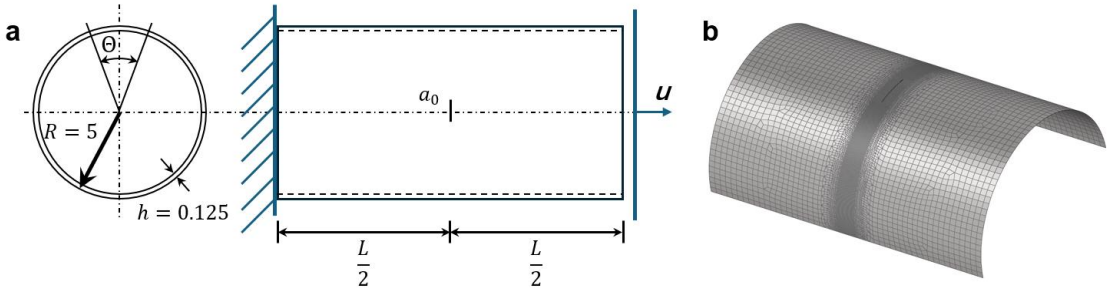

Figure 5.6 (a) Geometry and boundary condition for the uniaxial tension test on the notched cylinder shell; (b) mesh information for the symmetric half model

The force-displacement curves for specimens with four different critical fracture strains (ε_{cr} = 0.1, 0.2, 0.3 and 0.4) are plotted in Figure 5.7(a). The entire loading process

can be roughly divided into three stages. In the initial elastic stage, when the applied displacement is less than 0.05 mm, most of the material undergoes elastic deformation except for a very small region around the pre-crack tip. During this stage, the force-displacement curves exhibit a linear increase.

Next, as the applied displacement increases from 0.05 mm to 0.08 mm, the plastic region expands along the pre-crack orientation, forming a plastic band in the middle of the notched shell. This is indicated by the Mises stress distribution depicted in Figure 5.7 (b). Meanwhile, during this second stage, the plastic strain around the pre-crack tip develops rapidly and exceeds the critical fracture strain, leading to fracture initiation in that area. Due to the combined effects of plastic band formation and fracture initiation at the pre-crack tip, the reaction forces of all curves continue to increase but at a decreasing rate, reaching their peak values before starting to decline. It is also noted that as the critical fracture strain increases, fracture initiation is delayed, and the peak force decreases correspondingly. Since the fractured area in this stage is still quite small, the differences in peak force shown in Figure 5.7 (a) are relatively moderate.

After fracture initiation, phase field variables develop quickly along the pre-crack orientation, forming a through-cylinder crack path. The reaction forces experience an obvious decline, and the critical fracture strain has a significant effect on the rate of force decrease. As shown in Figure 5.7 (a), a larger critical fracture strain delays the formation of the fracture path and leads to a slower decrease in force. It is also noted that the dashed black line in the force-displacement curve represents the specimen without considering phase field damage and demonstrates a slight decrease with applied displacement. This is due to necking in the thickness direction caused by large deformation along the shell surface within the plastic band area.

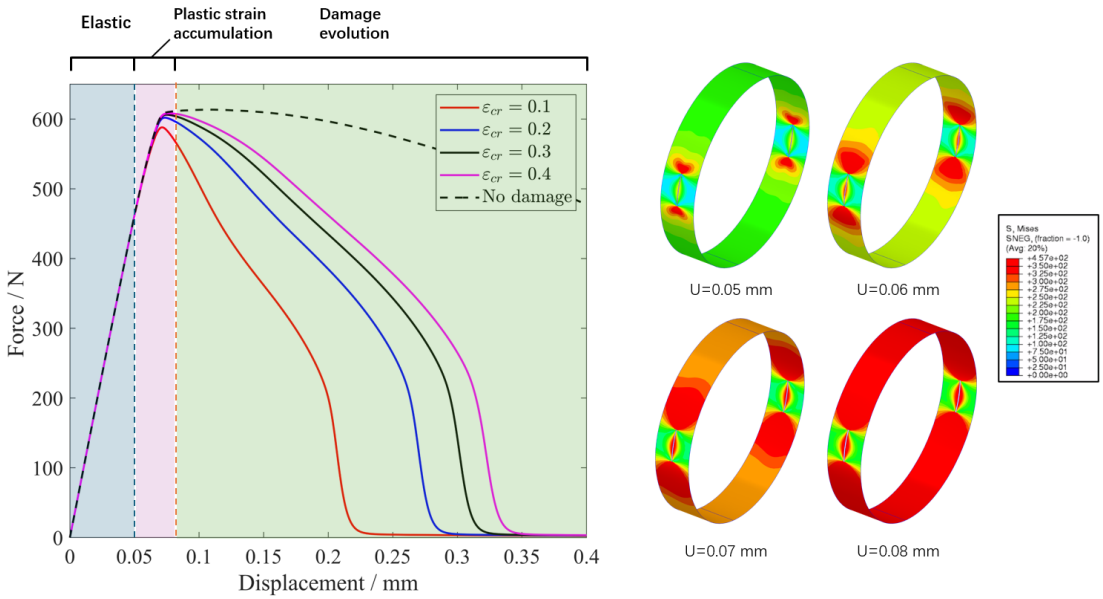

Figure 5.7 Force displacement curves for notched cylinder specimen under uniaxial tension load

The crack paths for specimens with different fracture strain (ε_{cr}=0.1, 0.2 and 0.4) are presented in Figure 5.8. As the applied displacement increases, all specimens initiate fracture at the pre-crack tip and develop along the middle cross section of the notched cylinder, forming a circumferential fracture band consistent with previous studies (Ambati and De Lorenzis 2016, Reinoso, Paggi et al. 2017, Ma, Sun et al. 2024). It can also be observed that the fracture strain has a significant effect on the evolution of fracture path. When the applied displacement increases from 0.08 mm to 0.15 mm, quicker crack path evolution occurs in specimens with smaller fracture strains. When the displacements reach 0.24 mm, 0.30 mm, and 0.36 mm, respectively, through-circumferential fracture bands are observed on the shell surfaces of these three specimens, corresponding to the reaction forces falling to zero in Figure 5.7 for the respective specimens.

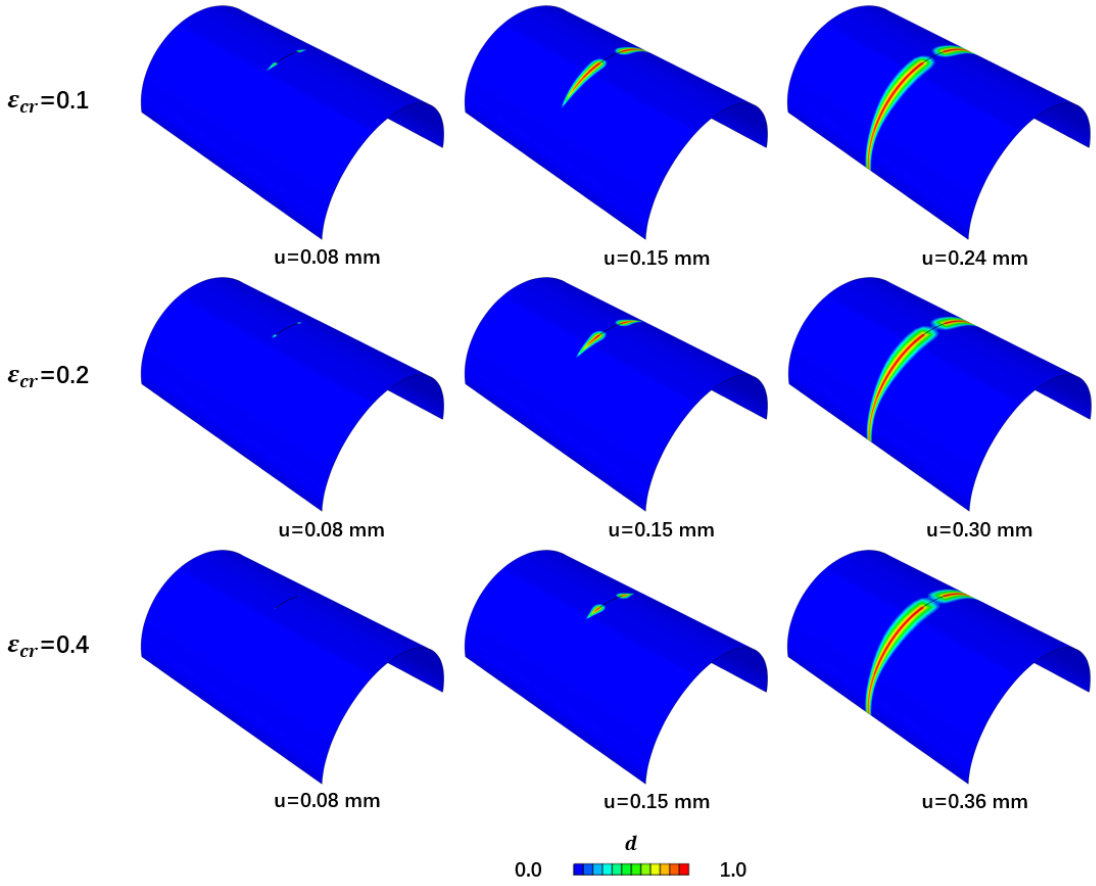

Figure 5.8 Evolution of fracture path for the notched cylinder tension specimen with different critical fracture strains.

Table 5.2 Model parameters for notched cylinder under axial tension test (Ambati and De Lorenzis 2016)

Type	Parameters	Value
Elastic	E	72.6 GPa
	υ	0.32
Plastic	σ_0	345 MPa
	h	250 MPa
Fracture	G_t	9.3 N/mm
	l_c	0.05 mm
	ε_{cr}	0.1, 0.2, 0.3 and 0.4

5.3.3 Notched cylinder under internal pressure

In this example, the fracture propagation on the axially notched cylinder was modelled by the proposed shell phase field model, which were been experimentally tested (Keesecker, Dávila et al. 2003) and numerically researched in many previous studies(Ulmer, Hofacker et al. 2012, Ambati and De Lorenzis 2016, Kiendl, Ambati et al. 2016, Wang, Han et al. 2022). Two distinct boundary conditions were studied in this section, where the notched cylinder was and was not constrained by two circumferential

straps. The geometry and boundary condition of the specimen are specified same as the experimental set up. As illustrated in Figure 5.9, the notched cylinder was under internal pressure, which are applied on the inner surface gradually until the breakage of the specimen. The model was meshed by 17642 and 35518 S4R elements for the unstrapped and strapped specimens, respectively, with the element size around the potential crack region set to be 1 mm. The elastic and plastic material parameters in this study also keep consistent with those in literature (Keesecker, Dávila et al. 2003). In terms of the fracture energy release rates, we refer to the previous numerical studies (Wang, Han et al. 2022).

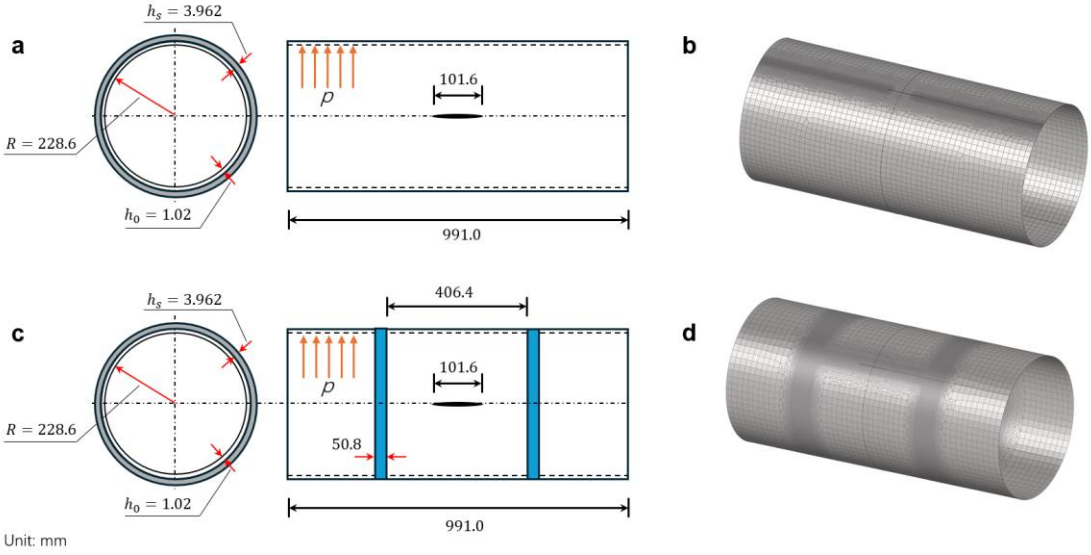

Figure 5.9 Geometry, loading condition and mesh information for axially notched cylinder specimen under internal pressure with and without strap constraint

The simulation results of phase field contour on deformed specimens without strap is demonstrated in Figure 5.10, where the element with phase field variable larger than 0.95 was removed for better visualisation. As the internal pressure continued to increase, the fracture initiated at the notch tip. Then the rising circumferential stress at notch tip promote the fracture propagation along the axial direction and formation a horizontal crack path towards to the two ends of the cylinder.

Compared with specimen without strap, the strapped cylinder also initiate fracture at the notch tip and develop along the axial direction until reaching the straps. Due to the constraint of the strap, the deformation of the cylinder along the circumferential direction is limited, while the axial stress continues to increase caused by the rising internal pressure and axial curvature. Once the axial stress is larger than hoop stress, the fracture path was turning to develop circumferentially, termed as ‘flapping’, which could avoid

the continuous crack propagation along the axial direction. Figure 5.11 also compared the experimental crack path with our simulation result, showing that our proposed shell phase field model could effectively model such flapping phenomena.

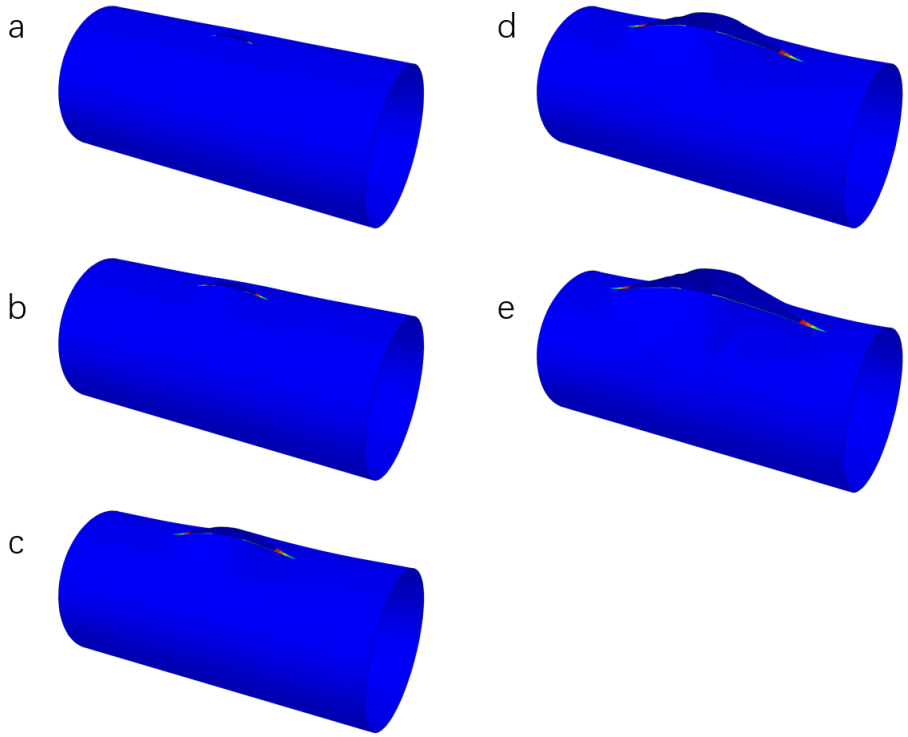

Figure 5.10 Fracture path evolution for the notched cylinder under internal pressure without strap

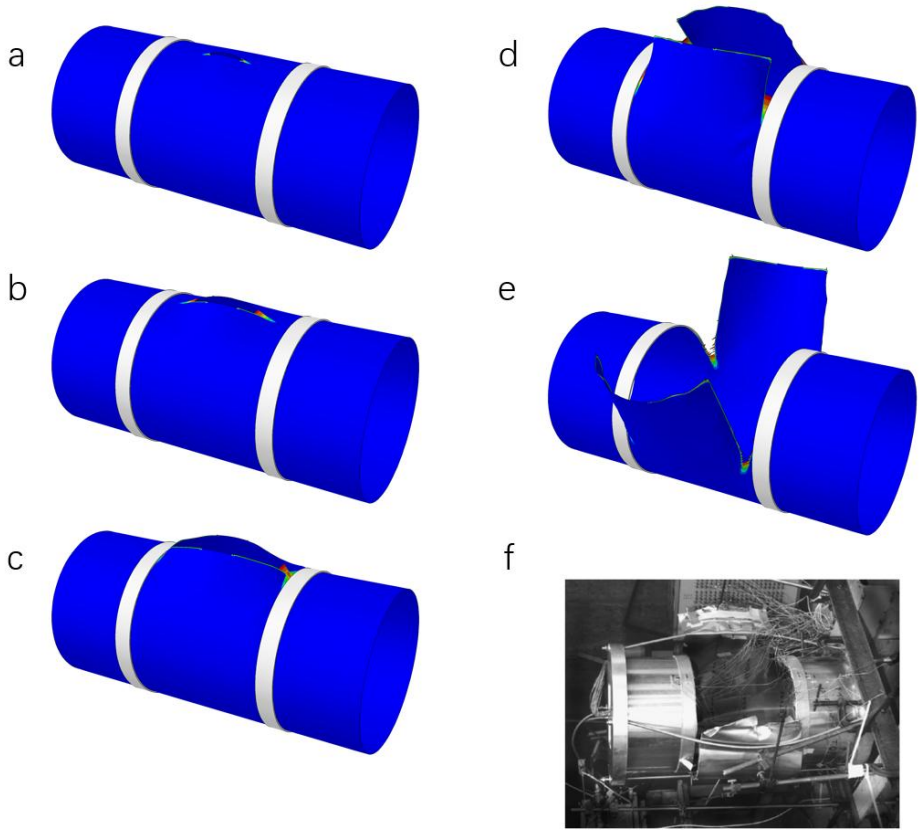

Figure 5.11 Fracture path evolution for the notched cylinder under internal pressure with strap

5.3.4 Validation by 316 steel tube tests

Although several shell phase field models have been proposed in the literature, their validation remains insufficient. Most of those models have been tested against only a limited number of benchmark numerical examples, with few studies comparing their results to experimental observations. Furthermore, when such comparisons are made, they predominantly focus on quantitative analysis rather than qualitative insights. In this study, a three-point bending test was conducted using a square tube specimen fabricated from 316L steel, and the proposed shell phase field model was applied to simulate the fracture behaviour and mechanical response observed in the experiment. By comparing experimental and numerical results, including force-displacement curves and structural deformation, the validity of the proposed model was rigorously assessed. Meanwhile, material parameters in this example were calibrated based on the material specimens to demonstrate the model's accuracy. This study provides evidence of the potential applicability of the shell phase field model for fracture modelling in real-world scenarios, offering supplementary validation through experimental data.

5.3.4.1 Material specimen

It has been discussed in literature that the fracture strain for metal material varies under distinct stress states instead of being constant. To accurately capture the fracture behaviour of the specimen in this example, the MMC formulation (see Eq.(5.19)) was employed to describe the fracture strain as a function of stress triaxiality and the Lode angle parameter, which has been proved a effective method for prediction of the fracture initiation in 316L steel. A group of material specimens were prepared for calibrating the the fracture strain parameters, including specimens for uniaxial tension, simple shear, notched tension with radius of 5 and 10 mm, and central hole tension, as demonstrated in Figure 5.12. The detailed experimental set up is referred in our previous publication(Li, Fang et al. 2024).

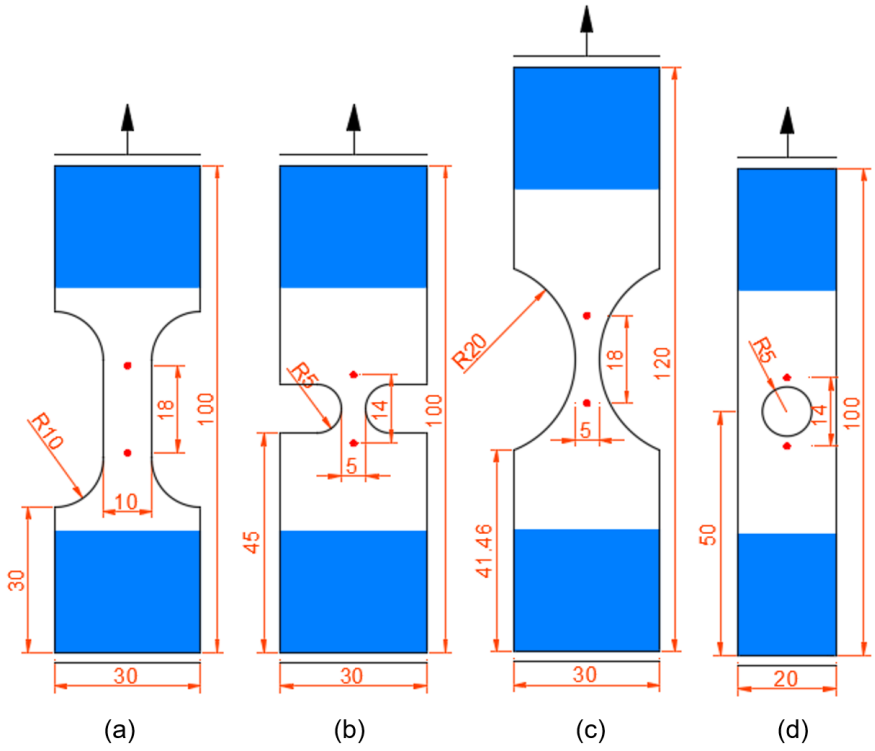

Figure 5.12 Geometry and boundary condition of the material specimens. (a) uniaxial tension; (b) notched tension with radius of 5 mm; (c) notched tension with radius of 20 mm; (d) central hole tension.

The material parameters were previously calibrated through 3D solid element analysis, as detailed in our earlier publication(Li, Fang et al. 2024), and listed in Table 5.3. In this study, these parameters were directly applied to the shell phase field fracture modelling due to their intrinsic characteristics.

The simulation results of those four material specimens are presented in Figure 5.13,

where both the force-displacement curves and fracture paths were compared with the experimental data. As shown, the numerical force-displacement curves for all four specimens can be divided into three distinct stages: elastic deformation, elastoplastic hardening and fracture evolution. The numerical results show excellent agreement with the experimental data during the whole loading process. The error in maximum reaction force between the numerical and experimental results was 2.4%, 0.5%, 3.5%, and 3.9% for the uniaxial tension, notched tension with a radius of 5 mm, notched tension with a radius of 20 mm, and central hole tension specimens, respectively. The errors in applied displacement corresponding to fracture initiation were 2%, 2.2%, 11.2%, and 5.7%. All of these errors are small and within acceptable limits. Moreover, the proposed shell phase field model can capture the fracture evolution path accurately as depictured in Figure 5.13. The strong agreement between experimental observations and numerical results demonstrates the correctness and applicability of the calibrated parameters for use in the shell phase field model.

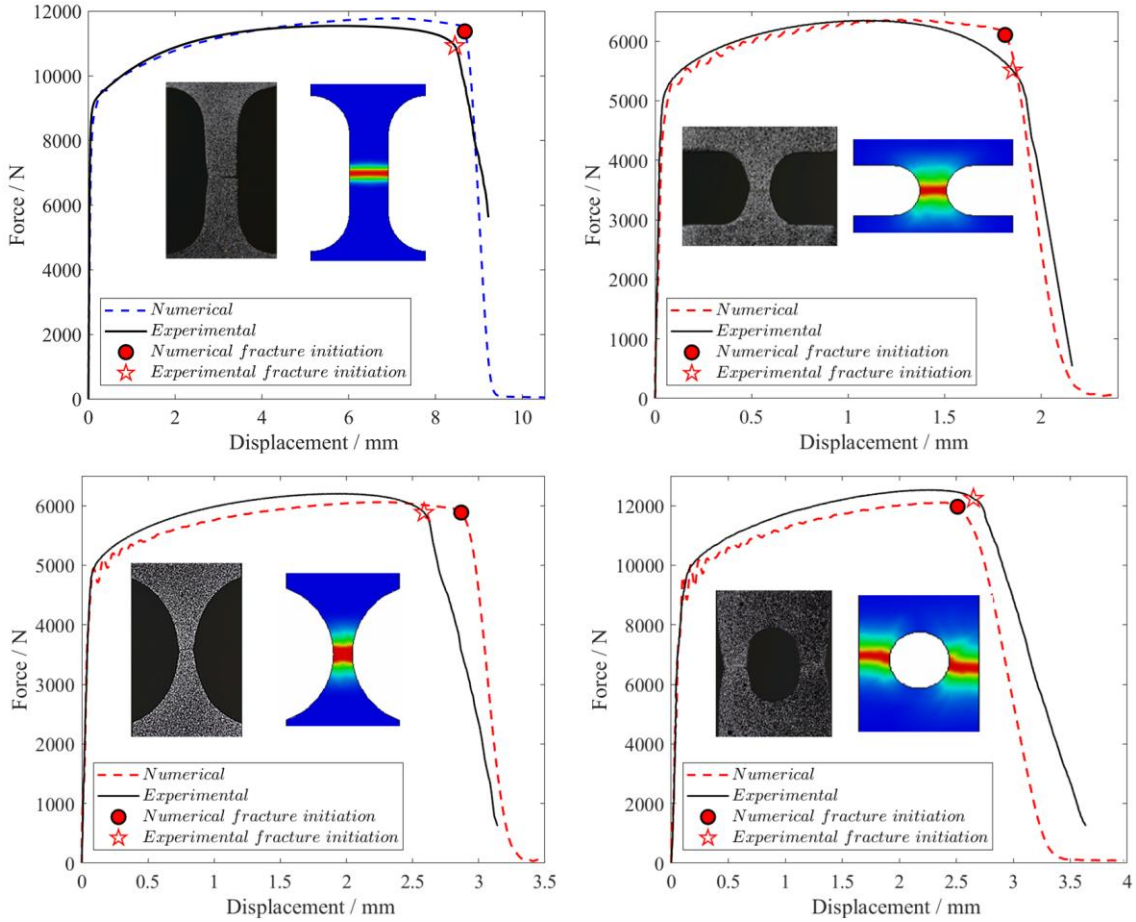

Figure 5.13 Force-displacement curve and final fracture path for material testing specimens. (a) uniaxial tension; (b) notched tension with radius of 5 mm; (c) notched tension with radius of 20 mm; (d) central hole with radius of 20 mm.

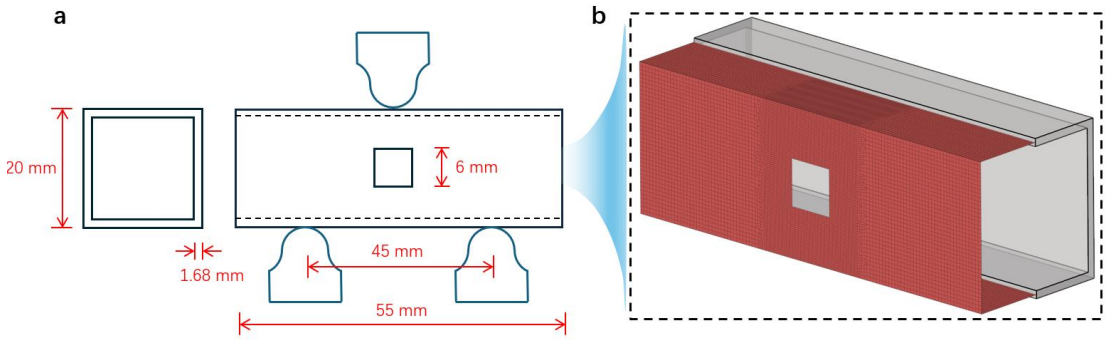

Figure 5.14 Experimental set up for the three-point bending test with square tube specimen

Table 5.3 Model parameters for 316L steel tube

Type	Parameters	Value
Elastic	E	72.6 GPa
	υ	0.32
Plastic	σ_0	345 MPa
	h	250 MPa
Fracture	G_t	9.3 N/mm
	l_c	0.05 mm
	ε_{cr}	0.1, 0.2, 0.3 and 0.4

5.3.4.2 Three-point bending test of 316 tube

The material parameters calibrated from the material specimens in previous section were utilised to simulate the three-point bending test of a square tube specimen. The geometry and boundary conditions are illustrated in Figure 5.14(a). The tube, with a thickness of 1.68 mm, features two square holes through its front and back surfaces. The specimen was loaded at the midpoint of its top surface, supported by two fixtures with span of 45 mm. Due to the symmetry of the loading condition, only half of the model was simulated with shell element, where its mid-surface was extracted and meshed by 13,975 S4R elements, as shown in Figure 5.14(b).

The force-displacement curve for this three-point test is plotted in Figure 5.16, accompanied by the experimental results. Overall, the simulation results closely match the experimental data. The whole loading process could be divided into six stages.

At initial stage, the structure underwent elastic deformation, and the reaction force increased linearly. As loading continued, plastic deformation began to develop around the loading point, causing the rate of force increase to slow. The first peak force of 10.8 kN was reached at a displacement of 1.8 mm, which is slightly lower than the experimental data.

In the second stage, a rapid drop in reaction force was observed until the displacement reached 6 mm. During this stage, the load-carrying capacity of the tube specimen was enhanced by material hardening on the top surface under bending but simultaneously weakened by the buckling effects on both side surfaces. As shown in Figure 5.15(b), the right-angle junction between the top and side surfaces collapsed, and significant plastic strain developed at the midpoint of the junction line. This initiated phase field damage, which reduced the constraint on the side surfaces, accelerating their buckling. Notably, the buckling of the side surfaces had a more significant impact on the structural response than the bending, causing the rapid force reduction during this stage.

The simulation predicted more noticeable buckling than observed experimentally (see Figure 5.15(b)), possibly due to weaker right-angle junctions in the shell element model.

In the third stage, with the applied displacement from 6 mm to 11 mm, the reaction force increased slowly. Continuous buckling on the side surface led to the formation of bulge straps at the square cut corners, angled 45 degrees towards the tube ends. These straps transferred the load to the entire tube, causing global bending, as demonstrated in Figure 5.15(c), and increased the reaction force. However, the experimental curve in Figure 5.16 showed a slight decrease during this stage, likely due to the delayed buckling in the experiment compared to the simulation, discussed in the last paragraph. Meanwhile, in this stage, phase field damage initiated at the top corners of the square cut on the outside surface, while the inside surface remained undamaged due to different stress state distribution along the tube thickness at those points.

In the fourth stage, as the load continued, the bulge strap grew and moved towards the tube ends, increasing the global bending deformation and reaction force. The stress states at the square cut corners also changed accordingly, with tensile stress switching to compressive stress on the outside surface, and compressive stress switching to tensile stress on the inside surface. This stress reversal caused crack propagation to stop on the outside surface while it continued on the inside surface at a 45-degree angle toward the tube ends.

In the fifth stage, two side surfaces under the loader was crushed to be horizontal orientation and the compressive stress dominated. The fracture propagation stopped on both inside and outside surfaces of the tube. At the same time, the reaction force rose rapidly due to the further global bending and reached its second peak force at 13.8 kN at displacement of 22.8 mm, as demonstrated in Figure 5.16.

In the last stage, large deformation caused obvious twisting at both ends of the tube (see Figure 5.15 (f)), which slipped from the supporters, leading to a sharp drop in the force-displacement curve, as observed in Figure 5.16.

5.3.5 Validation by TPMS compression test

Triply periodic minimal surface (TPMS) structures have attracted significant attention due to their potential applications in energy absorption, particularly with the rapid advancement of additive manufacturing technologies (Qiu, Wan et al. 2024). To gain deeper insights into the fracture behaviour of TPMS structures, the phase field model

has been employed for simulating crack propagation in earlier research (Préve, Lenarda et al. 2023, Wallat, Reder et al. 2023, Li, Fang et al. 2024). However, these studies predominantly discrete the model with three-dimension solid element, which necessitates a large number of mesh elements to achieve reliable results, leading to high computational demands, particularly as the number of cells in the TPMS structure increases. Despite these efforts, the application of the shell phase field model to TPMS structures remains unexplored. In the present study, we introduce a shell phase field model for simulating axial compression test on Gyroid TPMS structures. The reliability of the model was validated through comparison with experimental observations.

The experimental setup for the axial compression test is illustrated in Figure 5.17(a). The specimen was placed on the bottom fixture of a universal test machine and subjected to a load in z direction via the top fixture until densification, at loading rate of 1.2 mm/min. As shown in Figure 5.17(b), the Gyroid TPMS structure consisted of 5 cells in both the x and y dimensions, and 10 cells in the z dimension, with each cell measuring 4 mm × 4 mm × 4 mm. The volume fraction of the TPMS structure is 27%, and based on this, the average thickness of the Gyroid TPMS was calculated to be 0.349 mm. For numerical modelling, the Gyroid TPMS structure was meshed using 2270 S4R elements per cell, with an element size of 0.15 mm, as depicted in Figure 5.17(c), resulting in a total of 56,750 elements. The material parameters were taken from our earlier published paper (Li, Fang et al. 2024) and are list in Table 5.4.

Table 5.4 Model parameters for Ti-6Al-4V

Type	Parameters	Value
Elastic	E	110 GPa
	υ	0.3
Plastic	σ_0	750 MPa
	hardening parameters	(Li, Fang et al. 2024)
Fracture propagation	G_t	1.0 N/mm
	l_c	0.5 mm
Bao-Wierzbicki fracture initiation	B_1	0.3
	B_2	0.3
	B_3	2.0
	B_4	0.5
	B_5	20.0
	B_6	0.07
	η_t	0.33

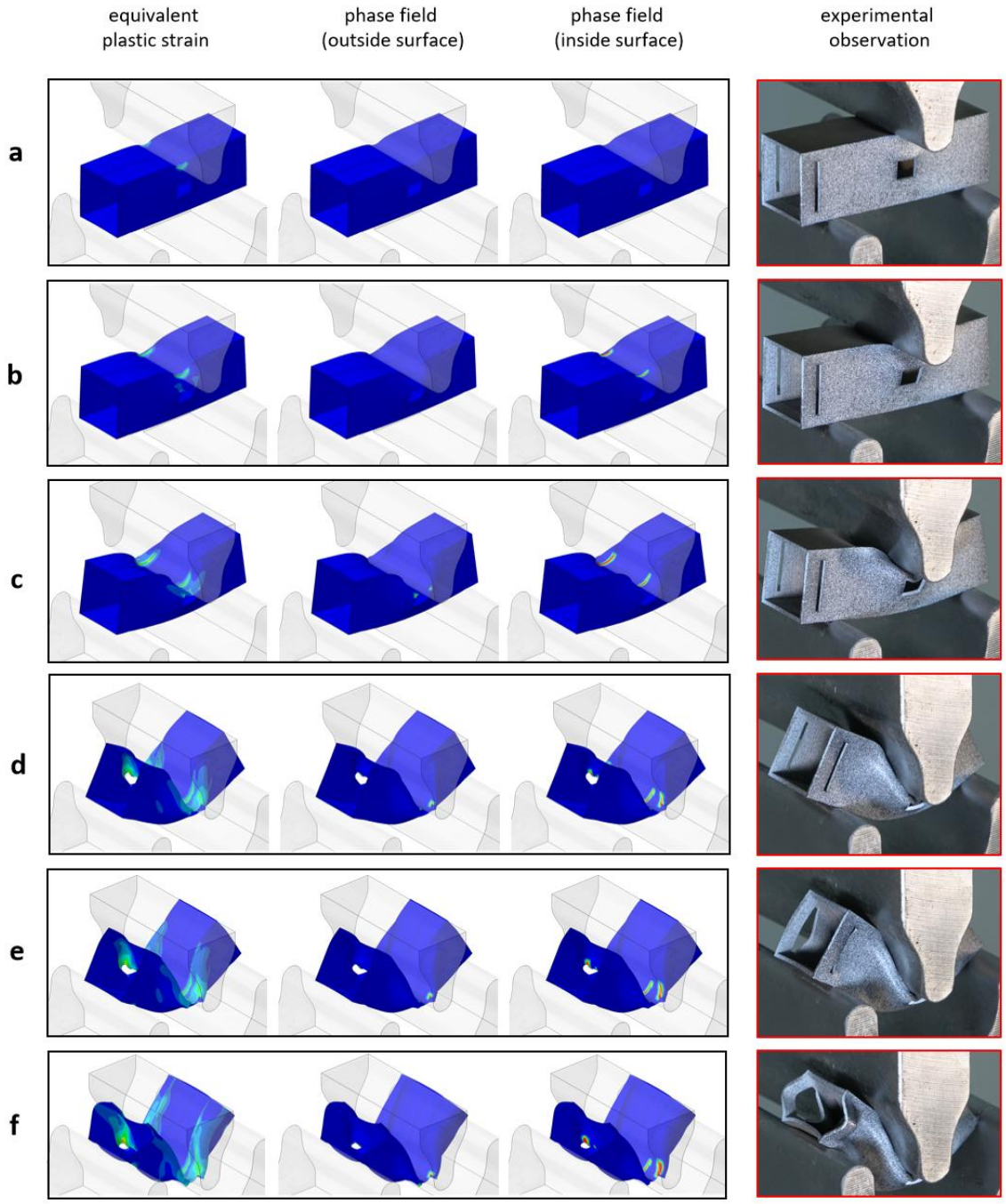

Figure 5.15 Simulation result of plastic strain and phase field distribution, accompanied with experimental observation of three-point bending test on the tube specimens during the loading process.(a) u=1.8 mm; (b) u=6 mm; (c) u=11 mm; (d) u=20 mm; (e) u=23 mm; (f) u=30 mm.

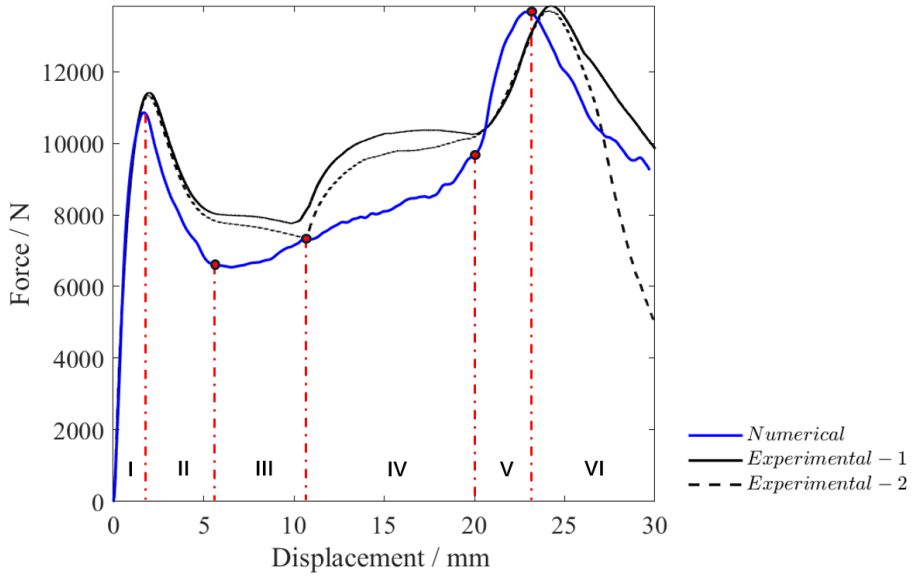

Figure 5.16 Force-displacement curve for tube three-point bending test.

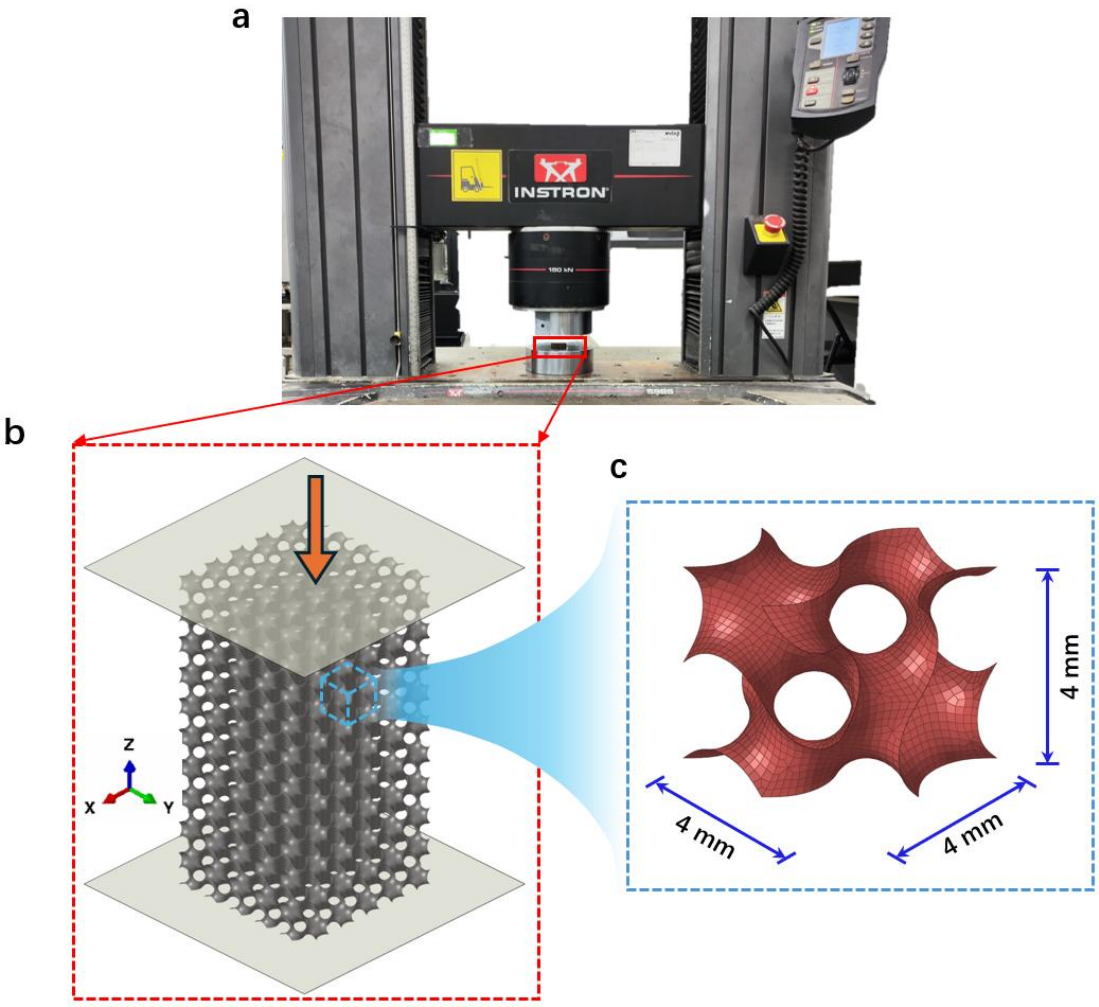

Figure 5.17 Set up of axial compression test on Gyroid TPMS structure and mesh information for one cell

5.3.5.1 Analysis of deformation characteristics during the loading process

The force-displacement curves for both the numerical and experimental data are presented in Figure 5.18. Both curves show an initial rapid linear increase, followed by a plateau phase, and conclude with structural densification, reflected by a sharp rise in reaction force at the final stage. Overall, the numerical and experimental results are in good agreement, despite a slight delay in densification in the numerical model, attributed to the automatic reduction of contact thickness for shell element in the ABAQUS algorithm. Although not perfectly synchronized, the primary deformation characteristics of the TPMS structure observed in the experiment were well captured by the simulation, as demonstrated in Figure 5.19. The equivalent plastic strain and phase field distribution on the deformed specimen during loading are compared with experimental observations. Based on the deformation mode, the loading process can generally be divided into five stages.

In the initial stage, the structure underwent a brief period of elastic deformation, corresponding to the linear increase of reaction force shown in Figure 5.18. Once the reaction force exceeded approximately 35 kN, plastic deformation set in, with only a slight increase in reaction force until the applied displacement reached 6 mm, at which point fracture initiation was observed in the cells from the second to the sixth layer on the front and back surfaces of the TPMS structure.

As the applied displacement increased further, the reaction force exhibited a slight decrease due to the initiation and evolution of phase field damage. In this stage, the damaged layer (second to sixth) of TPMS structure was gradually compacted.

At an applied displacement of 9 mm, a first contact line was observed in the fourth layer of the TPMS structure, which was also noted in the experimental data, though occurring at a displacement of 6 mm due to the earlier contact in the physical test. The simulated deformation during this stage corresponded well with experimental observations. Both the numerical and experimental results showed that deformation was dispersed across the upper layers (second to sixth), as seen in the plastic strain distribution contours from Figure 5.20(a). The significant plastic deformation contributed to the further development of phase field damage in these layers, and lateral expansion was observed on the side surfaces. Meanwhile, the simulated reaction force in Figure 5.18 showed a minimal increase due to self-contact within the TPMS structure, which was

consistent with the experimental results after the displacement reached 6 mm.

When the applied displacement increased to 19 mm, the upper area was fully densified as shown in Figure 5.19, while the lower layers (sixth to tenth) remained largely undeformed. As the applied displacement continued to increase, the lower layers began to exhibit significant deformation and phase field fracture development. Interestingly, deformation at this stage occurred layer by layer rather than the dispersed deformation seen in the previous stage, which aligned with experimental observations, as demonstrated in Figure 5.20(b).

By the time the applied displacement reached 30 mm in the numerical test, the entire structure had been crushed, except for the top and bottom end layers, corresponding to the experimental observation at a displacement of 24 mm. After this point, the top and bottom ends were crushed, and densification for the whole structure occurred as displacement increased, with both the experimental and simulation results showing a rapid rise in reaction force at the end of the test.

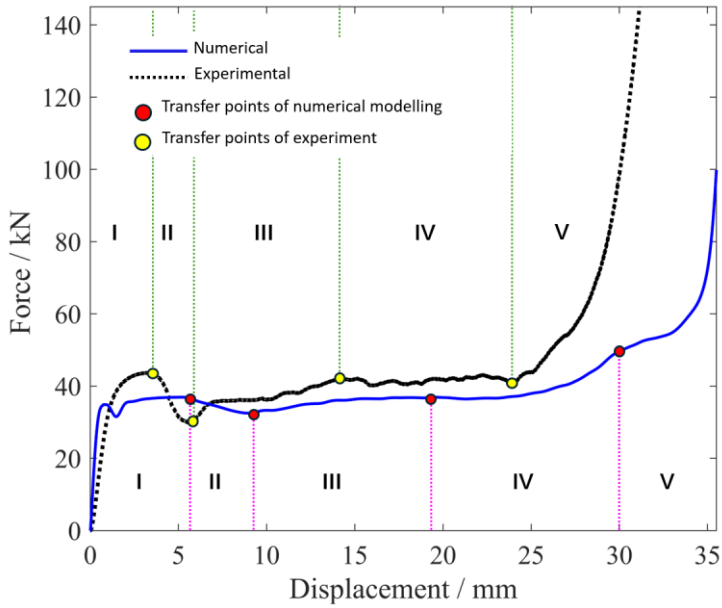

Figure 5.18 Force-displacement curves for Gyroid TPMS structure under axial compression load.

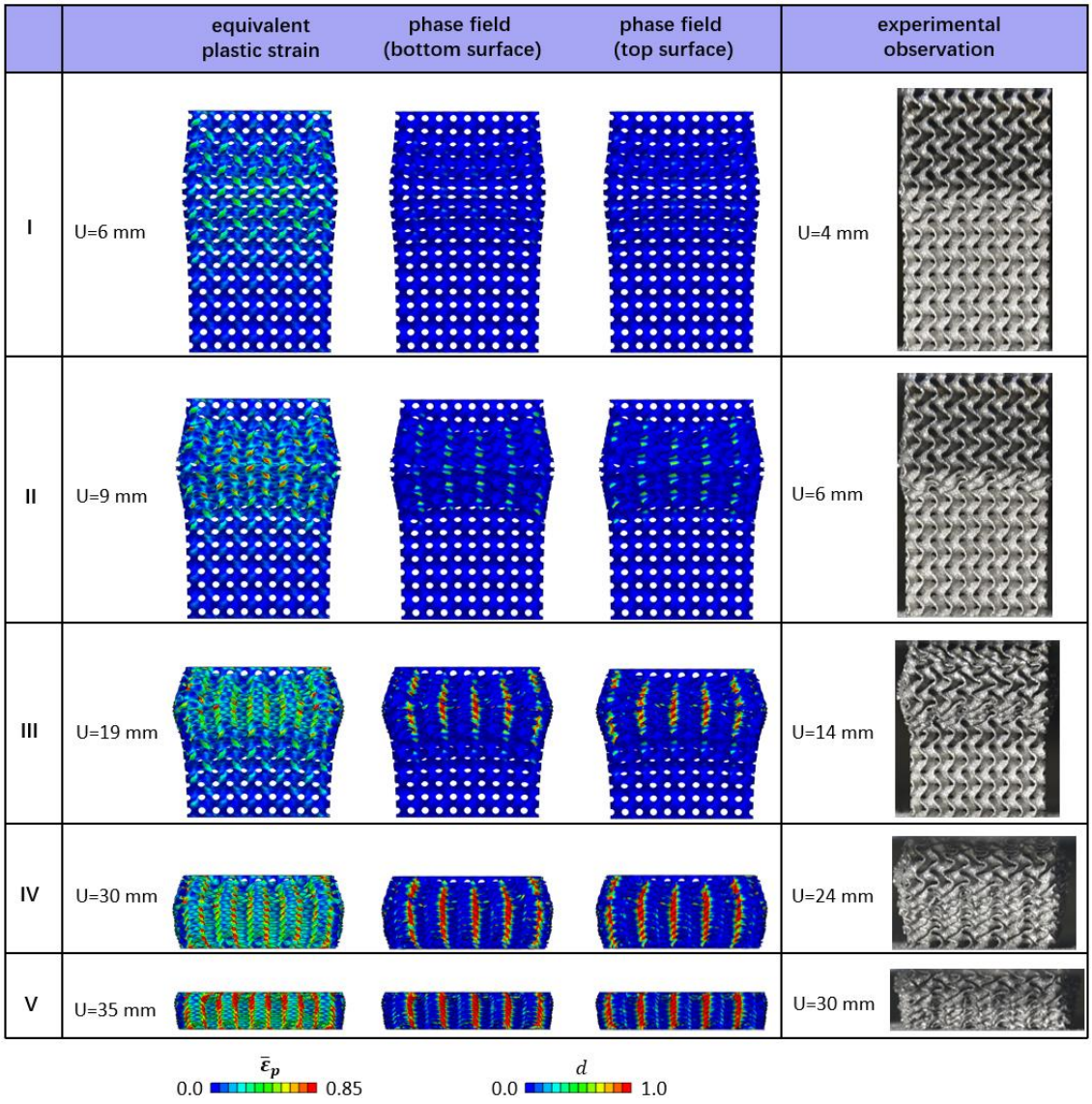

Figure 5.19 Plastic strain distribution and phase field damage contour on deformed specimen companied by experimental observations.

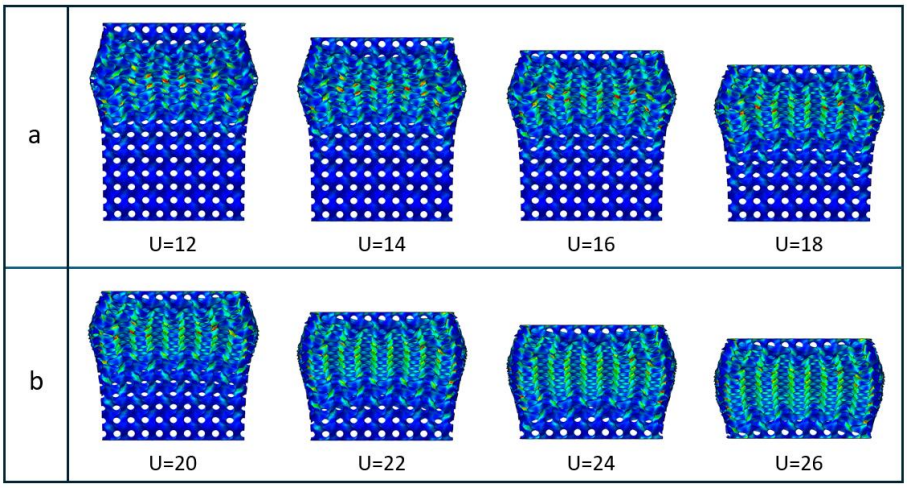

Figure 5.20 Different deformation mode in the third and fourth stage. (a) dispersive deformation; (b) layer-by-layer deformation

5.3.5.2 Analysis of fracture propagation

In this example, the Gyroid TPMS structure was manufactured with the Ti-6Al-4V alloy, and the Bao-Wierzbicki formulation was employed to capture its fracture initiation. As discussed in previous section, when the applied displacement reached 6 mm in the numerical modelling, fracture initiation occurred at the upper layers of the TPMS specimen, specifically on the front and back surfaces. The damage index variable distribution of the specimen at this point is presented in Figure 5.21(a). It is evident that, apart from the cells on the front and back surfaces, most of the interior cells remained undamaged. A comparison between a front surface cell and its adjacent interior cell at the applied displacement of 6 mm, shown in Figure 5.21(d) and (e), reveals that the interior cell exhibited a slightly larger plastic strain in the top front flange compared to the front surface cell. However, the stress triaxiality in the front cell was significantly higher than that in the adjacent interior cell, with values of approximately 0.66 and 0.3, respectively. This difference in stress states can be attributed to distinct boundary conditions: the front edge of the front cell was subject to free constraints, whereas the interior cell was constrained by the adjacent front cell. The higher triaxiality in the front cell resulted in a lower fracture strain threshold (see Figure 5.21(c)) and earlier fracture initiation in the front surface cells.

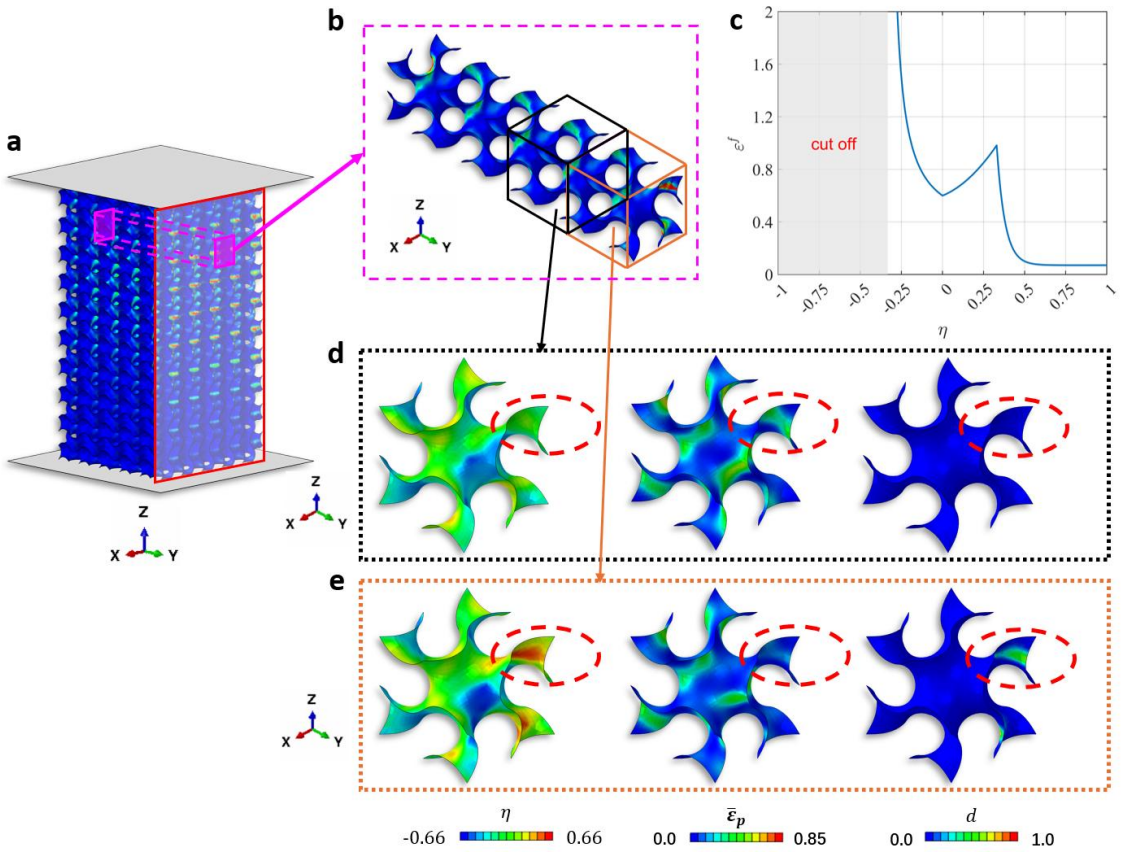

Figure 5.21 Simulation result for TPMS Gyroid structure at the displacement of 6 mm. (a) damage index contour; (b) fracture strain locus; (c) selected one column of cells along y direction; (d) and (e) contour of stress triaxiality, equivalent plastic strain and phase field on the front and second cell of the selected column.

In the previous paragraph, we analysed the distinct fracture behaviours initiated at different locations within the structure. Furthermore, it was observed that fracture propagation at the same location can vary across the thickness of the TPMS structure. To illustrate this, a representative cell from the middle of the fourth layer of the TPMS structure was selected for analysis, as shown in Figure 5.22(a) and (b). Within this selected cell, the top and bottom surfaces were marked by blue and red, respectively, as indicated in Figure 5.22(c). The contours of plastic strain, phase field, and stress triaxiality for these two surfaces were compared in Figure 5.22(d) and (e). The equivalent plastic strain distribution on both surfaces was similar, with high plastic strain concentrated in areas where the structure had a large inclination angle relative to the xy plane under load in the z direction. However, the distribution of stress triaxiality was the opposite on the top and bottom surfaces.

During the axial compression test on the TPMS structure, most of the deformation was driven by bending stresses. Across the thickness, the bending stress exhibited a linear

gradient, with opposite signs for upward and downward directions, one side undergoing tensile bending stress, and the other compressive stress. This resulted in different stress triaxiality distributions on the top and bottom surfaces, leading to a lower fracture initiation strain on the sides experiencing tensile stress. From the simulation results, it is evident that phase field fracture developed in regions with both high stress triaxiality and significant plastic strain accumulation on the top and bottom surfaces of the TPMS cell.

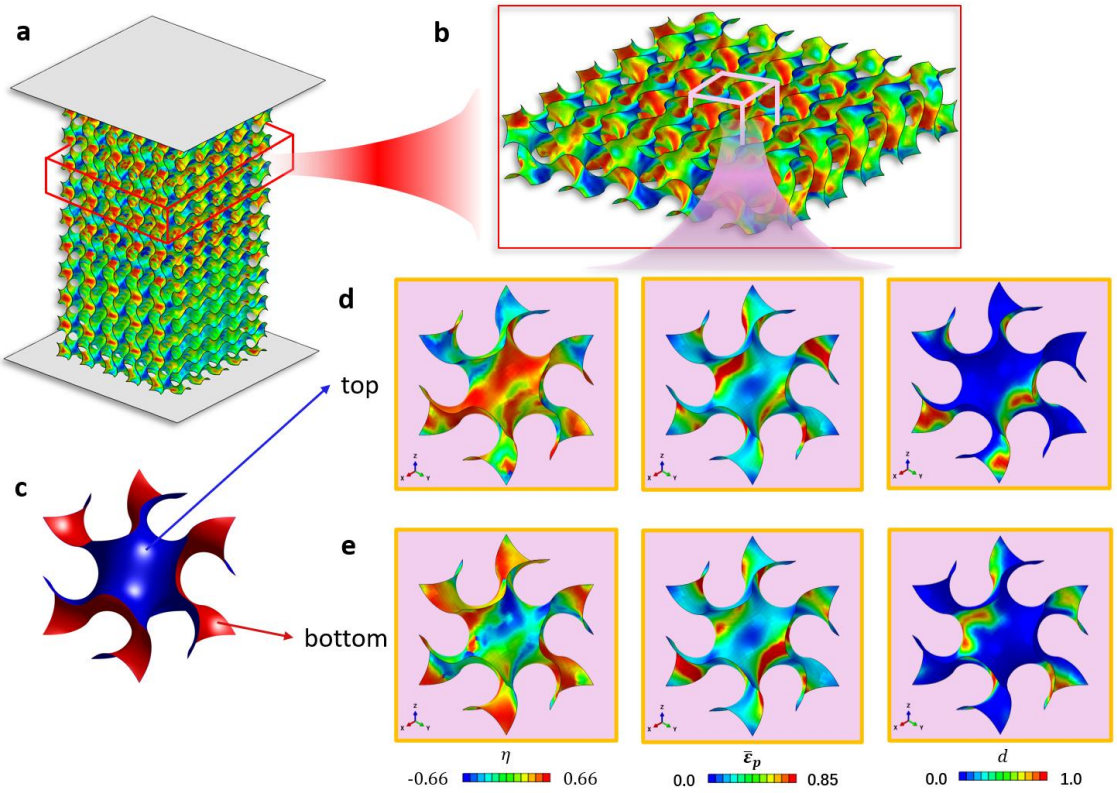

Figure 5.22 Stress triaxiality, equivalent plastic strain and phase field distribution on the top and bottom surfaces of one representative cell of Gyroid TPMS structure

5.4 Summary

In this paper, five layers of phase-field variables were introduced to represent the fracture progression along the thickness direction, corresponding to the five Simpson integration points through the shell thickness. This approach allowed for direct stress degradation at each integration point without the need for interpolation tools, as demonstrated in the current research. Moreover, fracture initiation at each layer was described using a stress-state-dependent fracture strain formulation, applying the MMC criterion for 316L steel and the Bao-Wierzbicki criterion for Ti-6Al-4V.

Several numerical examples were conducted to validate the proposed model. First, the model's implementation was verified by the convergence of numerical results as the

phase-field viscosity parameter decreased. In the notched cylinder under axial tension, the model accurately predicted a through-cylinder crack path, and it was found that fracture strain significantly influenced the force-displacement curve. In the third example, a notched cylinder with an axial pre-crack was subjected to internal pressure with two different boundary conditions: one with, and one without, circumferential straps at the ends of the specimen. The results showed that the straps effectively confined crack propagation within the limited area, aligning well with experimental observations and previous numerical studies. Finally, two experimental tests were simulated using the proposed shell phase-field model. In the three-point bending test of a square tube, the model successfully captured five distinct stages of deformation: elastic deformation, local indentation, side-surface buckling, bulge strap growth, and global bending, all of these showed strong agreement with the experimental data. In the final example, the Gyroid TPMS structure was subjected to axial compression. Despite a slight delay in densification due to the shell element configuration in the Abaqus algorithm, the two distinct deformation modes were accurately captured, and the global force-displacement curve closely matched the experimental results.

6. APPLICATION OF SHELL PHASE FIELD MODEL TO FRACTURE MODELLING OF BATTERY CASING

6.1 Introduction

The phase field fracture model, rooted in the variational formulation by Francfort and Marigo (Francfort and Marigo 1998), offers a non-local approach to fracture modelling. It regularizes the sharp crack topology into a smeared damage zone, with the extent of this zone governed by a length scale parameter. This model has gained significant attention for its robust implementation and its ability to automatically capture crack evolution based on energy minimization. Over the years, the phase field approach has been extended beyond its initial application in brittle fracture to cover a broad spectrum of problems, including ductile fracture (Ambati, Kruse et al. 2015, Borden, Hughes et al. 2016, Miehe, Aldakheel et al. 2016, Roth and Mohr 2016, Alessi, Marigo et al. 2018, Dittmann, Aldakheel et al. 2018, Fang, Wu et al. 2019, Fang, Wu et al. 2019, Li, Fang et al. 2022), dynamic fracture (Ren, Zhuang et al. 2019, Wang, Ye et al. 2019, Yang, Yang et al. 2021, Hu, Tan et al. 2023, Li, Fang et al. 2024), hydraulic fracture (Ehlers and Luo 2017, Chukwudozie, Bourdin et al. 2019, Chen, Sun et al. 2020, Aldakheel, Noii et al. 2021, Heider 2021), and fatigue fracture (Seiler, Linse et al. 2020, Ulloa, Wambacq et al. 2021, Golahmar, Kristensen et al. 2022), among many others. Despite these advancements, most studies have primarily focused on 3D solids or plane strain problems, with relatively few exploring the application of phase field models for thin-walled structures using shell element formulations.

In general, the shell kinematics description fall into two categories: the Reissner-Mindlin formulation (Reinoso, Paggi et al. 2017, Reinoso, Durand et al. 2019, Pillai, Triantafyllou et al. 2020, Kikis, Ambati et al. 2021), which allows transverse shear strains for moderately thick shells, and the Kirchhoff-Love formulation, suited for thin shells, neglecting shear effects, which is focused in this study. Ulmer (Ulmer, Hofacker et al. 2012) first extended the phase field model to Kirchhoff shells, incorporating a single through-thickness phase field and a deflection field as the basic variables, with the fracture driving forces derived from bending and membrane energies. Amiri et al. (Amiri, Millán et al. 2014) adopted this concept and implemented it with a meshfree strategy for fracture simulation within complex geometry topology. Alternatively, Kiendl (Kiendl,

Ambati et al. 2016) proposed a shell phase field model where the strain energy at each integration point was decomposed in a plane stress formulation to account for the tensile-compressive asymmetry. Meanwhile, Li et al. (Li, Millán et al. 2018) developed a higher-order phase field model to simulate tearing in brittle thin sheets. The above mentioned models all assume the uniform damage variable through thickness, which does not correspond to the real case especially for shell structure under bending. To overcome this shortcoming, Arei et al. (Areias, Rabczuk et al. 2016) introduced a dual phase field approach to account for damage evolution along the top and bottom surfaces of shells. Wang et al. (Wang, Han et al. 2022) assumed linear distribution of phase field variable along shell thickness. In addition, Ambati (Ambati, Heinzmann et al. 2022) proposed a mixed-dimension model which combines the shell kinematic description for the displacement field and solid element representation for the phase field evolution, allowing the varying damage distribution along the shell thickness.

The above mentioned studies have demonstrated the effectiveness of shell phase field models in simulating fracture. However, most existing phase field models for Kirchhoff-Love shells only consider the brittle fracture and ignored the plastic deformation and ductile fracture initiation. This limitation restricts the application of shell phase-field models to real-world structures, where materials often exhibit complex mechanical properties. For example, the plasticity must be considered for metal materials. To the authors' best knowledge, only one previous phase-field model (Wang, Han et al. 2022) considered ductile fracture for the Kirchhoff-Love shell. Though this study incorporated plasticity, it assumed a constant threshold of fracture driving force, which does not agree with plenty of experimental observations where the fracture initiation largely depends on the stress state (Bao and Wierzbicki 2004, Bai and Wierzbicki 2009, Brünig, Brenner et al. 2015, Mohr and Marcadet 2015, Li, Fang et al. 2022, Dou, Xu et al. 2023). Moreover, due to the manufacturing process, metal sheet often demonstrated obvious anisotropic mechanical characteristics (Fourmeau, Børvik et al. 2011, Zaman, Barlat et al. 2018, Mooney, Kourousis et al. 2019), which has not yet been considered in the existing studies. To bridge the above research gap, we recently developed a multi-layer shell phase field model, introducing five layers of phase field variables along the shell thickness, with the Hill 48 yield stress and Bao-Wierzbicki fracture locus incorporated to consider the material anisotropy and stress-state dependent fracture initiation. The results demonstrated its capability to simulate fracture behaviour in ductile

materials under complex stress conditions. In this study, we aimed to further explore its application for simulating fracture evolution in real structures.

The rapid growth of the global electric vehicle (EV) market has significantly increased the demand for lithium-ion batteries (LIBs), highlighting the importance of evaluating their safety under various loading conditions. Key abuse tests (Liu, Jia et al. 2020), such as bending (Greve and Fehrenbach 2012, Sahraei, Campbell et al. 2012, Xu, Liu et al. 2016), indentation (Sahraei, Campbell et al. 2012, Yang, Wang et al. 2019), radial compression (Greve and Fehrenbach 2012, Sahraei, Campbell et al. 2012, Xu, Liu et al. 2016), axial compression (Zhu, Zhang et al. 2016, Yang, Wang et al. 2019), and impact loading (Xia, Wierzbicki et al. 2014, Wang, Yang et al. 2020), have been employed to assess LIB resilience. Among the critical components of an LIB, the battery casing plays a pivotal role as the primary protective layer, offering high elastic modulus and strength to resist external loads (Zhang and Wierzbicki 2015, Wang, Yin et al. 2018, Wang, Yin et al. 2019, Chen, Kang et al. 2021). Despite its importance, limited studies have focused on accurately characterizing the mechanical properties of casing materials. Zhang and Wierzbicki (Zhang and Wierzbicki 2015) addressed this gap by calibrating anisotropic mechanical parameters through specimens extracted from cylindrical casings, revealing the influence of stress triaxiality and the Lode angle on fracture behaviour. Wang et al. (Wang, Yin et al. 2018) further examined dynamic fracture strain using the Johnson-Cook model. However, these studies predominantly utilized local damage models, which are prone to mesh dependency, neglect non-local damage evolution, and result in mass and energy loss (Bazant and Jirasek 2002, Alessi, Marigo et al. 2014, Ahmed, Voyiadjis et al. 2021, Li, Fang et al. 2024). The shell phase-field model offers a robust alternative by addressing these limitations, providing a more reliable framework for assessing the mechanical behaviour of LIB casings. Motivated by these challenges, this study extends our previously proposed multi-layer shell phase field model to simulate the fracture behaviour of LIB casings. It is the first time for applying the shell phase field model to the mechanical safety assessment of the cylindrical battery casing.

6.2 Formulation of shell phase field model

6.2.1 Kinematics of the thin shell elements

In this study, we focus on the mechanical behaviour of battery casing, where the ratio of width and thickness could reach more than 200. This high ratio allows us to utilise the

Kirchhoff-Love formulation (Ebenfeld 1999) to describe the kinematic of shell element, where the shear stress components outside the shell surface was assumed to be zero. As demonstrated in Figure 6.1, the crack on the the thin-wall structure can be represented on its reference surface (mid-surface). The local coordinate system ($\boldsymbol{t}_1$, $\boldsymbol{t}_2$ and $\boldsymbol{t}_3$) is also constructed based on the local reference surface to describe the shell element configuration, where $\boldsymbol{t}_3$ represents the local normal direction to the reference surface, while $\boldsymbol{t}_1$ and $\boldsymbol{t}_2$ are two orthogonal directions, following the below condition,

$$\boldsymbol{t}_i \cdot \boldsymbol{t}_j = \delta_{ij} \tag{6.1}$$

where δ_{ij} is the Kronecker delta. With the local coordinate system, the position of a material point within shell element is defined as,

$$\boldsymbol{x}(\boldsymbol{S}_i) = \bar{\boldsymbol{x}}(\boldsymbol{S}_\alpha) + \bar{f}_{33}(\boldsymbol{S}_\alpha)\boldsymbol{t}_3(\boldsymbol{S}_\alpha)S_3 \tag{6.2}$$

where $\boldsymbol{S}_\alpha$ (α ranges from 1 to 2) are local surface coordinates within reference plane, and $S_3 \in [-\frac{t}{2}, \frac{t}{2}]$ is the coordinate on $\boldsymbol{t}_3$ direction; $\boldsymbol{x}(\boldsymbol{S}_i)$ and $\bar{\boldsymbol{x}}(\boldsymbol{S}_\alpha)$ represent the position of material point $\boldsymbol{S}_i$ and its projecting point $\boldsymbol{S}_\alpha$ on the reference plane; $\bar{f}_{33}$ is the thickness increase factor, which is assumed to be constant along the thickness direction.

Based on Eq.(5.2), the gradient of the position can be expressed as,

$$\begin{cases} \dfrac{\partial \boldsymbol{x}}{\partial \boldsymbol{S}_\alpha} = \dfrac{\partial \bar{\boldsymbol{x}}}{\partial \boldsymbol{S}_\alpha} + \bar{f}_{33}\dfrac{\partial \boldsymbol{t}_3}{\partial \boldsymbol{S}_\alpha}S_3 \\ \dfrac{\partial \boldsymbol{x}}{\partial \boldsymbol{S}_3} = \bar{f}_{33}\boldsymbol{t}_3 \end{cases} \tag{6.3}$$

where the derivative of $\bar{f}_{33}$ with respect to $\boldsymbol{S}_\alpha$ has been neglected. Its components within the reference plane can be obtained as below,

$$f_{\alpha\beta} = \boldsymbol{t}_\alpha \cdot \frac{\partial \boldsymbol{x}}{\partial S_\beta} = \bar{f}_{\alpha\beta} + B_{\alpha\beta}\bar{f}_{33}S_3 \tag{6.4}$$

where the reference surface deformation gradient $\bar{f}_{\alpha\beta}$ and reference normal gradient $B_{\alpha\beta}$ are defined as follows,

$$\begin{cases} \bar{f}_{\alpha\beta} \overset{\text{def}}{=} \boldsymbol{t}_\alpha \cdot \dfrac{\partial \boldsymbol{x}}{\partial S_\beta}\Big|_{S_3=0} = \boldsymbol{t}_\alpha \cdot \dfrac{\partial \bar{\boldsymbol{x}}}{\partial S_\beta} \\ B_{\alpha\beta} \overset{\text{def}}{=} \boldsymbol{t}_\alpha \cdot \dfrac{\partial \boldsymbol{t}_3}{\partial S_\beta} \end{cases} \tag{6.5}$$

In the original shell configuration, $\bar{\boldsymbol{X}}$ represents the position of the projecting point on the reference plane. The original normal direction to reference plane $\boldsymbol{T}_3$ is defined by

$$\boldsymbol{T}_3 = \left(\frac{\partial \bar{\boldsymbol{X}}}{\partial S_a} \times \frac{\partial \bar{\boldsymbol{X}}}{\partial S_b}\right) \Big/ \left|\frac{\partial \bar{\boldsymbol{X}}}{\partial S_a} \times \frac{\partial \bar{\boldsymbol{X}}}{\partial S_b}\right| \tag{6.6}$$

where S_a and S_b are coordinates of two arbitrary two unparalleled directions within the

reference plane of shell element. Meanwhile, direction $\boldsymbol{T}_1$ is specified as one arbitrary direction parallel to the shell surface, for example, the projection of the global $\boldsymbol{x}$ direction on the shell surface or the roll direction for the rolled thin-wall structure. The remained $\boldsymbol{T}_2$ direction could be finally specified to be vertical to $\boldsymbol{T}_1$ within the shell reference surface.

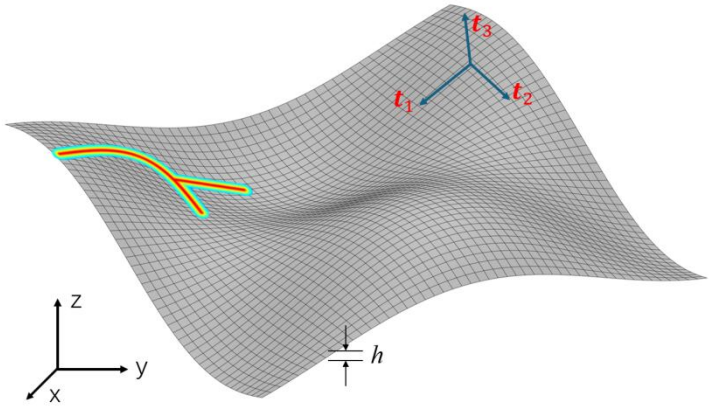

Figure 6.1 Shell crack representation in the global and local coordinate system

6.2.2 Regularisation of the fracture topology

Refer to our previously paper, five Simpson points along the shell thickness are adopted for stress integration. Meanwhile, five layers of phase field variables are introduced to describe the corresponding damage evolution on each layer. The fracture topology of shell structure is demonstrated in Figure 6.2(a). The shell solid Ω with thickness of t got a through-thickness sharp crack Γ, and it was under the constraint of Neumann boundary $\partial\Omega^s$ and Dirichlet boundary $\partial\Omega^h$. In each layer of the integration point, the sharp crack Γ is regularised with diffusive phase field variable d, from the totally broken state ($d = 1$) to the intact state ($d = 0$) of material with the length scale parameter l_c, demonstrated as Figure 6.2 (b) and (c). Accordingly, the crack surface density function γ is introduced referring to standard phase field formulation in three-dimension space, written as below,

$$\gamma(d, \nabla d) = \frac{d^2}{2l_c} + \frac{l_c}{2}|\nabla d|^2 \tag{6.7}$$

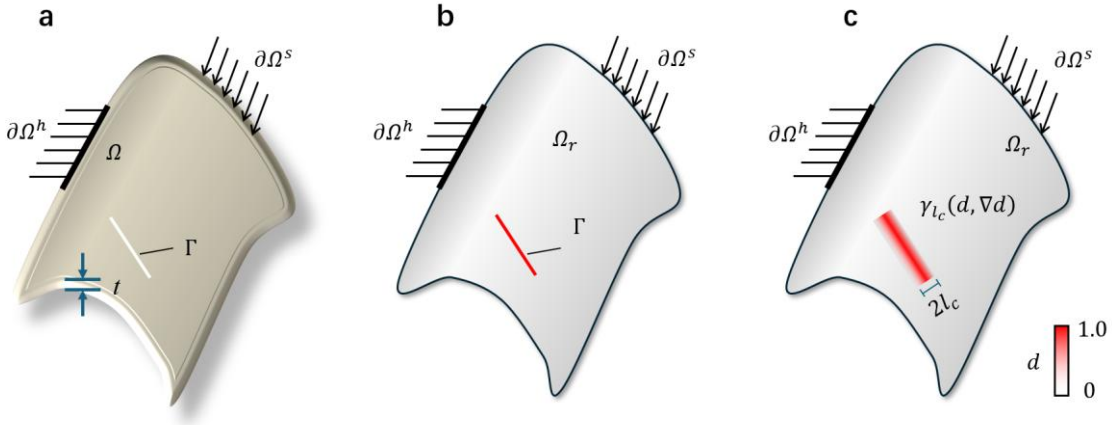

Figure 6.2 Regularisation of sharp crack to damage zone based on l_c. (a) fracture topology of the shell (b) sharp crack on shell reference surface; (c) regularised phase field distribution on shell reference surface

6.2.3 Energy function and governing equations

The total energy function within the shell could be written following our previous work (Fang, Wu et al. 2019, Li, Fang et al. 2022, Jiang, Li et al. 2023, Li, Fang et al. 2024) as below,

$$\Phi = \int_{-\frac{h}{2}}^{\frac{h}{2}} \int_{\Omega^r} \left(\psi^e + \psi^p + \psi^k + \psi^f + \psi^{vis}\right) \mathrm{d}S\mathrm{d}h - \int_{-\frac{h}{2}}^{\frac{h}{2}} \int_{\Omega^r} (\boldsymbol{t} \cdot \boldsymbol{u}) \mathrm{d}S\mathrm{d}h - \int_{\partial\Omega^r} (\boldsymbol{b} \cdot \boldsymbol{u}) \mathrm{d}s \tag{6.8}$$

where h is the shell thickness; $\boldsymbol{t}$, $\boldsymbol{b}$, and $\boldsymbol{u}$ denote the body force on Ω, boundary traction on $\partial\Omega^r$, and displacement within shell; ψ^e, ψ^p, ψ^k, ψ^f and ψ^{vis} represent the elastic strain energy, plastic work , kinematic energy, fracture energy, and damage viscosity energy density functions per area on Ω^r, respectively. The elastic strain energy density ψ^e can be obtained as follows,

$$\psi^e(\boldsymbol{u}, d) = \mathrm{g}(d) \cdot \psi_0^e = \frac{1}{2} \cdot \mathrm{g}(d) \cdot \bar{\boldsymbol{\sigma}} : \boldsymbol{\varepsilon}^e \tag{6.9}$$

where $\mathrm{g}(d) = (1-d)^2$ is quadratic strain energy degradation function. $\boldsymbol{\varepsilon}^e$ and $\bar{\boldsymbol{\sigma}}$ represent the elastic strain tensor and corresponding (undamaged) effective stress tensor. It is noted that the update of stress state for the shell element is based on the local coordinate $\boldsymbol{t}_1$-$\boldsymbol{t}_2$-$\boldsymbol{t}_3$,as shown in Figure 6.1. In this study, we focused on the thin shell element where the stress components $\bar{\sigma}_{33}$, $\bar{\sigma}_{13}$ and $\bar{\sigma}_{23}$ are all excluded for calculation, resulting in much lower computational efficiency compared with 3D phase field model. The plastic density ψ^p is calculated by,

$$\psi^p(\bar{\varepsilon}^p, d) = \mathrm{g}(d) \cdot \psi_0^p = \mathrm{g}(d) \cdot \int_0^{\bar{\varepsilon}^p} \bar{\sigma}_y(\bar{\varepsilon}^p)\, \mathrm{d}\bar{\varepsilon}^p \tag{6.10}$$

where $\bar{\varepsilon}^p$ and $\bar{\sigma}_y$ represent the accumulated plastic strain and corresponding (undamaged) effective yield stress. In Eq. (6.10), the plastic work is degraded as the phase field develops, leading to degraded yield stress, following our previous work (Fang, Wu et al. 2019, Fang, Wu et al. 2019, Li, Fang et al. 2022). The kinematic energy ψ^k is written as,

$$\psi^k(\dot{\boldsymbol{u}}) = \frac{1}{2}\rho\dot{\boldsymbol{u}}\cdot\dot{\boldsymbol{u}} \tag{6.11}$$

where ρ is the material density; $\dot{\boldsymbol{u}}$ denotes the displacement rate. The fracture energy ψ^f and damage viscosity energy density ψ^{vis} functions are given by

$$\psi^f(d,\nabla d) = G_f\cdot\left(\frac{d^2}{2l_c}+\frac{l_c}{2}|\nabla d|^2\right) \tag{6.12}$$

$$\psi^{vis}(\dot{d}) = \int_0^t\left(\frac{\omega}{2}\dot{d}\cdot\dot{d}\right)\mathrm{d}t \tag{6.13}$$

where G_f is the crack energy release rate, denoting the required energy for generating a unit area of crack surface; ω is the introduced viscosity parameter (Li, Fang et al. 2024); $\dot{d}$ denotes the damage evolution rate; t represents the current loading time.

Substitution of Eqs.(6.9)- (6.13) into Eq. (6.8) leads to the final total energy function Φ, as below,

$$\Phi(\boldsymbol{u},\bar{\varepsilon}^p,d) = \int_{-\frac{h}{2}}^{\frac{h}{2}}\int_{\Omega^r}\left\{\frac{1}{2}(1-d)^2\bar{\boldsymbol{\sigma}}:\boldsymbol{\varepsilon}^e+(1-d)^2\cdot\int_0^{\bar{\varepsilon}^p}\bar{\sigma}_y(\bar{\varepsilon}^p)\mathrm{d}\bar{\varepsilon}^p+\frac{1}{2}\rho\dot{\boldsymbol{u}}\cdot\dot{\boldsymbol{u}}+G_f\cdot\left(\frac{d^2}{2l_c}+\right.\right.$$

$$\left.\left.\frac{l_c}{2}|\nabla d|^2\right)+\int_0^t\left(\frac{\omega}{2}\dot{d}\cdot\dot{d}\right)\mathrm{d}\tau\right\}\mathrm{d}\Omega^r\mathrm{d}h-\int_{-\frac{h}{2}}^{\frac{h}{2}}\left\{\int_{\Omega^r}(\boldsymbol{t}\cdot\boldsymbol{u})\mathrm{d}\Omega^r-\int_{\partial\Omega_r^s}(\boldsymbol{b}\cdot\boldsymbol{u})\mathrm{d}s\right\}\mathrm{d}h \tag{6.14}$$

Based on the Hamilton theory (Dunne and Petrinic 2005), the governing equations for displacement field and phase field in strong form could be obtained as follows,

$$\begin{cases}\nabla\cdot\boldsymbol{\sigma}+\boldsymbol{b}=\rho\,\ddot{\boldsymbol{u}} & \text{in }\Omega\\ \boldsymbol{\sigma}\cdot\boldsymbol{n}-\boldsymbol{t}=0 & \text{on }\partial\Omega_r^s\\ \boldsymbol{u}=\bar{\boldsymbol{u}} & \text{on }\partial\Omega_r^h\end{cases} \tag{6.15}$$

$$\begin{cases}\dot{d}=\frac{1}{\omega}\langle 2(1-d)(\varphi_0^e+\psi_0^p)\ -\frac{G_f}{l_c}\left(d-{l_c}^2\Delta d\right)\rangle_+ & \text{in }\Omega\\ \nabla d\cdot\boldsymbol{n}=0 & \text{on }\partial\Omega\end{cases} \tag{6.16}$$

6.2.4 Hill 48 plastic yield criterion

In this study, we mainly consider the mechanical behaviour of the casing of cylinder 11850 lithium-ion battery. According to the existing study (Zhang and Wierzbicki 2015), the cylinder battery casing demonstrated obvious anisotropy due to the rolling process under mechanical loading. In this study, the Hill 48 yield stress formulation was adopted to capture the anisotropic mechanical characteristics of the battery casing. Since here we

only consider the plane stress state for shell elements, the Hill 48 yield criterion could be simplified as,

$$\bar{f}(\bar{\boldsymbol{\sigma}}) = \sqrt{(H+G)\bar{\sigma}_{11}{}^2 + (H+F)\bar{\sigma}_{22}{}^2 - 2H\bar{\sigma}_{11}\bar{\sigma}_{22} + 2N\bar{\sigma}_{12}{}^2} \tag{6.17}$$

where F, G, H, and N are material parameters; $\bar{\sigma}_{11}$ and $\bar{\sigma}_{22}$ represent the normal stress components along the hoop direction and axial direction for the battery casing, respectively, while $\bar{\sigma}_{12}$ denotes the shear stress components within the battery shell surface.

6.2.5 Fracture initiation criterion

It has been widely admitted that the ductile fracture strain for metal materials depends on stress state rather than a constant value (Bai and Wierzbicki 2009, Li, Fang et al. 2022, Li, Fang et al. 2023, Yang, Guo et al. 2023, Li, Fang et al. 2024). To capture the stress-state dependent fracture strain, the Bao-Wierzbicki model with (Bao and Wierzbicki 2004) was introduced to model the damage initiation of the battery casing, which has been widely adopted and proved effective in literature (Mahalle, Morchhale et al. 2020, Zhang, Liu et al. 2022, Li, Fang et al. 2024, Li, Fang et al. 2024). The formulation of the Bao-Wierzbicki model build connection between the plastic fractur strain with the stress triaxiality, written as below,

$$\varepsilon^f(\eta) = \begin{cases} B_2\left(\frac{3B_1+1}{3\eta+1}\right)^{B3} & -\frac{1}{3} < \eta \le B_1 \\ B_6(\eta - B_1)(\eta - B_4) + \frac{B_5 - B_2}{B_4 - B_1}(\eta - B_1) + B_2 & B_1 < \eta \le B_4 \\ (B_5 - B_7)e^{-B_8(\eta - B_4)} + B_7 & \eta > B_4 \end{cases} \tag{6.18}$$

where B_1, B_2, B_3, B_4, B_5, B_6, B_7 and B_8 are eight independent Bao-Wierzbicki fracture strain parameters. Moreover, the fracture strain is cut-off when the triaxiality is less than -0.33 to avoid the unrealistic fracture initiation for metal material under compression stress state.

Additionally, the above formulation only gives the fracture criterion for the material under proportional loading. For the nonproportional loading, a historical damage indicator *D* is introduced as below (Li, Fang et al. 2022),

$$D(\bar{\varepsilon}^p) = \int_0^{\bar{\varepsilon}^p} \frac{d\bar{\varepsilon}^p}{\varepsilon^f(\eta, \bar{\theta})} \tag{6.19}$$

where $\bar{\varepsilon}^p$ represents the equivalent plastic strian. As the accumulation of $\bar{\varepsilon}^p$ during the loading process, the indicator *D* increases with a stress state-dependent rate. With the indicator *D* in hand, the fracture energy threshold H^{ini} is then defined as the strain energy

when D firstly reached 1. Following (Miehe, Hofacker et al. 2015, Li, Fang et al. 2022, Jiang, Li et al. 2023), a state energy formulation $state(X,t)$ is introduced to indicate the crack crack driving force at position X and at time t within the shell Ω as below,

$$state(X,t) =< \varphi_0^e + \psi_0^p - H^{ini} >_+ \tag{6.20}$$

To avoid the unrealistic fracture healing, the history energy function H is then defined as the maximum state energy during the loading process,

$$H = \max_{\tau\in[0,t_n]} state^t(X,\tau) \tag{6.21}$$

Replacing the fracture driving force term $(\varphi_0^e + \psi_0^p)$ in Eq. (6.16) with H could lead to the final phase field evolution governing equations,

$$\begin{cases} \dot{d} = \frac{1}{\omega}\langle 2(1-d)H - \frac{G_f}{l_c}\left(d - {l_c}^2\Delta d\right)\rangle_+ & \text{in } \Omega \\ \nabla d \cdot \boldsymbol{n} = 0 & \text{on } \partial\Omega \end{cases} \tag{6.22}$$

6.3 Calibration of model parameters

6.3.1 Geometry design of material specimens

In this section, the mechanical behaviour of 18650 lithium-ion battery casing was investigated in material level. To calibrate the model parameters, a group of samples were cut from the flatten battery casing, the geometries of which are all presented in Figure 6.3. To analyse the anisotropic characteristics induced by rolling effect, uniaxial tension (UT) specimens were prepared along three orientations: the hoop direction, 45 degree direction and axial direction, as shown in Figure 6.3 (a)-(c). In addition, tests were conducted using notched tension (NT) and central-hole (CH) specimens, along with the UT specimens, to calibrate the stress-state-dependent fracture locus. To validate the calibrated parameters, a five-hole specimen was designed and tested. The thickness of the battery casing was measured to be approximately 0.25 mm, exhibiting slightly non-uniformity along the axial direction, where the material was thinner in the middle and thicker at the two ends. All samples were clamped at the two ends within the grey areas, as shown in Figure 6.3, and subjected to a loading rate of 0.2 mm/min to determine the quasi-static mechanical parameters. The loading process for all specimens was recorded using a camera and analysed with the Digital Image Correlation (DIC) technique. The two gauge points, indicated in Figure 6.3, were utilised to measure the displacement during loading through DIC.

6.3.2 Calibration of model parameters

The model parameters are calibrated by matching the experimental and numerical force-displacement curves and listed in Table 6.1. Specifically, the elastic parameters and Hill 48 yield function parameters are calibrated using UT specimens tested along different orientations, ensuring that the numerical yield stress aligns with the experimental results. Additionally, the Bao-Wierzbicki fracture initiation and damage evolution parameters are calibrated using UT, NT, and CH specimens oriented in the hoop direction, with a focus on accurately capturing the fracture initiation and the force decline in the post-fracture stage.

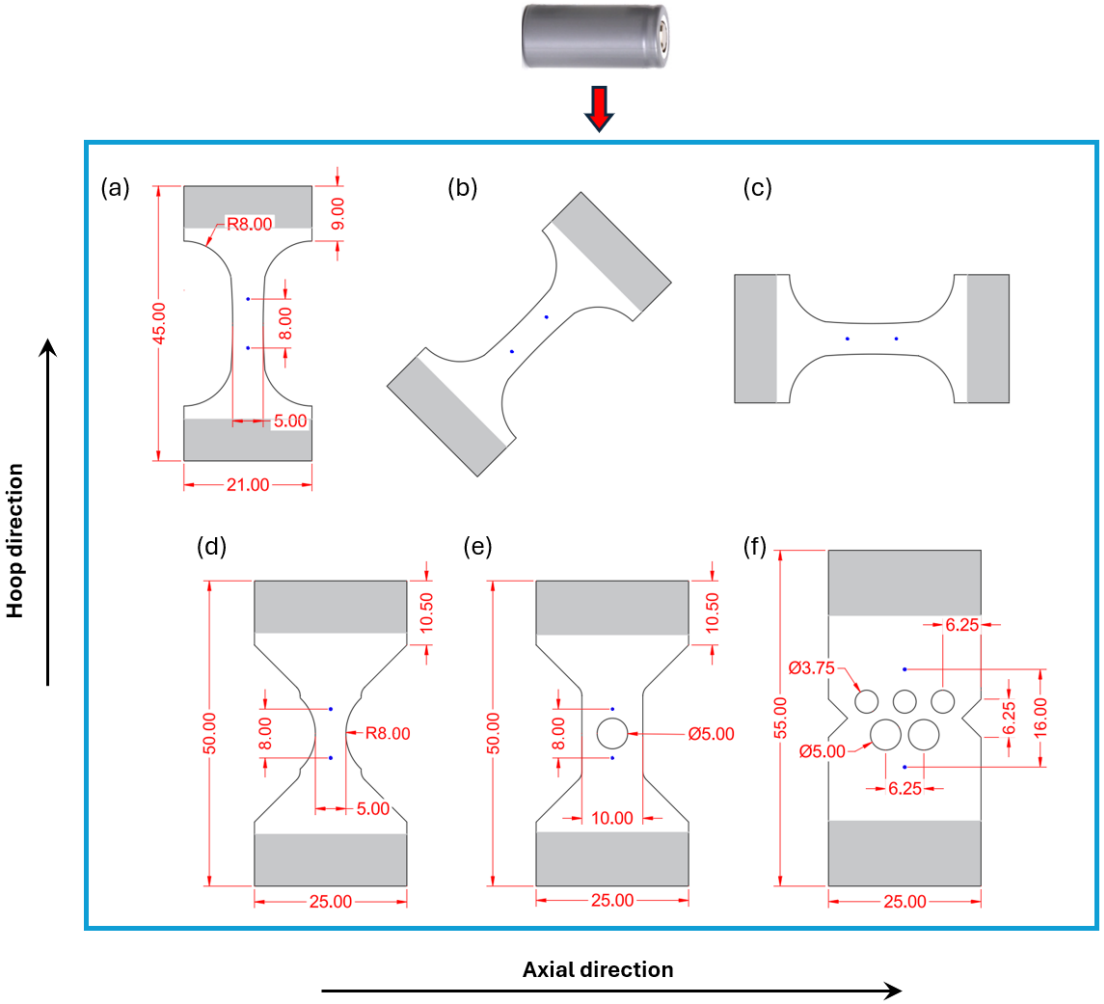

Figure 6.3 Geometry design of material specimens cut from the flatten lithium-ion battery casing.(a)-(c):uniaxial tension (UT) specimen along the hoop, 45 degree and axial direction; (c) notched tension (NT) specimen; (d) central hole (CH) specimen; (e) five-holes specimen.

The force-displacement curve of uniaxial tension (UT) specimens along the axial and hoop directions are presented in Figure 6.4(a), where the reaction forces for both axial

and hoop UT specimens exhibited linear increase during the initial elastic stage, indicating comparable elastic modulus in the two orientations. The divergence of the curves began at a displacement of approximately 0.025 mm, marking the onset of plastic deformation in both specimens. This transition was characterized by a nonlinear increase in load with a progressively decreasing growth rate. A plateau stage was observed for both specimens at the applied displacement of approximately 0.1 mm. However, the peak forces of specimens along different orientations differed to some extent, attributed to the plasticity anisotropy. Following the peak, the reaction force decreased till the end of loading, caused by crack initiation at the centre of specimen and propagation along the incline angle of 45 degree, as demonstrated in Figure 6.5(a) and (c). Notably, the force dropped for specimens in both directions at applied displacement of approximately 0.25 mm.

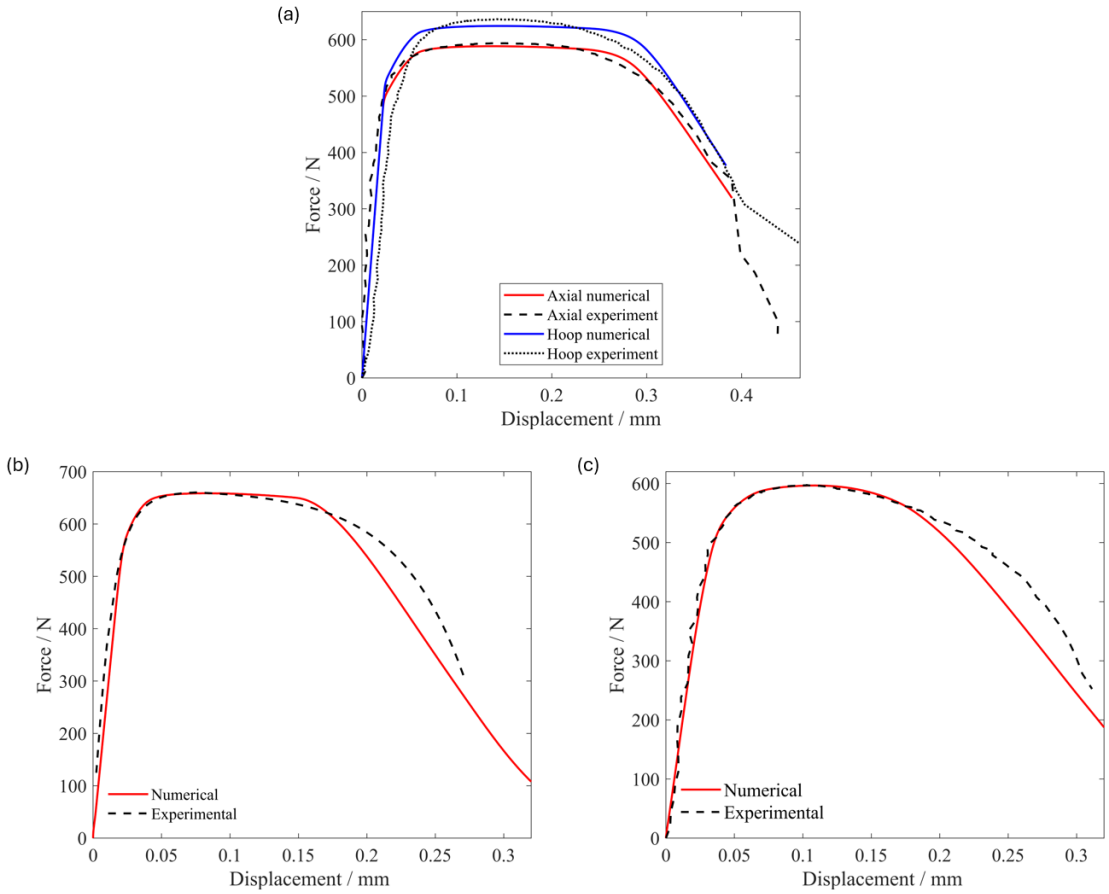

Figure 6.4 Comparison of experimental and numerical force-displacement curve for material specimens. (a) uniaxial tension (UT); (b) notched tension (NT); (c) central hole (CH).

Based on the experimental results discussed above, we only consider anisotropic plasticity, while assuming isotropic elasticity and fracture strain. The numerical force-

displacement curves with calibrated model parameters are presented in Figure 6.4, demonstrating close agreement with the experimental result for specimens orientated in both hoop and axial directions. Furthermore, the final numerical crack paths are also compared with the experimental observations in Figure 6.5(a) for the axial-orientated UT specimen and Figure 6.5(c) for the hoop-orientated UT specimen. In both cases, the crack paths develop along the 45° inclined lines at the centre of specimens, driven by the pronounced accumulation of plastic strain. Figure 6.5(b) and (d) show the strain contours from the numerical simulation and DIC data at the moment of fracture initiation. The shell phase field model predicted an X-shape strain concentration, while the DIC data exhibited strain localization along a single 45° inclined line. Such a discrepancy may stem from the defect-free assumption in the simulation. In contrast, the real specimen was not perfectly homogeneous, making strain concentration more likely along either 45° inclined line. Once larger strain concentration developed on the weaker one, the resulting stress distribution would amplify the asymmetrical deformation, guiding the fracture along the weaker inclined line.

Table 6.1 Material parameters for lithium-ion battery casing

Types	Parameters	Physical meaning	Value
Elasticity	E	Elastic modulus	148.5 GPa
	υ	Poisson's Ratio	0.3
Hill 48 yield stress	H	Four anisotropic yield stress parameters	0.534
	G		0.467
	F		0.588
	N		1.574
Fracture Initiation	B_1	Fracture locus parameters	0.25
	B_2		0.016
	B_3		1.2
	B_4		0.5
	B_5		0.28
	B_6		2.5
	B_7		0.03
	B_8		8.0
Phase field evolution	G_f	Crack energy release rate	20.0 N/mm
	η	Viscosity parameter	10^{-4} kN · s/mm^2

In this study, we adopted the Bao-Wierzbicki fracture locus to account for the stress-state dependent fracture strain threshold. The model parameters were calibrated by

matching the force-displacement curves of three specimens, namely uniaxial tension (UT), notch tension (NT) and central hole (CH), all of which are cut from battery casing along the hoop direction, considering the negligible effect of material orientation on the fracture strain.

As shown in Figure 6.4(b) and (c), the experimental and numerical force-displacement curves for the notch tension (NT) and central hole (CH) specimens presented excellent agreement with each other, demonstrating capacity of the proposed shell phase-field model to characterize mechanical behaviours for the battery casing. For the NT specimen, the reaction force increased linearly during the elastic stage, reaching 550 N at a displacement of 0.025 mm. Beyond this point, the reaction force exhibited a nonlinear increase at a decreasing rate, stabilizing at a plateau around 650 N. Fracture initiation occurred at the middle of the NT specimen at an applied displacement of 0.16 mm, leading to a sharp decline in the reaction force. The force-displacement response of the CH specimen followed a similar trend. During the initial elastic stage, the reaction force rose linearly to 500 N at an applied displacement of 0.03 mm. The plastic deformation stage followed, characterized by a rising reaction force at a decreasing rate. The load peaked at 600 N at an applied displacement of 0.1 mm, and the peak reaction force kept constant for a while, followed by fracture initiation when the displacement reached 0.14 mm, resulting in a rapid drop in load.

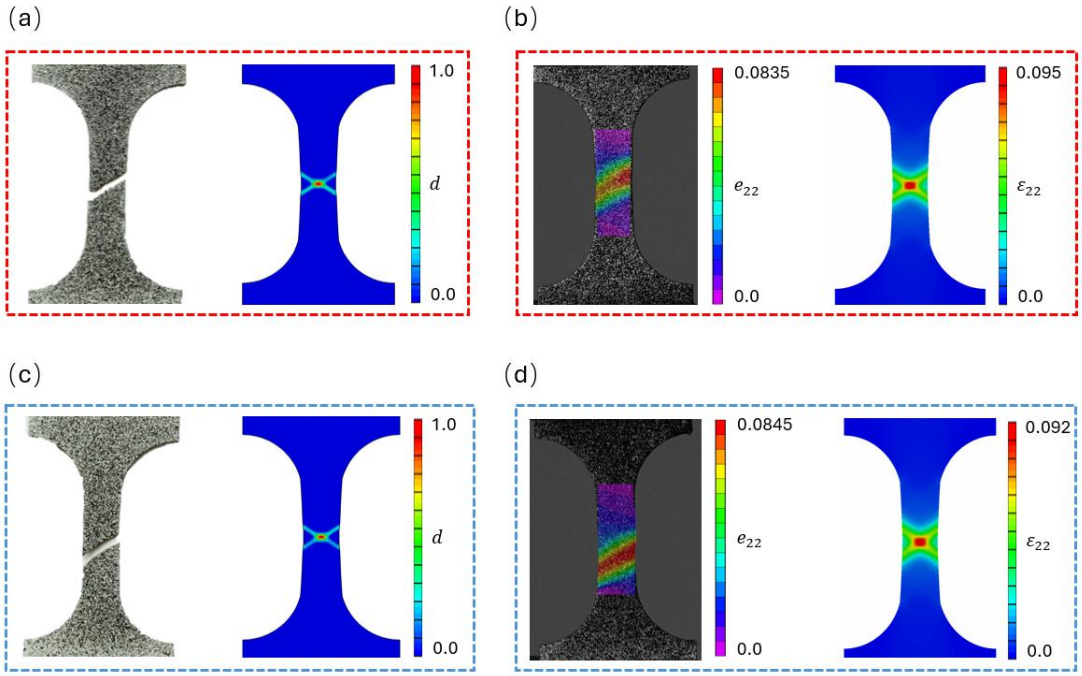

Figure 6.5 Comparison of numerical and experimental result of uniaxial tension specimens: (a) fracture path for UT axial specimen; (b) axial strain distribution for UT axial specimen; (c) fracture path for UT hoop specimen; (d) axial strain distribution for UT hoop specimen.

6.3.3 Model validation via five-holes specimen

With the previously calibrated model parameters in hand, a five-hole specimen was tested and simulated using the proposed shell phase-field model. The experimental and numerical results were compared to validate the calibrated shell phase-field model, strengthening confidence in their application to the battery casing and battery cell.

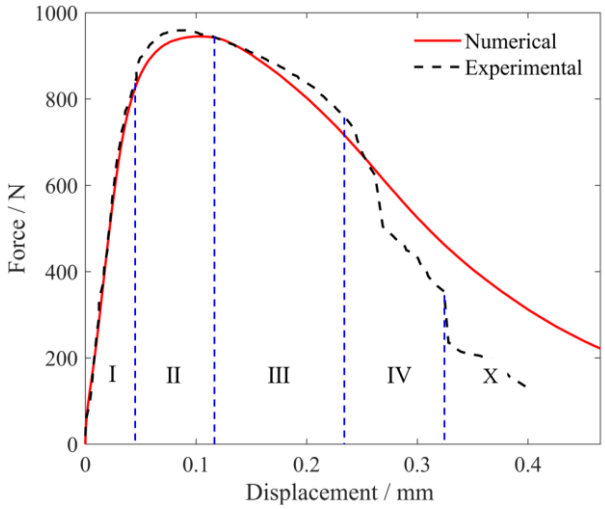

Figure 6.6 Force-displacement curve for the five-holes specimen

The force-displacement curve of the five-hole specimen is presented in Figure 6.6, where the loading process can be divided into five distinct stages. In the initial elastic

stage, the reaction force increased linearly to 800 N as the applied displacement reached 0.045 mm. Subsequently, plastic behaviour occurred, and the reaction force exhibited a nonlinear increase characterised by a progressively diminishing rate, signifying the onset of the second stage. During this phase, the reaction force peaked at 950 N at the applied displacement of 0.117 mm. At this moment, fracture initiation was observed at ligament A-B of the specimen, as depicted in Figure 6.7.

The specimen then entered the third stage, during which the reaction force decreased steadily until the applied displacement reached 0.231 mm. Correspondingly, the fracture gradually propagated at ligament A-B, while significant plastic deformation was accumulated at ligaments C-E and F-G. In the following fourth stage, due to the large plastic deformation, fracture paths at ligaments C-E and F-G developed, as illustrated in Figure 6.7. As the applied displacement increased to 0.331 mm, the load experienced a sharp decline, accompanied by the complete rupture of ligaments C-E and A-B and partial cracking of ligaments B-C, E-F, and F-G. In the last stage, fracture continued to develop, forming a clear crack path along ligaments A-B-C-D-E-F, leaving only a slight connection at ligament F-G. The reaction force continued decreasing to a small value by the end of the loading process.

As shown in Figure 6.6 and Figure 6.7, the numerical simulation closely matched the experimental results, especially during stages I, II, and III, with acceptable deviations in the later stages. Unlike the experimental results, where the reaction force exhibited two sharp decreases, the numerical results present a smoother decline. In the numerical simulation, the symmetric geometry caused simultaneous fracture development in ligaments A-B and F-G, as well as B-C and E-F. In contrast, the experimental tests revealed slight asymmetries due to sample cutting errors and material inhomogeneity, resulting in deviations from perfect symmetry. Despite these deviations, the overall force-displacement trend, including the peak force, fracture initiation, and the sequence of fracture path evolution, was well captured. This agreement validates the accuracy of the calibrated parameters and the shell phase-field model.

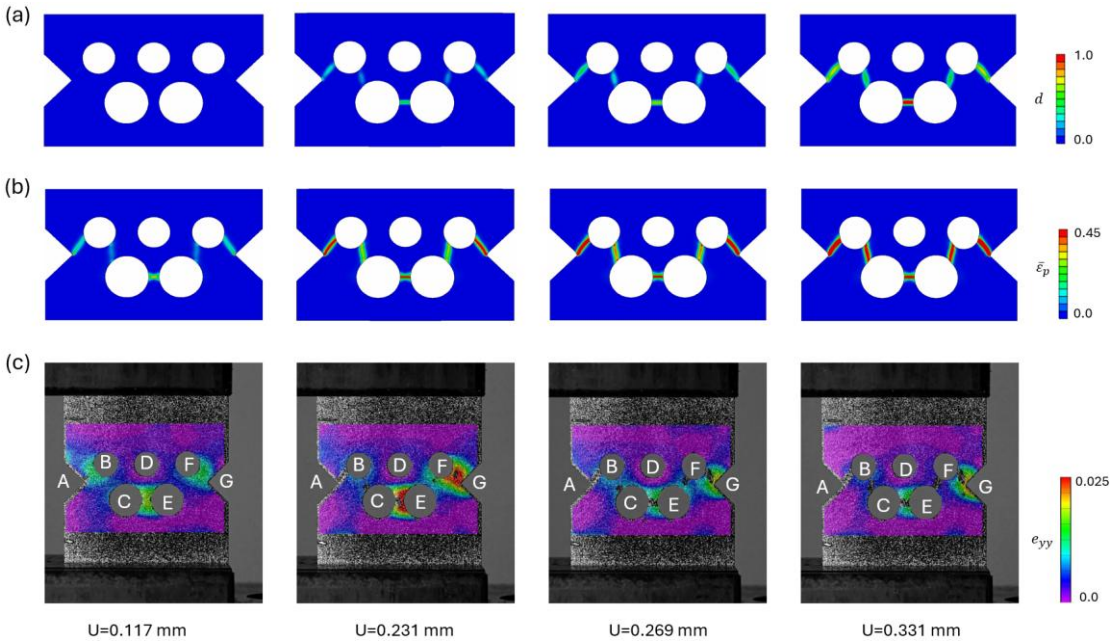

Figure 6.7 Force-displacement curve of Five holes specimen and comparison of fracture path between numerical results and experimental observations.

6.4 Simulation of fracture behaviour of the battery case and battery cell

In this section, battery casing specimens were prepared by extracting them from the battery cell and removing their two ends. The prepared casing specimen could be simplified as a cylinder with a length of 60 mm, a diameter of 18 mm in the numerical modelling. Three-point bending and axial compression tests were performed on the prepared specimens. The calibrated shell phase-field model from the previous section, was employed to simulate these two mechanical tests. Finally, a three-point bending test was conducted on the entire battery cell, both experimentally and numerically.

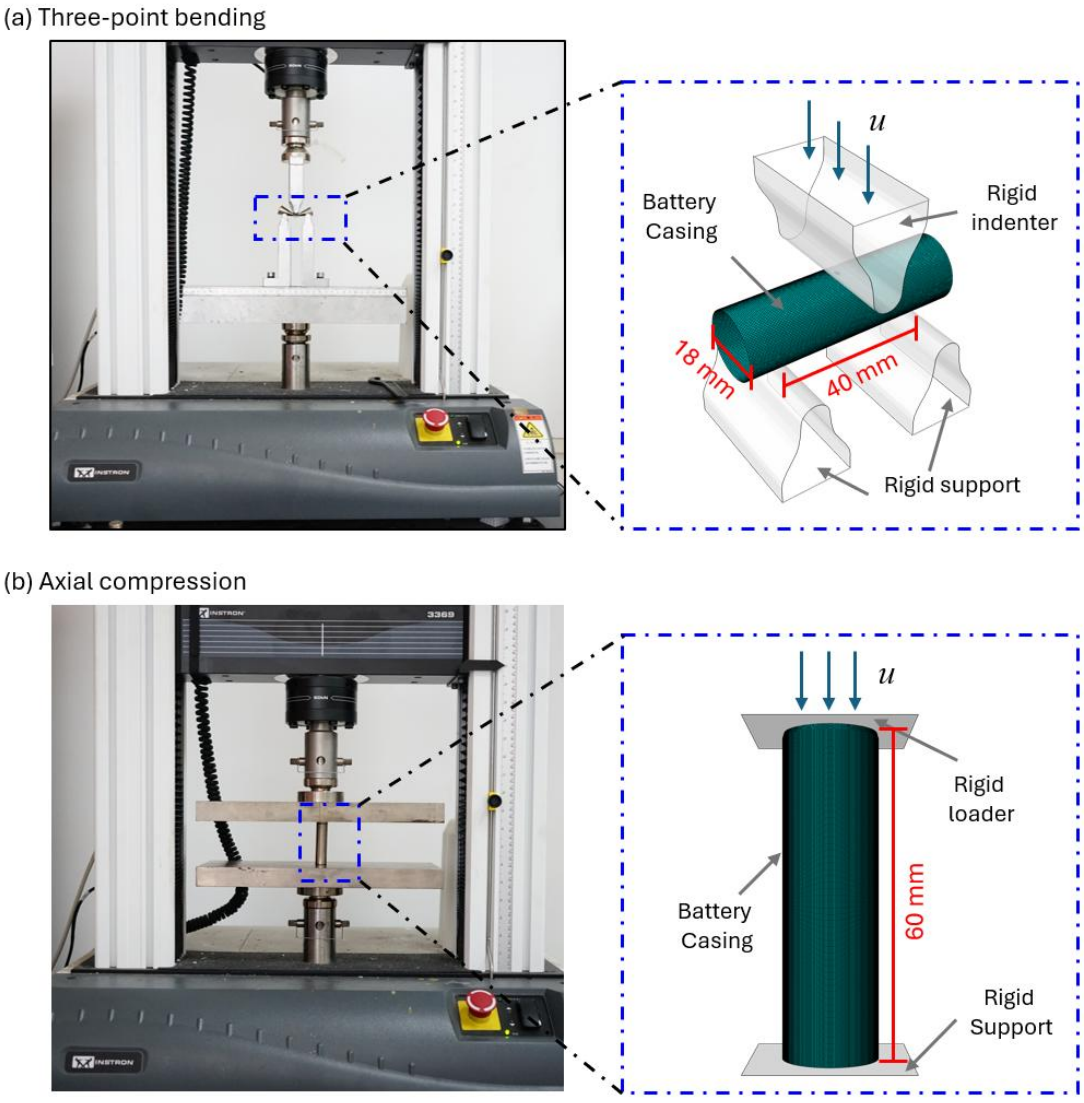

Figure 6.8 Experimental and numerical set up. (a) three-point bending test; (b) aixial compression test.

6.4.1 Three point bending test on the battery shell

The experimental and numerical set up for the three point bending test on battery casing are shown in Figure 6.8(a), where the span between two supports is set as 40 mm. A rigid indenter applies the downward displacement at the mid-span of the battery casing, at a rate of 2 mm/min. In the numerical model, the battery casing was meshed with 4-node, reduced-integration, quadrilateral shell (S4R) elements of 0.2 mm size. the viscosity parameter for the phase field model was set to 10^{-4} kN·s/mm^2 to achieve high computational efficiency while ensuring the artificial viscosity energy remained negligible. Accordingly, to satisfy the stability requirements for phase field damage evolution (Wang, Ye et al. 2019, Hu, Tan et al. 2023), the time increment was set to 10^{-8} s.

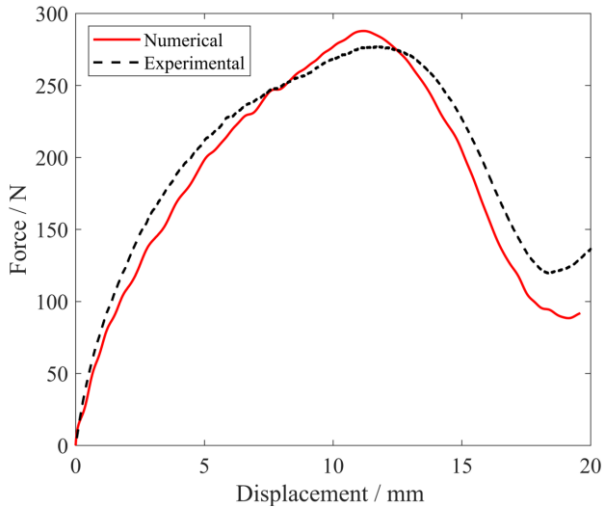

Figure 6.9 Force-displacement curve of battery shell under three point bending test

As shown in Figure 6.9, the experimental force-displacement curve for the three-point bending test was well captured by the numerical model. The reaction force showed a nonlinear increase at the beginning of loading. This behaviour resulted from significant local deformation around the indenter. During this stage, substantial local plastic deformation was observed at the plastic hinge A_m-B_m-C_m on the top surface at mid-span and the axial hinge A_l-A_m at mid-height, as depicted in Figure 6.10 (a). As the applied displacement increased to 12 mm, the reaction force peaked at around 275 N. This peak force corresponded to the fracture initiation at two hinge points, A_m and B_m, , due to severe plastic deformation, as demonstrated in Figure 6.10(b). Subsequently, the reaction force exhibited a decreasing trend as the indenter continued to increase. During this period, the phase field evolved radially from its initiation points, forming a damaged area at those two corners, as demonstrated in Figure 6.10 (c).

Interestingly, the reaction force showed a slight rebound when the indenter displacement was further increased, a phenomenon also captured in the numerical simulation. This behaviour can be attributed to the contact between the two semi-cylindrical surfaces at this stage, as indicated in Figure 6.10 (d). Notably, the lower semi-cylindrical surface had not undergone significant plastic deformation before this contact. Following the contact, further plastic hardening in this region contributed to the rebound in the loading force.

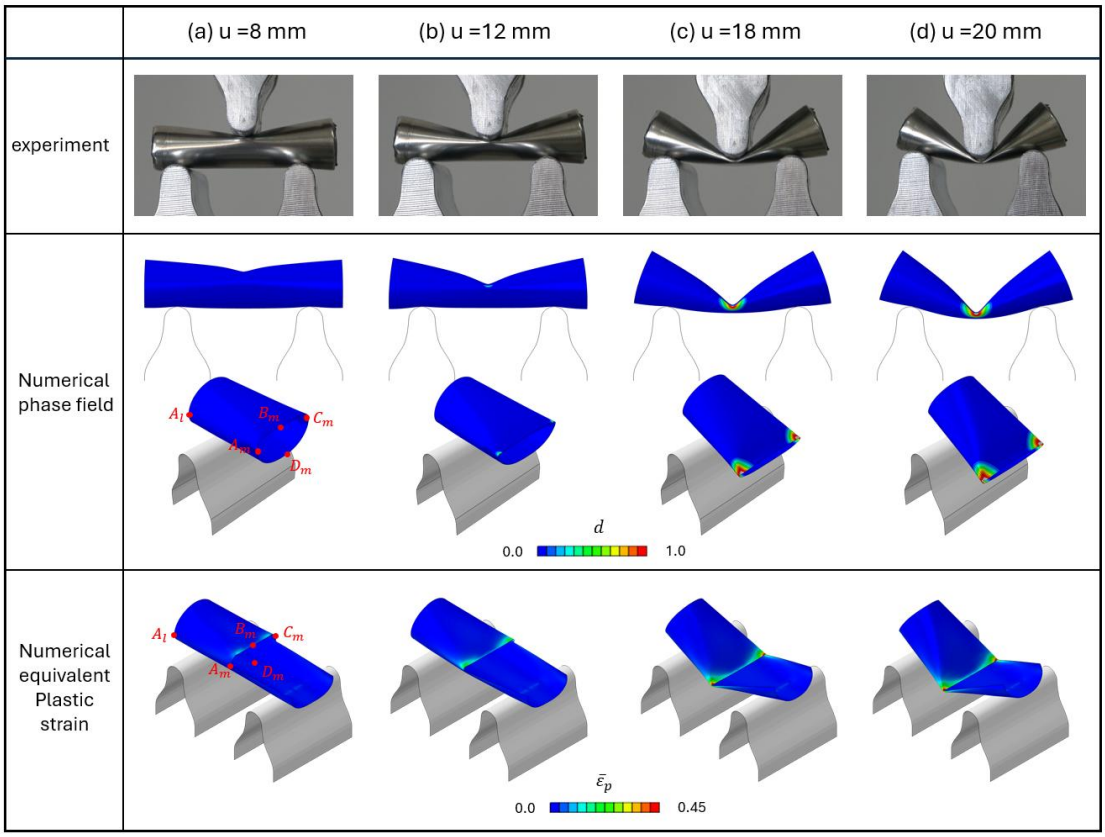

Figure 6.10 Comparison of fracture path of Battery shell under three point bending test between numerical results and experimental observations.

In order to analyse the different stress state and damage evolution for material at different depth along the shell thickness, the histogram of stress triaxiality η at the fracture initiation for five layers of section points are plotted in Figure 6.11(a). It is noted those five section points are denoted as SP1, SP2, SP3, SP4 and SP5, sequenced from bottom surface to top surface for simplification description below, as demonstrated in Figure 6.11. Most damage in this numerical model are initiated at section points close to the bottom or top surface, while only very little damage occurred at section points (SP2 and SP3) around the middle neutral surface. It is also interesting to note that the stress triaxiality at fracture initiation mostly fall into intervals of [0.5, 0.65] for SP1, while [0.1, 0.3] for SP4 and SP5. To further investigate this phenomenon, a representative element located at point A_m was selected, and its equivalent plastic and corresponding stress triaxiality during the whole loading process was plotted in Figure 6.12, accompanied with the fracture locus curve calibrated by material specimen in last section.

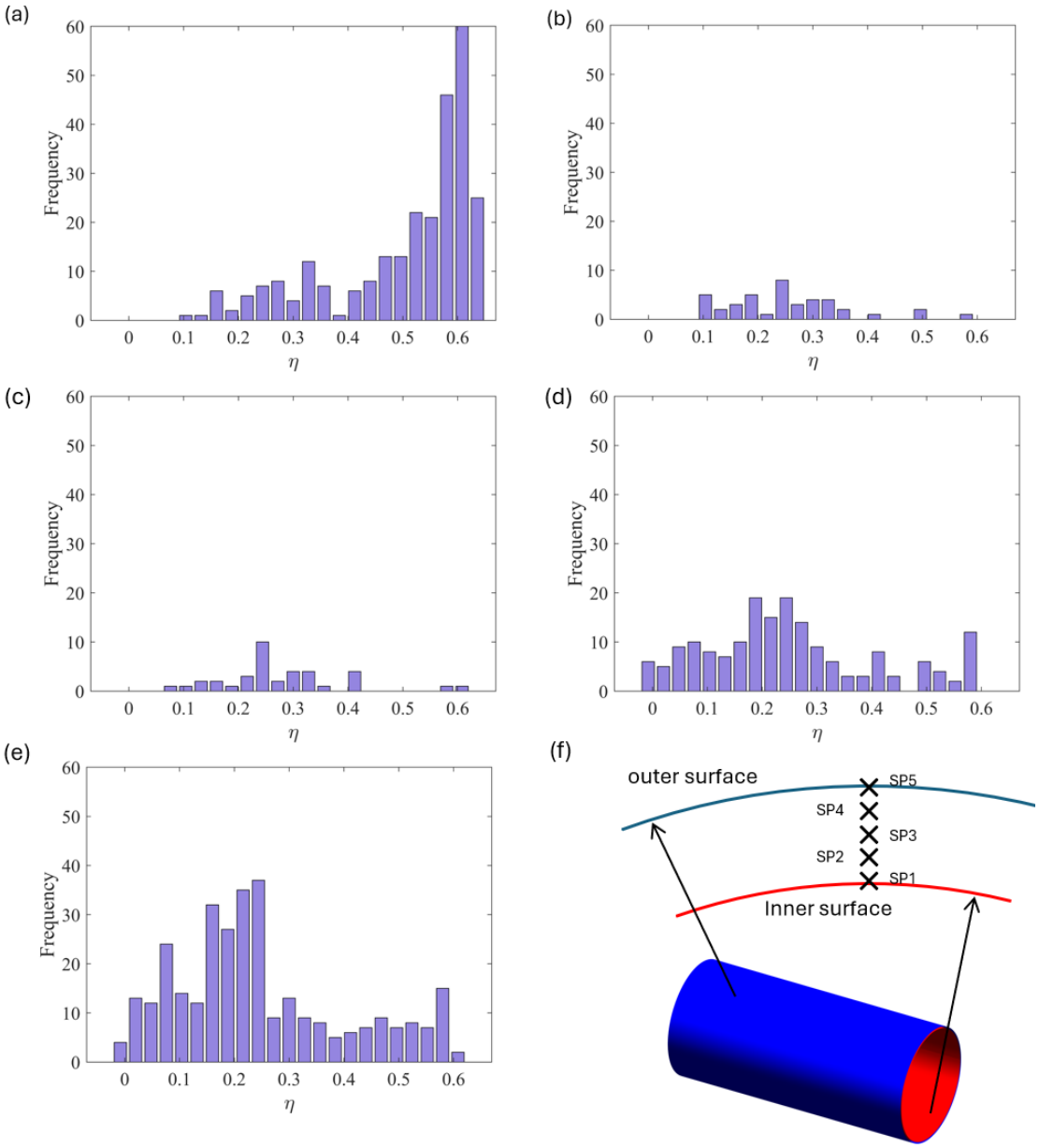

Figure 6.11 (a)-(e)Histogram of the stress triaxiality at fracture initiation at five section points(SP1, SP2, SP3, SP4 and SP5) for the three-point bending test on battery shell; (f) the location of section points along shell thickness.

At the initial loading, a hinge occurred along the sample edge A_l-A_m, and the selected element was bending inward, as demonstrated in Figure 6.12. Due to the bending, the shell element developed large plastic deformation along thickness, with tensile and compressive stress state for materials close to top and bottom surface respectively. Consequently, the damage index started to grow at section points of SP4 and SP5, where the fracture strain threshold was calculated as 0.2 at the stress triaxiality of approximately 0.5 according to Eq.(6.18). On the other hand, for other three section points, due to the negative stress triaxiality, the fracture locus was cut-off, and damage index parameter

remain zero despite of the development of equivalent plastic strain. As the intender continued moving downward, the axial hinge A_l-A_m gradually moved downward. The stress triaxiality at SP4 and SP5 gradually decreased to approximate 0.25, resulting in lower fracture strain locus, which accelerate the damage index growing and damage initiated at these two section points.

Afterward, as the continuous loading of indenter, it is interesting to note that the selected shell element started to bend outward, forming the hinge of A_m-B_m-C_m, as demonstrated in Figure 6.12. Due to the transfer of bending direction, the stress triaxiality at section points close to bottom surface rose quickly from negative cut-off region to large value, resulting the decrease of fracture strain threshold. The damage index parameter developed quickly at the SP1 with the growing plastic strain, and fracture initiated at the stress triaxiality of approximately 0.5. In contrast to SP1, material at SP2 and SP3 only developed limited plastic strain attributed to the relatively small bending stress close to middle neutral surface, and the fracture was not initiated until the end of loading.

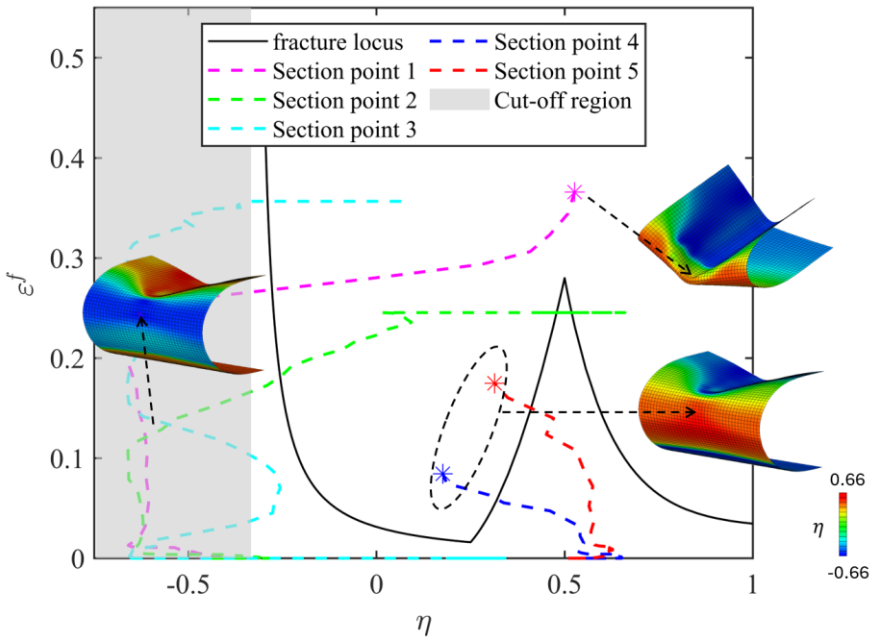

Figure 6.12 Evolution of equivalent plastic strain and stress triaxiality at five section points of selected element located at point A_m during the loading process

6.4.2 Axial compression test on the battery shell

The experimental set up for the axial compression test is presented in Figure 6.8(b), the battery casing is placed on support and subjected to loading using the loader at the rate of 2 mm/min. The numerical parameter setting, including geometry mesh, time increment, and viscosity parameter kept consistent with the three-point bending test.

As plotted in Figure 6.13, the overall trend of the experimental force-displacement curve can be well captured by the numerical results, both of which fluctuated up and down during the loading process with an average value at around 2000 N. The first peak force occurred at approximately 3000 N when the applied displacement reached around 2 mm, followed by the appearance of the first valley at around 1200 N when the displacement increased at around 6 mm, which have been exactly reproduced in the simulation result. Subsequently, the force-displacement curve continued to experience nine obvious fluctuations until the applied displacement increased to 50 mm. Finally, the reaction force soared to more than 12000 N quickly till the end of the load due to the structure densification. Notably, in the shell phase field simulation, the densification was delayed, resulting from the automatic reduction of contact thickness between stacked shell elements in the ABAQUS algorithm.

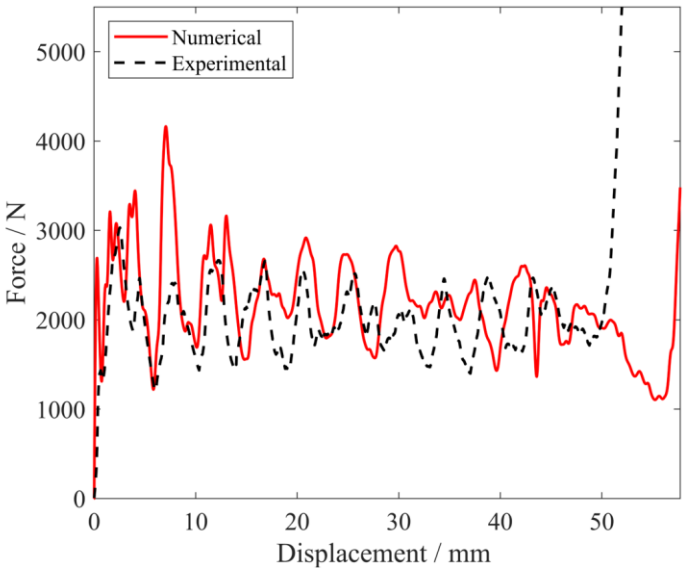

Figure 6.13 Force-displacement curve of Battery shell under axial compression test

The numerical structural deformation was compared with experimental observations in Figure 6.14. The figure displays three columns of damage contours, illustrating the phase field evolution at mid-thickness points of the shell. These contours are presented for the deformed, undeformed, and half-scaled deformed shapes. Additionally, the equivalent plastic strain contour is included to provide further insight into the influence of deformation hinges on damage evolution.

The classic diamond deformation mode is clearly observed in the experimental test. This finding aligns with previous studies, such as (Yu and Xue 2022), which demonstrated that the diamond mode is more likely to occur in cylindrical shells with a large diameter-

to-thickness ratio under axial compression. However, the numerical results in this study initially exhibited ring-mode deformation. This discrepancy can be attributed to the defect-free conditions assumed in the simulation, which allowed the material under the loader to deform asymmetrically, leading to ring-mode buckling at the onset of loading. As the applied displacement increased to approximately 10 mm, the deformation of the battery casing transitioned to a non-axisymmetric pattern due to contact and destabilization effects, ultimately converting to the diamond mode. Notably, this transition in deformation mode contributed to a higher second peak reaction force in the numerical simulation results compared to the experimental data, as shown in Figure 6.13.

Subsequently, three pairs of inclined hinges formed at three bulged points and propagated downward along the ±45° directions. These hinges intersected at the swollen regions of the material, creating new bulged points at a lower height of the battery casing. As the applied displacement increased, the hinges compacted, forming a horizontal crease. The materials on either side of the crease came into contact, completing one cycle of wrinkling formation. This process repeated, leading to the development of diamond-mode wrinkling layer by layer. The final wrinkling pattern emerged at an applied displacement of 40 mm, exhibiting a slightly different configuration due to its proximity to the end boundary. Specifically, the final wrinkle spanned approximately 10 mm along the casing, compared to the earlier wrinkles, which were confined to about 5 mm. Additionally, the deformation of the final layer initiated simultaneously at both the top and bottom edges. As shown in Figure 6.15, the simulation results effectively captured the key mechanical characteristics of the battery casing during the formation of the final wrinkling.

To analyse the mechanical response of the shell structure at different section points along its thickness, Figure 6.15 presents numerical results for the outer and inner surfaces of the battery casing at the end of loading. Interestingly, the stress triaxiality on the two surfaces exhibited opposite patterns. On the outer surface, the stress triaxiality showed high values along the hinges but was negative along the horizontal crease. Conversely, the inner surface displayed the opposite behaviour. However, due to slight hinge movement during loading, the stress triaxiality on the inner and outer surfaces shifted accordingly, leading to the evolution of phase field damage on both sides of the shell casing. In contrast, experimental observations did not reveal such large-scale fracture paths. This overestimation of damage development in the numerical results may be attributed to the large plastic strain along the hinges, as shown in Figure 6.14, resulting

from the local plasticity formulation adopted in this study.

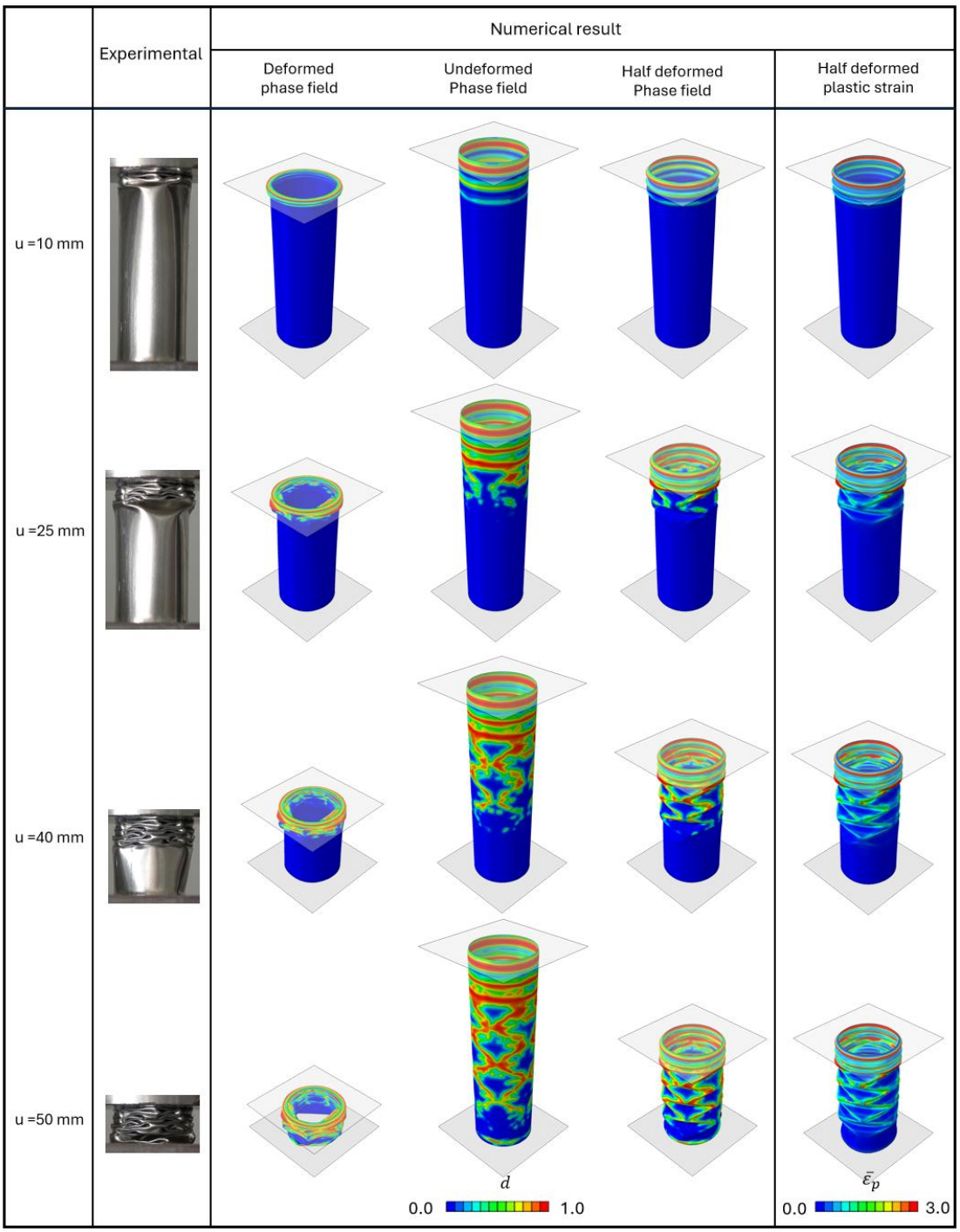

Figure 6.14 Comparison of damage evolution and equivalent plastic strain distribution with experimental observations during the loading process

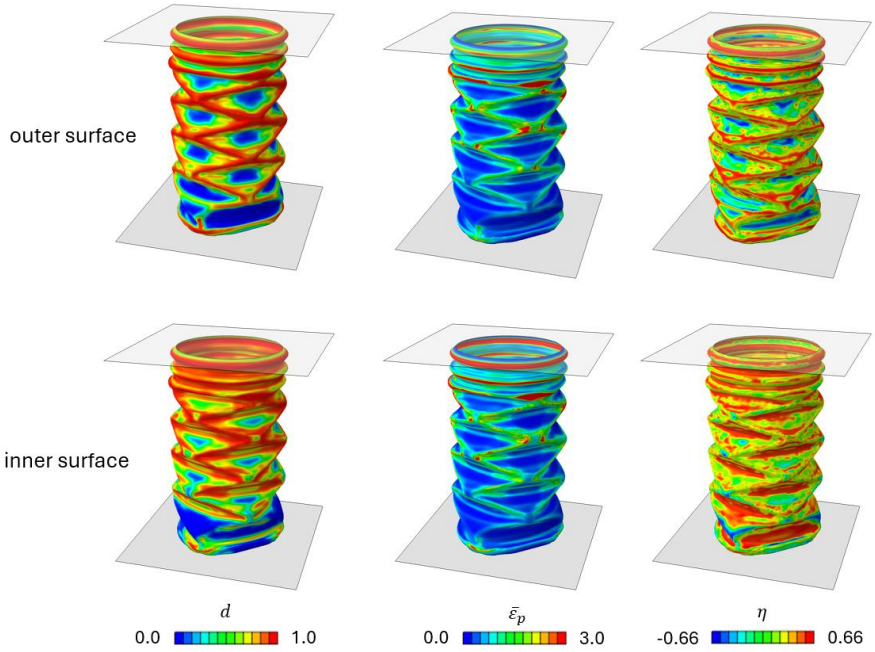

Figure 6.15 Half scaled contour of phase field, equivalent plastic strain and stress triaxiality distribution on the inner and outer surface of battery casing in the end of axial compressive test.

6.4.3 Three point bending test on the whole battery cell

In the final example, a three-point bending test was conducted on the entire battery cell using the experimental setup shown in Figure 6.8(a). The battery cell was simplified into four primary components: the cover, jellyroll, winding, and battery casing, as illustrated in Figure 6.16. The cover was modelled as an elastic material due to its low stress state and minimal influence on the test results. The winding was assumed to behave as an elasto-plastic material, which did not develop any damage in the experimental observation. The jellyroll, composed of multiple layers of anodes, cathodes, and diaphragms, has been extensively studied in the literature for its mechanical properties. For this study, a simplified homogenized elasto-plastic material model was chosen for numerical simulations, which effectively captures the jellyroll mechanical behaviour, characterized by an initial soft response during loading, followed by hardening as the stacked layers of anodes, cathodes, and diaphragms densify. Material parameters for all battery components, except for the battery casing, are detailed in Table 2, which refers to our recently submitted paper.

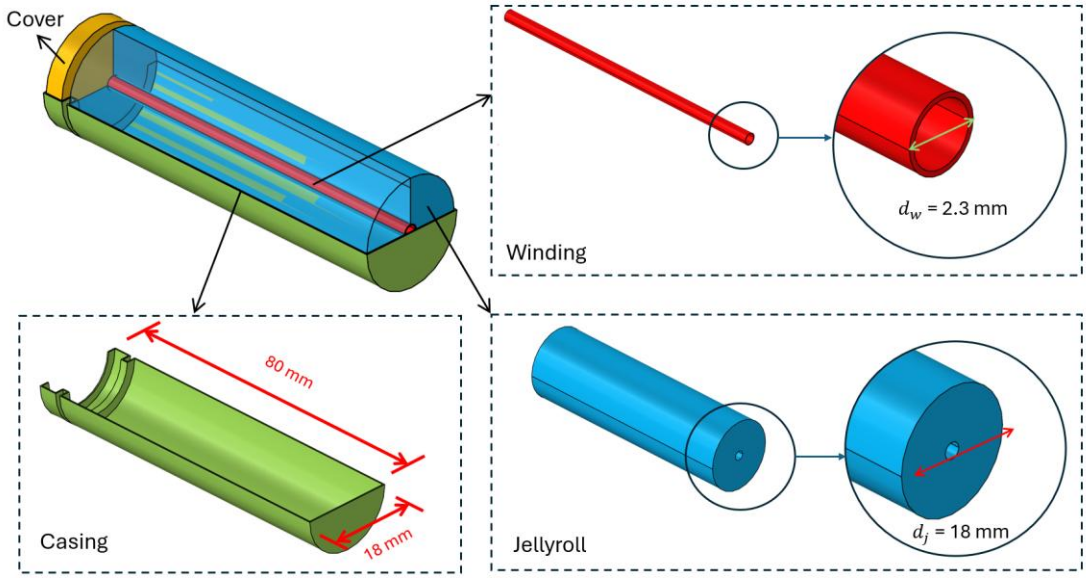

Figure 6.16 Assembly of the components of an 11865 lithium-ion battery

The numerical and experimental force-displacement curves for the three-point bending test, presented in Figure 6.17, demonstrate good agreement. At the initial stage of loading, the reaction force exhibited a brief linear increase, attributed to the indentation of the loader on the battery casing, followed by a phase of gradually decreasing growth rate. When the applied displacement reached approximately 1.5 mm, the growth rate of the reaction force significantly increased. This behaviour resulted from the contact and local densification of the jellyroll, which strengthened the battery structure, as illustrated in Figure 15. Subsequently, the force-displacement curve entered a period of steady increase until the applied displacement reached 6 mm. At this point, the experimental force peaked at approximately 4800 N, closely matched by the numerical prediction of around 4500 N. Finally, a sudden drop in the reaction force occurred after the peak in both the experimental and numerical results. This drop corresponded to the formation of a through-crack along the lower semi-cylindrical curve in the middle of the battery casing, signifying complete structural failure.

The simulation results of battery deformation are presented alongside experimental observations during the loading process in Figure 6.18. For the battery casing, the first two rows illustrate the phase field evolution from front and upward views, while the third and fourth rows display the Mises stress and equivalent plastic strain contours. Additionally, the Mises stress distribution of the jelly roll and winding is shown in subsequent rows. Overall, the simulation results align well with the general deformation characteristics observed experimentally.

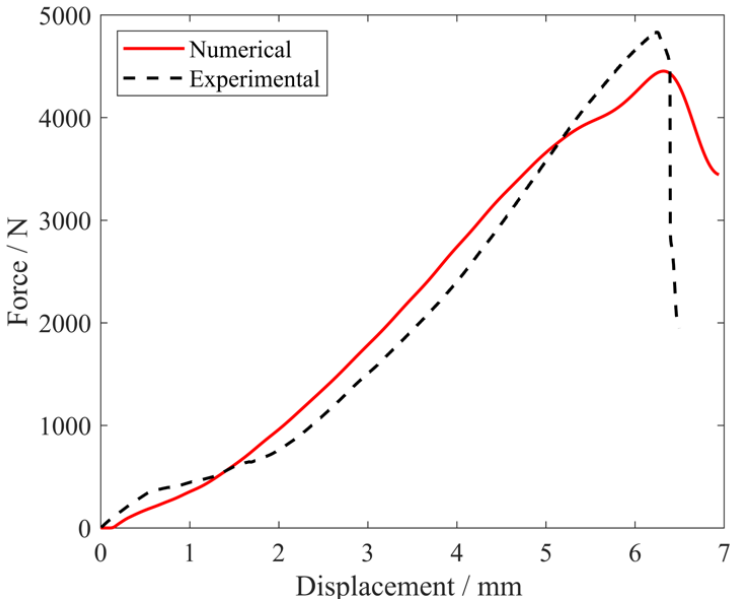

Figure 6.17 Force-displacement curve of Battery cell under three-point bending test

At an applied displacement of 1.5 mm, most materials in the battery casing, jelly roll, and winding experienced low stress levels, except at the contact points on the casing. As the applied displacement increased to 5.3 mm, significant deformation became apparent, particularly around the contact points. High stress levels developed at the bottom and the middle cylindrical edge of the casing, whereas plastic strain emerged at the upper semi-cylindrical edge in the middle of the battery casing. However, due to the compressive stress state, the phase field did not initiate, consistent with the fracture strain locus, indicated by Eq.(6.18). Notably, yielding began in the winding at its middle position, which likely contributed to the slower rise in reaction force observed in the numerical force-displacement curve in Figure 6.17. Simultaneously, the high-stress region in the jelly roll expanded radially from the contact points.

At a displacement of 6.0 mm, fracture initiation occurred at the bottom of the middle cylindrical edge of the casing, where significant plastic strain accumulated under a tensile stress state. Damage initiation caused a marked stress reduction in adjacent areas. In the final stage, at a displacement of 7.1 mm, a through-crack formed at the bottom of the middle cylindrical edge of the casing, accurately reproducing the experimental crack path.

Table 6.2 Material parameters for battery components inside the casing

Components	Parameters	Physical meaning	Value
Cover	E	Elastic modulus	150 GPa
	υ	Poisson's Ratio	0.2
Winding	E	Elastic modulus	150 GPa
	υ	Poisson's Ratio	0.2
	σ_y	Yield stress	1100 MPa
JellyRoll	E	Elastic modulus	327 MPa
	υ	Poisson's Ratio	0.3

To understand the stress state within the battery casing at different section points along the shell thickness and its influence on fracture damage initiation, Figure 6.19 presents a histogram of the stress state at fracture initiation for five section points in the numerical model. It is observed that the majority of damage occurs at SP1 and SP5, which are located near the bottom and top surfaces, respectively, followed by SP4. In contrast, minimal damage is observed at SP2 and SP3, which are situated close to the neutral surface of the shell structure. Furthermore, damage initiation is most likely to occur within the stress triaxiality intervals of [0.1, 0.3] and [0.55, 0.65], attributed to the lower fracture strain in these regions.

Figure 6.20(a-b) depicts the final contours of the damage index parameter *D* on the inner and outer surfaces of the casing. A magnified view of the central region of the battery, highlighting the primary damage zone, is provided in Figure 6.20(c), alongside corresponding experimental observations in Figure 6.20(d). The material damage in this test can be categorized into three distinct regions. First, a pronounced through-thickness semi-cylindrical crack path is observed in the bottom central region of the battery casing, contrasting with the three-point bending test on the casing alone, where no damage was observed in the bottom half. Second, damage initiation is evident on the outer surface of the front and back sides of the casing due to significant swelling. Additionally, phase field damage is initiated at the top of the specimen, where the material directly contacts the indenter. To further investigate the stress state and plastic strain evolution in these regions during loading, points A, B, and C were selected from each region, and their damage evolution was analysed, as illustrated in Figure 6.20(e)-(g).

For point A, located in the swelling region, the stress triaxialities at section points SP1, SP2, and SP3 remain around -0.5, within the cut-off region, preventing damage initiation. Conversely, the stress triaxialities at SP4 and SP5 initially exhibit high values

around 0.5, gradually decreasing during swelling formation, thereby reducing the fracture strain threshold. Damage at these section points initiates at a stress triaxiality of approximately 0.2.

For point B, situated beneath the indenter, the stress triaxialities along the shell thickness fluctuate significantly between -0.5 and 0.5. This variation is attributed to the changing bending direction caused by the moving hinge under continuous indenter loading. Consequently, damage is more likely to initiate on the outer or inner surfaces of this region, accompanied by substantial plastic strain development.

For point C, located at the middle bottom of the shell casing, the stress triaxiality and plastic strain evolution exhibit high consistency, as shown in Figure 6.20(g). Unlike the three-point bending test on the casing alone, where the upper half of the semi-cylindrical casing bears most of the load, in the battery cell test, the bending force from the indenter is distributed across both the upper and lower parts of the cylindrical casing via the internal jellyroll. The upper half of the casing experiences compressive axial stress, inducing bending deformation and swelling, while the lower half is subjected to tensile stress. As a result, the stress state at the middle bottom area is dominated by membrane tensile stress, with all sections demonstrating a consistent stress triaxiality of approximately 0.5 until phase field damage initiation.

This analysis underscores that the stress state of materials in real-world structures undergoes significant changes during loading. Moreover, the evolution of plastic strain and stress state remains consistent under membrane tensile-dominant conditions but varies considerably under bending-dominant conditions. Therefore, it is crucial to account for stress-state-dependent crack initiation at multiple levels across the shell thickness to accurately capture fracture behaviour and mechanical response, which is well characterized in this proposed shell phase field model.

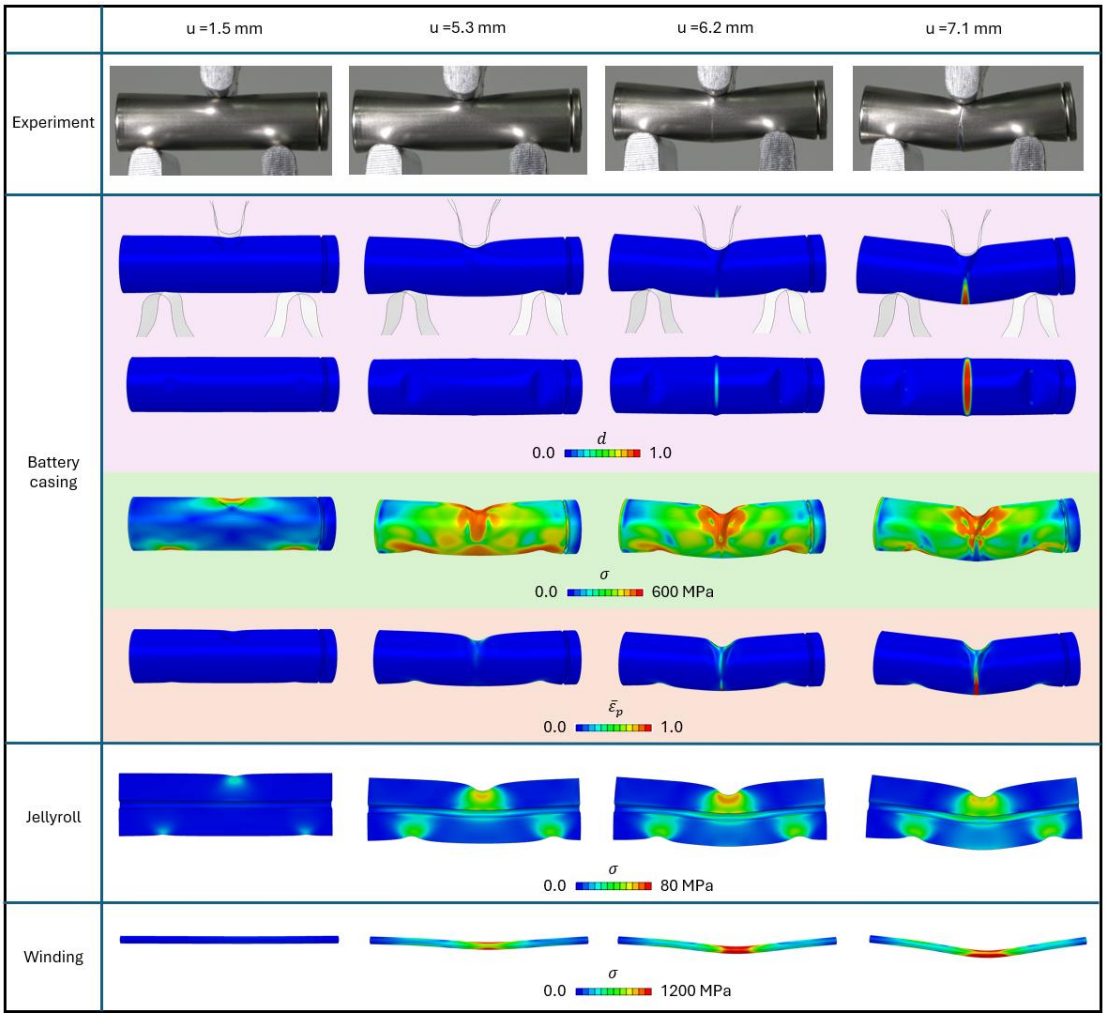

Figure 6.18 Comparison of numerical crack path evolution with the experimental observation for battery cell under three-point bending test

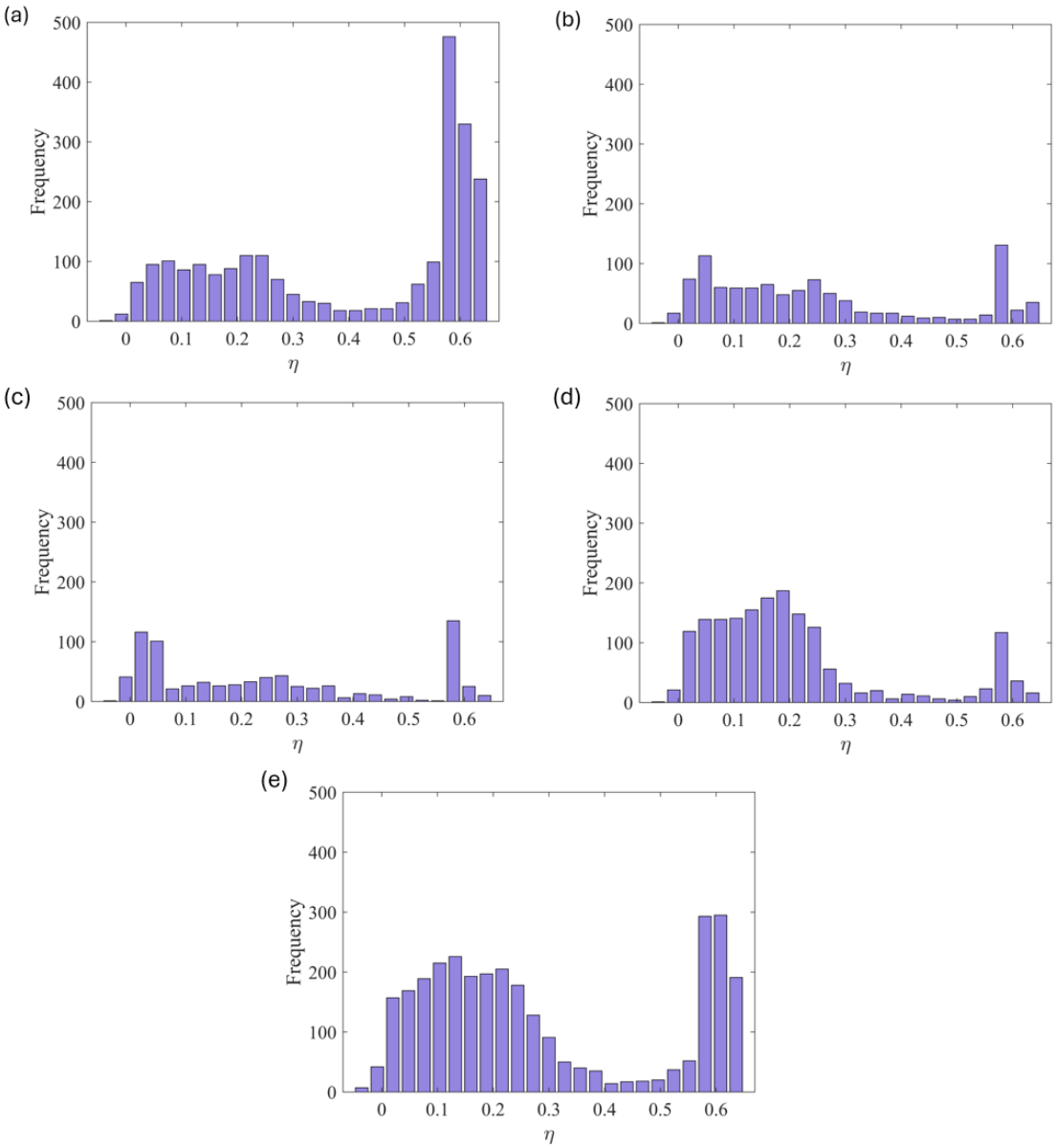

Figure 6.19 (a)-(e)Histogram of the stress triaxiality at fracture initiation at five section points(SP1, SP2, SP3, SP4 and SP5) for the three-point bending test on battery cell.

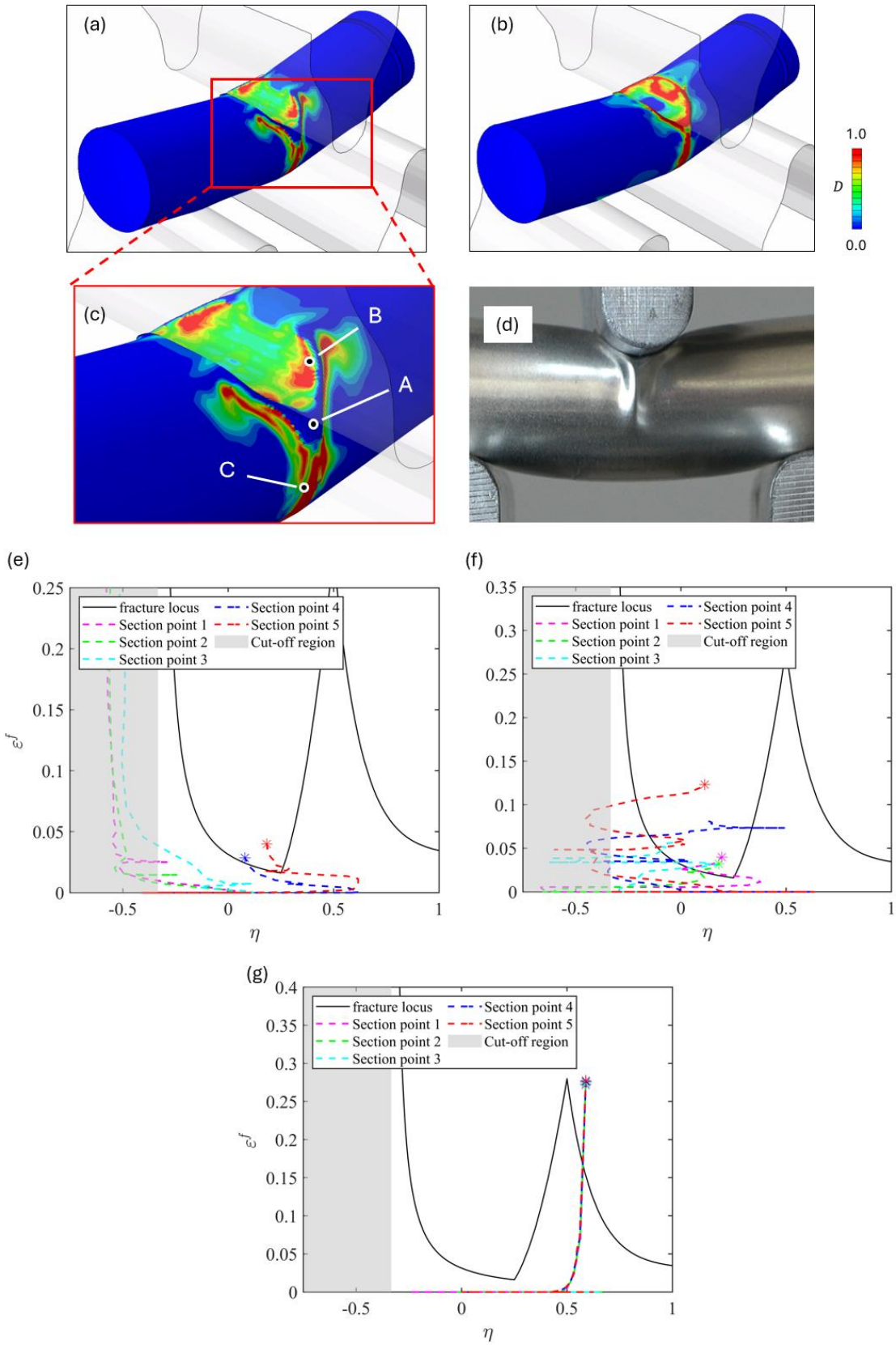

Figure 6.20 Load history for three representative points on the battery casing for the three-point bending test on the battery

6.5 Summary

In this study, the shell phase-field model previously developed was employed to simulate the crush behaviour of a 11850 lithium-ion battery casing. Extensive material testing was conducted to calibrate the model parameters accurately. Experimental results from uniaxial tension specimens along three distinct orientations revealed pronounced anisotropy in yield stress, effectively captured using the Hill 48 stress model with appropriately calibrated parameters. In contrast, the elastic modulus and fracture strain demonstrated minimal sensitivity to material orientation. To account for the stress-state dependence of fracture strain, the Bao-Wierzbicki fracture criterion was adopted. Model parameters were calibrated by correlating experimental and numerical force-displacement curves derived from a series of tests, including uniaxial tension, notched tension, and central hole specimens. Validation was further performed using a five-hole specimen test, with the simulated fracture behaviour and force-displacement curves showing strong agreement with experimental results.

The calibrated parameters were subsequently applied to simulate three-point bending and axial compression tests on the battery casing. For the battery casing, the three-point bending test indicated that damage was concentrated at the front and back equatorial points where the element bending direction transitioned from inward to outward as the indenter advanced, leading to damage initiation in the material near the outer and inner surfaces. In the axial compressive loading, the fluctuated numerical force-displacement curves generally aligned with the experimental result despite of a slight delay in densification, which is attributed to the automatic thickness reduction in Abaqus contact algorithm for stacked shell elements. In the three-point bending test on the battery cell, damage within battery casing primarily occurring at section points near the inner and outer surfaces, with stress triaxiality mainly falling into intervals of [0.1, 0.3] and [0.55, 0.65]. The analysis of three representative elements showed significant depth-dependent variation in stress states and plastic strain under bending-dominant conditions, with consistent behaviour observed under membrane tensile-dominant conditions.

The numerical and experimental analyses in this study reveal that the stress state of materials in real-world structures undergoes significant changes during loading and varies considerably along the shell thickness, particularly under bending-dominant load conditions. Consequently, it is essential to account for stress-state-dependent crack

initiation at multiple levels across the shell thickness to accurately capture fracture behaviour and mechanical response, a capability well-characterized by the proposed shell phase-field model. Despite its effectiveness and robustness in simulating the mechanical behaviour and damage evolution of battery casings, the proposed model still has several limitations that warrant further investigation. For instance, incorporating a nonlocal plastic formulation could enhance its applicability to thin-walled structures undergoing large deformations. Additionally, while this study focuses on the mechanical deformation of batteries under abuse loading, the coupled electrical-mechanical response of the battery casing remains unexplored and presents a promising avenue for future research

7. DYNAMIC SHELL PHASE FIELD FRACTURE MODELLING

In practical engineering applications, thin-walled structures such as battery casings, pressure vessels, and aerospace components are often subjected to dynamic loading conditions, including impact, blast, and rapid deformation. Under such conditions, both the strain-rate dependence of material behaviour and the interaction between dynamic effects and fracture evolution play crucial roles in determining the structural integrity and failure mode.

Building upon the quasi-static shell phase-field formulation developed in Chapter 5, this section extends the model to account for dynamic fracture processes within thin-walled structures. The dynamic shell phase-field framework incorporates inertia effects through the balance of linear momentum and introduces a rate-dependent constitutive relationship to capture the strain-rate sensitivity of the material's flow stress and fracture energy.

7.1 Formulation of dynamic shell phase field model

7.1.1 Shell kinematics

In this study, we mainly study the dynamic fracture for Kirchhoff-Love shell (Ebenfeld 1999), with high ratio of width and thickness, where the only stress components within the shell reference are considered. As demonstrated in Figure 6.1, the crack on the the thin-wall structure can be represented on its reference surface (mid-surface). The local coordinate system ($\boldsymbol{t}_1$, $\boldsymbol{t}_2$ and $\boldsymbol{t}_3$) is also constructed based on the local reference surface to describe the shell element configuration, where $\boldsymbol{t}_3$ represents the local normal direction to the reference surface, while $\boldsymbol{t}_1$ and $\boldsymbol{t}_2$ are two orthogonal directions, following the below condition,

$$\boldsymbol{t}_i \cdot \boldsymbol{t}_j = \delta_{ij} \tag{7.1}$$

where δ_{ij} is the Kronecker delta. With the local coordinate system, the position of a material point within shell element is defined as,

$$\boldsymbol{x}(\boldsymbol{S}_i) = \overline{\boldsymbol{x}}(\boldsymbol{S}_\alpha) + \bar{f}_{33}(\boldsymbol{S}_\alpha)\boldsymbol{t}_3(\boldsymbol{S}_\alpha)S_3 \tag{7.2}$$

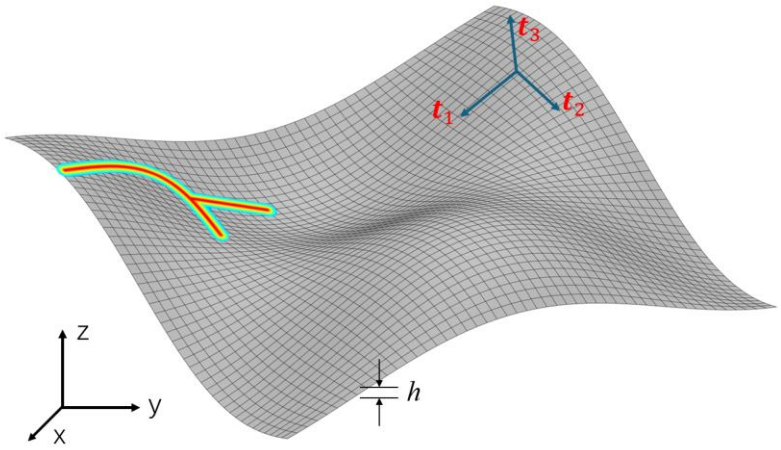

Figure 7.1 Shell crack representation in the global and local coordinate system

where $\boldsymbol{S}_\alpha$ (α ranges from 1 to 2) are local surface coordinates within reference plane, and $S_3 \in [-\frac{t}{2}, \frac{t}{2}]$ is the coordinate on $\boldsymbol{t}_3$ direction; $\boldsymbol{x}(\boldsymbol{S}_i)$ and $\overline{\boldsymbol{x}}(\boldsymbol{S}_\alpha)$ represent the position of material point $\boldsymbol{S}_i$ and its projecting point $\boldsymbol{S}_\alpha$ on the reference plane; $\bar{f}_{33}$ is the thickness increase factor, which is assumed to be constant along the thickness direction.

Based on Eq.(5.2), the gradient of the position can be expressed as,

$$\begin{cases} \dfrac{\partial \boldsymbol{x}}{\partial \boldsymbol{S}_\alpha} = \dfrac{\partial \overline{\boldsymbol{x}}}{\partial \boldsymbol{S}_\alpha} + \bar{f}_{33} \dfrac{\partial \boldsymbol{t}_3}{\partial \boldsymbol{S}_\alpha} S_3 \\ \dfrac{\partial \boldsymbol{x}}{\partial \boldsymbol{S}_3} = \bar{f}_{33} \boldsymbol{t}_3 \end{cases} \tag{7.3}$$

where the derivative of $\bar{f}_{33}$ with respect to $\boldsymbol{S}_\alpha$ has been neglected. Its components within the reference plane can be obtained as below,

$$f_{\alpha\beta} = \boldsymbol{t}_\alpha \cdot \frac{\partial \boldsymbol{x}}{\partial S_\beta} = \bar{f}_{\alpha\beta} + B_{\alpha\beta} \bar{f}_{33} S_3 \tag{7.4}$$

where the reference surface deformation gradient $\bar{f}_{\alpha\beta}$ and reference normal gradient $B_{\alpha\beta}$ are defined as follows,

$$\begin{cases} \bar{f}_{\alpha\beta} \overset{\text{def}}{=} \boldsymbol{t}_\alpha \cdot \left.\dfrac{\partial \boldsymbol{x}}{\partial S_\beta}\right|_{S_3=0} = \boldsymbol{t}_\alpha \cdot \dfrac{\partial \overline{\boldsymbol{x}}}{\partial S_\beta} \\ B_{\alpha\beta} \overset{\text{def}}{=} \boldsymbol{t}_\alpha \cdot \dfrac{\partial \boldsymbol{t}_3}{\partial S_\beta} \end{cases} \tag{7.5}$$

In the original shell configuration, $\overline{\boldsymbol{X}}$ represents the position of the projecting point on the reference plane. The original normal direction to reference plane $\boldsymbol{T}_3$ is defined by

$$\boldsymbol{T}_3 = \left(\frac{\partial \overline{\boldsymbol{X}}}{\partial S_a} \times \frac{\partial \overline{\boldsymbol{X}}}{\partial S_b}\right) \Big/ \left|\frac{\partial \overline{\boldsymbol{X}}}{\partial S_a} \times \frac{\partial \overline{\boldsymbol{X}}}{\partial S_b}\right| \tag{7.6}$$

where S_a and S_b are coordinates of two arbitrary two unparalleled directions within the reference plane of shell element. Meanwhile, direction $\boldsymbol{T}_1$ is specified as one arbitrary

direction parallel to the shell surface, for example, the projection of the global $\boldsymbol{x}$ direction on the shell surface or the roll direction for the rolled thin-wall structure. The remained $\boldsymbol{T}_2$ direction could be finally specified to be vertical to $\boldsymbol{T}_1$ within the shell reference surface.

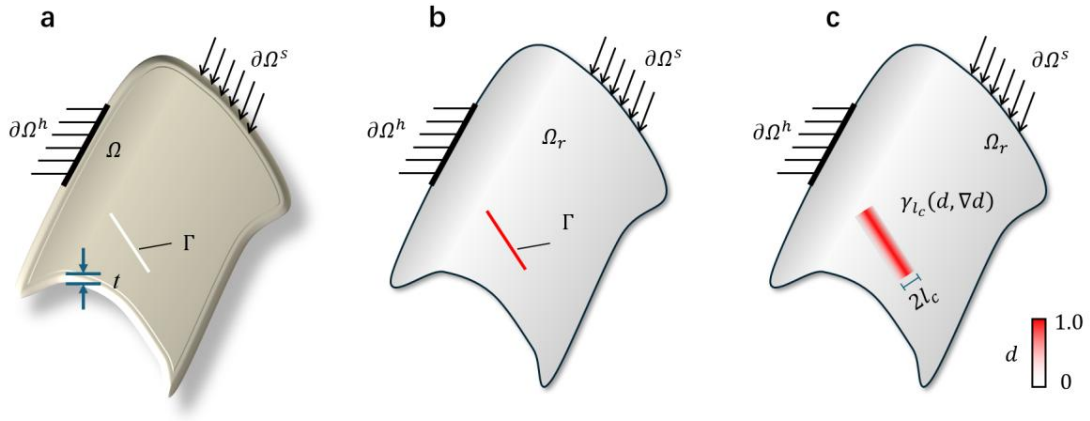

Figure 7.2 Regularisation of sharp crack to damage zone. (a) fracture topology of the shell solid (b) sharp crack on shell reference surface; (c) regularised phase field distribution on shell reference surface

7.1.2 Energy functional

7.1.2.1 Crack topology regularisation

Based on the Kirchhoff-Love shell kinematics, the fracture topology of shell structure is demonstrated in Figure 7.2(a). The shell solid Ω with thickness of t got a through-thickness sharp crack Γ, and it was under the constraint of Neumann boundary $\partial\Omega^s$ and Dirichlet boundary $\partial\Omega^h$, which satisfy $\partial\Omega^h \cap \partial\Omega^s = \emptyset$ and $\partial\Omega = \overline{\partial\Omega^h \cup \partial\Omega^s}$. In each section layer, the sharp crack Γ is regularised with phase field damage variable d, from the totally broken state ($d = 1$) to the intact state ($d = 0$) of material with the length scale parameter l_c, demonstrated as Figure 6.2(b) and (c). Accordingly, the crack surface density function γ is introduced referring to standard phase field formulation in three-dimension space, written as below,

$$\gamma(d, \nabla d) = \frac{d^2}{2l_c} + \frac{l_c}{2}|\nabla d|^2 \tag{7.7}$$

With the introduction of critical energy release rate G_f, which indicates the required energy for generating per area crack surface within Griffith fracture theory, the fracture energy E_{fra} within shell could be given by,

$$E_{fra} = \int_{\Omega} G_f \cdot \left(\frac{d^2}{2l_c} + \frac{l_c}{2}|\nabla d|^2\right) \mathrm{d}\Omega \tag{7.8}$$

7.1.2.2 Total power

Within the shell solid Ω, the deformation rate at position $\boldsymbol{x}$ within Ω is denoted as $\boldsymbol{D}$, with its elastic and plastic component represented by $\boldsymbol{D}^e$ and $\boldsymbol{D}^p$, respectively. Therefore, the elastic P_{ela} and plastic power P_{pla} can be written as follows,

$$P_{ela} = \int_{\Omega} (1-d)^2 \boldsymbol{D}^e : \overline{\boldsymbol{\sigma}} \, \mathrm{d}\Omega \tag{7.9}$$

$$P_{pla} = \int_{\Omega} [(1-d)^2(1-\chi)\boldsymbol{D}^p : \overline{\boldsymbol{\sigma}} + \chi \boldsymbol{D}^p : \overline{\boldsymbol{\sigma}}] \mathrm{d}\Omega \tag{7.10}$$

In Eq.(7.10), parameter χ denotes the fraction of dissipated plastic work that is converted into heat (You, Waisman et al. 2021), while the remained plastic work is conserved and contribute to phase damage evolution. In addition, according to the plastic work equivalisation, the plastic work in Eq.(7.10) could also be expressed by the equivalent plastic strain rate $\dot{\bar{\varepsilon}}^p$ and its conjugate effective yield stress $\bar{f}(\overline{\boldsymbol{\sigma}})$ as follows,

$$P_{pla} = \int_{\Omega} \left[(1-d)^2(1-\chi)\bar{f}(\overline{\boldsymbol{\sigma}}) \cdot \dot{\bar{\varepsilon}}^p\right] \mathrm{d}\Omega \tag{7.11}$$

The kinetic power P_{kin} is integrated within shell solid in the following formulation (Li, Liu et al. 2025),

$$P_{kin} = \int_{\Omega} \rho \dot{\boldsymbol{u}} \cdot \ddot{\boldsymbol{u}} \, \mathrm{d}\Omega \tag{7.12}$$

where $\dot{\boldsymbol{u}}$ and $\ddot{\boldsymbol{u}}$ represent the velocity and acceleration, respectively.

The fracture power can be derived from Eq.(7.8) as follows,

$$P_{fra} = \frac{dE_f}{dt} = \int_{\partial\Omega} \left(G_f l_c \boldsymbol{n} \cdot \nabla d\dot{d}\right) \mathrm{dS} - \int_{\Omega} \frac{G_f}{l_c} \left({l_c}^2 \Delta d\dot{d} - d\dot{d}\right) \mathrm{d}\Omega \tag{7.13}$$

In this study, we consider the rate-dependent viscosity energy for the fracture evolution, and the viscosity power is written as,

$$P_{vis} = \int_{\Omega} \frac{\omega}{2} \dot{d} \cdot \dot{d} \, \mathrm{d}\Omega \tag{7.14}$$

where ω denotes the viscosity parameter in consistent with previous study. In addition, the power of external work could be obtained via the body force $\boldsymbol{f}$ and traction force $\boldsymbol{t}$ on boundary $\partial\Omega^s$, as follows,

$$P_{ext} = \int_{\Omega} (\boldsymbol{f} \cdot \dot{\boldsymbol{u}}) \, \mathrm{d}\Omega + \int_{\partial\Omega^s} (\boldsymbol{t} \cdot \dot{\boldsymbol{u}}) \, \mathrm{d}\Omega \tag{7.15}$$

The rate potential functional can be written as follows (Hofacker and Miehe 2012, Li, Liu et al. 2025),

$$\Pi\left(\dot{\boldsymbol{u}}, \dot{d}, \dot{\bar{\varepsilon}}^p\right) = P_{ela} + P_{pla} + P_{kin} + P_{fra} + P_{vis} + P_{ext} \tag{7.16}$$

Based on the Hamilton theory (Dunne and Petrinic 2005, Li, Liu et al. 2025), the governing equations for displacement field and phase field in strong form could be obtained as follows,

$$\begin{cases} \nabla \cdot \boldsymbol{\sigma} + \boldsymbol{b} = \rho\, \ddot{\boldsymbol{u}} & \text{in } \Omega \\ \boldsymbol{\sigma} \cdot \boldsymbol{n} - \boldsymbol{t} = 0 & \text{on } \partial\Omega_r^s \\ \boldsymbol{u} = \bar{\boldsymbol{u}} & \text{on } \partial\Omega_r^h \end{cases} \tag{7.17}$$

$$\begin{cases} \dot{d} = \frac{1}{\omega}\langle 2(1-d)(\varphi_0^e + \psi_0^p) - \frac{G_f}{l_c}\left(d - {l_c}^2 \Delta d\right)\rangle_+ & \text{in } \Omega \\ \nabla d \cdot \boldsymbol{n} = 0 & \text{on } \partial\Omega \end{cases} \tag{7.18}$$

where φ_0^e and ψ_0^p represent the bulk elastic energy density and conserved plastic work at time *s* within the shell, and can be calculated as below,

$$\varphi_0^e(\boldsymbol{x}, s) = \int_0^s \boldsymbol{\sigma} : \boldsymbol{D}^e \, \mathrm{d}s \tag{7.19}$$

$$\varphi_0^p(\boldsymbol{x}, s) = \int_0^s (1-\chi)\boldsymbol{\sigma} : \boldsymbol{D}^p \, \mathrm{d}s \tag{7.20}$$

The formulation of equivalent plastic strain can be derived from Eq.(7.16),

$$\Phi^p\left(\boldsymbol{u}, \bar{\varepsilon}^p, \dot{\bar{\varepsilon}}^p, T\right) = \bar{f}(\bar{\boldsymbol{\sigma}}) - \sigma_y\left(\bar{\varepsilon}^p, \dot{\bar{\varepsilon}}^p, T\right) \tag{7.21}$$

where $\overline{\sigma_y}$ represents the effective (undamaged) flow stress. In this study, its hardening behaviour incorporates the dynamic effect, thermal effect, and the evolution of equivalent plastic strain, which will be discussed in detail in a later section.

7.1.3 Thermal evolution

In high-rate experiments, such as those involving impact, shock loading, or high-speed deformation, the temperature within a structure can indeed increase significantly due to the conversion of plastic work into thermal energy. This phenomenon is a result of the material's internal dissipation mechanisms during plastic deformation. Here temperature evolution was calculated using the following equation,

$$dT = \frac{\chi(\dot{\bar{\varepsilon}}^p)}{\rho C_p} \bar{\sigma}_y d\bar{\varepsilon}^p \tag{7.22}$$

where dT represents the temperature increment; C_p represents the specific heat capacity. In this study, the fraction of dissipated plastic work χ was assumed to be variable depending on the equivalent plastic strain rate, as referred in (Roth and Mohr 2014, Li, Liu et al. 2025), written as follows,

$$\chi\left(\dot{\bar{\varepsilon}}^p\right) = \begin{cases} 0 & \dot{\bar{\varepsilon}}^p < \dot{\varepsilon}_{it} \\ \frac{\left(\dot{\bar{\varepsilon}}^p - \dot{\varepsilon}_{it}\right)^2 \left(3\dot{\varepsilon}_a - 2\dot{\bar{\varepsilon}}^p - \dot{\varepsilon}_{it}\right)}{\left(\dot{\varepsilon}_a - \dot{\varepsilon}_{it}\right)^3} \cdot \chi_0 & \dot{\varepsilon}_{it} \le \dot{\bar{\varepsilon}}^p < \dot{\varepsilon}_a \\ \chi_0 & \dot{\bar{\varepsilon}}^p \ge \dot{\varepsilon}_a \end{cases} \tag{7.23}$$

where $\dot{\varepsilon_{it}}$, $\dot{\varepsilon_a}$ and χ_0 are rate-dependent thermal model parameters.

7.1.4 Constitutive model

7.1.4.1 Hill48 yield stress formulation

Additive manufactured shell structures can behave anisotropic mechanical characteristics, which is attributed to the printing direction in the production process. To capture this anisotropy, the Hill 48 yield stress formulation is adopted here as,

$$\bar{f}(\bar{\boldsymbol{\sigma}}) = \sqrt{(H+G)\bar{\sigma}_{xx}{}^2 + (H+F)\bar{\sigma}_{yy}{}^2 - 2H\bar{\sigma}_{xx}\bar{\sigma}_{yy} + 2N\bar{\sigma}_{xy}{}^2} \tag{7.24}$$

where $\bar{\sigma}_{xx}$ and $\bar{\sigma}_{yy}$ represent normal stresses along x and y directions within shell surface, with direction x aligned to the building direction in the local coordinate system; $\bar{\sigma}_{xy}$ represents the shear stress component within the shell surface; H, G, F, and N are four Hill 48 model parameters. The conjugated equivalent plastic strain associated with the yield stress could be derived from Eq.(7.24) based on the plastic work equivalence, written as follows,

$$\dot{\bar{\varepsilon}}^p = \sqrt{\frac{(F+H)\dot{\varepsilon}_{xx}^p + (G+H)\dot{\varepsilon}_{yy}^p + 2H\dot{\varepsilon}_{xx}^p\dot{\varepsilon}_{yy}^p}{FH+FG+GH} + \frac{2\dot{\varepsilon}_{xy}^p{}^2}{N}} \tag{7.25}$$

7.1.4.2 Johnson-cook yield stress formulation

To account for the dynamic and thermal effects, the Johnson-Cook flow stress in Eq.(7.21) can be defined as follows,

$$\sigma_y\left(\bar{\varepsilon}^p, \dot{\bar{\varepsilon}}^p, T\right) = \sigma_{y0}(\bar{\varepsilon}^p) \cdot \left[1 + C_0 e^{C_1\bar{\varepsilon}^p} ln\left(\frac{\dot{\bar{\varepsilon}}^p}{\dot{\bar{\varepsilon}}_0^p}\right)\right]\left(1 - \hat{T}^m\right) \tag{7.26}$$

In Eq.(7.26), the first term $\sigma_{y0}(\bar{\varepsilon}^p)$ represents the yield stress under the quasi-static loading condition at room temperature; the second term describes the Johnson-Cook dynamic effect on the flow stress. It is also noted that the total equivalent plastic strain $\bar{\varepsilon}^p$ was also incorporated in this formulation, following our previous study (Li, Liu et al. 2025). C_0, C_1 and $\dot{\bar{\varepsilon}}_0^p$ are model parameters. The temperature soften was captured by the third term, where $\hat{T}^m$ is defined as follows,

$$\hat{T}^m = \begin{cases} 0 & T < T_{room} \\ \frac{T - T_{room}}{T_{melt} - T_{room}} & T_{room} \le T < T_{melt} \\ 1 & T \ge T_{melt} \end{cases} \tag{7.27}$$

where room temperature T_{room} and melting temperature T_{melt} are two thermal model parameters.

7.1.5 Ductile fracture criterion

7.1.5.1 Rate-dependent modified Mohr-Column (MMC) fracture strain

The previous studies (Bai and Wierzbicki 2009, Li, Fang et al. 2022, Kumar and Patel 2024) have proved that the ductile fracture initiation is influenced by the stress state, which is characterised by the stress triaxiality η and Lode angle parameter $\bar{\theta}$. The Mohr-Column (MMC) formulation has been modified to capture the equivalent plastic at fracture initiation for elasto-plastic materials under the quasi-static loading. Here we further consider the dynamic effect on the it, and the formulation is written as below,

$$\varepsilon^f(\eta, \tilde{\theta}, \dot{\bar{\varepsilon}^p}) = \varepsilon_0^f(\eta, \tilde{\theta}) \cdot b(\dot{\bar{\varepsilon}^p}) \tag{7.28}$$

The ε_0^f in Eq.(7.28) is the fracture strain under quasi-static loading, and could be calculated by (Bai and Wierzbicki 2009, Li, Fang et al. 2022),

$$\varepsilon_0^f(\eta, \tilde{\theta}) = \left\{\frac{A}{c_2}\left[c_3 + \frac{3(1-c_3)}{2\sqrt{3}-3}\left(\sec\left(\frac{\tilde{\theta}\pi}{6}\right) - 1\right)\right]\left[\sqrt{\frac{1+{c_1}^2}{3}}\cos\left(\frac{\tilde{\theta}\pi}{6}\right) + c_1\left(\eta + \frac{1}{3}\sin\left(\frac{\tilde{\theta}\pi}{6}\right)\right)\right]\right\}^{-\frac{1}{n}} \tag{7.29}$$

The dynamic factor b in Eq.(7.28) is defined by the rate of equivalent plastic strain $\dot{\bar{\varepsilon}^p}$ as follows,

$$b(\dot{\bar{\varepsilon}^p}) = \begin{cases} 1 & \dot{\bar{\varepsilon}^p} < \dot{\varepsilon_{d0}} \\ \max\left(b_0, 1 - \gamma ln\left(\frac{\dot{\bar{\varepsilon}^p}}{\dot{\varepsilon_{d0}}}\right)\right) & \dot{\bar{\varepsilon}^p} \geq \dot{\varepsilon_{d0}} \end{cases} \tag{7.30}$$

Here, $\dot{\varepsilon_{d0}}$ represents the threshold of the equivalent plastic strain rate $\dot{\bar{\varepsilon}^p}$, beyond which the dynamic begins to influence the fracture strain. The parameter b_0 denotes the ultimate dynamic factor, which is achieved when plastic strain rate $\dot{\bar{\varepsilon}^p}$ reaches a sufficiently high value. In addition, γ is a model parameter that governs the rate of degradation of the fracture strain as the loading rate increases.

7.1.5.2 Anisotropic accumulated plastic strain

The MMC fracture strain in Eq.(7.28) could be directly employed to the equivalent plastic strain, defined as Eq.(7.25) for isotropic materials. However, for anisotropic materials, the equivalent plastic strain at fracture imitation may still vary when the structure was loaded in different directions, even undergoing identical stress state. To account for the effect of material orientation on the fracture initiation, the anisotropic equivalent plastic strain $\bar{\varepsilon}^{p,ani}$ is introduced as below,

$$\dot{\bar{\varepsilon}}^{p,ani} = \sqrt{\frac{2}{3}[\boldsymbol{\beta} \cdot (\dot{\boldsymbol{\varepsilon}}^{p})]^{T} \cdot [\boldsymbol{\beta} \cdot (\dot{\boldsymbol{\varepsilon}}^{p})]} \tag{7.31}$$

where $\dot{\boldsymbol{\varepsilon}}^{p} = \left[\dot{\varepsilon}^{p}_{xx}, \dot{\varepsilon}^{p}_{yy}, \dot{\varepsilon}^{p}_{zz}, \sqrt{2}\dot{\varepsilon}^{p}_{xy}\right]^{T}$ is the Voigt notation of plastic strain rate; $\boldsymbol{\beta}$ is the anisotropic mapping matrix, defined as,

$$\boldsymbol{\beta} = \begin{bmatrix} \beta_{xx} & 0 & 0 & 0 \\ 0 & \beta_{yy} & 0 & 0 \\ 0 & 0 & \beta_{zz} & 0 \\ 0 & 0 & 0 & \beta_{xy} \end{bmatrix} \tag{7.32}$$

With Eq.(7.31), fracture imitation criterion in this study would be employed on the $\bar{\varepsilon}^{p,ani}$ to indicate the effect of material orientation. It is also noted that when $\beta_{xx} = \beta_{yy} = \beta_{zz} = \beta_{xy} = 1$, the anisotropic equivalent plastic strain was degraded into the isotropic equivalent plastic strain.

7.1.5.3 Fracture criterion under non-proportional loading

Eq.(7.28) gives the threshold of equivalent plastic strain at the fracture initiation for materials under consistent stress state. However, in practical engineering, the stress state within materials varies during the loading. To capture the fracture behaviour for such non-proportional loading, the damage index *D* is introduced as follows (Li, Fang et al. 2022, Li, Liu et al. 2025),

$$D(\bar{\varepsilon}^{p}) = \int_{0}^{\bar{\varepsilon}^{p}} \frac{\dot{\bar{\varepsilon}}^{p}}{\varepsilon^{f}(\eta, \tilde{\theta}, \dot{\bar{\varepsilon}}^{p})} \tag{7.33}$$

As the development, the damage index $D(\bar{\varepsilon}^{p})$, and fracture initiates at material points where the value of damage index *D* exceeds 1.

With the above non-proportional loading fracture criterion, the fracture energy threshold H^{ini} is then defined as the sum of bulk elastic and plastic energy density when damage index *D* first reached 1. Following (Miehe, Hofacker et al. 2015, Li, Fang et al. 2022, Jiang, Li et al. 2023, Li, Liu et al. 2025), a state energy formulation $state(X, t)$ is introduced to indicate the crack crack driving force at position *X* and at time t within the shell Ω as below,

$$state(\boldsymbol{X}, t) = < \int_{0}^{t} [\bar{\boldsymbol{\sigma}} : \boldsymbol{D^{e}} + (1 - \varsigma\chi)\bar{\boldsymbol{\sigma}} : \boldsymbol{D^{p}}] d\tau - H^{ini} >_{+} \tag{7.34}$$

where the bracket operator $\langle * \rangle_{+} = \frac{1}{2}(* + |*|)$. To avoid the unrealistic fracture healing, the history energy is introduced as the maximum state energy during the loading process as follows (Miehe, Welschinger et al. 2010, Ulmer, Hofacker et al. 2012, Miehe, Schänzel

et al. 2015, Jiang, Li et al. 2023),

$$\mathcal{H}(\boldsymbol{X}) = \max_{\tau\in[0,t_n]} state(\boldsymbol{X},\tau) \tag{7.35}$$

Substitution the fracture driving force in Eq.(7.18) leads to the final governing equation for the shell phase field evolution, as follows,

$$\begin{cases} \dot{d} = \frac{1}{\omega}\langle 2(1-d)\mathcal{H} - \frac{G_f}{l_c}\left(d - {l_c}^2\Delta d\right)\rangle_+ & \text{in } \Omega \\ \nabla d \cdot \boldsymbol{n} = 0 & \text{on } \partial\Omega \end{cases} \tag{7.36}$$

7.2 Numerical examples

7.2.1 Material sample

To calibrate the parameters of the proposed dynamic shell phase-field model, a series of material tests were conducted. All samples were fabricated using the Laser Powder Bed Fusion (LPBF) method with steel 316L powder. These tests included uniaxial tension, notched tension, simple shear, and hollow centre specimens, as shown in Figure 7.3, where the thickness of all samples is 1.5 mm. For each sample type, four specimens were printed transversely and tested at different loading rates of 0.3 m/s, 1.0 m/s, 4.0 m/s, and 8.0 m/s. Additionally, one specimen was printed longitudinally and tested at a loading rate of 1.0 m/s. During loading, the bottom of each specimen was fixed, while displacement was applied at the top. A high-speed camera was used to capture the deformation process.

All the model parameters used in this study were adopted from our previous research (Li, Liu et al. 2025), where they were meticulously calibrated using the 3D explicit dynamic phase-field model. These parameters are listed in Table 7.1.

7.2.1.1 Uniaxial tension samples under various loading velocities

To study the effect of strain rate on the mechanical characteristics of material, the force-displacement diagram of UT specimen subjected to different load rates were demonstrated in Figure 7.4. All of the force-displacement curves exhibited similar trend, which could be divided into three stages. Firstly, it underwent short elastic stage with rapid increase of reaction force. Then in the following elasto-plastic stage, reaction force increased nonlinearly with decreasing rate and then stayed stable resulting from the plastic hardening. Finally, as the plastic strain continuously developed and reached the fracture strain threshold, the specimens broke characterised by sudden drop of reaction force. In general, the numerical results showed good agreement with experimental data.

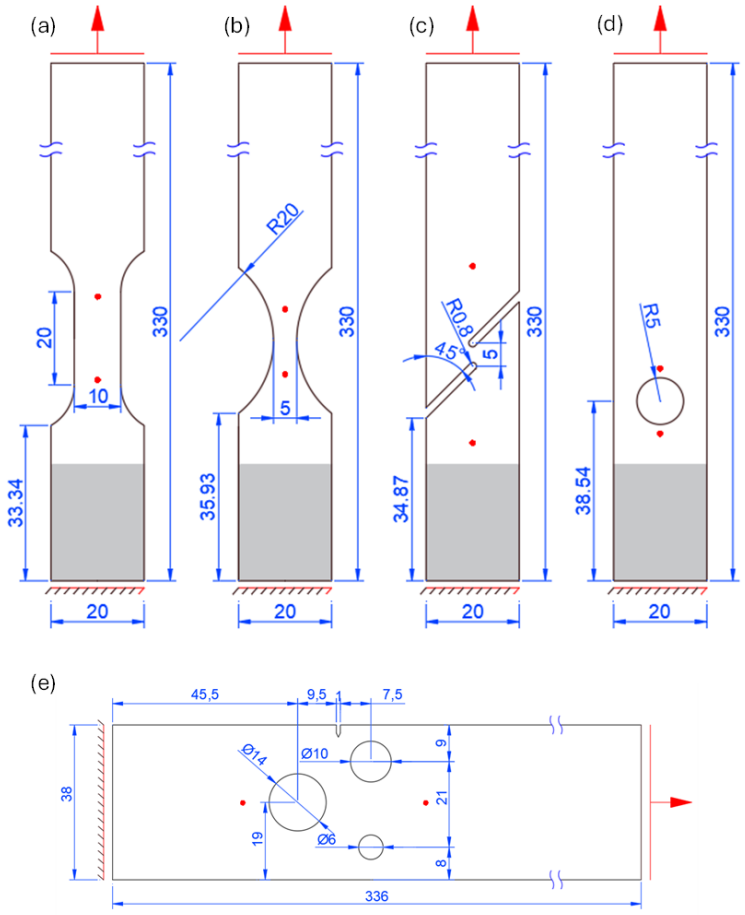

Figure 7.3 Design of parameter-calibration samples. (a) uniaxial tensile; (b) notched tensile; (c) pure shear; (d) hollow centre; (e) three holes samples

By comparing the reaction force of samples subjected to various loading rates in Figure 7.4, it is found that the fluctuations in the experimental curves are more pronounced at higher loading rates, which can be attributed to dynamic effects. Meanwhile, specimens tested under higher loading rate exhibited greater peak reaction forces in the experiments, with value of 11.8, 12.0, 12.4 and 12.7 kN for loading rates ranging from 0.3 m/s to 8.0 m/s, which are well captured by the simulation results. In the proposed constitutive model, the strain rate hardening effect was incorporated via the Johnson-Cook formulation (see Eq.(7.26)). During loading, the nominal strain rates for these specimens were 16.7, 55.6, 222.2, and 444.4 s^{-1}, corresponding to strain rate hardening factors of 1.27, 1.31, 1.35 and 1.37, respectively, as calculated from Eq.(7.26). This increase in strain rate hardening led to a higher flow stress with increasing loading rates.

Table 7.1 Material constitutive model parameters (Li, Liu et al. 2025)

Types	Parameters	Physical meaning	value
Elastic	E	Elastic modulus	145000 MPa
	υ	Poisson's ratio	0.3
Hill48	F	Hill48 yield stress parameters	0.5
	G		0.386
	H		0.5
	N		1.448
Johnson-Cook formulation	C_0	Plasticity hardening	0.0312
	C_1		-3.412
	$\dot{\bar{\varepsilon}}_0^p$		0.0028
	T_{room}	Thermal effect parameters	20.0 ℃
	T_{melt}		1398.0 ℃
	m		0.921
Fracture initiation	A	MMC fracture parameters	1338.8 MPa
	n		0.7
	c_1		0.01
	c_1	Rate dependency	466 MPa
	c_1		0.74
	b_0		0.66
	γ		0.025 s
	β_{xx}	Orientation dependency	1.0
	β_{yy}		0.2
	β_{zz}		1.0
	β_{xy}		1.5
Temperature evolution	C_p	Heat capacity	460 J/(kg· ℃)
	χ_0	Ultimo proportion of plastic work for the thermal evolution	0.7
	$\dot{\varepsilon}_a$	Adiabatic limit strain rate	1.5 s^{-1}
	ρ	Density	7850 kg/m^3

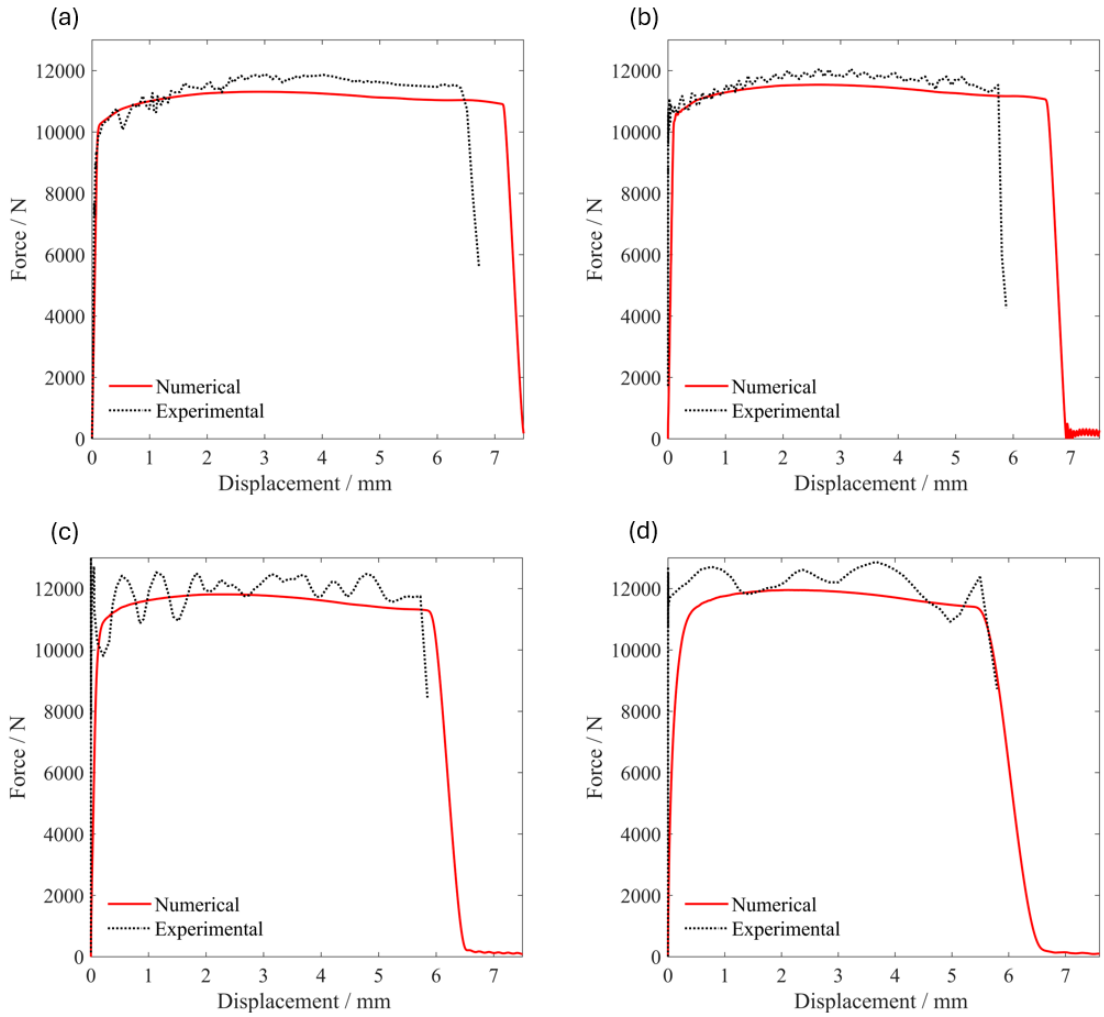

Figure 7.4 Force-displacement curve for transversely orientated uniaxial tension specimen (UT) under different load rates. (a) 0.3 m/s; (b) 1.0 m/s; (c) 4.0 m/s; (d) 8.0 m/s.

As shown in Figure 7.4, the applied displacement at fracture initiation decreased from 6.3 to 5.8 mm for UT specimen when the loading rate increased from 0.3 to 1.0 m/s in the experimental test. The numerical results predicted slightly delayed ductile fracture initiation for these cases. When the loading rate increased further beyond 4.0 m/s (i.e. at 4.0 and 8.0 m/s), fracture initiation occurred at an applied displacement of approximately 5.8 mm, which were well captured by the proposed shell phase field model. In the proposed rate-dependent fracture strain formulation, the strain-rate-related term in Eq.(7.30) decreases as the increase of the strain rate; however, this decrease reaches a threshold beyond a certain strain rate. The close alignment between the numerical and experimental results in predicting fracture initiation demonstrates the effectiveness of this shell phase-field model for accurately modelling dynamic fracture behaviour.

The final fracture paths for the UT samples subjected to loading rate of 0.3, 1.0 and 8.0 m/s are presented in Figure 7.5. In each specimen, fracture initiated at the centre of the sample and developed horizontally in the middle of samples. When the fracture evolution approached two sides of the samples, an inclined fracture path emerged, particularly in specimens subjected to high-speed loading (i.e. v=8.0 m/s in Figure 7.5). This phenomenon was successfully captured by the proposed shell phase-field model.

Figure 7.5 also demonstrates the numerical contour of anisotropic equivalent plastic strain at the onset of fracture, which is obviously localised in the middle region of the samples. The corresponding values are 0.46, 0.44, and 0.41 for loading rates of 0.3, 1.0, and 8.0 m/s, respectively. Since temperature in this study evolved as a state variable at the material point and is dependent on plastic strain, it exhibited a similar trend to the anisotropic equivalent plastic strain, with values of 106, 103 and 98 ℃. The strain rate contours in the simulation results are primarily influenced by the propagation of stress waves within the material and are localised in the central region of the sample. The strain rates were found to be 46, 133 and 933 s^{-1}, approximately 2.5 times the nominal values in their respective contour regions.

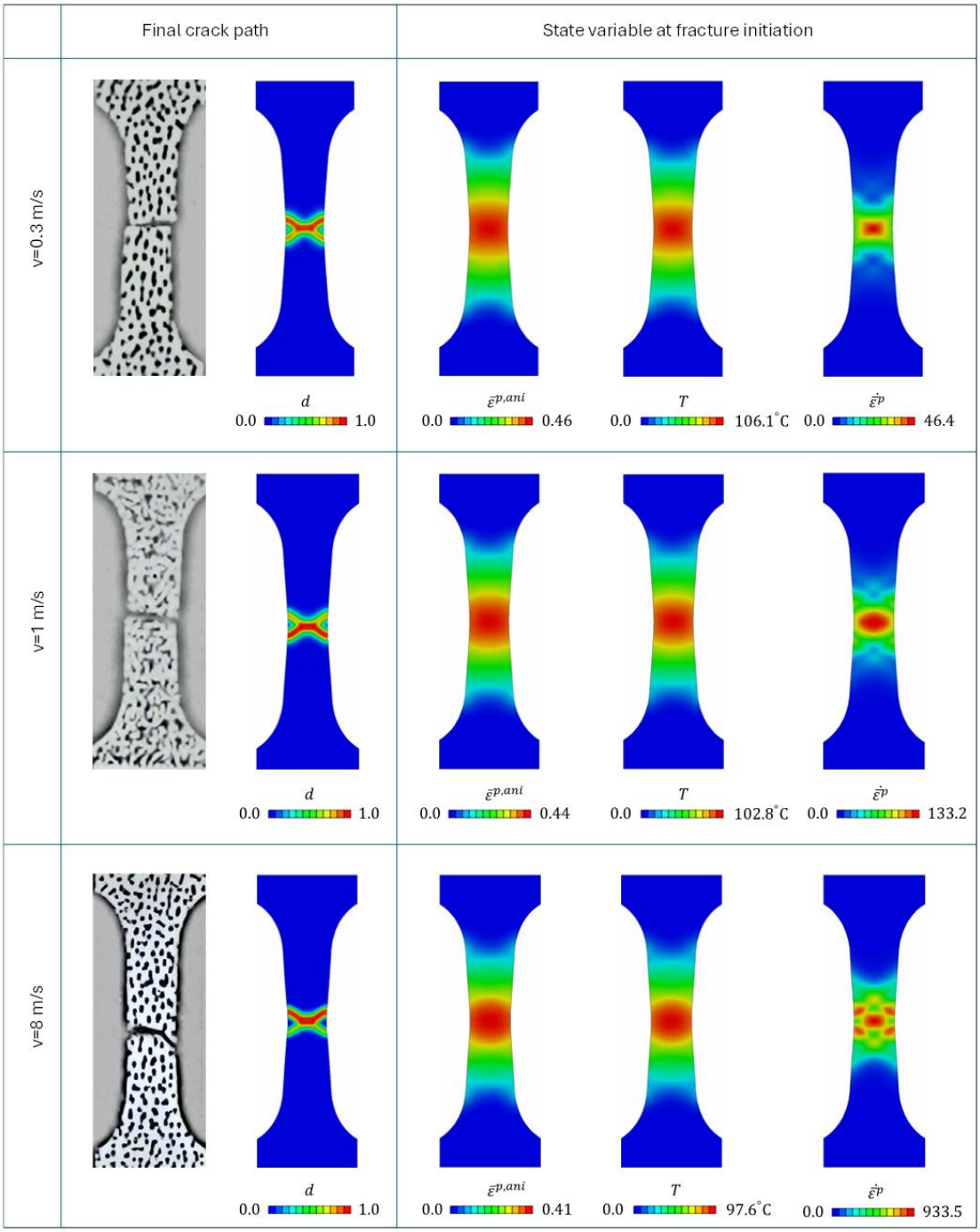

Figure 7.5 Final crack path and the corresponding contours of anisotropic equivalent plastic strain, temperature, and strain rate for the uniaxial tension specimen.

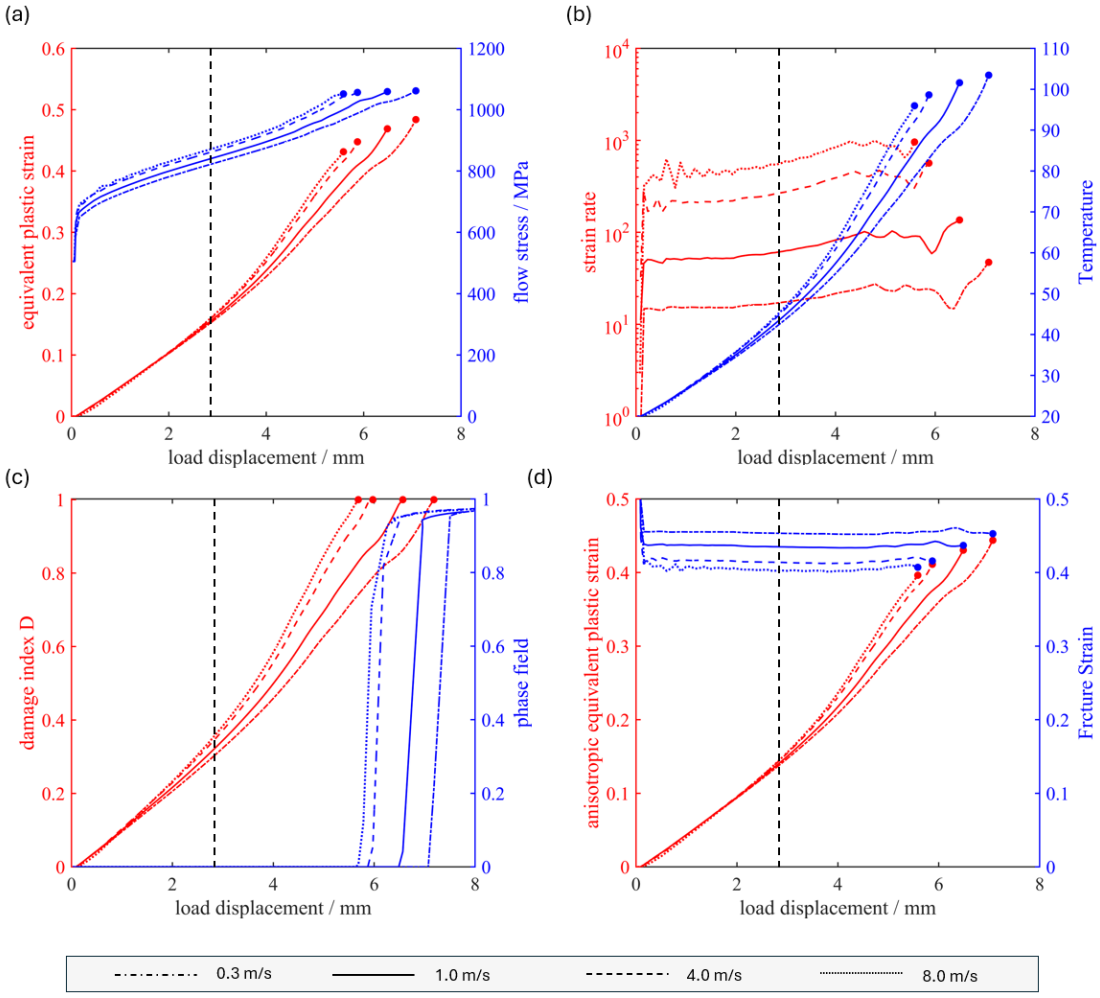

Figure 7.6 Simulation results of state variables at representative elements in UT specimen under different load rates. (a) equivalent plastic strain and flow stress; (b) strain rate and temperature; (c) anisotropic equivalent plastic strain and fracture strain; (d) damage index parameter *D* and phase field

To examine the influence of strain rate on the fracture mechanical properties of the material, Figure 7.6 presents the development of $\bar{\varepsilon}^p$, hardening stress σ_y, strain rate, fracture strain, anisotropic equivalent plastic strain, damage index parameter, and phase field at the critical element for specimens subjected to various loading rates.

The loading process could be generally divided into two stages. In the first stage, as the loading displacement increased to 0.28 mm, a homogeneous mechanical response was observed. The equivalent plastic strain for specimens under different loading velocities exhibited a consistent linear increase to 0.13, as shown in Figure 7.6(a). Likewise, the temperature evolutions for specimens subjected to various loading rates, governed by the plastic deformation, demonstrated a uniform increase to approximately 40 ℃, as illustrated in Figure 7.6(b). Figure 7.6(b) also depicted the strain rate at critical elements

for different loading rates during the whole loading process. It was observed that in the first stage, where the homogeneous mechanical response prevailed, the actual strain rate remained relatively stable. Furthermore, the flow stress, which is influenced by the strain rate according to the Johnson-Cook model, varied even in the homogeneous first stage due to differences in strain rate.

In the second stage, when the loading displacement exceeds 2.8 mm, strain localisation was observed in the specimens, and the development of material state variables began to diverge. Specimens subjected to higher loading rates developed larger equivalent plastic strains and the greater temperature at the same loading displacement. Moreover, due to coupling effect of temperature, strain rate, and plastic strain evolution, the divergence became more and more pronounced as the loading displacement continued to increase. I realized that recognise

Figure 7.6(c) illustrated the evolution of damage index parameter D for different loading velocities during loading process. While the overall trend of D remained the same across all cases, the rate of evolution varied. In the first stage, despite the anisotropic equivalent plastic strains for different loading velocities remained consistent due to the homogeneous response, the fracture strain was influenced by the strain rate, as indicated by Eq.(7.28). Materials subjected to higher loading rate exhibited lower fracture strain, as demonstrated in Figure 7.6(d), leading to a more rapid accumulation of damage index parameter. In the second stage, the divergence of the evolution of damage index parameter D became more evident due to the combined effects of anisotropic equivalent plastic strain and fracture strain. Following the fracture initiation points, the phase field variables evolve rapidly to 0.9 before gradually reaching unity, consistent with the theoretical solutions presented in previous studies (Wang, Ye et al. 2020, Jiang, Li et al. 2023).

Figure 7.6(d) also depicted the evolution of anisotropic plastic strain in conjunction with fracture strain. It is evident that the fracture strain remains relatively stable throughout the loading process, attributed to proportional loading with a stable strain rate. Consequently, the evolution of equivalent plastic strain intersects with the fracture strain at the fracture initiation point for all four cases with different loading velocities.

7.2.1.2 Notched tension, hollow centre and simple shear samples

To further analyse impact of the stress triaxiality and Lode angle on fracture initiation in materials subjected to dynamic loading, Figure 7.7 presented the

experimental reaction force diagram for notched tension (NT), hollow centre (CH) and simples shear (SS) specimens subjected to loading velocity of 300 and 1000 mm/s. Similar to the UT specimens discussed earlier, the entire loading process consists of three stages: the elastic stage, characterised by a rapid increase of reaction force; the strain-hardening stage where the reaction force plateaus; and fracture evolution stage, during which the reaction force declined sharply. The proposed shell phase field model well captured these mechanical characteristics, particularly in predicting fracture initiation for different cases.

Firstly, it is evident that a higher strain rate leads to earlier fracture initiation across all three samples, which is consistent to the UT samples. Secondly, the fracture strain varied among the specimens even under identical loading rates, which can be attributed to the different stress states. As indicated in Figure 7.8, the anisotropic equivalent plastic strains at fracture initiation were were 0.44, 0.42 and 0.49 respectively for NT, CH and SS specimen under loading velocity of 1.0 m/s, where the corresponding stress triaxialities were 0.42, 0.36 and 0.04 at the critical elements in those specimens. This result illustrates the necessities to consider the stress-state-dependent fracture initiation criterion in this proposed numerical model.

As shown in Figure 7.8, the equivalent plastic strains $\bar{\varepsilon}^p$ at fracture initiation for the NT and CH specimens were 0.47 and 0.46, respectively, which closely matched their anisotropic equivalent plastic strains $\bar{\varepsilon}^{p,ani}$. However, the equivalent plastic strain $\bar{\varepsilon}^p$ for the SS specimen was 0.36, significantly lower than its anisotropic equivalent plastic strain $\bar{\varepsilon}^{p,ani}$. In this study, $\bar{\varepsilon}^{p,ani}$ is defined by Eq.(7.31) to incorporate the effect of material orientation on fracture initiation, which depends on the components of the plastic strain tensor and the corresponding anisotropic model parameters (i.e. β_{xx}, β_{yy} and β_{xy}). The plastic strain in the x-direction dominated the UT and CH specimens, whereas the deviatoric components were dominant in the SS specimen. One the other hand, β_{xx} and β_{xy} were calibrated as 1.0 and 1.5, respectively, leading to close values of $\bar{\varepsilon}^p$ and $\bar{\varepsilon}^{p,ani}$ for NT and CH specimen, whereas the SS specimen exhibited a larger $\bar{\varepsilon}^{p,ani}$ compared with $\bar{\varepsilon}^p$. Additionally, temperature evolution in this study is governed by plastic work, which is controlled by the equivalent plastic strain. As a result, the SS specimen exhibited the lowest temperature at fracture initiation.

Regarding the fracture path, as shown in Figure 8, the proposed shell phase-field

model also provided accurate numerical predictions for all specimens analysed in this study.

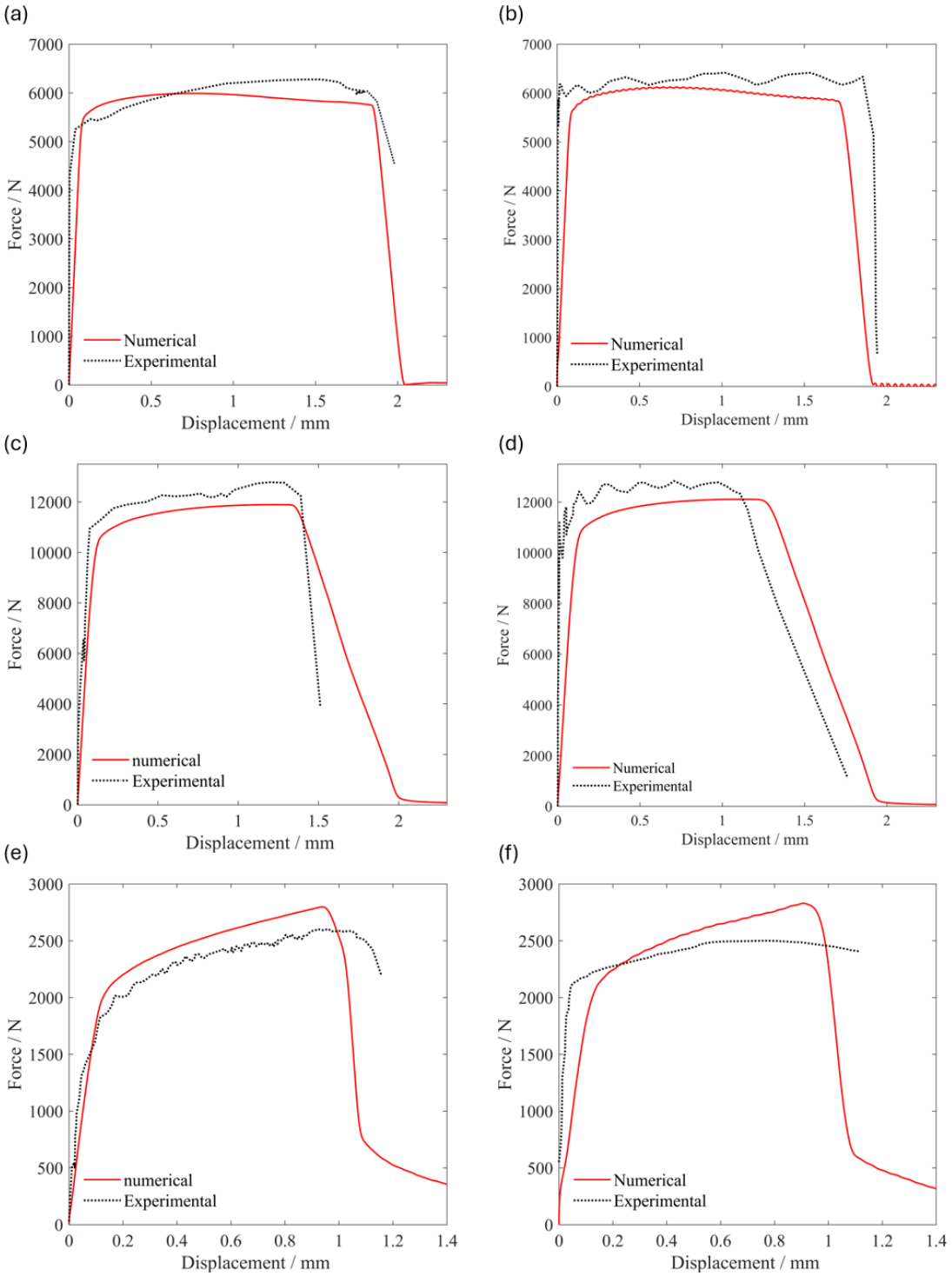

Figure 7.7 Force-displacement curves transversely orientated specimens. (a) NTR20 specimen under 0.3 m/s; (b) NTR20 specimen under 1.0 m/s; (c) CH specimen under 0.3 m/s; (d) CH specimen under 1.0 m/s; (e) SS specimen under 0.3 m/s; (f) SS specimen under 1.0 m/s;

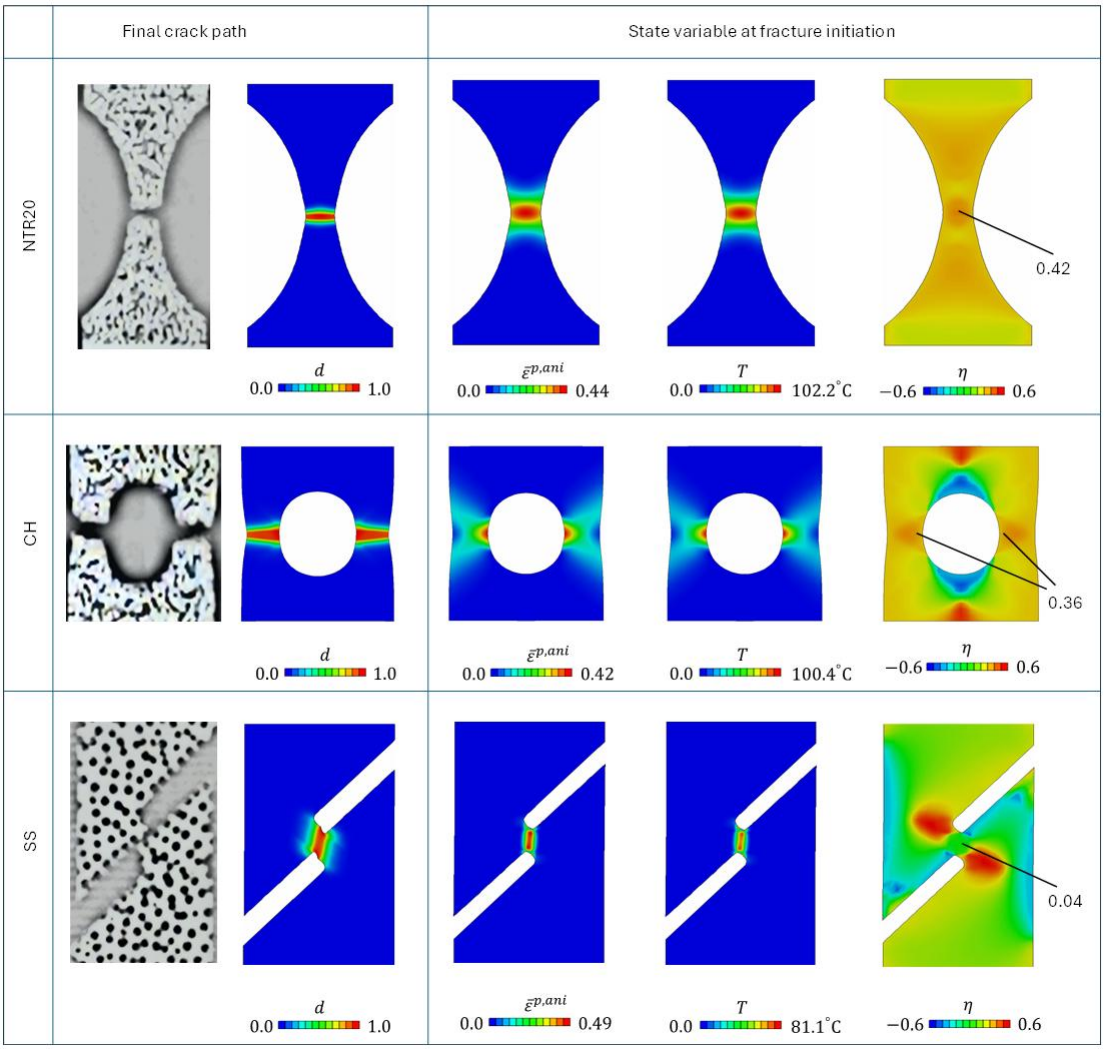

Figure 7.8 Contours of phase field evolution, anisotropic equivalent plastic strain and temperature at fracture initiation for material samples.

The MMC fracture envelope in this study is presented in Figure 7.9, along with the evolution histories of plastic strains corresponding to the stress state at critical points in the UT, NT, CH, and SS specimens subjected to a loading rate of 1.0 m/s. Although the strain rate at these elements may vary throughout the loading process, the differences are negligible. Therefore, an average strain rate of 240 s^{-1} was adopted to calculate the MMC fracture strain locus based on Eq.(7.28). As observed, these four specimens encompass a wide range of stress states, and the accurate simulation results obtained using the proposed shell phase-field model validate its effectiveness and flexibility. Furthermore, due to the approximately proportional loading conditions, particularly for the UT and NT specimens, their fracture initiation points are close to the fracture envelope surface.

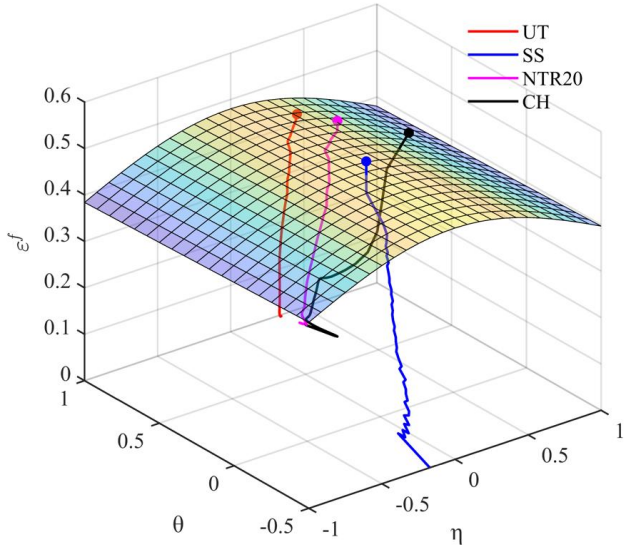

Figure 7.9 MMC fracture envelope and load history for critical material points in UT, SS, NTR20 and CH specimens.

7.2.2 Three hole samples

In this section, we further validate the proposed shell phase field model via a three hole sample, the geometry of which was presented in Figure 7.3(e). Two tests were conducted on the three-hole specimens subjected to loading rate of 1.0 and 4.0 m/s respectively.

Figure 7.10 (a) and (b) presented the corresponding experimental results for both loading rates, alongside the numerical predictions from the proposed shell phase-field model. The strong agreement between experimental and numerical results confirms the effectiveness of the proposed model in accurately capturing the dynamic response and fracture evolution of shell structures under complex stress states and varying loading rates. A comparison of Figure 7.10(a) and (b) reveals that specimens subjected to higher loading rates exhibit greater peak forces, while the overall trend of the reaction force remains similar. Therefore, in the subsequent analysis, we only focus on the case with a loading rate of 1.0 m/s.

As shown in Figure 7.10(a), the loading process can generally be divided into four stages. In the first stage, the reaction force increased rapidly, reaching a peak at approximately 23 kN, and then remained stable due to the strain hardening until the applied displacement increased to 1.5 mm in the numerical results (occurring slightly earlier in experimental test). At this moment, two fracture initiations, accompanied by significant plastic strain concentration, were observed at notch D and circle A in both experimental and numerical results, as indicated in Figure 7.11.

In the second stage, the global force decreased from 23 kN to 18 kN as the applied displacement increased by a further 0.5 m. This reduction corresponded to the rapid crack propagation from circle A to sample edge in the horizontal direction, as shown in Figure 7.11. During this stage, fracture initiated at the notch D exhibited only minor propagation. The simulation results accurately predict the fracture propagation and mechanical response in this stage.

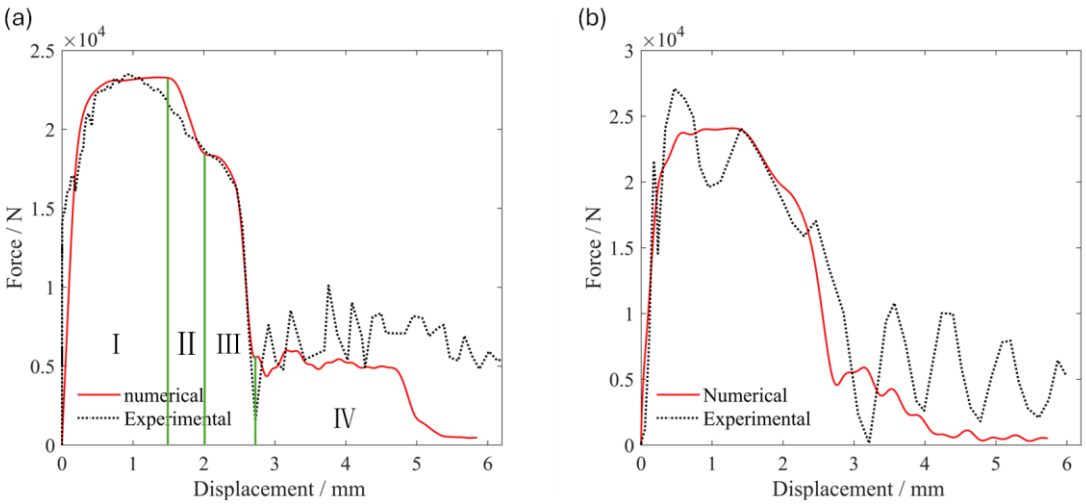

Figure 7.10 Force-displacement curves of Three Hole specimens. (a) 1.0 m/s; (b) 4.0 m/s.

In the third stage, the reaction force underwent a significant decline, as depicted in Figure 7.10(a), which was well captured by the numerical simulation. The sharp reduction in global force was attributed to damage evolution from notch D towards circle B in a left-downward direction, where the material bears the majority of the global load. Compared with the experimental observations, the numerical simulation predicts a crack path with a slightly smaller inclination angle; however, the discrepancy remains within an acceptable range, as shown in Figure 7.11 (u=2.8 mm). Notably, the material along this path experiences high stress triaxiality, leading to a lower fracture strain in this region.

In the fourth stage, the simulated reaction force remained stable before the applied displacement reached 4.6 mm, after which it gradually declined to zero. In contrast, the experimental reaction force remained relatively stable, though fluctuations were observed, likely attributed to inertial effects. At this stage, the final fracture initiated at circle A and propagated toward circle B. Initially, the fracture path inclined at approximately 30 degrees to the horizontal, with the material experiencing high stress triaxiality along the path. Notably, when the applied displacement reached 4.6 mm, the propagation angle

shifted to 60 degrees, with the material in the new direction also undergoing high stress triaxiality. This transition was successfully reproduced in the simulation, as shown in Figure 7.11.

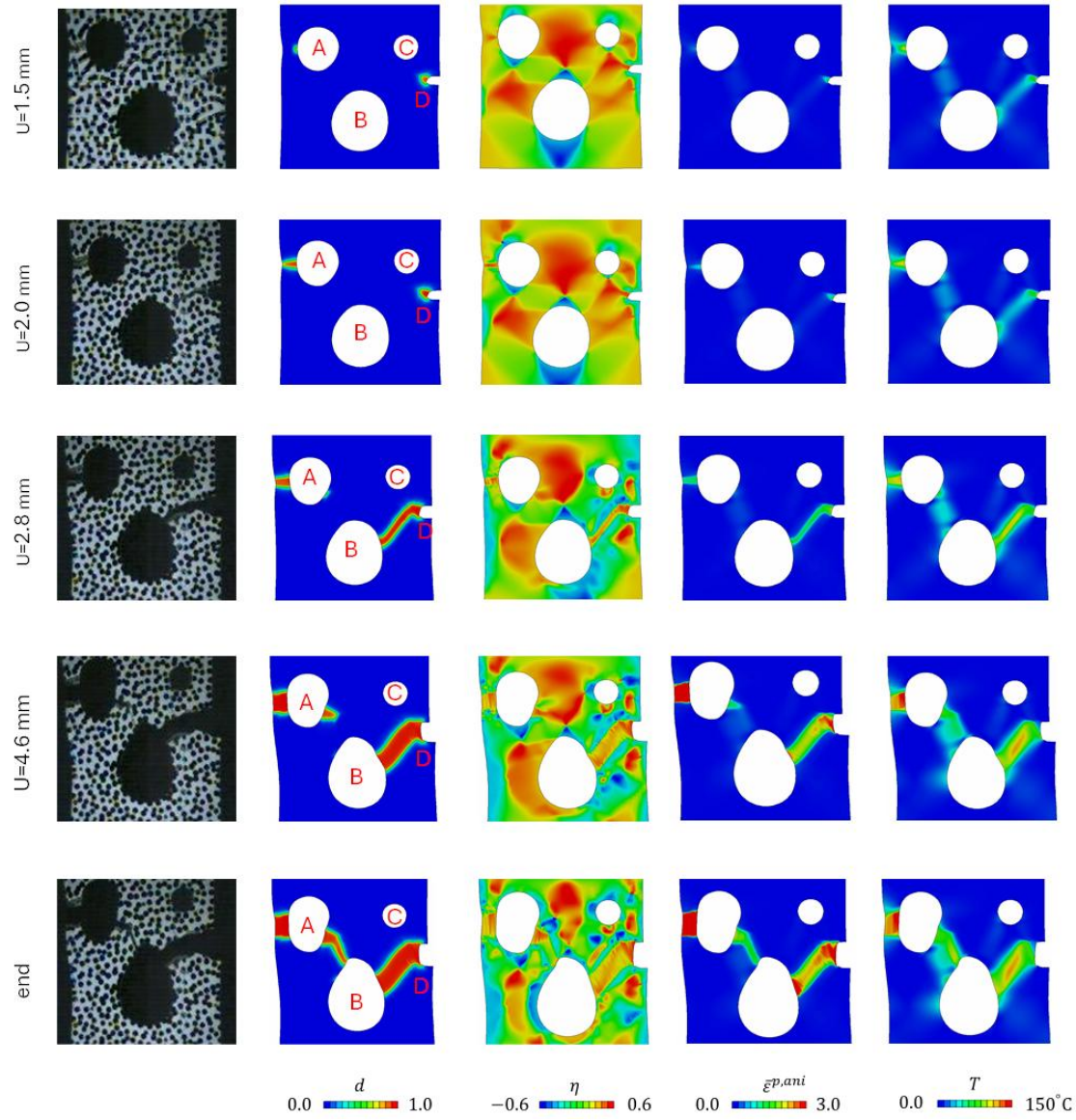

Figure 7.11 Comparison of experimental and numerical fracture path of single-notched sample with three holes.

7.3 Summary

In this study, an explicit shell phase-field model was developed to simulate dynamic fracture behaviour in thin-walled structures. Within this framework, temperature was incorporated as a state variable, governed by dissipated plastic work, while material anisotropy was captured using the Hill48 yield stress formulation. The constitutive model integrated temperature, strain rate, and equivalent plastic strain through a thermally and

rate-dependent Johnson-Cook flow stress model. Fracture initiation in ductile materials under dynamic loading was characterized using the modified Mohr-Coulomb (MMC) fracture strain, coupled with strain rate effects. Furthermore, an anisotropic plastic strain measure was introduced to account for material orientation-dependent fracture initiation. The evolution of the phase-field damage variable was governed by elastic energy and retained plastic work.

To calibrate the model parameters, a series of material tests were conducted. In the uniaxial tension (UT) tests, the loading process were divided into two stages: an initial homogeneous response, where equivalent plastic strain and temperature increased uniformly, and a second stage of strain localization, where divergence in plastic strain and temperature evolution was observed. Moreover, the applied displacement at fracture initiation decreased significantly when the loading rate increased from 0.3 to 1.0 m/s, while demonstrated no obvious change when loading rate further increase beyond 1.0 m/s. This phenomenon was effectively captured by the proposed shell phase-field model, which incorporates a maximum limit on a strain-rate-dependent factor in the fracture strain formulation.

Additional tests on notched tension (NT), hollow centre (CH), and simple shear (SS) specimens revealed that the SS specimen exhibited a higher threshold for fracture strain. The numerical simulations effectively captured the fracture behaviours of these samples, highlighting the necessity of incorporating a stress-state-dependent fracture criterion. Besides, temperature evolution was found to depend on the dissipated plastic work, controlled by the equivalent plastic strain and strain rate.

Finally, the model was further validated using single-notched specimens with three holes. The force-displacement process was divided into four stages: an initial rapid force increase followed by strain hardening, fracture propagation from circle A to sample edge, fracture propagation from notch D to circle B, and final fracture evolution from circle A to circle B. The model accurately predicted fracture initiation and propagation paths, including transitions in fracture evolution direction due to high stress triaxiality. The successful reproduction of fracture transitions further validates the capability of the proposed model in capturing dynamic responses and fracture evolution under complex stress states.

8. CONCLUSIONS AND FUTURE WORK

8.1 Conclusions

8.1.1 Double phase field model with crack-directional decomposition

To model fracture propagation in 3D solids for different crack modes, this study has proposed a double phase field model with strain energy decomposition based on the crack-orientation-based coordinate system. The tensile and shear components of decomposed strain energy contribute to the crack propagation of tensile and shear damage phase field d_{t} and d_{c}, respectively. The plastic contribution for crack evolution is coupled by associating the decomposed tensile and shear plastic strains with the correspond fracture energy release rates G_t and G_c. This proposed model is implemented through ABAQUS subroutines UEL and UMAT with a staggered solution method for tensile/shear damage phase field and displacement field.

Five numerical examples are conducted for parametric analysis and model effectiveness verification. In the first example of one element under tension and compression loading, the agreement between the numerical results and analytical solutions indicates the correctness of the implementation of this proposed model. The second example of single-edge notch specimens with different values of a_t and b_t subject to uniaxial tension have demonstrated that a larger a_t as well as a smaller b_t lead to lower material strength, while the effect of b_t could be negligible when it is smaller than 0.01. The third simulation on single-edge shear loading specimens have proven that the G_c/G_t plays great roles on the crack mode: when G_c/G_t is less than or equal to 1.4, shear crack dominate the specimen failure, when G_c/G_t is equal to 2, mixed crack mode appears, and when G_c/G_t is larger or equal than 2.4, tensile crack dominates the failure. Meanwhile, the mixed crack mode specimen has showed the highest load bearing capability among all specimens. In the fourth numerical example, a group of uniaxial tension, simple shear and tension-shear specimens is considered, which shows good agreement with experiment data in terms of crack path and load versus displacement curve, which demonstrates the capability of this proposed double phase field model for different crack mode modelling. Lastly, the third Sandia challenge example is modelled and compared with experiment data, demonstrating capability of this proposed phase field model for complex 3D crack propagation modelling.

8.1.2 Unified strain energy decomposition method

To capture the fracture behaviour under all kinds of complex stress states properly, this study proposed a unified strain energy decomposition approach, where the strain energy is split on the local coordinate system into three components, namely tensile, shear and compression parts. The local coordinate is determined by maximising the *F*-criterion function energy, the sum of the tensile and shear strain energy normalised by corresponding tensile/shear crack energy release rate. An innovative method focusing on three normal stresses is proposed to search for its optimized configuration. This proposed a unified strain energy decomposition approach could recast to the commonly adopted spectral, V-D and crack-surface-based strain energy decomposition under specific load conditions. Also, the proposed model can reveal the competition between tensile and shear energy dissipation under complex stress states, which depends on the stress states, tensile/shear fracture toughness and the Poison's ratio. The proposed unified phase field model is implemented explicitly via the ABAQUS subroutines VUEL and VUMAT. This implementation is validated via the one element test, where uniaxial tension and uniaxial compression test is conducted, and the numerical results matches the homogenous analytical solution.

In this study, the unified decomposition method for phase field modelling is compared with isotropic, V-D, and spectral approaches through a series of numerical examples, covering various stress states loading, including tensile, compression, tensile-shear, compression-shear. In the dogbone compression test, the spectral model showed unphysical load-displacement curve with infinite growth even though the phase field damage has fully developed; The unified and V-D model demonstrated similar load-force curve, while they have predicted different crack path, with unrealistic X-shape for V-D model, and inclined fracture surface for unified model. For the perforated asymmetric bending test (PABT) where the tensile stress dominates, the simulation result by unified and spectral model showed proper mechanical response, similar to the isotropic damage model, while the V-D model predicted larger loading-carry capacity caused by the unsuitable deviatoric energy dissipation for the tensile dominant fracture in this specimen. In the last triaxial compression test specimen, the proposed unified strain energy showed best performance for reproducing the experimental fracture propagation process, compared with other approaches.

8.1.3 Five-layer shell phase field model with fracture initiation criterion

In this study, five layers of phase-field variables were introduced to represent the fracture progression along the thickness direction, corresponding to the five Simpson integration points through the shell thickness. This approach allowed for direct stress degradation at each integration point without the need for interpolation tools, as demonstrated in the current research. Moreover, fracture initiation at each layer was described using a stress-state-dependent fracture strain formulation, applying the MMC criterion for 316L steel and the Bao-Wierzbicki criterion for Ti-6Al-4V.

Several numerical examples were conducted to validate the proposed model. First, the model's implementation was verified by the convergence of numerical results as the phase-field viscosity parameter decreased. In the notched cylinder under axial tension, the model accurately predicted a through-cylinder crack path, and it was found that fracture strain significantly influenced the force-displacement curve. In the third example, a notched cylinder with an axial pre-crack was subjected to internal pressure with two different boundary conditions: one with, and one without, circumferential straps at the ends of the specimen. The results showed that the straps effectively confined crack propagation within the limited area, aligning well with experimental observations and previous numerical studies. Finally, two experimental tests were simulated using the proposed shell phase-field model. In the three-point bending test of a square tube, the model successfully captured five distinct stages of deformation: elastic deformation, local indentation, side-surface buckling, bulge strap growth, and global bending, all of which showed good consistence with the experimental observation. In the final example, the Gyroid TPMS structure was subjected to axial compression. Despite a slight delay in densification due to the shell element configuration in the Abaqus algorithm, the two distinct deformation modes were accurately captured, and the global force-displacement curve closely matched the experimental results.

8.1.4 Application of shell phase field model for battery casing

In this study, the developed shell phase field model was employed to simulate the crush behaviour of a 11850 lithium-ion battery casing. Extensive material testing was conducted to calibrate the model parameters accurately. The Hill48 yield stress was adopted to indicate the anisotropic mechanical response. To account for the stress-state dependence of fracture strain, the Bao-Wierzbicki fracture criterion was adopted. Model

parameters were calibrated by correlating experimental and numerical force-displacement curves derived from a series of tests, including uniaxial tension, notched tension, and hollow centre specimens. Validation was further performed using a five-hole specimen test, with the simulated fracture behaviour and force-displacement curves showing strong agreement with experimental results.

The calibrated parameters were subsequently applied to simulate three-point bending and axial compression tests on the battery casing. For the battery casing, the three-point bending test indicated that damage was concentrated at the front and back equatorial points where the element bending direction transitioned from inward to outward as the indenter advanced, leading to damage initiation in the material near the outer and inner surfaces. In the axial compressive loading, the fluctuated numerical force-displacement curves generally aligned with the experimental result despite of a slight delay in densification, which is attributed to the automatic thickness reduction in Abaqus contact algorithm for stacked shell elements. In the three-point bending test on the battery cell, damage within battery casing primarily occurring at section points near the inner and outer surfaces, with stress triaxiality mainly falling into intervals of [0.1, 0.3] and [0.55, 0.65]. The analysis of three representative elements showed significant depth-dependent variation in stress states and plastic strain under bending-dominant conditions, with consistent behaviour observed under membrane tensile-dominant conditions.

8.1.5 Dynamic shell phase field model

In this study, an explicit shell phase-field model was developed to simulate dynamic fracture behaviour in thin-walled structures. Within this framework, temperature was incorporated as a state variable, governed by dissipated plastic work, while material anisotropy was captured using the Hill48 yield stress formulation. The constitutive model integrated temperature, strain rate, and equivalent plastic strain through a thermally and rate-dependent Johnson-Cook flow stress model. Fracture initiation in ductile materials under dynamic loading was characterized using the modified Mohr-Coulomb (MMC) fracture strain, coupled with strain rate effects. Furthermore, an anisotropic plastic strain measure was introduced to account for material orientation-dependent fracture initiation. The evolution of the phase-field damage variable was governed by elastic energy and retained plastic work.

To calibrate the model parameters, a series of material tests were conducted. In the

uniaxial tension (UT) tests, the loading process were divided into two stages: an initial homogeneous response, where equivalent plastic strain and temperature increased uniformly, and a second stage of strain localization, where divergence in plastic strain and temperature evolution was observed. Additional tests on notched tension (NT), hollow centre (CH), and simple shear (SS) specimens revealed that the SS specimen exhibited a higher threshold for fracture strain. The numerical simulations effectively captured the fracture behaviours of these samples, highlighting the necessity of incorporating a stress-state-dependent fracture criterion. Besides, temperature evolution was found to depend on the dissipated plastic work, controlled by the equivalent plastic strain and strain rate.

Finally, the model was further validated using single-notched specimens with three holes. The force-displacement process was divided into four stages: an initial rapid force increase followed by strain hardening, fracture propagation from circle A to sample edge, fracture propagation from notch D to circle B, and final fracture evolution from circle A to circle B, as depicted in Figure 7.11. The model accurately predicted fracture initiation and propagation paths, including transitions in fracture evolution direction due to high stress triaxiality. The successful reproduction of fracture transitions further validates the capability of the proposed model in capturing dynamic responses and fracture evolution under complex stress states.

8.1.6 Contribution summary

The overall significant contribution of this dissertation could be summarised as below:

- Established a **comprehensive phase-field framework** unifying solid, shell, and dynamic formulations for **ductile and brittle fracture modelling**.
- Provided an **efficient computational implementation** within ABAQUS, validated by both **numerical benchmarks** and **experimental correlations**.
- Offered new insights into **mode-dependent fracture behaviour**, **stress-state effects**, and **dynamic failure mechanisms** in complex engineering structures such as thin shells and battery casings.

8.2 Recommendation for future research

8.2.1 Uncertainty analysis

In this study, we conducted only a deterministic analysis of the fracture behaviour

of materials. However, in practical engineering applications, materials are inherently heterogeneous throughout the structure. For instance, the fracture initiation parameters examined in this study have a significant impact on the mechanical response, where even small variations can lead to substantial differences. Therefore, incorporating uncertainty analysis into the phase-field model framework is crucial for providing a more accurate safety assessment, ensuring reliability in structural design and optimization.

8.2.2 Multi-physical coupled problems

The phase-field model in this study primarily focuses on mechanical fracture modelling. In the future, it could be further extended to incorporate multi-physical couplings. For example, the shell phase-field model could be coupled with the hydrogen diffusion process to simulate hydrogen embrittlement phenomena. Additionally, the phase-field model can be integrated with thermal, chemical, electrical, and fluid flow phenomena to enhance its applicability in complex engineering and scientific problems.

8.2.3 Incorporate the non-local plasticity into the shell phase field model

Large plastic deformation can occur in thin-walled structures. However, the proposed shell phase-field model still employs a local plasticity model, which neglects the non-local effects on plastic strain evolution and the localization of damage due to plasticity concentration. To address this limitation, future work could incorporate a non-local plasticity formulation into the shell phase-field model, enhancing its applicability to thin-walled structures undergoing large deformations.

Appendix

A1 Analytical solution of unified phase field model for uniaxial tension loading

As depicted in Figure 4.9(a). the asymmetric loading condition in $\boldsymbol{x}$ and $\boldsymbol{y}$ directions resulting in identical lateral axial strains. Hence the strain tensor for the uniaxial tension loading could be written as,

$$\boldsymbol{\varepsilon} = \begin{bmatrix} \varepsilon_{xx} & 0 & 0 \\ 0 & \varepsilon_{xx} & 0 \\ 0 & 0 & \varepsilon_{\mathrm{zz}} \end{bmatrix} \tag{A1}$$

With the elastic strain $\boldsymbol{\varepsilon}$, the effective stress $\overline{\boldsymbol{\sigma}}$ could be obtained as,

$$\overline{\boldsymbol{\sigma}} = \frac{E}{(\nu+1)(1-2\nu)} \begin{bmatrix} \varepsilon_{xx} + \varepsilon_{\mathrm{zz}}\nu & 0 & 0 \\ 0 & \varepsilon_{xx} + \varepsilon_{\mathrm{zz}}\nu & 0 \\ 0 & 0 & \varepsilon_{\mathrm{zz}}(1-\nu) + 2\varepsilon_{xx}\nu \end{bmatrix} \tag{A2}$$

According to the LCSD decomposition strategy of Eqs.(4.17)-(4.21), the decomposed three part of effective stress is written as,

$$\begin{cases} \overline{\boldsymbol{\sigma}}_{\boldsymbol{I}}^{+} = \frac{E[\varepsilon_{\mathrm{zz}}(1-\nu)+2\varepsilon_{xx}\nu]}{(\nu+1)(1-2\nu)} \begin{bmatrix} \frac{\nu}{1-\nu} & 0 & 0 \\ 0 & \frac{\nu}{1-\nu} & 0 \\ 0 & 0 & 1 \end{bmatrix} \\ \overline{\boldsymbol{\sigma}}_{\boldsymbol{II}}^{+} = \mathbf{0} \\ \overline{\boldsymbol{\sigma}}^{-} = \frac{E\varepsilon_{xx}}{1-\nu} \begin{bmatrix} 1 & 0 & 0 \\ 0 & 1 & 0 \\ 0 & 0 & 0 \end{bmatrix} \end{cases} \tag{A3}$$

Hence, the nominal stress can be calculated by Eq.(4.22) and the component of σ_{zz} and σ_{xx} is written as,

$$\begin{cases} \sigma_{xx} = E\frac{(1-\nu)(\varepsilon_{\mathrm{zz}}\nu+\varepsilon_{xx})-\nu[1-(1-d)^2](\varepsilon_{\mathrm{zz}}-\varepsilon_{\mathrm{zz}}\nu+2\varepsilon_{xx}\nu)}{(1-\nu)(1+\nu)(1-2\nu)} \\ \sigma_{zz} = \frac{E(1-d)^2(\varepsilon_{\mathrm{zz}}-\varepsilon_{\mathrm{zz}}\nu+2\varepsilon_{xx}\nu)}{(\nu+1)(1-2\nu)} \end{cases} \tag{A4}$$

Considering the free boundary of tested one element in $\boldsymbol{x}$ and $\boldsymbol{y}$ directions, zero axial stress response in that two directions should be achieved. Based on this statement, the axial strain ε_{xx} is be solved by ensuring σ_{xx} equal to zero, as follows,

$$\varepsilon_{xx} = -\frac{\varepsilon_{\mathrm{zz}}\nu(1-d)^2(1-\nu)}{2\nu^2(1-d)^2+(1+\nu)(1-2\nu)} \tag{A5}$$

Substitution Eq.(A5) into Eq.(A4) leads to the analytical solution of stress response σ_{zz}, as below,

$$\sigma_{zz} = \frac{E(1-d)^2(\varepsilon_{zz}-\varepsilon_{zz}\nu+2\varepsilon_{xx}\nu)}{(\nu+1)(1-2\nu)} \tag{A6}$$

Substituting Eqs.(A3) and (A5) into Eq.(4.28), fracture driving force for uniaxial tension loading of unified model is obtained as,

$$\mathrm{H} = \frac{1}{2}\overline{\boldsymbol{\sigma}}_I^+ : \boldsymbol{\varepsilon}^{\mathrm{e}} = \frac{E{\varepsilon_{zz}}^2(1-\nu)(1+\nu)(1-2\nu)}{2(2d^2\nu^2-4d\nu^2-\nu+1)^2} \tag{A7}$$

A2 Analytical solution of unified and isotropic model for biaxial tension loading

The boundary condition of the biaxial tension loading is demonstrated in Figure 4.9(a), the single element is extracted in *x* and *y* direction, while remained free in z direction. Similar to the uniaxial tension loading, the axial strain ε_{xx} and ε_{yy} keep consistent due to the asymmetric loading condition. Hence the formulation of the elastic strain and effective stress tensor are identical to the uniaxial tension loading, expressed by Eqs.(A1) and (A2).

(1) Analytical solution for the unified phase field model

The decomposition of the effective stress is written according to Eqs.(4.17)-(4.21) which belongs to the third decomposition type listed in Table 4.1.

$$\begin{cases} \overline{\boldsymbol{\sigma}}_{\boldsymbol{I}}^+ = \frac{E(\varepsilon_{xx}+\varepsilon_{zz}\nu)}{(\nu+1)(1-2\nu)}\begin{bmatrix}1 & 0 & 0\\ 0 & 1 & 0\\ 0 & 0 & 2\nu\end{bmatrix} \\ \overline{\boldsymbol{\sigma}}_{\boldsymbol{II}}^+ = \mathbf{0} \\ \overline{\boldsymbol{\sigma}}^- = E\varepsilon_{zz}\begin{bmatrix}0 & 0 & 0\\ 0 & 0 & 0\\ 0 & 0 & 1\end{bmatrix} \end{cases} \tag{A8}$$

Similar to the uniaxial tension loading, the nominal stress of biaxial tension loading is calculated, and the stress component σ_{zz} and σ_{xx} are given by

$$\begin{cases} \sigma_{xx} = \frac{E(1-d)^2(\varepsilon_{xx}+\varepsilon_{zz}\nu)}{(1+\nu)(1-2\nu)} \\ \sigma_{zz} = -E\frac{2\nu(\varepsilon_{xx}+\varepsilon_{zz}\nu)(1-(1-d)^2)-2\varepsilon_{xx}\nu+\varepsilon_{zz}\nu-\varepsilon_{zz}}{(1+\nu)(1-2\nu)} \end{cases} \tag{A9}$$

For the biaxial tension loading, the stress component σ_{zz} is supposed to be equal to zero due to the free constrain in z direction, by which ε_{zz} can be solved as,

$$\varepsilon_{zz} = -\frac{2\varepsilon_{xx}\nu(1-d)^2}{2\nu^2(1-d)^2+(1+\nu)(1-2\nu)} \tag{A10}$$

With ε_{zz} solved, the stress response σ_{xx} and fracture driving force can be obtained, similar to the deduction of analytical solution of uniaxial tension loading test, given by

$$\sigma_{xx} = \frac{(1-d)^2 E\varepsilon_{xx}}{2\nu^2(1-d)^2+(1+\nu)(1-2\nu)} \tag{A11}$$

$$\mathrm{H} = \frac{1}{2}\overline{\boldsymbol{\sigma}}_I^+ : \boldsymbol{\varepsilon}^{\mathrm{e}} = \frac{E\varepsilon_{xx}{}^2(1+\nu)(1-2\nu)}{(2d^2\nu^2-4d\nu^2-\nu+1)^2} \tag{A12}$$

(2) Analytical solution for isotropic phase field model

For the isotropic phase field model, we just need to solve the elastic strain ε_{zz} easily by ensuring the component $\bar{\sigma}_{zz}$ in effective stress tensor to be zero. The calculated result is written as below,

$$\varepsilon_{zz} = -\frac{2\varepsilon_{xx}\nu}{1-\nu} \tag{A13}$$

The nominal stress response of σ_{xx} for isotropic phase field model is then easily obtained as,

$$\sigma_{xx} = (1-d)^2\bar{\sigma}_{xx} = \frac{(1-d)^2 E\varepsilon_{xx}}{1-\nu} \tag{A14}$$

The phase field driving force then can be calculated according to Eq.(4.23).

$$\mathrm{H} = \frac{1}{2}\overline{\boldsymbol{\sigma}} : \boldsymbol{\varepsilon}^{\mathrm{e}} = \frac{E\epsilon_{11}^2}{1-\nu} \tag{A15}$$

REFERENCES

Ahmed, B., G. Z. Voyiadjis and T. Park (2021). "Local and non-local damage model with extended stress decomposition for concrete." International Journal of Damage Mechanics **30**(8): 1149-1191.

Aldakheel, F., S. Mauthe and C. Miehe (2014). "Towards Phase Field Modeling of Ductile Fracture in Gradient-Extended Elastic-Plastic Solids." Pamm **14**(1): 411-412.

Aldakheel, F., N. Noii, T. Wick and P. Wriggers (2021). "A global–local approach for hydraulic phase-field fracture in poroelastic media." Computers & Mathematics with Applications **91**: 99-121.

Aldakheel, F., P. Wriggers and C. Miehe (2017). "A modified Gurson-type plasticity model at finite strains: formulation, numerical analysis and phase-field coupling." Computational Mechanics **62**(4): 815-833.

Alessi, R., M. Ambati, T. Gerasimov, S. Vidoli and L. De Lorenzis (2018). Comparison of Phase-Field Models of Fracture Coupled with Plasticity. Advances in Computational Plasticity: A Book in Honour of D. Roger J. Owen. E. Oñate, D. Peric, E. de Souza Neto and M. Chiumenti. Cham, Springer International Publishing**:** 1-21.

Alessi, R., J.-J. Marigo, C. Maurini and S. Vidoli (2018). "Coupling damage and plasticity for a phase-field regularisation of brittle, cohesive and ductile fracture: One-dimensional examples." International Journal of Mechanical Sciences **149**: 559-576.

Alessi, R., J.-J. Marigo and S. Vidoli (2014). "Gradient Damage Models Coupled with Plasticity and Nucleation of Cohesive Cracks." Archive for Rational Mechanics and Analysis **214**(2): 575-615.

Ambati, M. and L. De Lorenzis (2016). "Phase-field modeling of brittle and ductile fracture in shells with isogeometric NURBS-based solid-shell elements." Computer Methods in Applied Mechanics and Engineering **312**: 351-373.

Ambati, M., T. Gerasimov and L. De Lorenzis (2014). "A review on phase-field models of brittle fracture and a new fast hybrid formulation." Computational Mechanics **55**(2): 383-405.

Ambati, M., T. Gerasimov and L. De Lorenzis (2015). "Phase-field modeling of ductile fracture." Computational Mechanics **55**(5): 1017-1040.

Ambati, M., J. Heinzmann, M. Seiler and M. Kästner (2022). "Phase‐field modeling of brittle fracture along the thickness direction of plates and shells." International Journal for Numerical Methods in Engineering **123**(17): 4094-4118.

Ambati, M., R. Kruse and L. De Lorenzis (2015). "A phase-field model for ductile fracture at finite strains and its experimental verification." Computational Mechanics **57**(1): 149-167.

Amiri, F., D. Millán, Y. Shen, T. Rabczuk and M. Arroyo (2014). "Phase-field modeling of fracture in linear thin shells." Theoretical and Applied Fracture Mechanics **69**: 102-109.

Amor, H., J.-J. Marigo and C. Maurini (2009). "Regularized formulation of the variational brittle fracture with unilateral contact: Numerical experiments." Journal of the Mechanics and Physics of Solids **57**(8): 1209-1229.

Annavarapu, C., M. Hautefeuille and J. E. Dolbow (2012). "Stable imposition of stiff constraints in explicit dynamics for embedded finite element methods." International Journal for Numerical Methods in Engineering **92**(2): 206-228.

Areias, P., T. Rabczuk and M. A. Msekh (2016). "Phase-field analysis of finite-strain plates and shells including element subdivision." Computer Methods in Applied

Mechanics and Engineering **312**: 322-350.
Areias, P. M. A. and T. Belytschko (2004). "Non-linear analysis of shells with arbitrary evolving cracks using XFEM." International Journal for Numerical Methods in Engineering **62**(3): 384-415.
Azinpour, E., R. Darabi, J. Cesar de Sa, A. Santos, J. Hodek and J. Dzugan (2020). "Fracture analysis in directed energy deposition (DED) manufactured 316L stainless steel using a phase-field approach." Finite Elements in Analysis and Design **177**.
Azinpour, E., J. P. S. Ferreira, M. P. L. Parente and J. C. de Sa (2018). "A simple and unified implementation of phase field and gradient damage models." Advanced Modeling and Simulation in Engineering Sciences **5**(1).
Azinpour, E., J. C. d. Sa and A. D. d. Santos (2020). "Micromechanically-motivated phase field approach to ductile fracture." International Journal of Damage Mechanics **30**(1): 46-76.
B.Shen and O.Stephansson (1994). "Modification of the G-criterion for Crack Propagation Subjected to Compression." Engineering Fracture Mechanics **47**(2): 177-189.
Bai, Y. and T. Wierzbicki (2009). "Application of extended Mohr–Coulomb criterion to ductile fracture." International Journal of Fracture **161**(1): 1-20.
Bao, Y. (2003). Prediction of Ductile Crack Formation in Uncracked Bodies. Doctor of Philosphy, Massachusetts Institute of Technology.
Bao, Y. and T. Wierzbicki (2004). "On fracture locus in the equivalent strain and stress triaxiality space." International Journal of Mechanical Sciences **46**(1): 81-98.
Bazant, Z. P. and M. Jirasek (2002). "Nonlocal Integral Formulations of Plasticity and Damage Survey of Progress." Journal of Engineering Mechanics **128**(11).
Behera, A. K., K. H. Sudeep and M. M. Rahaman (2023). "Thermodynamically consistent volumetric–deviatoric decomposition-based phase-field model for thermo-electro-mechanical fracture." Engineering Fracture Mechanics **290**.
Behzadinasab, M. and J. T. Foster (2019). "The third Sandia Fracture Challenge: peridynamic blind prediction of ductile fracture characterization in additively manufactured metal." International Journal of Fracture **218**(1-2): 97-109.
Behzadinasab, M. and J. T. Foster (2020). "Revisiting the third Sandia Fracture Challenge: a bond-associated, semi-Lagrangian peridynamic approach to modeling large deformation and ductile fracture." International Journal of Fracture **224**(2): 261-267.
Belytschko, T. and T. Black (1999). "Elastic crack growth in finite elements with minimal remeshing." International journal for numerical methods in engineering **45**: 601-620.
Borden, M. J., T. J. R. Hughes, C. M. Landis, A. Anvari and I. J. Lee (2016). "A phase-field formulation for fracture in ductile materials: Finite deformation balance law derivation, plastic degradation, and stress triaxiality effects." Computer Methods in Applied Mechanics and Engineering **312**: 130-166.
Borden, M. J., C. V. Verhoosel, M. A. Scott, T. J. R. Hughes and C. M. Landis (2012). "A phase-field description of dynamic brittle fracture." Computer Methods in Applied Mechanics and Engineering **217-220**: 77-95.
Bourdin, B., G. A. Francfort and J.-J. Marigo (2000). "Numerical experiments in revisited brittle fracture." Journal of the Mechanics and Physics of Solids **48**(2000): 797-826.
Bourdin, B., G. A. Francfort and J.-J. Marigo (2008). "The Variational Approach to Fracture." Journal of Elasticity **91**(1-3): 5-148.
Brünig, M., D. Brenner and S. Gerke (2015). "Stress state dependence of ductile damage and fracture behavior: Experiments and numerical simulations." Engineering Fracture

Mechanics **141**: 152-169.
Bryant, E. C. and W. Sun (2018). "A mixed-mode phase field fracture model in anisotropic rocks with consistent kinematics." Computer Methods in Applied Mechanics and Engineering **342**: 561-584.
Cao, Y., W. Wang, W. Shen, X. Cui and J. Shao (2022). "A new hybrid phase-field model for modeling mixed-mode cracking process in anisotropic plastic rock-like materials." International Journal of Plasticity **157**.
Chen, B., Y. Sun, B. R. Barboza, A. R. Barron and C. Li (2020). "Phase-field simulation of hydraulic fracturing with a revised fluid model and hybrid solver." Engineering Fracture Mechanics **229**.
Chen, L., B. Li and R. Borst (2020). "Adaptive isogeometric analysis for phase-field modeling of anisotropic brittle fracture." International Journal for Numerical Methods in Engineering.
Chen, Y., Y. Kang, Y. Zhao, L. Wang, J. Liu, Y. Li, Z. Liang, X. He, X. Li, N. Tavajohi and B. Li (2021). "A review of lithium-ion battery safety concerns: The issues, strategies, and testing standards." Journal of Energy Chemistry **59**: 83-99.
Chen, Z., C. Han, M. Gao, S. Y. Kandukuri and K. Zhou (2021). "A review on qualification and certification for metal additive manufacturing." Virtual and Physical Prototyping **17**(2): 382-405.
Chessa, J., P. Smolinski and T. Belytschko (2001). "The extended finite element method (XFEM) for solidification problems." International Journal for Numerical Methods in Engineering **53**(8): 1959-1977.
Choo, J. and W. Sun (2018). "Coupled phase-field and plasticity modeling of geological materials: From brittle fracture to ductile flow." Computer Methods in Applied Mechanics and Engineering **330**: 1-32.
Chukwudozie, C., B. Bourdin and K. Yoshioka (2019). "A variational phase-field model for hydraulic fracturing in porous media." Computer Methods in Applied Mechanics and Engineering **347**: 957-982.
Cirak, F., M. Ortiz and A. Pandolfi (2005). "A cohesive approach to thin-shell fracture and fragmentation." Computer Methods in Applied Mechanics and Engineering **194**(21-24): 2604-2618.
Cotterell, B. and J.R.Rice (1980). "Slightly curved or kinked cracks." International Journal of Fracture **16**(2): 155-169.
da Silva, M. N., F. P. Duda and E. Fried (2013). "Sharp-crack limit of a phase-field model for brittle fracture." Journal of the Mechanics and Physics of Solids **61**(11): 2178-2195.
Da Silva Santos, I., D. F. B. Sarzosa and M. Paredes (2022). "Ductile fracture modeling using the modified Mohr–Coulomb model coupled with a softening law for an ASTM A285 steel." Thin-Walled Structures **176**.
de Borst, R. and C. V. Verhoosel (2016). "Gradient damage vs phase-field approaches for fracture: Similarities and differences." Computer Methods in Applied Mechanics and Engineering **312**: 78-94.
Dinachandra, M. and A. Alankar (2020). "A phase-field study of crack propagation and branching in functionally graded materials using explicit dynamics." Theoretical and Applied Fracture Mechanics **109**.
Dittmann, M., F. Aldakheel, J. Schulte, F. Schmidt, M. Krüger, P. Wriggers and C. Hesch (2020). "Phase-field modeling of porous-ductile fracture in non-linear thermo-elasto-plastic solids." Computer Methods in Applied Mechanics and Engineering **361**.
Dittmann, M., F. Aldakheel, J. Schulte, P. Wriggers and C. Hesch (2018). "Variational

phase-field formulation of non-linear ductile fracture." Computer Methods in Applied Mechanics and Engineering **342**: 71-94.
Dou, W., Z. Xu, Y. Han and F. Huang (2023). "A ductile fracture model incorporating stress state effect." International Journal of Mechanical Sciences **241**.
Du, Z., G. Zhang, T. Guo, S. Tang and X. Guo (2020). "Tension-compression asymmetry at finite strains: A theoretical model and exact solutions." Journal of the Mechanics and Physics of Solids **143**.
Dunne, F. and N. Petrinic (2005). Introduction to Computational Plasticity. New York, Oxford University Press.
Ebenfeld, S. (1999). "A comparison of the plate theories in the sense of Kirchhoff-Love and Reissner-Mindlin." Mathematical Methods in the Applied Sciences **22**(17): 1505-1534.
Ehlers, W. and C. Luo (2017). "A phase-field approach embedded in the Theory of Porous Media for the description of dynamic hydraulic fracturing." Computer Methods in Applied Mechanics and Engineering **315**: 348-368.
Elices, M., G. V. Guinea, J. G. omez and J. Planas (2002). "The cohesive zone model: advantages, limitations and challenges." Engineering Fracture Mechanics **69**: 137-163.
Fan, M., Y. Jin and T. Wick (2021). "A quasi-monolithic phase-field description for mixed-mode fracture using predictor–corrector mesh adaptivity." Engineering with Computers.
Fang, J., C. Wu, J. Li, Q. Liu, C. Wu, G. Sun and Q. Li (2019). "Phase field fracture in elasto-plastic solids: Variational formulation for multi-surface plasticity and effects of plastic yield surfaces and hardening." International Journal of Mechanical Sciences **156**: 382-396.
Fang, J., C. Wu, T. Rabczuk, C. Wu, C. Ma, G. Sun and Q. Li (2019). "Phase field fracture in elasto-plastic solids: Abaqus implementation and case studies." Theoretical and Applied Fracture Mechanics **103**.
Fang, J., C. Wu, T. Rabczuk, C. Wu, G. Sun and Q. Li (2020). "Phase field fracture in elasto-plastic solids: a length-scale insensitive model for quasi-brittle materials." Computational Mechanics **66**(4): 931-961.
Fei, F. and J. Choo (2021). "Double-phase-field formulation for mixed-mode fracture in rocks." Computer Methods in Applied Mechanics and Engineering **376**.
Feng, Y., Q. Wang, D. Wu, Z. Luo, X. Chen, T. Zhang and W. Gao (2021). "Machine learning aided phase field method for fracture mechanics." International Journal of Engineering Science **169**.
Feng, Y., D. Wu, M. G. Stewart and W. Gao (2023). "Past, current and future trends and challenges in non-deterministic fracture mechanics: A review." Computer Methods in Applied Mechanics and Engineering **412**.
Fourmeau, M., T. Børvik, A. Benallal, O. G. Lademo and O. S. Hopperstad (2011). "On the plastic anisotropy of an aluminium alloy and its influence on constrained multiaxial flow." International Journal of Plasticity **27**(12): 2005-2025.
Francfort, G. A. and J.-J. Marigo (1998). "Revisiting brittle fracture as an energy minimization problem." Journal of mechanics and physics of solids **46**(8): 1319-1342.
Freddi, F. and F. Iurlano (2017). "Numerical insight of a variational smeared approach to cohesive fracture." Journal of the Mechanics and Physics of Solids **98**: 156-171.
Gavagnin, C., L. Sanavia and L. De Lorenzis (2020). "Stabilized mixed formulation for phase-field computation of deviatoric fracture in elastic and poroelastic materials." Computational Mechanics **65**(6): 1447-1465.

Geelen, R., J. Plews, M. Tupek and J. Dolbow (2020). "An extended/generalized phase-field finite element method for crack growth with global-local enrichment." International Journal for Numerical Methods in Engineering **121**(11): 2534-2557.
Giovan, M. N. and G. Sines (2006). "Biaxial and Uniaxial Data for Statistical Comparisons of a Ceramic's Strength." Journal of the American Ceramic Society **62**(9-10): 510-515.
Golahmar, A., P. K. Kristensen, C. F. Niordson and E. Martínez-Pañeda (2022). "A phase field model for hydrogen-assisted fatigue." International Journal of Fatigue **154**.
Greve, L. and C. Fehrenbach (2012). "Mechanical testing and macro-mechanical finite element simulation of the deformation, fracture, and short circuit initiation of cylindrical Lithium ion battery cells." Journal of Power Sources **214**: 377-385.
Griffiths, D. V. (1986). "Some theoretical observations on conical failure criteria in principal stress space." International Journal of Solids and Structures **22**(5): 553-565.
Han, J., S. Matsubara, S. Moriguchi, M. Kaliske and K. Terada (2021). "Crack phase-field model equipped with plastic driving force and degrading fracture toughness for ductile fracture simulation." Computational Mechanics **69**(1): 151-175.
Hannon, A. and P. Tiernan (2008). "A review of planar biaxial tensile test systems for sheet metal." Journal of Materials Processing Technology **198**(1-3): 1-13.
Heider, Y. (2021). "A review on phase-field modeling of hydraulic fracturing." Engineering Fracture Mechanics **253**.
Hesammokri, P., H. Yu and P. Isaksson (2023). "An extended hydrostatic–deviatoric strain energy density decomposition for phase-field fracture theories." International Journal of Solids and Structures **262-263**.
Hofacker, M. and C. Miehe (2012). "Continuum phase field modeling of dynamic fracture: variational principles and staggered FE implementation." International Journal of Fracture **178**(1-2): 113-129.
Hu, T., B. Talamini, A. J. Stershic, M. R. Tupek and J. E. Dolbow (2021). "A variational phase-field model For ductile fracture with coalescence dissipation." Computational Mechanics **68**(2): 311-335.
Hu, X., S. Tan, D. Xia, L. Min, H. Xu, W. Yao, Z. Sun, P. Zhang, T. Quoc Bui, X. Zhuang and T. Rabczuk (2023). "An overview of implicit and explicit phase field models for quasi-static failure processes, implementation and computational efficiency." Theoretical and Applied Fracture Mechanics **124**.
Huang, C. and X. Gao (2019). "Development of a phase field method for modeling brittle and ductile fracture." Computational Materials Science **169**.
Huang, D., D. Gu, C. Yang, R. Huang and G. Fu (2015). "Investigation on Mechanical Behaviors of Sandstone with Two Preexisting Flaws under Triaxial Compression." Rock Mechanics and Rock Engineering **49**(2): 375-399.
Jeong, H., S. Signetti, T.-S. Han and S. Ryu (2018). "Phase field modeling of crack propagation under combined shear and tensile loading with hybrid formulation." Computational Materials Science **155**: 483-492.
Jiang, Y., C. Li, C. Wu, T. Rabczuk and J. Fang (2023). "A double-phase field method for mixed mode crack modelling in 3D elasto-plastic solids with crack-direction-based strain energy decomposition." Computer Methods in Applied Mechanics and Engineering **405**: 115886.
Karlson, K. N., C. Alleman, J. W. Foulk Iii, K. L. Manktelow, J. T. Ostien, M. E. Stender, A. J. Stershic and M. G. Veilleux (2019). "Sandia Fracture Challenge 3: detailing the Sandia Team Q failure prediction strategy." International Journal of Fracture **218**(1-2):

149-170.
Karma, A., D. A. Kessler and H. Levine (2001). "Phase-field model of mode III dynamic fracture." Phys Rev Lett **87**(4): 045501.
Keesecker, A. L., C. G. Dávila, E. R. Johnson and J. H. Starnes (2003). "Crack path bifurcation at a tear strap in a pressurized shell." Computers & Structures **81**(16): 1633-1642.
Khodadadian, A., N. Noii, M. Parvizi, M. Abbaszadeh, T. Wick and C. Heitzinger (2020). "A Bayesian estimation method for variational phase-field fracture problems." Comput Mech **66**(4): 827-849.
Kiendl, J., M. Ambati, L. De Lorenzis, H. Gomez and A. Reali (2016). "Phase-field description of brittle fracture in plates and shells." Computer Methods in Applied Mechanics and Engineering **312**: 374-394.
Kienle, D., F. Aldakheel and M.-A. Keip (2019). "A finite-strain phase-field approach to ductile failure of frictional materials." International Journal of Solids and Structures **172-173**: 147-162.
Kikis, G., M. Ambati, L. De Lorenzis and S. Klinkel (2021). "Phase-field model of brittle fracture in Reissner–Mindlin plates and shells." Computer Methods in Applied Mechanics and Engineering **373**.
Kramer, S. L. B., T. A. Ivanoff, J. D. Madison and A. P. Lentfer (2019). "Evolution of damage and failure in an additively manufactured 316L SS structure: experimental reinvestigation of the third Sandia fracture challenge." International Journal of Fracture **218**(1-2): 63-84.
Kramer, S. L. B., A. Jones, A. Mostafa, B. Ravaji, T. Tancogne-Dejean, C. C. Roth, M. G. Bandpay, K. Pack, J. T. Foster, M. Behzadinasab, J. C. Sobotka, J. M. McFarland, J. Stein, A. D. Spear, P. Newell, M. W. Czabaj, B. Williams, H. Simha, M. Gesing, L. N. Gilkey, C. A. Jones, R. Dingreville, S. E. Sanborn, J. L. Bignell, A. R. Cerrone, V. Keim, A. Nonn, S. Cooreman, P. Thibaux, N. Ames, D. O. Connor, M. Parno, B. Davis, J. Tucker, B. Coudrillier, K. N. Karlson, J. T. Ostien, J. W. Foulk, C. I. Hammetter, S. Grange, J. M. Emery, J. A. Brown, J. E. Bishop, K. L. Johnson, K. R. Ford, S. Brinckmann, M. K. Neilsen, J. Jackiewicz, K. Ravi-Chandar, T. Ivanoff, B. C. Salzbrenner and B. L. Boyce (2019). "The third Sandia fracture challenge: predictions of ductile fracture in additively manufactured metal." International Journal of Fracture **218**(1-2): 5-61.
Kristensen, P. K. and E. Martínez-Pañeda (2020). "Phase field fracture modelling using quasi-Newton methods and a new adaptive step scheme." Theoretical and Applied Fracture Mechanics **107**.
Kuhn, C., A. Schlüter and R. Müller (2015). "On degradation functions in phase field fracture models." Computational Materials Science **108**: 374-384.
Kumar, S. and B. P. Patel (2024). "Stress triaxiality and Lode angle parameters driven phase field coupled finite deformation plasticity formulation of ductile fracture." Computer Methods in Applied Mechanics and Engineering **432**.
Lancioni, G. and G. Royer-Carfagni (2009). "The Variational Approach to Fracture Mechanics. A Practical Application to the French Panthéon in Paris." Journal of Elasticity **95**(1-2): 1-30.
Lemaitre, J. (1985). "A Continuous Damage Mechanics Model for Ductile Fracture." Journal of Engineering Materials and Technology **107**(7): 83-89.
Li, B., D. Millán, A. Torres-Sánchez, B. Roman and M. Arroyo (2018). "A variational model of fracture for tearing brittle thin sheets." Journal of the Mechanics and Physics of Solids **119**: 334-348.
Li, C., J. Fang, N. Qiu, C. Wu, G. Steven and Q. Li (2024). "On fracture mechanism of

additively manufactured triply periodic minimal surface structures using an explicit phase field model." Additive Manufacturing **86**.
Li, C., J. Fang, N. Qiu, C. Wu, G. Steven and Q. Li (2024). "Phase field fracture in elasto-plastic solids: Considering complex loading history for crushing simulations." International Journal of Mechanical Sciences **268**.
Li, C., J. Fang, Y. Wan, N. Qiu, G. Steven and Q. Li (2023). "Phase field fracture model for additively manufactured metallic materials." International Journal of Mechanical Sciences **251**.
Li, C., J. Fang, C. Wu, G. Sun, G. Steven and Q. Li (2022). "Phase field fracture in elasto-plastic solids: Incorporating phenomenological failure criteria for ductile materials." Computer Methods in Applied Mechanics and Engineering **391**.
Li, C., J. Liu, L. Dong, C. Wu, G. Steven, Q. Li and J. Fang (2025). "Phase field fracture in elastoplastic solids: a stress-state, strain-rate, and orientation dependent model in explicit dynamics and its applications to additively manufactured metals." Journal of the Mechanics and Physics of Solids **197**.
Li, Z., Y. Shen, F. Han and Z. Yang (2021). "A phase field method for plane-stress fracture problems with tension-compression asymmetry." Engineering Fracture Mechanics **257**.
Liu, B., Y. Jia, C. Yuan, L. Wang, X. Gao, S. Yin and J. Xu (2020). "Safety issues and mechanisms of lithium-ion battery cell upon mechanical abusive loading: A review." Energy Storage Materials **24**: 85-112.
Liu, S., Z. Wang, Y. Zhang, M. Kou and J. Bi (2022). "The phase-field simulations of blasting failure in granites." International Journal of Impact Engineering **167**.
Løland, K. E. (1980). "Continuous damage model for load-response estimation of concrete." Cement and Concrete Research **10**(3): 395-402.
Lorentz, E., S. Cuvilliez and K. Kazymyrenko (2011). "Convergence of a gradient damage model toward a cohesive zone model." Comptes Rendus Mécanique **339**(1): 20-26.
Lorentz, E. and V. Godard (2011). "Gradient damage models: Toward full-scale computations." Computer Methods in Applied Mechanics and Engineering **200**(21-22): 1927-1944.
Luo, C., L. Chen and Y. Huang (2021). "A phase-field crack model based on a directional strain decomposition and a stress-driven Crack-Opening Indicator." Computer Methods in Applied Mechanics and Engineering **384**.
Ma, R., W. Sun and T. Guo (2024). "Phase‐field model for ductile fracture in the stress resultant geometrically exact shell." International Journal for Numerical Methods in Engineering **125**(13).
Mahalle, G., A. Morchhale, N. Kotkunde, A. K. Gupta, S. K. Singh and Y. C. Lin (2020). "Forming and fracture limits of IN718 alloy at elevated temperatures: Experimental and theoretical investigation." Journal of Manufacturing Processes **56**: 482-499.
Mandal, T. K., V. P. Nguyen and A. Heidarpour (2019). "Phase field and gradient enhanced damage models for quasi-brittle failure: A numerical comparative study." Engineering Fracture Mechanics **207**: 48-67.
Marigo, J.-J., C. Maurini and K. Pham (2016). "An overview of the modelling of fracture by gradient damage models." Meccanica **51**(12): 3107-3128.
Martínez-Pañeda, E., A. Golahmar and C. F. Niordson (2018). "A phase field formulation for hydrogen assisted cracking." Computer Methods in Applied Mechanics and Engineering **342**: 742-761.
McAuliffe, C. and H. Waisman (2016). "A coupled phase field shear band model for

ductile–brittle transition in notched plate impacts." Computer Methods in Applied Mechanics and Engineering **305**: 173-195.
Miehe, C., F. Aldakheel and A. Raina (2016). "Phase field modeling of ductile fracture at finite strains: A variational gradient-extended plasticity-damage theory." International Journal of Plasticity **84**: 1-32.
Miehe, C., M. Hofacker, L. M. Schänzel and F. Aldakheel (2015). "Phase field modeling of fracture in multi-physics problems. Part II. Coupled brittle-to-ductile failure criteria and crack propagation in thermo-elastic–plastic solids." Computer Methods in Applied Mechanics and Engineering **294**: 486-522.
Miehe, C., M. Hofacker and F. Welschinger (2010). "A phase field model for rate-independent crack propagation: Robust algorithmic implementation based on operator splits." Computer methods in applied mechanics and engineering **199**(45): 2765-2778.
Miehe, C. and S. Mauthe (2016). "Phase field modeling of fracture in multi-physics problems. Part III. Crack driving forces in hydro-poro-elasticity and hydraulic fracturing of fluid-saturated porous media." Computer Methods in Applied Mechanics and Engineering **304**: 619-655.
Miehe, C., L.-M. Schänzel and H. Ulmer (2015). "Phase field modeling of fracture in multi-physics problems. Part I. Balance of crack surface and failure criteria for brittle crack propagation in thermo-elastic solids." Computer Methods in Applied Mechanics and Engineering **294**: 449-485.
Miehe, C., F. Welschinger and F. Aldakheel (2014). "Variational gradient plasticity at finite strains. Part II: Local–global updates and mixed finite elements for additive plasticity in the logarithmic strain space." Computer Methods in Applied Mechanics and Engineering **268**: 704-734.
Miehe, C., F. Welschinger and M. Hofacker (2010). "Thermodynamically consistent phase-field models of fracture: Variational principles and multi-field FE implementations." International Journal for Numerical Methods in Engineering **83**(10): 1273-1311.
Mohr, D. and S. J. Marcadet (2015). "Micromechanically-motivated phenomenological Hosford–Coulomb model for predicting ductile fracture initiation at low stress triaxialities." International Journal of Solids and Structures **67-68**: 40-55.
Molnár, G. and A. Gravouil (2017). "2D and 3D Abaqus implementation of a robust staggered phase-field solution for modeling brittle fracture." Finite Elements in Analysis and Design **130**: 27-38.
Mooney, B., K. I. Kourousis and R. Raghavendra (2019). "Plastic anisotropy of additively manufactured maraging steel: Influence of the build orientation and heat treatments." Additive Manufacturing **25**: 19-31.
Munjiza, A., Z. Lei, V. Divic and B. Peros (2013). "Fracture and fragmentation of thin shells using the combined finite–discrete element method." International Journal for Numerical Methods in Engineering **95**(6): 478-498.
Neto, E. A. d. S., D. Peric and D. R. Owen (2011). Computational methods for plasticity: theory and applications, John Wiley & Sons Ltd.
Nguyen, N. H. T., H. H. Bui, G. D. Nguyen and J. Kodikara (2017). "A cohesive damage-plasticity model for DEM and its application for numerical investigation of soft rock fracture properties." International Journal of Plasticity **98**: 175-196.
Nguyen, T. T., J. Yvonnet, D. Waldmann and Q. C. He (2020). "Implementation of a new strain split to model unilateral contact within the phase field method." International Journal for Numerical Methods in Engineering **121**(21): 4717-4733.
Noii, N., A. Khodadadian, J. Ulloa, F. Aldakheel, T. Wick, S. François and P. Wriggers

(2021). "Bayesian inversion for unified ductile phase-field fracture." Computational Mechanics **68**(4): 943-980.
Oliver, J. (1996). "Modelling strong discontinuities in solid mechanics via strain softening constitutive equations. Part 1: fundamentals." International journal for numerical methods in engineering **39**: 3575-3600.
Pham, K. H., K. Ravi-Chandar and C. M. Landis (2017). "Experimental validation of a phase-field model for fracture." International Journal of Fracture **205**(1): 83-101.
Pillai, U., S. P. Triantafyllou, I. Ashcroft, Y. Essa and F. M. de la Escalera (2020). "Phase-field modelling of brittle fracture in thin shell elements based on the MITC4+ approach." Computational Mechanics **65**(6): 1413-1432.
Prakash, V., A. K. Behera and M. M. Rahaman (2022). "A phase-field model for thermo-mechanical fracture." Mathematics and Mechanics of Solids **28**(2): 533-561.
Préve, D., P. Lenarda, I. Maskery and M. Paggi (2023). "A comprehensive characterization of fracture in unit cell open foams generated from Triply Periodic Minimal Surfaces." Engineering Fracture Mechanics **277**.
Proserpio, D., M. Ambati, L. De Lorenzis and J. Kiendl (2020). "A framework for efficient isogeometric computations of phase-field brittle fracture in multipatch shell structures." Computer Methods in Applied Mechanics and Engineering **372**.
Proserpio, D., M. Ambati, L. De Lorenzis and J. Kiendl (2021). "Phase-field simulation of ductile fracture in shell structures." Computer Methods in Applied Mechanics and Engineering **385**.
Qiu, N., Y. Wan, Y. Shen and J. Fang (2024). "Experimental and numerical studies on mechanical properties of TPMS structures." International Journal of Mechanical Sciences **261**.
Reinoso, J., P. Durand, P. Budarapu and M. Paggi (2019). "Crack Patterns in Heterogenous Rocks Using a Combined Phase Field-Cohesive Interface Modeling Approach: A Numerical Study." Energies **12**(6).
Reinoso, J., M. Paggi and C. Linder (2017). "Phase field modeling of brittle fracture for enhanced assumed strain shells at large deformations: formulation and finite element implementation." Computational Mechanics **59**(6): 981-1001.
Ren, H. L., X. Y. Zhuang, C. Anitescu and T. Rabczuk (2019). "An explicit phase field method for brittle dynamic fracture." Computers & Structures **217**: 45-56.
Richard, H. A., B. Schramm and N. H. Schirmeisen (2014). "Cracks on Mixed Mode loading – Theories, experiments, simulations." International Journal of Fatigue **62**: 93-103.
Rodriguez, P., J. Ulloa, C. Samaniego and E. Samaniego (2018). "A variational approach to the phase field modeling of brittle and ductile fracture." International Journal of Mechanical Sciences **144**: 502-517.
Roth, C. C. and D. Mohr (2014). "Effect of strain rate on ductile fracture initiation in advanced high strength steel sheets: Experiments and modeling." International Journal of Plasticity **56**: 19-44.
Roth, C. C. and D. Mohr (2016). "Ductile fracture experiments with locally proportional loading histories." International Journal of Plasticity **79**: 328-354.
Roubin, E., A. Vallade, N. Benkemoun and J.-B. Colliat (2015). "Multi-scale failure of heterogeneous materials: A double kinematics enhancement for Embedded Finite Element Method." International Journal of Solids and Structures **52**: 180-196.
Ruan, H., S. Rezaei, Y. Yang, D. Gross and B. Xu "A thermo-mechanical phase-field fracture model application to hot cracking simulations in additive manufacturing."
Sahraei, E., J. Campbell and T. Wierzbicki (2012). "Modeling and short circuit detection

of 18650 Li-ion cells under mechanical abuse conditions." Journal of Power Sources **220**: 360-372.
Samaniego, C., J. Ulloa, P. Rodríguez, G. Houzeaux, M. Vázquez and E. Samaniego (2021). "A phase-field model for ductile fracture with shear bands: A parallel implementation." International Journal of Mechanical Sciences **200**.
Santillán, D., J. C. Mosquera and L. Cueto-Felgueroso (2017). "Phase-field model for brittle fracture. Validation with experimental results and extension to dam engineering problems." Engineering Fracture Mechanics **178**: 109-125.
Scheunemann, L., P. S. B. Nigro, J. Schröder and P. M. Pimenta (2020). "A novel algorithm for rate independent small strain crystal plasticity based on the infeasible primal-dual interior point method." International Journal of Plasticity **124**: 1-19.
Seiler, M., T. Linse, P. Hantschke and M. Kästner (2020). "An efficient phase-field model for fatigue fracture in ductile materials." Engineering Fracture Mechanics **224**.
Shen, Z., W. Liu, S. Sang and T. Ma (2019). "Modified F-criterion and its influence on potential crack deflection range." International Journal of Solids and Structures **160**: 134-147.
Spear, A. D., M. W. Czabaj, P. Newell, K. DeMille, B. R. Phung, D. Zhao, P. Creveling, N. Briggs, E. Brodbine, C. Creveling, E. Edelman, K. Matheson, C. M. Arndt, M. Buelte, S. Childs, I. Nelson, F. Safazadeh, J. French, C. Audd, A. J. Smith, E. J. Dorrian, G. Clark, J. Tayler and R. Ichi (2019). "The third Sandia Fracture Challenge: from theory to practice in a classroom setting." International Journal of Fracture **218**(1-2): 171-194.
Spetz, A., R. Denzer, E. Tudisco and O. Dahlblom (2020). "Phase-field fracture modelling of crack nucleation and propagation in porous rock." International Journal of Fracture **224**(1): 31-46.
Spetz, A., R. Denzer, E. Tudisco and O. Dahlblom (2021). "A Modified Phase-Field Fracture Model for Simulation of Mixed Mode Brittle Fractures and Compressive Cracks in Porous Rock." Rock Mechanics and Rock Engineering **54**(10): 5375-5388.
Steinke, C. and M. Kaliske (2018). "A phase-field crack model based on directional stress decomposition." Computational Mechanics **63**(5): 1019-1046.
Steinke, C., J. Storm and M. Kaliske (2022). "Energetically motivated crack orientation vector for phase-field fracture with a directional split." International Journal of Fracture.
Storm, J., D. Supriatna and M. Kaliske (2019). "The concept of representative crack elements for phase-field fracture: Anisotropic elasticity and thermo-elasticity." International Journal for Numerical Methods in Engineering **121**(5): 779-805.
Strobl, M. and T. Seelig (2015). "A novel treatment of crack boundary conditions in phase field models of fracture." Pamm **15**(1): 155-156.
Strobl, M. and T. Seelig (2016). "On constitutive assumptions in phase field approaches to brittle fracture." Procedia Structural Integrity **2**: 3705-3712.
Sun, P., Z. Lu, Z. Wang and J. Wu (2023). "A phase-field formulation based on an extended F-criterion for rock fracture." International Journal for Numerical and Analytical Methods in Geomechanics **48**(1): 250-269.
System, D. (2000). ABAQUS user's maual.
T.N.Bittencourt (1996). "Quasi-automatica simulation of crack propagation for 2D lefm problems." Engineering Fracture Mechanics **55**(2): 321-334.
Tancogne-Dejean, T., M. B. Gorji, K. Pack and C. C. Roth (2019). "The third Sandia Fracture Challenge: deterministic and probabilistic modeling of ductile fracture of additively-manufactured material." International Journal of Fracture **218**(1-2): 209-229.
Tang, S., G. Zhang, T. F. Guo, X. Guo and W. K. Liu (2019). "Phase field modeling of

fracture in nonlinearly elastic solids via energy decomposition." Computer Methods in Applied Mechanics and Engineering **347**: 477-494.
Ulloa, J., J. Wambacq, R. Alessi, G. Degrande and S. François (2021). "Phase-field modeling of fatigue coupled to cyclic plasticity in an energetic formulation." Computer Methods in Applied Mechanics and Engineering **373**.
Ulmer, H., M. Hofacker and C. Miehe (2012). "Phase Field Modeling of Fracture in Plates and Shells." Pamm **12**(1): 171-172.
Ulmer, H., M. Hofacker and C. Miehe (2013). "Phase Field Modeling of Brittle and Ductile Fracture." Pamm **13**(1): 533-536.
Voce, E. (1955). "A practical strain hardening function." Metallurgia **51**: 219-226.
Wallat, L., M. Reder, M. Selzer, F. Poehler and B. Nestler (2023). "Shape optimization of porous structures by phase-field modeling with strain energy density reduction." Materials Today Communications **37**.
Wambacq, J., J. Ulloa, G. Lombaert and S. François (2021). "A dissipation-based path-following technique for the phase-field approach to brittle and ductile fracture." International Journal for Numerical Methods in Engineering **122**(15): 3919-3940.
Wang, F., J. Shao and H. Huang (2021). "A phase-field modeling method for the mixed-mode fracture of brittle materials based on spectral decomposition." Engineering Fracture Mechanics **242**.
Wang, L., S. Yin and J. Xu (2019). "A detailed computational model for cylindrical lithium-ion batteries under mechanical loading: From cell deformation to short-circuit onset." Journal of Power Sources **413**: 284-292.
Wang, L., S. Yin, Z. Yu, Y. Wang, T. X. Yu, J. Zhao, Z. Xie, Y. Li and J. Xu (2018). "Unlocking the significant role of shell material for lithium-ion battery safety." Materials & Design **160**: 601-610.
Wang, M., Z. Yu, Y. Jin and J. Shao (2021). "Modeling of damage and cracking in heterogeneous rock-like materials by phase-field method." Mechanics Research Communications **114**.
Wang, Q., Y. T. Feng, W. Zhou, Y. Cheng and G. Ma (2020). "A phase-field model for mixed-mode fracture based on a unified tensile fracture criterion." Computer Methods in Applied Mechanics and Engineering **370**.
Wang, T., H. Han, G. Huang, Z. Liu and Z. Zhuang (2022). "Three-layer phase-field model of finite strain shell for simulating quasi-static and dynamic fracture of elasto-plastic materials." Engineering Fracture Mechanics **267**.
Wang, T., X. Ye, Z. Liu, D. Chu and Z. Zhuang (2019). "Modeling the dynamic and quasi-static compression-shear failure of brittle materials by explicit phase field method." Computational Mechanics **64**(6): 1537-1556.
Wang, T., X. Ye, Z. Liu, X. Liu, D. Chu and Z. Zhuang (2020). "A phase-field model of thermo-elastic coupled brittle fracture with explicit time integration." Computational Mechanics **65**(5): 1305-1321.
Wang, W., S. Yang, C. Lin, W. Shen, G. Lu, Y. Li and J. Zhang (2020). "Investigation of mechanical property of cylindrical lithium-ion batteries under dynamic loadings." Journal of Power Sources **451**.
Wang, Y., W. Wang, B. Zhang and C.-Q. Li (2020). "A review on mixed mode fracture of metals." Engineering Fracture Mechanics **235**.
Wheeler, M. F., T. Wick and S. Lee (2020). "IPACS: Integrated Phase-Field Advanced Crack Propagation Simulator. An adaptive, parallel, physics-based-discretization phase-field framework for fracture propagation in porous media." Computer Methods in Applied

Mechanics and Engineering **367**.
Wilson-Heid, A. E. and A. M. Beese (2019). "Fracture of laser powder bed fusion additively manufactured Ti–6Al–4V under multiaxial loading: Calibration and comparison of fracture models." Materials Science and Engineering: A **761**.
Wilson, Z. A. and C. M. Landis (2016). "Phase-field modeling of hydraulic fracture." Journal of the Mechanics and Physics of Solids **96**: 264-290.
Wong, L. N. Y. and H. H. Einstein (2009). "Systematic evaluation of cracking behavior in specimens containing single flaws under uniaxial compression." International Journal of Rock Mechanics and Mining Sciences **46**(2): 239-249.
Wu, C., J. Fang, Z. Zhang, A. Entezari, G. Sun, M. V. Swain and Q. Li (2020). "Fracture modeling of brittle biomaterials by the phase-field method." Engineering Fracture Mechanics **224**.
Wu, J.-Y. (2017). "A unified phase-field theory for the mechanics of damage and quasi-brittle failure." Journal of the Mechanics and Physics of Solids **103**: 72-99.
Wu, J.-Y. (2018). "A geometrically regularized gradient-damage model with energetic equivalence." Computer Methods in Applied Mechanics and Engineering **328**: 612-637.
Wu, J.-Y. and M. Cervera (2018). "A novel positive/negative projection in energy norm for the damage modeling of quasi-brittle solids." International Journal of Solids and Structures **139-140**: 250-269.
Wu, J.-Y., Y. Huang, H. Zhou and V. P. Nguyen (2021). "Three-dimensional phase-field modeling of mode I + II/III failure in solids." Computer Methods in Applied Mechanics and Engineering **373**.
Wu, J.-Y., T. K. Mandal and V. P. Nguyen (2020). "A phase-field regularized cohesive zone model for hydrogen assisted cracking." Computer Methods in Applied Mechanics and Engineering **358**.
Wu, J.-Y. and V. P. Nguyen (2018). "A length scale insensitive phase-field damage model for brittle fracture." Journal of the Mechanics and Physics of Solids **119**: 20-42.
Wu, J.-Y., V. P. Nguyen, H. Zhou and Y. Huang (2020). "A variationally consistent phase-field anisotropic damage model for fracture." Computer Methods in Applied Mechanics and Engineering **358**.
Wu, J.-Y. and S.-L. Xu (2013). "Reconsideration on the elastic damage/degradation theory for the modeling of microcrack closure-reopening (MCR) effects." International Journal of Solids and Structures **50**(5): 795-805.
Wu, T. and L. De Lorenzis (2016). "A phase-field approach to fracture coupled with diffusion." Computer Methods in Applied Mechanics and Engineering **312**: 196-223.
Xia, Y., T. Wierzbicki, E. Sahraei and X. Zhang (2014). "Damage of cells and battery packs due to ground impact." Journal of Power Sources **267**: 78-97.
Xie, D. and A. M. Waas (2006). "Discrete cohesive zone model for mixed-mode fracture using finite element analysis." Engineering Fracture Mechanics **73**(13): 1783-1796.
Xu, J., B. Liu and D. Hu (2016). "State of Charge Dependent Mechanical Integrity Behavior of 18650 Lithium-ion Batteries." Sci Rep **6**: 21829.
Yang, L., Y. Yang, H. Zheng and Z. Wu (2021). "An explicit representation of cracks in the variational phase field method for brittle fractures." Computer Methods in Applied Mechanics and Engineering **387**.
Yang, S., W. Wang, C. Lin, W. Shen and Y. Li (2019). "Improved constitutive model of the jellyroll for cylindrical lithium ion batteries considering microscopic damage." Energy **185**: 202-212.
Yang, X., Y. Guo and Y. Li (2023). "A new ductile failure criterion with stress triaxiality and Lode dependence." Engineering Fracture Mechanics **289**.

Yang, X., Y. Li, W. Jiang, M.-g. Duan, D. Chen and B. Li (2021). "Ductile fracture prediction of additive manufactured Ti6Al4V alloy based on an extended GTN damage model." Engineering Fracture Mechanics **256**.
Yin, B. and M. Kaliske (2020). "A ductile phase-field model based on degrading the fracture toughness: Theory and implementation at small strain." Computer Methods in Applied Mechanics and Engineering **366**.
Yin, B., C. Steinke and M. Kaliske (2019). "Formulation and implementation of strain rate-dependent fracture toughness in context of the phase-field method." International Journal for Numerical Methods in Engineering **121**(2): 233-255.
You, T., H. Waisman and Q.-Z. Zhu (2021). "Brittle-ductile failure transition in geomaterials modeled by a modified phase-field method with a varying damage-driving energy coefficient." International Journal of Plasticity **136**.
You, T., Q.-Z. Zhu, P.-F. Li and J.-F. Shao (2020). "Incorporation of tension-compression asymmetry into plastic damage phase-field modeling of quasi brittle geomaterials." International Journal of Plasticity **124**: 71-95.
Yu, H., L. Hao, R. Shen, L. Guo, Z. Shen and Y. Li (2022). "A phase field model with the mixed-mode driving force of power-law relation." Engineering Fracture Mechanics **264**.
Yu, T. and P. Xue (2022). Utilizing plastic deformation for energy absorption. Introduction to Engineering Plasticity**:** 293-326.
Yu, Z., J. Shao, G. Duveau, M.-N. Vu and G. Armand (2021). "Numerical modeling of deformation and damage around underground excavation by phase-field method with hydromechanical coupling." Computers and Geotechnics **138**.
Zaman, S. B., F. Barlat and J.-H. Kim (2018). "Deformation-induced anisotropy of uniaxially prestrained steel sheets." International Journal of Solids and Structures **134**: 20-29.
Zarrinzadeh, H., M. Z. Kabir and A. Varvani-Farahani (2020). "Static and dynamic fracture analysis of 3D cracked orthotropic shells using XFEM method." Theoretical and Applied Fracture Mechanics **108**.
Zavattieri, P. D. (2006). "Modeling of Crack Propagation in Thin-Walled Structures Using a Cohesive Model for Shell Elements." Journal of applied mechanics **73**(6): 948-958.
Zhang, B. and J. Luo (2021). "A phase field model for fracture based on the strain gradient elasticity theory with hybrid formulation." Engineering Fracture Mechanics **256**.
Zhang, F., W. Huang, X. Li and S. Zhang (2018). "Moving mesh finite element simulation for phase-field modeling of brittle fracture and convergence of Newton's iteration." Journal of Computational Physics **356**: 127-149.
Zhang, H., H. Peng, X.-y. Pei, P. Li, T.-g. Tang and L.-c. Cai (2021). "A phase-field model for spall fracture." Journal of Applied Physics **129**(12).
Zhang, X., S. W. Sloan, C. Vignes and D. Sheng (2017). "A modification of the phase-field model for mixed mode crack propagation in rock-like materials." Computer Methods in Applied Mechanics and Engineering **322**: 123-136.
Zhang, X. and T. Wierzbicki (2015). "Characterization of plasticity and fracture of shell casing of lithium-ion cylindrical battery." Journal of Power Sources **280**: 47-56.
Zhang, Y., Y. Liu and F. Yang (2022). "Ductile fracture modelling of steel plates under tensile and shear dominated states." Journal of Constructional Steel Research **197**.
Zhang, Z. F. and J. Eckert (2005). "Unified tensile fracture criterion." Phys Rev Lett **94**(9): 094301.
Zhao, Z., K. Huang, C. Li, C. Wang and H. Qin (2020). "A Novel Plastic Phase-Field Method for Ductile Fracture with GPU Optimization." Computer Graphics Forum **39**(7):

105-117.
Zhou, C., M. Hu, D. Xie, Z. Shu and J. He (2022). "Research on crack propagation of 3D printed material with complex cracks based on the phase-field fracture model." Acta Mechanica.
Zhou, S., X. Zhuang and T. Rabczuk (2019). "Phase field modeling of brittle compressive-shear fractures in rock-like materials: A new driving force and a hybrid formulation." Computer Methods in Applied Mechanics and Engineering **355**: 729-752.
Zhou, X., D. Lu, Y. Zhang, X. Du and T. Rabczuk (2022). "An open-source unconstrained stress updating algorithm for the modified Cam-clay model." Computer Methods in Applied Mechanics and Engineering **390**.
Zhu, J., X. Zhang, E. Sahraei and T. Wierzbicki (2016). "Deformation and failure mechanisms of 18650 battery cells under axial compression." Journal of Power Sources **336**: 332-340.
Zhu, Q.-Z. (2016). "A New Rock Strength Criterion from Microcracking Mechanisms Which Provides Theoretical Evidence of Hybrid Failure." Rock Mechanics and Rock Engineering **50**(2): 341-352.
Zi, G. and T. Belytschko (2003). "New crack-tip elements for XFEM and applications to cohesive cracks." International Journal for Numerical Methods in Engineering **57**(15): 2221-2240.